InGaN alloys and heterostructures: impact of localization effects on light-matter interaction in planar microcavities

THÈSE N^{O} 6415 (2014)

PRÉSENTÉE LE 21 NOVEMBRE 2014

À LA FACULTÉ DES SCIENCES DE BASE

LABORATOIRE EN SEMICONDUCTEURS AVANCÉS POUR LA PHOTONIQUE ET L'ÉLECTRONIQUE

PROGRAMME DOCTORAL EN PHOTONIQUE

ÉCOLE POLYTECHNIQUE FÉDÉRALE DE LAUSANNE

POUR L'OBTENTION DU GRADE DE DOCTEUR ÈS SCIENCES

PAR

Marlene GLAUSER

acceptée sur proposition du jury:

Prof. C. Moser, président du jury
Prof. N. Grandjean, Dr R. Butté, directeurs de thèse
Dr B. Gil, rapporteur
Dr M. Portella Oberli, rapporteuse
Prof. T. Suski, rapporteur

ÉCOLE POLYTECHNIQUE
FÉDÉRALE DE LAUSANNE

Suisse
2014

Dedicated to

Jonas Häner
my parents, Katharina and Andreas
my sisters, Isabelle and Alexandra

Abstract

The III-nitride semiconductor material system - (InAlGa)N - is of highest interest for optoelectronic applications due to its direct bandgap, tunable from the ultraviolet to the infrared spectral range. The most well-known are white light-emitting diodes, which are presently revolutionizing the general lighting market, and 405 nm laser diodes, the key elements of the Blu-ray Disc^{TM} technology. Furthermore, sophisticated devices like electrically-driven vertical-cavity surface-emitting lasers, which are microcavity based lasers, have been demonstrated recently, paving the way for electrically-driven low threshold room temperature polariton lasers. In 1996 Imamoğlu and coworkers predicted the possibility of achieving such a low threshold coherent light source from a polariton condensate in a suitable microcavity. The eigenmodes of such a microcavity are exciton-polaritons, admixed particles resulting from the strong coupling between a photonic mode and an excitonic resonance. Thanks to their very light effective mass at the center of the Brillouin zone (10^5 times lighter than that of a free electron) and efficient relaxation mechanism a phase transition toward an exciton-polariton condensate might occur at elevated temperatures (observed up to 340 K in GaN-based microcavities).

The goal of the present study is to provide a detailed theoretical analysis of the main emission features of electrically-driven polariton lasers based on planar GaN microcavities with embedded InGaN/GaN multiple quantum wells and to further derive the stringent requirements necessary for their experimental implementation. The complete polariton phase diagram is established for two experimentally relevant pumping geometries. Furthermore, the steady-state, the high-speed current modulation response, the relative intensity noise, and the Schawlow-Townes linewidth of those two geometries are derived. The resulting general expressions can be applied to any inorganic semiconductor polariton laser diodes.
Then the building blocks of such microcavities are experimentally analyzed separately, i.e., the bottom III-nitride based distributed Bragg reflector, the active medium, and the top dielectric Bragg reflector. An innovative optical characterization method allows to study the effect of the substrate on lattice-matched InAlN/GaN Bragg reflectors. The best optical quality is obtained for such Bragg reflectors when grown on high quality free-standing GaN substrates. Furthermore, particular attention is paid to the excitonic localization via simulations and optical characterizations. For this purpose, a photoreflectance setup allowing the determination of the Stokes shift in the InGaN alloys grown on free-standing GaN substrates either as thick layers or as heterostructures (quantum wells) was carefully designed to operate from cryogenic

to room temperature. The stacking of several $In_{0.1}Ga_{0.9}N/GaN$ quantum wells results in a detrimental increase in the Stokes shift and thus the absorption linewidth, which is incompatible with the requirements of the strong coupling regime. Various possible reasons such as inhomogeneous built-in field distribution among the quantum wells and their partial strain relaxation are then identified, hence explaining why it is presently not possible to achieve the strong coupling regime with such an active region embedded in a semi-hybrid microcavity. Alternative solutions for the microcavity design to achieve the strong coupling regime with the InGaN alloy are discussed, supported by results obtained from transfer matrix simulations. The inhomogeneous absorption linewidth of thick InGaN layers is deduced from transmission measurements and for low In content layers ($x < 12\%$) it is successfully reproduced by a model based on a stochastic distribution of indium atoms at the atomic scale. It is finally proposed that gain dilution in green laser diodes should not be much higher than in blue laser diodes provided that the In content within the QWs is homogeneous and abrupt interfaces are present.

Keywords: III-nitrides, gallium nitride, indium gallium nitride, Stokes shift, inhomogeneous broadening, localization, strain relaxation, critical layer thickness, distributed Bragg reflectors, microcavities, in-plane disorder, polaritons, strong coupling regime, polariton laser diodes, rate equations, high-speed current modulation, relative intensity noise.

Zusammenfassung

Das Halbleitermaterialsystem der Gruppe-III-Nitride - (InAlGa)N - ist dank seiner direkten Bandlücke, die vom ultravioletten bis zum infrarot Spektralbereich verändert werden kann, höchst interessant für optoelektronische Bauelemente. Die bekanntesten dieser Bauelemente sind weisse Leuchtdioden, welche den Beleuchtungsmarkt in den letzten Jahren grundlegend verändert haben, und blaue Laserdioden, die das Herzstück der Blu-ray Disc^{TM} Technologie sind. Zusätzlich wurden ausgeklügeltere Laserdioden, wie die sogenannten Oberflächenemitter oder VCSEL (von englisch vertical-cavity surface-emitting laser), erst kürzlich der Wissenschaftsgemeinde vorgeführt. Sie ebnen den Weg für elektrisch angetriebene, niederschwelligen Polaritonenlaserdioden bei Raumtemperatur. Schon im Jahre 1996 prognostizierten Imamoğlu und seine Arbeitskollegen die Möglichkeit einer solchen niedrigschwelligen, kohärenten Lichtquelle durch ein Polariton-Kondensat, entstanden in einem optischen Mikroresonator. Die Eigenmodi eines Mikroresonators sind Exziton-Polaritonen, entstanden durch die starke Kopplung zwischen einem optischen Modus und einer exzitonischen Resonanz. Dank ihrer leichten effektiven Masse im Zentrum der Brillouinzone, wo sie bis zu 10^5 mal leichter als ein Elektron sind, und effizienten Relaxationsprozessen, findet ein Phasenübergang zu einem Exziton-Polaritonenkondensat statt. Dieser kann auch bei hohen Temperaturen eintreffen (in GaN-basierenden Mikroresonatoren wurde er bis 340 K beobachtet).

Ein Ziel der vorliegenden Arbeit ist die detaillierte, theoretische Analyse der Hauptemissionseigenschaften elektrisch angetriebener Polaritonenlaserdioden, die auf GaN basierten, planaren Mikroresonatoren mit eingebetteten InGaN/GaN Quantengräben beruhen. Zudem sollen die notwendigen Bedingungen für deren experimentelle Umsetzung eruiert werden. Das komplette Polaritonen-Phasendiagram wurde für zwei Strukturen, die für die experimentelle Realisierung massgeblich sind, berechnet. Für beide Strukturen wurden zusätzlich der stationäre Zustand, die Antwort auf eine Hochfrequenz-Strommodulation, das relative Intensitätsrauschen und die Schawlow-Townes Linienbreite hergeleitet. Die resultierenden Gleichungen können für alle aus anorganischem Halbleitermaterial bestehenden Polaritonenlaserdioden eingesetzt werden.
Dann wurden die einzelnen Bausteine, d.h. der untere Nitrid-basierte Bragg-Spiegel, das aktive Medium und der obere dielektrische Bragg-Spiegel, solcher Mikroresonatoren experimentell analysiert. Eine innovative, optische Charakterisierungsmethode erlaubt, den Effekt des Substrates auf gitterangepasste InAlN/GaN Bragg-Spiegel zu studieren. Die beste optische Qualität solcher Bragg-Spiegel ergibt sich unter Verwendung von freistehenden GaN Substra-

ten. Besondere Aufmerksamkeit wird mittels Simulation und optischer Charakterisierung der exzitonischen Lokalisierung gewidmet. Dazu wurde ein Photoreflexionssystem aufgebaut. Es erlaubt, die Stokes'sche Verschiebung in auf InGaN-basierenden Strukturen bei Tiefst- und bei Raumtemperatur zu bestimmen. Das Aufeinanderschichten von $In_{0.1}Ga_{0.9}N/GaN$ Quantengräben verursacht eine steigende Stokes'sche Verschiebung und dadurch auch eine breitere Absorptionslinie, was nicht mit den Bedingungen des Regimes der starken Kopplung vereinbar ist. Mehrere Ursachen, wie zum Beispiel die inhomogene Feldverteilung unter den Quantengräben und deren partielle plastische Relaxation, werden identifiziert. Sie fungieren als Erklärung für die schwache Licht-Materie-Wechselwirkung, welche beobachtet wird, wenn ein solches Material in einem semihybriden Mikroresonator eingebettet wird. Basierend auf Resultaten von Transfermatrixsimulationen werden verschiedene potenzielle Strukturdesigns für InGaN-basierte Mikroresonatoren diskutiert.
Die inhomogene Verbreiterung der Absorptionslinie dicker, InGaN-basierter Schichten wurde durch Transmissionsmessungen bestimmt. Für indiumarme Schichten ($x < 12\%$) lässt sie sich erfolgreich mit einem Model, das auf einer stochastische Verteilung von Indium Atomen auf atomarer Ebene basiert, vergleichen. Auf dieser Grundlage wird vorgeschlagen, dass die Verminderung der optischen Verstärkung in grünen Lichtdioden nicht viel grösser ist als in blauen, solange die Quantengräben homogen und durch abrupte Grenzflächen limitiert sind.

Stichwörter: Gruppe-III-Nitride, Galliumnitrid, Indiumgalliumnitrid, Stokes'sche Verschiebung, Inhomogene Verbreiterung, Lokalisierung, Spannungsrelaxation, Kritische Schichtdicke, Bragg-Spiegel, Mikroresonator, Unordnung in der Wachstumsebene, Polaritonen, Regime der starken Kopplung, Ratengleichungen, Hochfrequenz-Strommodulation, relatives Intensitätsrauschen

Résumé

Les semiconducteurs à base de nitrures d'éléments III - (InAlGa)N – sont très intéressants pour des applications optoélectroniques grâce à leur gap direct qui s'étend de l'ultraviolet à l'infrarouge. Les plus répandues sont les diodes électroluminescentes blanches, qui sont en train de révolutionner le marché de l'éclairage, et les diodes laser bleues, l'élément clé de la technologie Blu-ray Disc^{TM}. Des dispositifs plus sophistiqués comme les lasers à cavité verticale à émission par la surface ont également été réalisés récemment, ouvrant la voie à la fabrication de lasers à polaritons injectés électriquement. En 1996 Imamoğlu et ses collègues ont proposé la possibilité d'obtenir de telles sources de lumière cohérente à partir d'un condensat de polaritons dans des microcavités au design adapté. Les modes propres d'une telle microcavité sont des exciton-polaritons, des quasi-particules résultant du couplage fort entre un mode photonique et une résonance excitonique. Grâce à leur masse effective très légère au centre de la zone de Brillouin (10^5 moindre que celle de l'électron) et des processus de relaxation efficaces, une transition de phase vers un condensat d'exciton-polaritons peut avoir lieu à des températures élevées (observé jusqu'à 340 K dans des microcavités à base de GaN).

Le but de cette thèse est d'établir une analyse théorique des principales propriétés d'émission de lasers à polaritons injectés électriquement et basés sur des microcavités planaires de GaN avec des multi puits quantiques d'InGaN/GaN. En outre les exigences nécessaires à la faisabilité de telles structures sont établies. Ainsi, les diagrammes de phase de deux géométries différentes sont présentés ainsi que les charactéristiques de l'état stationnaire, la réponse à une modulation de courant de haute fréquence, le bruit d'intensité relatif, et la largeur de Schawlow-Townes. Les expressions finales peuvent être appliquées à tous les lasers à polaritons fabriqués à partir de semiconducteurs inorganiques.
Dans une seconde partie, chaque composante de base de ces microcavités est analysée expérimentalement : le miroir de Bragg inférieur à base de nitrures d'éléments III, la région active, et le miroir de Bragg supérieur qui est composé de matériaux diélectriques. Une méthode innovante de caractérisation optique donne la possibilité d'étudier l'effet du substrat sur les miroirs de Bragg à base de bicouches InAlN/GaN en accord de maille. La meilleure qualité optique pour ces miroirs est obtenue lorsqu'ils sont crûs sur des substrats de GaN de haute qualité. Une attention particulière est portée sur l'étude de la localisation excitonique par des simulations et des caractérisations optiques. Pour ces dernières, un montage de photoréflectance a été assemblé et a notamment permis de déterminer, à différentes témperatures, le

Stokes shift d'alliages d'InGaN crûs sur des substrats de GaN soit comme couches épaisses ou comme hétérostructures (puits quantiques). L'empilement de puits quantiques conduit à une augmentation du Stokes shift et donc de la largeur de la raie d'absorption, ce qui est incompatible avec les exigences du régime de couplage fort. Plusieurs raisons différentes sont identifiées comme par exemple la distribution inhomogène du champ électrique interne dans les puits quantiques et la relaxation partielle de la contrainte. Ceci donne un premier aperçu des raison pour lesquelles le régime de couplage fort n'a pas encore pu être obtenu avec de telles régions actives insérées dans des microcavités semi-hybrides. Des solutions alternatives pour la conception des microcavités sont discutées à partir de résultats de simulation de matrice de transfert.
La largeur inhomogène de la raie d'absorption des couches épaisses d'InGaN a également été déduite de mesures de transmission. Celle est bien reproduite par un modèle basé sur une distribution statistique des atomes d'indium à l'échelle atomique pour les couches à faible composition ($x < 12\%$). Finalement, il est proposé que la dilution du gain dans les diodes laser vertes ne devrait pas être beaucoup plus grande que pour les diodes laser bleues à condition que les puits quantiques soient homogènes et présentent des interfaces abruptes.

Mots clefs : Nitrures d'éléments III, nitrure de gallium, nitrure d'indium, Stokes shift, élargissement inhomogène, localisation, relaxation de la contrainte, épaisseur de couche critique, miroir de Bragg, microcavités, désordre d'interface, polaritons, régime de couplage fort, diode laser à polaritons, équation bilan, réponse à une modulation de courant haute fréquence, bruit d'intensité relatif

Contents

Abstract (English/Français/Deutsch) **v**

Table of contents **xiii**

Introduction **1**

1 Generalities on III-nitride semiconductors and cavity polaritons **7**
1.1 Material properties of III-nitrides 7
1.1.1 Structural properties 7
1.1.2 Optical properties 12
1.1.3 Excitons in bulk layers and quantum wells 14
1.2 III-nitride based cavity polaritons 15
1.2.1 Planar Microcavities 15
1.2.2 The strong coupling regime in III-nitride based microcavities 19

2 Theoretical study of emission properties of III-nitride polariton laser diodes **27**
2.1 Introduction 27
2.2 Design of III-nitride polariton laser diodes 28
2.3 Polariton condensation phase diagram 31
2.3.1 Polariton Bose Condensation 31
2.3.2 Coupled semiclassical Boltzmann equations for III-nitride polariton laser diodes 34
2.4 Figures of merit of polariton laser diodes 39
2.4.1 Simplified rate equations and their steady-state solutions 39
2.4.2 High-speed current modulation treatment: determining the modulation bandwidth 43
2.4.3 Relative intensity noise 48
2.4.4 Emission linewidth 55
2.5 Polariton laser vs. VCSEL 58
2.6 Summary of the results 60

3 Design of microcavities and critical aspects **61**
3.1 High-quality dielectric Bragg mirrors 61
3.1.1 Determination of the complex refractive index 61

3.1.2 Improvement of dielectric materials . . . 63
3.1.3 Dielectric DBRs . . . 65
3.2 High-quality III-nitride Bragg mirrors . . . 66
3.2.1 An introduction to III-nitride DBRs . . . 66
3.2.2 Optical properties of GaN and InAlN layers . . . 67
3.2.3 LM InAlN/GaN DBRs grown onto different substrates . . . 68
3.3 Design of microcavities . . . 73
3.3.1 Semi-hybrid and full-hybrid approach . . . 73
3.3.2 Optical properties of InGaN layers . . . 75
3.3.3 Optical properties of InGaN layers including excitonic effects . . . 77
3.3.4 Modeling: Transfer matrix simulations . . . 77
3.4 Summary of the results . . . 80

4 Active medium: Low In content InGaN/GaN QWs and InGaN bulk layers 81
4.1 Low indium content InGaN/GaN QWs grown onto different substrates . . . 81
4.2 Relaxation issues for InGaN/GaN MQW structures and InGaN bulk layers . . . 84
4.2.1 Strain relaxation of heterostructures of (0001) InGaN on GaN . . . 84
4.2.2 Relaxation issues in the case of MC structures based on InGaN/GaN MQWs 85
4.2.3 A promissing solution: MCs based on interlayers . . . 88
4.3 On the nature of localization in InGaN/GaN QWs and InGaN bulk layers . . . 89
4.3.1 Carrier localization mechanism . . . 89
4.3.2 Optical properties of InGaN/GaN SQWs at low temperature . . . 90
4.3.3 On the suitability of the envelope function formalism for optical transitions in InGaN/GaN SQWs . . . 92
4.3.4 Estimation of Γ_{inh}: absorption-like measurements at low temperature . 93
4.3.5 Temperature-dependent studies of InGaN/GaN MQWs and bulk InGaN layers . . . 100
4.3.6 Discussions: intrinsic and extrinsic properties of InGaN alloys . . . 108
4.4 Summary of the results . . . 114

5 Light-matter interaction in InGaN-based microcavities 117
5.1 Semihybrid MC structures . . . 117
5.2 Experimental features of semi-hybrid cavity structures . . . 118
5.3 Hybrid MC structures . . . 125
5.4 Origin of lasing processes in InGaN-based structures . . . 126
5.5 Summary of the results . . . 127

6 Conclusion 129

A Appendix 133
A.1 The transfer matrix formalism . . . 133
A.2 Langevin Noise . . . 136
A.2.1 The correlation strengths between noise sources: applied to polariton LDs136

A.2.2 Coefficient related to the transfer function 138
A.3 Modulation spectroscopy: Photo- and electroreflectance 139
A.3.1 Principle 139
A.3.2 Setup specificities 139
A.3.3 Critical aspects 141
A.4 Fourier imaging 142
A.4.1 Principle 142
A.4.2 Critical aspects 143
A.4.3 Setup specificities 144

Bibliography **170**

Nomenclature **171**

Remerciements **177**

Curriculum Vitae **179**

Introduction

The revolution of III-nitrides

Since the invention of “electric” light using an incandescent light bulb in the 19th century, there has been a search for more reliable, more efficient, and brighter lighting sources. Massive industries have been created to satisfy the global lighting market which is today divided into three major sectors, namely, general lighting, automotive lighting, and backlighting. General lighting, by far the largest, contains well-known lighting elements such as filament and fluorescent lamps for interior applications, sodium-discharge lamps for streets, and neon signs for advertising. Triggered by a recent revolutionary lightning advancement, the white light-emitting diode (LED), the global market for general lighting reached market revenues of approximately EUR 55 billion in 2011 and is expected to rise to around EUR 83 billion by 2020 [1]. Note that LEDs covered only 4% of the general lighting market in 2011 but are expected to attain 63% by 2020.

Although the first LED and its companion, the laser diode (LD), were already demonstrated in 1962 [2, 3], devices suitable for general lighting were far from being achieved as the corresponding material system, III-nitride based semiconductors, was still in its infancy.
The earliest work on III-nitride based material goes back to 1862 when the first AlN samples in form of powder were synthesized [4]. About a century later, by placing some suitable source material in a zone furnace under flowing ammonia (NH_3) even some small single crystals of GaN and AlN of very good quality were achieved. Thus, the first report of low temperature (LT) stimulated emission of optically-pumped GaN needles grown by heating GaN powder in a stream of NH_3 goes back to 1971 [5]. However, for the realization of GaN-based optoelectronic devices a few milestones had to be overcome: namely, the development of thin film growth techniques, the choice of an adequate substrate, and finally the achievement of an efficient p-type doping. The latter was eventually reported by Amano *et al.* in 1989 [6]. As a result, the first efficient blue LED based on InGaN/GaN quantum wells (QWs) was demonstrated in the mid-nineties by S. Nakamura and co-workers [7]. The demonstration of white LED lighting was reported shortly after: by coating those efficient blue LEDs with a yellow phosphor, the blue light is partially converted to white light [8].

The achievement of the first blue LD in 1996 by Nakamura *et al.* [9] sets the basis for the high density digital optical disc data storage format Blu-ray Disc^{TM} unveiled as a first prototype by Sony in 2000 and officially released together with the Blu-ray Disc^{TM} player in 2006. Furthermore, several other coherent light-emitting devices based on III-nitride materials have seen the light of day: photonic crystal surface-emitting laser diodes [10, 11], superluminescent light emitting diodes (SLEDs) [12], and vertical-cavity surface-emitting lasers (VCSELs) [13–19]. Note however, that these devices are not yet commercially available.

Besides optoelectronic devices, several GaN-based devices have found applications in high power electronics such as high-electron-mobility transistors [20]. Thanks to their intrinsic properties such as high break-down voltage, high electron saturation mobility, and higher thermal conductivity, GaN-based devices operate at high voltages, high switching frequencies, handle higher power densities, and offer enhanced power efficiency than the pure Si devices. They are currently attracting interest for a wide range of applications as inverters (and converters), radio frequency (RF) devices, and power supply modules being used from cell phone and wireless infrastructures (base stations) to high performance military electronics.

On the interest of polariton laser diodes

Ever since the demonstration of the first laser, made from ruby in 1960 by T. H. Maiman [27], there has been a drive for easily integrable, cheap, reliable, and efficient (mainly low threshold current) laser sources covering a large spectral range and various applications. The report of room temperature (RT) continuous-wave (cw) operation of the first semiconductor double-heterostructure (DHS) laser in 1970 [28] by Z. I. Alferov, winner of the 2000 Nobel prize in physics, and coworkers produced an explosion of interest in physics and technology of semiconductor heterostructures. Tremendous improvements of the material quality of such heterostructures thanks to epitaxial growth techniques such as molecular beam epitaxy (MBE) and metalorganic vapor phase epitaxy (MOVPE) led to lasers using quantum-size heterostructures as active medium. As originally introduced by Dingle and Henry in 1976 [29],

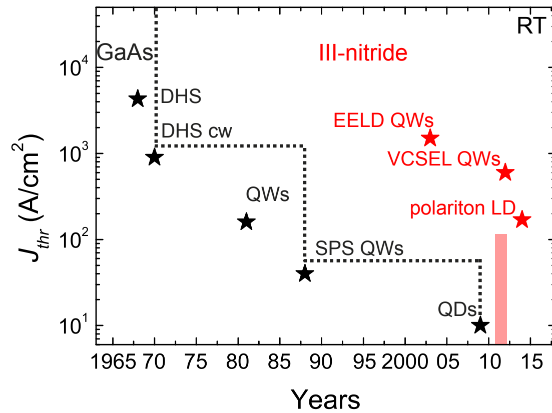

Figure 1: Evolution of the threshold current density of semiconductor lasers at RT in the case of GaAs- (black stars and black line as guide to the eye) and III-nitride (red stars) based LDs. Typical threshold current densities (J_{thr}) for blue edge emitting laser diodes (EELDs) [21, 22], lowest J_{thr} ever reported for a III-nitride VCSEL [23] and the first bulk GaN-based III-nitride polariton LD [24]. The red shaded area corresponds to the theoretically predicted J_{thr} for QW-based III-nitride polariton LDs [25, 26].

the decreasing density of states when reducing the dimensionality lead to a drastic reduction of the threshold current density (J_{thr}) as graphically illustrated in Fig. 1. Note that at currents above J_{thr} the laser output is dominated by stimulated rather than spontaneous emission and the laser is said to be lasing. In other words, the stimulated emission condition as defined by Bernard and Duraffourg [30] is more easily fulfilled when decreasing the dimensionality of the active region and thus the power consumption of the laser is reduced. However, the achieved values for J_{thr} of a single quantum well (SQW) in combination with short-period superlattices (SPSs) (J_{thr} = 40 A/cm^2 in 1988 [31]) and a quantum dot (QD) (J_{thr} = 10.4 A/cm^2 in 2009 [32]) based LD are close to their theoretical limit. Thus, in order to drive further the search for lower threshold current a change in paradigm was needed. In 1996, Imamoğlu *et al.* [33] suggested the use of a non-equilibrium polariton condensate to produce a low threshold coherent light source referred to as a polariton laser.

The strong coupling between excitons and cavity-photons in semiconductor microcavities (MCs) leads to the formation of novel quasi-particles, cavity-polaritons. Such polaritons can exhibit characteristic bosonic properties such as macroscopic occupation of an individual quantum state possessing long temporal and spatial coherence, namely it can undergo a transition to a polariton condensate sharing close similarities with a Bose-Einstein condensate. Bose-Einstein condensation (BEC) as predicted in 1925 by A. Einstein [34] is a phase transition for bosons taking place below a certain critical temperature (T_{crit}). Note that for the experimental observation of the latter in a dilute vapor of atoms at ultra-low temperatures (T_{crit} $\approx 10^{-7}$ K) Wolfgang Ketterle, Eric Cornell and Carl Wieman were awarded by the Nobel prize in Physics in 2001 [35, 36]. Cavity-polaritons are characterized by a very light effective mass, which is inherited from their photonic component, typically one billion times lighter than that of an atom. Hence they are expected to undergo a phase transition towards a condensate at much higher temperatures, as T_{crit}, as a first approximation, is inversely proportional to the boson mass. Ever since the first demonstration of polariton condensation at cryogenic temperatures in a CdTe microcavity (MC) in 2006 [37] the polaritonic field attracted a lot of attention with observations such as integer [38] and half-integer quantum vortices [39], superfluidity [40–42], as well as bright and dark solitons [43, 44] in polariton fluids. Note that the latter observations and current experiments rely on optical pumping with specific and often bulky pump lasers. Thus, the ability to create interacting Bose condensates by pure electrical means on a compact platform, i.e., a situation akin to a lab-on-a-chip, provides additional legitimacy to the polariton LD as it would add an extra degree of flexibility for such studies.

Electrical injection of cavity polaritons has been reported in organic semiconductors [45–47] and in GaAs-based cavities operating up to RT [48–50]. Lately, hints for polaritonic nonlinearities occurring under electrical injection have also been observed in the latter system at cryogenic temperatures [51, 52]. However, it is likely that the realization of GaAs-based polariton LDs operating at RT will be prevented due to the small exciton binding energy in this

material system. Indeed, it was previously shown that the cut-off temperature leading to the observation of polariton-based optical nonlinearities matches the exciton binding energy [53]. Keeping the latter in mind together with issues regarding practical realization of polariton LDs able to operate at RT III-nitrides emerge as a main contender [25]. They exhibit highly stable excitons up to RT and polariton lasing has been reported under nonresonant optical pumping at RT in both bulk GaN and GaN/AlGaN multiple quantum well (MQW) based MC structures [54, 55]. However, as the availability of transparent conductive oxide (TCO) layers in the corresponding wavelength region and achieving efficient p-type doping becomes progressively more difficult when increasing the Al content, MCs with embedded InGaN/GaN MQWs have to be considered for electrical injection purposes. An electrically driven III-nitride-based device would present a threshold current density between 5 and 100 A/cm^2 at RT [25, 26], i.e., two orders of magnitude below state of the art values reported for edge emitting laser diodes (EELD) (cf. Fig. 1). However, the successful realization of QW-based polariton LDs is closely linked to that of blue III-nitride VCSELs, which were demonstrated under electrical pumping at RT only recently [13–18] as they share very similar sample designs [26]. Note that only recently the first RT electrically pumped bulk GaN-based polariton LD has been reported to exhibit a low J_{thr} of 169 A/cm^2 [24].

Thesis objectives

The objectives of this thesis deal with the development of electrically-driven III-nitride based polariton LDs. The main emission features of electrically-driven polariton lasers based on planar GaN MCs with embedded InGaN/GaN MQWs are studied theoretically. Then, this work focuses on the design of such MCs and the development of key building blocks, namely, highly reflective distributed Bragg reflectors (DBRs), made either of InAlN/GaN (for the bottom mirror) or dielectric bilayers (for the upper mirror) and the active medium. The impact of various parameters governing the characteristics of planar MCs based on an InGaN/GaN MQW active region for the subsequent realization of polariton LDs are analyzed. Particular attention is paid to the influence of excitonic disorder via simulations and optical characterizations. Experiments probing absorption and emission properties have been performed not only on InGaN/GaN MQWs but as well on 100 nm thick InGaN layers with In contents ranging between 2 and 20% in order to get a glance at the poorly understood carrier mechanisms at play in the InGaN alloy.

Outline of this PhD dissertation

A brief overview of the main structural and optical properties of the wurtzite III-nitride material system is given in Chapter 1. Prior to introducing the reader to III-nitride based cavity polaritons, the basic concepts of excitons, cavities, and DBRs are recalled. Polariton's dispersion relations and important parameters characterizing the strong light-matter interaction such as the exciton-cavity photon detuning (δ), the vacuum Rabi splitting (Ω_{VRS}), and the

sources of broadening are defined. Eventually, the state of the art of strong coupling studies performed in III-nitride based materials is given.

The main emission characteristics of electrically-driven polariton LDs based on planar GaN MCs with embedded InGaN QWs are studied theoretically in chapter 2. Two experimentally relevant pumping geometries are considered, namely the direct injection of electrons and holes into the strongly coupled MC region and intracavity optical pumping via an embedded LED. Using a quasi-analytical model the steady-state and the high-speed current modulation including the relaxation oscillation frequency features are derived. Through this analysis it is shown that the exciton population in the reservoir gets clamped above the condensation threshold and is governed by the exciton-exciton scattering rate and the ground state polariton lifetime. Other important figures of merit, namely the relative intensity noise (RIN) and the modified Schawlow-Townes linewidth are also determined within this theoretical framework, which overall allows establishing a direct comparison with the main emission features of conventional LDs.

The realization of highly-reflective lattice-matched (LM) InAlN/GaN DBRs grown on free-standing (FS) GaN substrates is described, and the impact of several parameters affecting the overall quality of those DBRs is considered in chapter 3. The focus lies mainly on the photonic disorder in MCs made from a dielectric and an InAlN/GaN DBR, whose minimization is crucial for strong coupling applications as well as for VCSELs. The energy-dependent complex refractive indices are given for all materials appearing in GaN MCs with embedded InGaN QWs allowing to perform transfer matrix simulations (TMS) in order to fix the requirements in terms of QW absorption features, number of QWs (N_{QW}), and the optical cavity length (L_c) for achieving the strong coupling regime (SCR) in such MCs.

The fourth chapter describes the MOVPE-growth of high-quality low In content InGaN/GaN single QWs (SQWs) on FS-GaN substrates, exhibiting a narrow LT photoluminescence (PL) linewidth of 33 meV together with a low excitonic disorder for which the microscopic origin responsible for this broadening is qualitatively discussed. When stacking several InGaN/GaN QWs a departure from such a narrow linewidth value, compatible with SCR requirements, is observed. Various possible reasons such as strain relaxation, inhomogeneous built-in field distribution among the QWs are then identified, hence explaining why it is presently not possible to achieve the SCR with such an active region. Complementary, thick InGaN layers grown on FS-GaN substrates have also been characterized in order to better understand some of the observed features in temperature-dependent absorption and emission measurements acquired on the InGaN/GaN QWs.

In chapter 5 the light-matter interaction of $In_xGa_{1-x}N$ MQWs and thick $In_xGa_{1-x}N$ layers with $x \sim 0.1$ when inserted in III-nitride based semihybrid MCs is analyzed. Low-threshold

lasing in the weak coupling regime at RT is reported for both cavities in accordance with TMS. Finally, the main experimental results are briefly reviewed and an alternative solution for the MC design to achieve the SCR with the InGaN alloy is discussed.

The present work was supported by the NCCR Quantum Photonics program of the Swiss National Science Foundation.

1 Generalities on III-nitride semiconductors and cavity polaritons

1.1 Material properties of III-nitrides

1.1.1 Structural properties

III-nitride semiconductors are usually grown by MOVPE or MBE. The preferential crystalline structure is the hexagonal wurtzite phase (α-phase), whereas they can also be grown in the metastable cubic zincblende phase (β-phase) under peculiar growth conditions [56, 57]. As the present work focuses on the hexagonal wurtzite structure, the cubic zincblende phase will not be considered hereafter. The III-nitride material system encompasses the binary compounds gallium nitride (GaN), indium nitride (InN), and aluminum nitride (AlN), as well as ternary and quaternary compounds satisfying $Al_xIn_yGa_{1-x-y}N$ with $0 \leq x \leq 1$ and $0 \leq y \leq 1$. The covalent binding of the cation (Ga, Al, or In atom) with the anion (N atom), which is an sp^3-hybridization of the valence electrons, determines the tetrahedral atomic arrangement

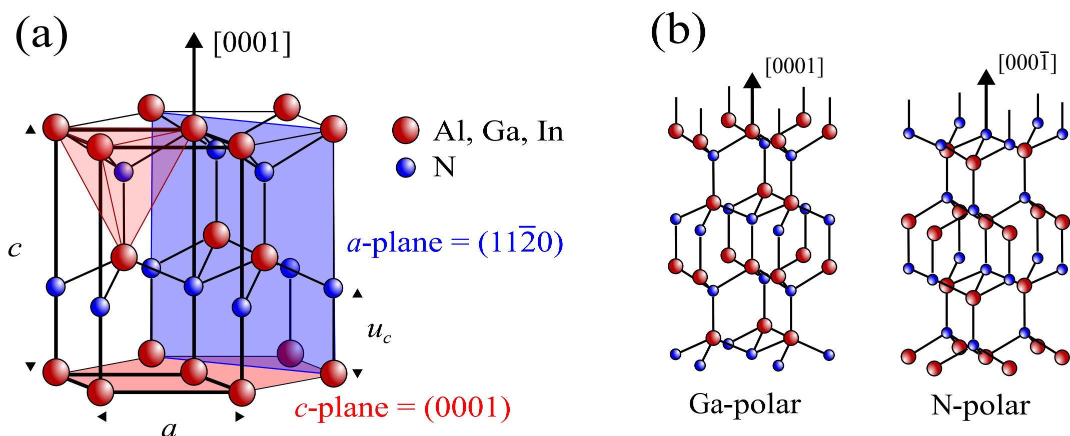

Figure 1.1: (a) Wurtzite structure of III-nitride compounds. The tetrahedral shaded area highlights the covalent binding between anion (N) and cation (Ga, Al, In) atoms. The *c* and *a*-planes are also indicated. The hexagonal unit cell is highlighted with bold lines. (b) Ga- and N- polar surface terminations.

Compounds	AlN	GaN	InN
a (Å) [60]	3.112	3.189	3.545
c (Å) [60]	4.982	5.185	5.703
u [61]	0.380	0.376	0.377
P^{sp} (C/m^2) [62]	-0.09	-0.034	-0.042

Table 1.1: Lattice parameters and spontaneous polarization of III-nitride binary compounds [60–62].

(cf. Fig. 1.1(a)). However, due to the strong difference in electronegativity between the cation and the anion (Al: 1.61 Ga: 1.81 In: 1.78 N: 3.04 [58]) the bonding has also a significant ionic character. In addition, due to the lack of inversion symmetry hexagonal wurtzite crystals are strongly anisotropic which affects their optical, mechanical, thermodynamic, and polarization properties.

The wurtzite structure is characterized by 3 lattice parameters: a, c, which describe the hexagonal unit cell (cf. bold lines in Fig. 1.1(a)), and u_c, which gives the anion-cation bond length along the [0001]-direction (c-axis). The corresponding experimental values are given for AlN, GaN, and InN in Table 1.1, whereas instead of u_c it is common to give the relative anion-cation bond length $u = u_c/c$. The lattice parameters for ternary and quaternary alloys are obtained by Vegard's law, i.e., by linear interpolation. The best known growth axis is the c-axis resulting in Ga- or N-polar GaN as schematically drawn in Fig. 1.1(b). In the case of N-polar material the surface terminates with N atoms. The latter is thermodynamically unstable as N-N bonds are formed and the resulting N_2 desorbs from the surface. Recently a lot of interest has been dedicated to non-polar (a- and m-plane) and semipolar III-nitride materials [59]. The non-polar a-plane stands perpendicular to the $[1\bar{2}10]$ direction as indicated in Fig. 1.1(a) whereas the m-plane is rotated around the c-axis by 60°, i.e., it corresponds to the $(10\bar{1}0)$ plane.

Spontaneous and Piezoelectric Polarizations

In the ideal wurtzite structure, ions reside in perfect tetrahedral sites and from pure geometrical arguments it can be shown that the c/a-ratio is equal to $\sqrt{8/3}$ and $u = 3/8 = 0.375$. In this case the net spontaneous polarization (P^{sp}) of the material is small as only originating from the influence of the second nearest neighbors [63]. However, it is known from experiment and as well from theoretical predictions that neither u, nor the c/a-ratio are ideal in III-nitride compounds [63]. A net polarization vector along the $[000\bar{1}]$-direction for Ga-polar material or the [0001]-direction for N-polar material is present as shown schematically in Fig. 1.2(a). Crystals exhibiting spontaneous polarization without external excitation are also referred to as pyroelectric crystals, not to confuse with ferroelectric crystals, whose spontaneous polarization can be turned around by external electric fields. Although, the spontaneous polarization in III-nitrides is found to be strong (cf. values in Tab. 1.1), the pyroelectric constants, describing the change of P^{sp} with temperature, are rather small (e.g., $\mathrm{d}P^{sp}_{AlN}/\mathrm{d}T = 7.5\ \mu\mathrm{C/Km^2}$, at

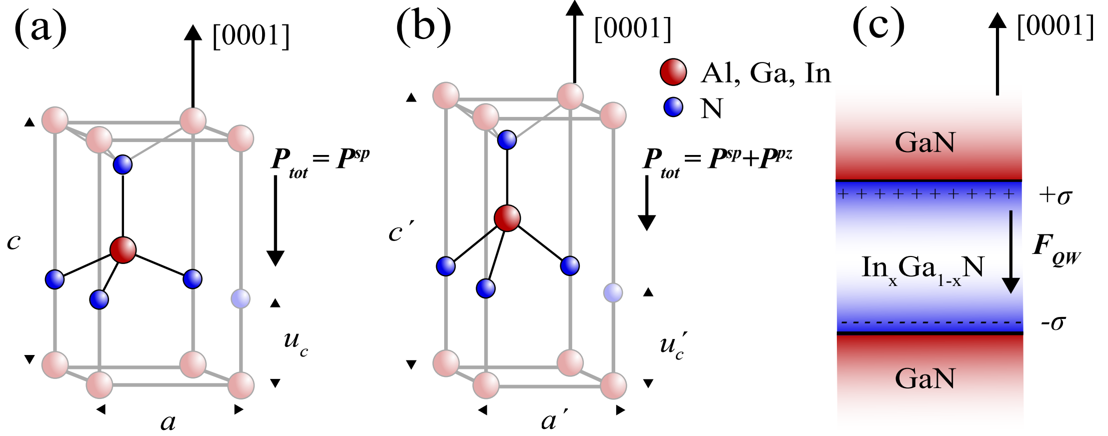

Figure 1.2: (a) Ball and stick configuration of an unstrained (relaxed) III-nitride binary compound with Ga-polarity presenting a net non zero total polarization (P_{tot}) equal to the crystal's spontaneous polarization along the $[000\bar{1}]$ direction. (b) An in-plane compressive strain induces a variation of $\boldsymbol{P_{tot}}$. In this case the piezoelectric polarization is oriented in direction opposite to the spontaneous one, i.e., along the [0001] direction. (c) Discontinuities in the polarization of a heterostructure introduce bound surface charges: shown in the case of an $In_xGa_{1-x}N/GaN$ QW.

RT [64, 65]), which is a key advantage considering devices suffering from temperature changes such as high power, high frequency transistors, LEDs, and LDs. As in the present work not only binary compounds have been studied but as well ternary alloys, it is of practical use to know the values for the spontaneous polarization in the latter in order to calculate the built-in field in heterostructures. Hereafter, we consider the relations deduced by V. Fiorentini and co-workers from *ab initio* calculations (expressed in C/m^2) [66]:

$$\begin{aligned} P^{sp}_{Al_xGa_{1-x}N} &= -0.09x - 0.034(1-x) + 0.019x(1-x), \\ P^{sp}_{In_xGa_{1-x}N} &= -0.042x - 0.034(1-x) + 0.038x(1-x), \\ P^{sp}_{Al_xIn_{1-x}N} &= -0.09x - 0.042(1-x) + 0.071x(1-x). \end{aligned} \tag{1.1}$$

Note that pyroelectric crystals are always piezoelectric and the piezoelectric polarization (P^{pz}) corresponds to the change in polarization that might occur through crystal deformation. Contrary to the case of spontaneous polarization, the piezoelectric polarization of ternary alloys can be calculated using Vegard's law, i.e., by linear interpolation of the corresponding P^{pz} for the binary compounds, given hereafter (in C/m^2) [66]:

$$\begin{aligned} P^{pz}_{AlN} &= \begin{cases} -1.808\epsilon_{||} + 5.624\epsilon_{||}^2 & \text{for } \epsilon_{||} < 0 \\ -1.808\epsilon_{||} - 7.888\epsilon_{||}^2 & \text{for } \epsilon_{||} > 0, \end{cases} \\ P^{pz}_{GaN} &= -0.918\epsilon_{||} + 9.541\epsilon_{||}^2, \\ P^{pz}_{InN} &= -1.373\epsilon_{||} + 7.559\epsilon_{||}^2, \end{aligned} \tag{1.2}$$

where $\epsilon_{||} = (a_{sub} - a(x))/a(x)$ is the in-plane deformation of the layer under consideration, with a_{sub} and $a(x)$ the in-plane lattice parameter of the substrate and the alloy with composition x,

respectively. In Fig. 1.2(b) the effect of in-plane compressive strain, which occurs for example when $In_xGa_{1-x}N$ is pseudomorphically grown onto GaN, is shown in the ball and stick diagram again for the Ga-polar case.
In heterostructures, charge accumulation at each interface due to changes of polarization occurs as illustrated in Fig. 1.2(c) in the case of an $In_xGa_{1-x}N$/GaN QW. The relation between the charge and polarization follows basically from Gauss's law: the bound charge density at the interface is given by: $\sigma = -\nabla\cdot \mathbf{P}$. Those polarization induced interface charges in QWs are in general not significantly screened by electrons and ionized donors and act similar as two condensator plates: an electric field builds up in between, respectively in the well. To calculate the latter, the following steps have to be done (adapted from Ref. [67]). Using Hookes' law, which relates the stress field $\tilde{\boldsymbol{\sigma}}$ to the strain field $\tilde{\boldsymbol{\epsilon}}$:

$$\tilde{\boldsymbol{\sigma}}_{\boldsymbol{i}} = \tilde{\boldsymbol{C}}_{\boldsymbol{ij}}\tilde{\boldsymbol{\epsilon}}_{\boldsymbol{j}}, \tag{1.3}$$

where Einstein's convention is used, i.e., repeated indices imply summation. $\tilde{\boldsymbol{C}}$ is the elastic coefficient tensor and can be found in Ref. [67]. Then one can relate the electrostatic displacement $\mathbf{D}$ to the electric field and the built-in polarization. Electrical neutrality of the medium, supposed undoped, ensures that:

$$\nabla\cdot\mathbf{D} = 0. \tag{1.4}$$

This leads to an expression for the built-in electric field along the $[000\bar{1}]$ direction in a single QW (SQW):

$$F_{SQW} = \frac{P_B^{sp} - P_W^{sp}}{\epsilon_W} + \frac{P_B^{pz} - P_W^{pz}}{\epsilon_W}, \tag{1.5}$$

where the subscripts W and B stand for QW and barrier, respectively, and ϵ_W is the dielectric constant of the QW. In Fig. 1.3(a) the built-in electric field for $In_xGa_{1-x}N$/GaN and GaN/$Al_xGa_{1-x}N$ SQWs is shown (cf. solid lines) as a function of the In (Al) content, respectively. In the case of a MQW sample, due to a partial redistribution of the built-in field in the barriers, the built-in electric field in each well is decreased compared to the SQW case. The latter is known as the so-called geometrical effect and given by the following, on the sample geometry relaying approximation [68, 69]:

$$F_{MQW} = F_{SQW}\frac{\epsilon_W l_B}{\epsilon_W l_B + \epsilon_B l_W}, \tag{1.6}$$

where ϵ_B is the barrier dielectric constant, and l_W (l_B) is the well (barrier) thickness. The field computed for $In_xGa_{1-x}N$ (2 nm)/GaN (3 nm) and GaN (1.2 nm)/$Al_xGa_{1-x}N$ (3.6 nm) MQWs is displayed as a function of the In and Al content, respectively, in Fig. 1.3(a). It is obvious that $In_xGa_{1-x}N$/GaN SQWs suffer from a stronger built-in field than GaN/$Al_xGa_{1-x}N$ SQWs with the same content of Al instead of In.

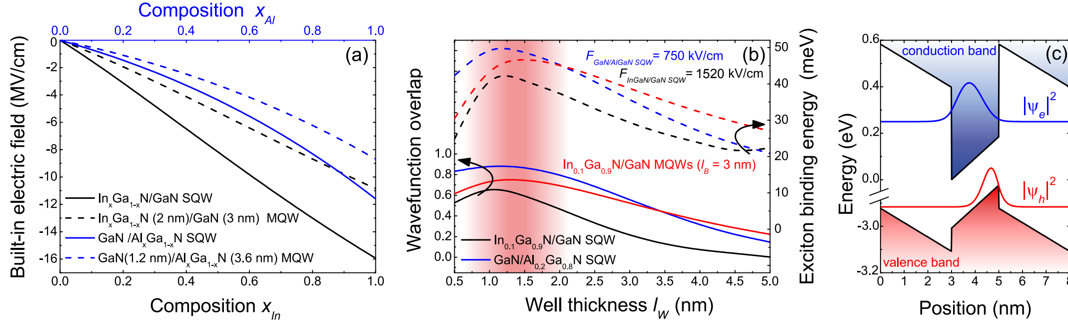

Figure 1.3: (a) Built-in electric field computed for a SQW (black line) and a MQW (black dashed line) $In_xGa_{1-x}N$/GaN heterostructure pseudomorphically grown on a *c*-plane GaN epilayer versus In content. Similar calculations have been performed for a GaN/$Al_xGa_{1-x}N$ heterostructure versus Al content (SQW (blue line) and MQW (blue dashed line)). (b) Evolution of the overlap between the electron and hole wavefunctions (continuous lines) and exciton binding energy (dashed lines) for a GaN/$Al_{0.2}Ga_{0.8}N$ SQW (blue lines), an $In_{0.1}Ga_{0.9}N$/GaN SQW (black lines), and an $In_{0.1}Ga_{0.9}N$/GaN (l_B = 3 nm) MQW (red lines) as a function of the well thickness deduced from envelope function calculations (see text for details). (c) The electron (blue) and hole (red) presence probability $|\Psi_h|^2$ and $|\Psi_e|^2$, respectively, are calculated in the envelope wavefunction approximation for an $In_{0.1}Ga_{0.9}N$ (2 nm)/GaN (3 nm) MQW.

Quantum confined Stark effect in heterostructures

This large field present in QW structures leads to the quantum confined Stark effect (QCSE), which describes the effect of an electric field upon light emission and absorption in a QW.

In Fig. 1.3(c) the square modulus of the hole and electron wavefunctions $|\Psi_h|^2$ and $|\Psi_e|^2$, respectively, calculated in the envelope wavefunction approximation for a 2 nm thick $In_{0.1}Ga_{0.9}N$/GaN MQW surrounded by 3 nm thick barriers, is depicted. The most striking changes induced by the built-in field on the emission and absorption properties of the QWs are (i) the spatial separation of electron and hole wavefunctions and (ii) the decrease of the fundamental transition energy ($E_{e_1-hh_1}$), which writes as a first approximation:

$$E_{e_1-hh_1} = E_{g,W} + e_1 + hh_1 - E_B - eF_{SQW,MQW}\, l_W, \qquad (1.7)$$

where $E_{g,W}$ is the bandgap of the well material, e_1 and hh_1 are the confinement energies of the electron and hole, respectively, and E_B is the exciton binding energy, given in section 1.1.3. Note that in the case of sufficiently large QWs, whenever the QCSE dominates over confinement effects, the transition energy $E_{e_1-hh_1}$ might even go below the value of the bulk $E_{g,W}$. Experimental evidence of the latter is given for GaN/AlGaN QWs in Ref. [69]. The spatial separation of the electron and hole wavefunctions leads to a reduced wavefunction overlap with increasing QW thickness, as reported in Fig. 1.3(b) for an $In_{0.1}Ga_{0.9}N$/GaN SQW and MQW and a GaN/$Al_{0.2}Ga_{0.8}N$ SQW.[1] A further signature of the QCSE, also reported in Fig.

[1] Only low In content QWs are considered, as they fit best to strong coupling requirements (cf. chapter 3). In the case of GaN/$Al_xGa_{1-x}N$ QWs the choice of the Al content is motivated through the observation of strong coupling

1.3(b), is the decrease of the exciton binding energy with increasing well width, which can be understood qualitatively by an increase of the two dimensional exciton Bohr radius, i.e., the Coulomb interaction energy between the electron and the hole is reduced [71]. Note that the wavefunction overlap and the exciton binding energy are deduced from envelope function calculations.

1.1.2 Optical properties

For the realization of light-emitting devices the III-nitride compounds are of high interest because of their direct bandgap, which spans the energy range going from 0.64 to 6.14 eV at 300 K, thus including the whole visible region and extending well into the ultraviolet (UV) range (cf. Fig. 1.4(a)). The bandgap values of the alloys can be obtained by applying a modified form of Vegard's law including bandgap bowing parameters (b_{BG}) [72]:

$$\begin{aligned} E_{g,Al_xGa_{1-x}N}(x) &= xE_{g,AlN} + (1-x)E_{g,GaN} - 1x(1-x), \\ E_{g,In_xGa_{1-x}N}(x) &= xE_{g,InN} + (1-x)E_{g,GaN} - 2.5x(1-x), \\ E_{g,Al_xIn_{1-x}N}(x) &= xE_{g,AlN} + (1-x)E_{g,InN} - 5.4x(1-x). \end{aligned} \tag{1.8}$$

Note that the bandgap is a temperature-dependent quantity, with a functional form often fitted to the empirical Varshni formula: [73]

$$E_g(T) = E_g(T=0) - \frac{\alpha_V T^2}{T + \beta_V}, \tag{1.9}$$

where α_V and β_V are adjustable (Varshni) parameters. Examples of the latter for the binary compounds are given in Tab. 1.2. We whish to point out that other, more physically justified and possibly quantitatively accurate, functional forms have been proposed [74], [75]. Among them an often used model, with a more adapted dependence in the cryogenic region, is the Bose-Einstein-related model function [75]:

$$E_g(T) = E_g(T=0) - \frac{a_{BE}\Theta_{BE}}{e^{\Theta_{BE}/T} - 1}, \tag{1.10}$$

where the parameter a_{BE} represents the limiting magnitude of the slope (= entropy [76]),

$$S(T) = \frac{-dE_g(T)}{dT}, \tag{1.11}$$

of the $E_g(T)$ curve when $T \to \infty$, i.e., $S(\infty)$, and Θ_{BE} is approximately equal to the average phonon temperature.

As a direct bandgap semiconductor, the valence band maximum and conduction band minimum of GaN are both located at the center of the first Brillouin zone (Γ). In Fig. 1.4(b) a sketch of the bandstructure of GaN around $\mathbf{k} = 0$ (around the Γ point) is reported. For a more

regime in a microcavity based on $GaN/Al_{0.2}Ga_{0.8}N$ MQWs [70].

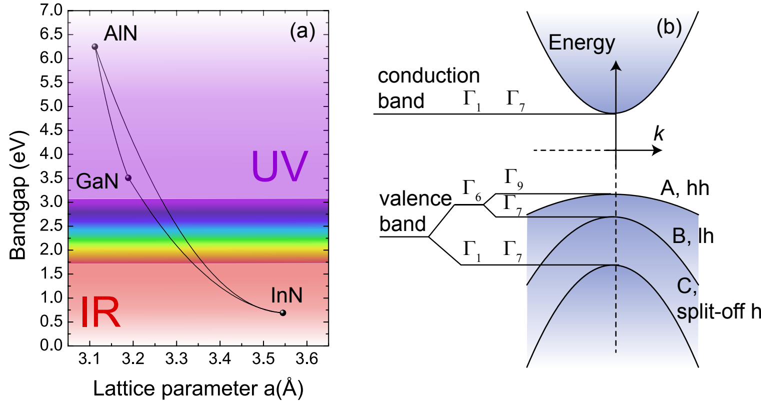

Figure 1.4: (a) Bandgap of wurtzite III-nitride compounds versus their in-plane lattice constant *a*. Values are taken from Tab. 1.2 at 0 K and for the bandgap bowing Ref. [72] is considered. (b) GaN band structure around $k = 0$ illustrating the degeneracy lift of the valence band leading to the formation of A (heavy hole (hh)), B (light-hole (lh)), and C (split-off hole) exciton.

refined picture the interested reader might consider Ref. [77], where the bandstructure of GaN is calculated in the framework of density-functional theory in the local-density approximation. In the effective mass approximation, the dispersion of the bands close to the center of the first Brillouin zone are modeled by a parabola, as shown in Fig. 1.4(b). The energy of the conduction band ($E_c(\mathbf{k})$) and that of the valence band ($E_v(\mathbf{k})$), for 0 value at the bands edge, are thus given by:

$$E_c(\mathbf{k}) = \frac{\hbar^2 k^2}{2m_e^*} \text{ and } \quad E_v(\mathbf{k}) = -\frac{\hbar^2 k^2}{2m_h^*}, \tag{1.12}$$

where m_e^* and m_h^* are the electron and hole effective masses, respectively.

In III-nitrides, similar to other semiconductors (e.g., group IV elements) the upper valence band is formed by bonding *p*-like states, while the conduction band is formed by antibonding *s*-like states. As illustrated in Fig. 1.4(b), the structural anisotropy leads to a lift of the threefold degeneracy of the valence band: the valence band is split by the crystal field coupling into a Γ_1- and a Γ_6-band. Taking into account the spin-orbit interaction the two-fold degeneracy of the Γ_6-band is further lift and splits into Γ_7- (light hole) and Γ_9-band (heavy hole), whereas the Γ_1-band is as well affected and changes into a Γ_7-band (split-off hole).

The A, B, and C interband transitions do have different oscillator strengths (f_{osc}) depending on the light polarization and the strain state of the III-nitride compound [78]. For relaxed bulk GaN, whenever the polarization of the electric field vector **E** is perpendicular to the *c*-axis (which is the case for vertical incident light on III-nitride compounds grown along the *c*-axis), the A and B transitions are dominating ($f_{osc,A\perp} \sim f_{osc,B\perp}$ and $f_{osc,C\perp} \sim f_{osc,A\perp}/8$), whereas the C transition is dominating ($f_{osc,A||} = 0$ and $f_{osc,B||} \sim f_{osc,C||}/7$) in the case of **E** parallel to the *c*-axis [79, 80].
As already mentioned crystal deformations arising from large differences in the lattice parameters of III-nitride compounds with respect to each other and as well with respect to

Compounds	AlN	GaN	InN
$E_g(T = 0$ K) (eV)	6.25	3.51	0.69 [82]
$E_g(T = 300$ K) (eV)	6.14	3.43	0.64 [82]
α_V (meV/K)	1.799	0.909	0.245
β_V (K)	1462	830	624

Table 1.2: Bandgap values are extracted from Ref. [60] unless specified.

foreign substrates[2] affect strongly the band structure and thus the optical properties: for a compressive strain the bandgap increases and for tensile strain it decreases [78, 81].

1.1.3 Excitons in bulk layers and quantum wells

Excitons in bulk layers

Through photon absorption in a semiconductor it is possible to promote an electron from the valence band to the conduction band leaving a hole (a positively charged particle) in the valence band. The electron interacts with the hole, i.e., it feels an attractive Coulomb potential. Thus the electron and the hole form a quasi-particle, the so-called exciton. For very strong electron-hole interaction such as in ionic crystals, the excitons are known as Frenkel excitons. In this case the electron and hole, tightly bound to each other, share the same or nearest-neighbor unit cell. This is not the case in semiconductors, where the binding is much weaker and excitons usually extend over several unit cells. In semiconductors excitons are referred to as the Wannier-Mott excitons.
An exciton represents a solid-state analog of a hydrogen atom and in this sense the exciton binding energy $E_{B,3D}$ and Bohr radius a_B can be given:

$$E_{B,3D} = \frac{1}{n^2}\frac{\mu e^4}{2\hbar^2(4\pi\epsilon_0\epsilon_r)^2} = \frac{\mu^*}{m_0\epsilon_r^2}\frac{R_{y,H}}{n^2} \quad \text{and } a_B = \frac{\hbar^2 4\pi\epsilon_0\epsilon_r}{\mu^* e^2}n = \frac{m_0}{\mu^*}\epsilon_r a_{B,H} n, \tag{1.13}$$

where n is the principal quantum number of the hydrogen-like orbital, $R_{y,H} = 13.6$ eV is the Rydberg energy of the hydrogen atom, $a_{B,H} = 0.53$ nm is the Bohr radius of the hydrogen atom, $\mu^* = m_e^* m_h^*/(m_e^* + m_h^*)$ is the reduced mass, and ϵ_r is the relative permittivity defined by the dielectric function (ϵ) of the material and the vacuum permittivity (ϵ_0): ϵ/ϵ_0. As already mentioned in equation 1.7 the exciton binding energy reduces the transition energy. The experimentally observed $E_{B,3D}$ value measured on GaN bulk layers amounts to 25 meV [83], whereas in InN and In-rich alloys excitonic effects are much smaller and usually hidden by the linewidth. The excitonic Bohr radius in GaN is estimated to be about 3 nm [84].

[2] C-plane sapphire (Al_2O_3) is a common substrate with an in-plane lattice parameter a of 4.763 Å. However, III-nitride compounds are under compressive strain when grown on sapphire as they align to the sublattice of the aluminum atoms (a_{Al}= 2.75 Å).

Excitons in QWs

In the strict 2D-limit for vanishing well width and infinite barrier height the exciton binding energy and the Bohr radius are given by:

$$E_{B,2D} = \frac{\mu^*}{m_0\epsilon_r^2}\frac{R_{y,H}}{(n-1/2)^2} \quad \text{and } a_B = \frac{m_0}{\mu^*}\epsilon_r a_{B,H}(n-1/2). \tag{1.14}$$

The binding energy of the ground state ($n=1$) is therefore enhanced with respect to the 3D case, i.e., $E_{B,2D} = 4E_{B,3D}$. However, in realistic situations, dealing with a finite barrier height, the binding energy reaches a maximum and decreases toward the 3D value of the barrier material when the well width goes to zero (cf. Fig. 1.3(b)). The latter occurs because the wavefunctions leak into the barrier material for small well widths. For large well widths the two dimensional confinement is lost and thus the exciton binding energy decreases to the 3D value of the well material.

1.2 III-nitride based cavity polaritons

This section will present the strong coupling between cavity photons and excitons, leading to so-called cavity polaritons, in III-nitrides materials. As these quasiparticles are obtained when an active medium is inserted into a planar microcavity, the next section is devoted to planar microcavities.

1.2.1 Planar Microcavities

Fabry-Perot cavity

Here we first describe the ideal Fabry-Perot resonator before discussing the specific case of semiconductor cavities, which differ by the type of mirrors used.

A Fabry-Perot cavity contains two reflecting interfaces: an air-cavity-medium interface and a cavity-medium-air interface spaced by L_c (see Fig. 1.5(a)). The phase difference between two reflected beams R_1 and R_2 is given by $e^{ik_0n_c\delta_1 - ik_0\delta_2} = e^{ik_0\delta_c}$, where δ_1 corresponds to the red path and δ_2 to the blue path in Fig. 1.5(a), i.e.:

$$\delta_c = \frac{2n_cL_c}{\cos\theta_i} - \frac{2L_c}{\cos\theta_i}\sin\theta_i\sin\theta_e = 2n_cL_c\cos\theta_i, \tag{1.15}$$

where n_c is the refractive index of the cavity, θ_e is the external angle, and θ_i is the internal angle. The latter are related through Snell's law $n_c sin\theta_i = sin\theta_e$. The total transmission is given by a convergent geometric series in equation 1.16 and can be seen in Fig. 1.5(b) for two

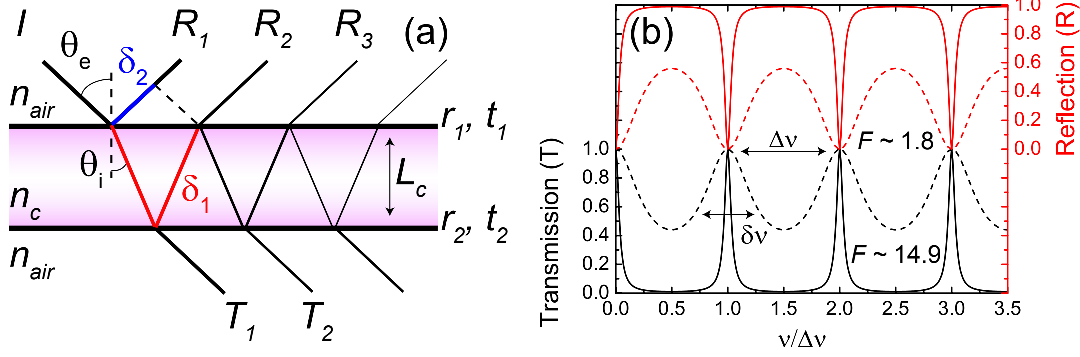

Figure 1.5: (a) Schematic description of a Fabry-Perot cavity where n_{air} is the refractive index of air, I is the incident beam, R_1, R_2 are reflected beams, T_1, T_2 are transmitted beams, and $r_{1(2)}$, $t_{1(2)}$ are the amplitude reflectivity and transmission coefficients of the first (second) interface (mirror), respectively. (b) Transmission (black) and reflectivity (red) spectra for a Fabry-Perot cavity with a finesse $F \sim 14.9$ (i.e., $r_1 = r_2 = 0.9$) (continuous lines) and one with $F \sim 1.8$ (i.e., $r_1 = r_2 = 0.45$) (dashed lines). In both cases, t_1 and t_2 are taken so that $t_{1,2} = \sqrt{1 - r_{1,2}^2}$ (lossless case). The mode spacing $\Delta\nu$ as well as the full width at half maximum $\delta\nu$ are indicated for the cavity with the lower F value.

different Fabry-Perot cavities:

$$T = |t_1 t_2 e^{ik_0\delta_c} \sum_{n=0}^{\infty} (r_1 r_2 e^{2ik_0\delta_c})^n|^2 = \frac{(t_1 t_2)^2}{1 + (r_1 r_2)^2 - 2 r_1 r_2 \cos(k_0 \delta_c)}. \tag{1.16}$$

Note that this latter expression can also be derived using the transfer matrix approach (cf. Appendix A.1 and Ref. [85]). It can be seen in the same figure that the criterion to have cavity modes is $k_0\delta_c = \frac{2\pi\nu}{c}\delta_c = 2\pi q$, with ν the frequency of the incoming light, c the speed of light in vacuum, and q an integer corresponding to the order of the cavity. Thus, the cavity displays transmission maxima separated by:

$$\Delta\nu = \frac{c}{\delta_c} = \frac{c}{2 n_c L_c} \tag{1.17}$$

at normal incidence. $\Delta\nu$ corresponds to the mode spacing and is also referred to as the *free spectral range*. Note however, that the mode spacing is not constant in a wavelength dependent spectrum. As an illustration if we have a 3λ-cavity, i.e., $q = 6$, and from the latter in order to have a cavity mode at perpendicular incidence ($\theta_i = 0$), the cavity length is given by $L_c = q\,\lambda/2n_c$ and the distance to the next higher or lower mode is $\Delta\lambda=\lambda(1/(q+1))$ or $\Delta\lambda=\lambda(1/(q\text{-}1))$, respectively.

The finesse of a cavity (F) is defined as the mode spacing ($\Delta\nu$) over the full width at half maximum (FWHM) of the transmission spectrum ($\delta\nu$):

$$F = \frac{\Delta\nu}{\delta\nu} = \pi \frac{\sqrt{r_1 r_2}}{1 - r_1 r_2}. \tag{1.18}$$

However, frequently the *cavity quality factor Q* rather than the finesse is used. The quality factor is defined as the cavity mode frequency (or energy) (ν_0) over the FWHM of the transmission spectrum ($\delta\nu$):

$$Q = \frac{\nu_0}{\delta\nu} = q\pi\frac{\sqrt{r_1 r_2}}{1 - r_1 r_2} \text{ and } q \in \mathbb{N}^*. \quad (1.19)$$

The energy of the modes is given by $\hbar c k_0 = \hbar c \frac{k_c}{n_c} = \frac{hcq}{2n_c L_c cos\theta_i}$. To get the angular dispersion of photonic modes one has to express the mode energy as a function of the cavity wave vector k_c (using its parallel component $k_{c||} = k_{0||}$ and its perpendicular component $k_{c\perp} = \frac{2\pi q}{2L_c}$):[3]

$$k_c = \sqrt{k_{c||}^2 + k_{c\perp}^2} = \sqrt{k_{0||}^2 + \left(\frac{\pi q}{L_c}\right)^2}, \quad (1.20)$$

and

$$E_q = \frac{\hbar q \pi c}{L_c n_c}\sqrt{1 + \left(\frac{L_c k_{||}}{q\pi}\right)^2}. \quad (1.21)$$

In general, the approximation $k_{0||} \ll \frac{q\pi}{n_c L_c}$ is used, leading to the parabolic approximation:

$$E_q \approx \frac{\hbar q \pi c}{L_c n_c}\left(1 + \frac{1}{2}\left(\frac{L_c k_{0||}}{q\pi}\right)^2\right) = E_{q,0} + \frac{\hbar^2 k_{0||}^2}{2m_{ph}^*}, \quad (1.22)$$

where $E_{q,0}$ is the photon energy at $k_{0||} = 0$ and m_{ph}^* is the photon effective mass:

$$E_{q,0} = \frac{\hbar q \pi c}{n_c L_c}, \quad m_{ph}^* = \frac{\hbar q \pi n_c}{c L_c}. \quad (1.23)$$

In all the microcavities presented in this work, DBRs (described in detail in the next section) are used and thus the effective photon mass has to be expressed as a function of the effective cavity length L_{eff}, the effective cavity refractive index n_{eff} and the effective order q^* [86].

$$m_{ph}^* = \frac{\hbar q^* \pi n_{eff}}{c L_{eff}}, \quad (1.24)$$

[3] The interference condition of the cavity layer being applied to the part of the electromagnetic wave propagating in the normal direction, the normal wavevector is given by: $k_{c\perp} 2L_c = 2\pi q$.

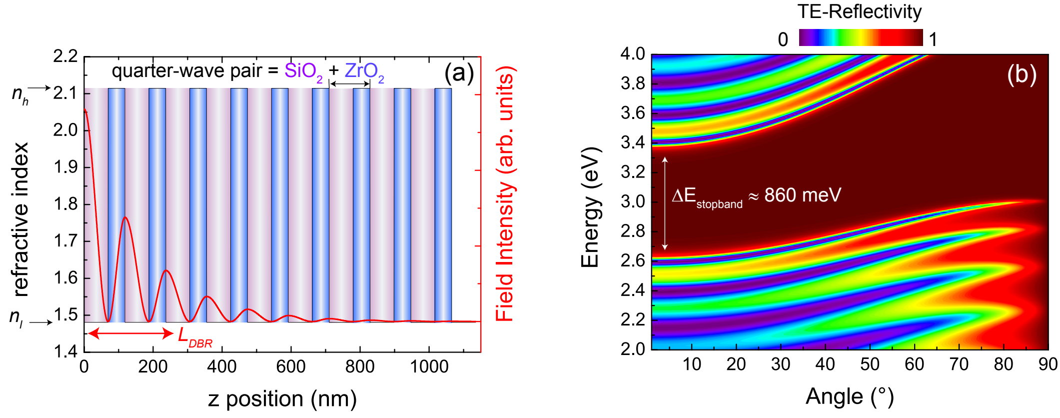

Figure 1.6: (a)Illustration of a SiO_2-ZrO_2 10 pair DBR centered at $\lambda_0 \sim 413$ nm ($E_{DBR} = 3$ eV) together with the field intensity calculated within the transfer matrix formalism. L_{DBR} corresponds to the mirror penetration depth. (b) Corresponding angle-resolved reflectivity spectrum for the TE-polarization.

$$L_{eff} = L_c + L_{DBR_1} + L_{DBR_2}, \quad q^* = q + \left(\frac{n_h n_l}{(n_h+n_l)(n_h-n_l)}\right)_{DBR_1} + \left(\frac{n_h n_l}{(n_h+n_l)(n_h-n_l)}\right)_{DBR_2}, \quad (1.25)$$

where L_{DBR_1} and L_{DBR_2} are the mirror penetration depths, given in equation 1.28, and n_h (n_l) stands for the higher (lower) refractive index for each type of DBR bilayers.

Distributed Bragg reflectors

Metal mirrors are limited to reflectivities ~ 95%, whereas DBRs might reach values over 99%. Furthermore, the light extraction of planar semiconductor microcavity devices such as VCSELs and resonant-cavity LEDs (RCLEDs) occurs either from the top or the bottom surface, which is impossible in the case of metallic mirrors, as the latter are absorbing. DBRs are made of periodic stacks of bilayers, each with an optical thickness of $\lambda_0/4$, i.e., a quarter-wave and with a physical thickness of $\lambda_0/(4n(\lambda_0))$, where $n(\lambda_0)$ is referring to the refractive index of the considered layer at λ_0. In Fig. 1.6(a) a schematic illustration of a DBR is given highlighting the quarter-wave pairs formed by two quarter-wave layers of material with a high (n_h) and a low (n_l) refractive index, respectively.

Furthermore, DBRs are characterized by a narrow band of high reflectivity centered at λ_0 denoted as *stop band*. Its spectral width ($\Delta\lambda_{SB}$) is given by [87, 88]:

$$\Delta\lambda_{SB} = \frac{4\lambda_0}{\pi}\frac{n_h - n_l}{n_l + n_h} \text{ or } \Delta E_{SB} = \frac{4E_{DBR}}{\pi}\frac{n_h - n_l}{n_l + n_h}, \quad (1.26)$$

where $E_{DBR} = hc/\lambda_0$. The maximum of the DBR reflectivity arising from multiple reflections at the interfaces of the bilayers and their constructive interference depends on the number of

quarter-wave pairs (m) and the refractive index contrast of the latter (with $n_l < n_h$) [88]:

$$R = \left(\frac{1 - \frac{n_{out}}{n_{in}} \left(\frac{n_l}{n_h} \right)^{2m}}{1 + \frac{n_{out}}{n_{in}} \left(\frac{n_l}{n_h} \right)^{2m}} \right)^2 , \tag{1.27}$$

where n_{in} (n_{out}) is the refractive index of the incident medium (exit medium, respectively). In the limit case of a Bragg mirror with an infinite number of pairs, the penetration depth is given by [86]:

$$L_{DBR} = \frac{\lambda_0}{4n_{in}} \left(\frac{n_{l,i}}{n_{h,i}} \right) \frac{n_h}{n_h - n_l} \tag{1.28}$$

where λ_0 is the central wavelength and $n_{l,i}/n_{h,i}$ is the ratio of the refractive indices at the interface between the incident medium (subscript i) and the first quarter-wave mirror layer.

1.2.2 The strong coupling regime in III-nitride based microcavities

The QW exciton and the cavity mode represent two oscillators which can be coupled to each other. In the formalism of the second quantization the non-interacting Hamiltonian of cavity photons and QW excitons can be expressed as:

$$H_0 = \sum_{\boldsymbol{k}_{||}} E_X(\boldsymbol{k}_{||}) b^{\dagger}_{\boldsymbol{k}_{||}} b_{\boldsymbol{k}_{||}} + \sum_{\boldsymbol{k}_{||}} E_C(\boldsymbol{k}_{||}) a^{\dagger}_{\boldsymbol{k}_{||}} a_{\boldsymbol{k}_{||}}, \tag{1.29}$$

where $b^{\dagger}_{\boldsymbol{k}_{||}}$ ($b_{\boldsymbol{k}_{||}}$) is the creation (annihilation) operator of the uncoupled exciton and $a^{\dagger}_{\boldsymbol{k}_{||}}$ ($a_{\boldsymbol{k}_{||}}$) is the creation (annihilation) operator of the uncoupled cavity photon of in-plane wavevector $\boldsymbol{k}_{||}$. The linear exciton-photon interacting term is given by [89]:

$$H_{int} = \sum_{\boldsymbol{k}_{||}} g b^{\dagger}_{\boldsymbol{k}_{||}} a_{\boldsymbol{k}_{||}} + \sum_{\boldsymbol{k}_{||}} g a^{\dagger}_{\boldsymbol{k}_{||}} b_{\boldsymbol{k}_{||}}, \tag{1.30}$$

where g is the light-matter coupling constant. Thus, the following Hamiltonian can be written for the coupled system ($H = H_0 + H_{int}$):

$$H = \sum_{\boldsymbol{k}_{||}} \begin{pmatrix} b^{\dagger}_{\boldsymbol{k}_{||}} & a^{\dagger}_{\boldsymbol{k}_{||}} \end{pmatrix} \begin{pmatrix} E_X(\boldsymbol{k}_{||}) & g \\ g & E_C(\boldsymbol{k}_{||}) \end{pmatrix} \begin{pmatrix} b_{\boldsymbol{k}_{||}} \\ a_{\boldsymbol{k}_{||}} \end{pmatrix}. \tag{1.31}$$

One has to diagonalize this matrix to determine the eigenenergies and eigenstates of the coupled photons and excitons at a given $\boldsymbol{k}_{||}$. The eigenenergies are then given by the following expressions:

$$E_{LP}(\boldsymbol{k}_{||}) = \frac{1}{2}\left[E_X(\boldsymbol{k}_{||}) + E_C(\boldsymbol{k}_{||}) - \sqrt{(E_X(\boldsymbol{k}_{||}) - E_C(\boldsymbol{k}_{||}))^2 + 4g^2}\right], \quad (1.32)$$

$$E_{UP}(\boldsymbol{k}_{||}) = \frac{1}{2}\left[E_X(\boldsymbol{k}_{||}) + E_C(\boldsymbol{k}_{||})) + \sqrt{(E_X(\boldsymbol{k}_{||}) - E_C(\boldsymbol{k}_{||}))^2 + 4g^2}\right], \quad (1.33)$$

where LP and UP stand for lower and upper polariton, respectively. The corresponding normalized eigenvectors are:

$$\begin{pmatrix} X_{\boldsymbol{k}_{||}} \\ C_{\boldsymbol{k}_{||}} \end{pmatrix} \text{and} \begin{pmatrix} C_{\boldsymbol{k}_{||}} \\ -X_{\boldsymbol{k}_{||}} \end{pmatrix}, \quad (1.34)$$

where $X_{\boldsymbol{k}_{||}}$ and $C_{\boldsymbol{k}_{||}}$ are the Hopfield coefficients [90], which are given by:

$$X_{\boldsymbol{k}_{||}} = \frac{1}{\sqrt{1 + \left(\frac{E_{LP}-E_X}{g}\right)^2}} \text{ and } C_{\boldsymbol{k}_{||}} = -\frac{1}{\sqrt{1 + \left(\frac{g}{E_{LP}-E_X}\right)^2}}. \quad (1.35)$$

They can be used to express the exciton $|X_{\boldsymbol{k}_{||}}|^2$ and photon $|C_{\boldsymbol{k}_{||}}|^2$ fractions of the polaritons. In Fig. 1.7(c) the exciton and photon fraction are calculated as a function of the external angle for the lower polariton branch displayed in Figs. 1.7(a) and 1.7(b).

We have to give two definitions that are used in the following chapters: the difference $\delta = E_C(0)$ - $E_X(0)$ between the uncoupled modes (the cavity photon and the exciton) is the so-called detuning. The vacuum field Rabi splitting ($\hbar\Omega_{VRS}$) is the energy splitting (i.e., the energy difference between the upper and the lower polariton branch) at zero detuning. It is given by $\hbar\Omega_{VRS} = 2g$ (in the case where sources of broadening are neglected).[4] In the inset of Fig. 1.7(b) the definitions of δ and Ω_{VRS} are illustrated. Excitons and polaritons with in-plane wave vector $\boldsymbol{k}_{||}$ (with modulus $k_{||}$) couple to photons with the same momentum. However, if the energy of the latter is below the light cone, i.e., $E_{X,LPB,UPB}(k_{||})<(\hbar c/n_{air})k_{||}$, they are evanescent in the material and cannot couple to the electric field outside the cavity. In Fig. 1.7(a) the light cone is illustrated in red and radiative modes are possible for $|\boldsymbol{k}_{||}| < 20\ \mu m^{-1}$. Thus $k_{||}$ can be expressed as a function of the external angle θ_e:

$$\tan\theta_e = \frac{k_{||}}{k_z} = \frac{k_{||}}{\sqrt{\left(\frac{E}{\hbar c}\right)^2 - k_{||}^2}} \Longrightarrow k_{||} = \frac{E}{\hbar c}\sin\theta_e. \quad (1.36)$$

[4] In the following the energy splitting at zero detuning is denoted only by Ω_{VRS} instead of $\hbar\Omega_{VRS}$.

Furthermore all the dispersion curves can be computed as a function of the external angle (cf. Fig. 1.7(b)), which is very useful for comparison with experimental data. Note that the anticrossing behavior of the lower and upper polariton branches can be observed only for negative detunings.

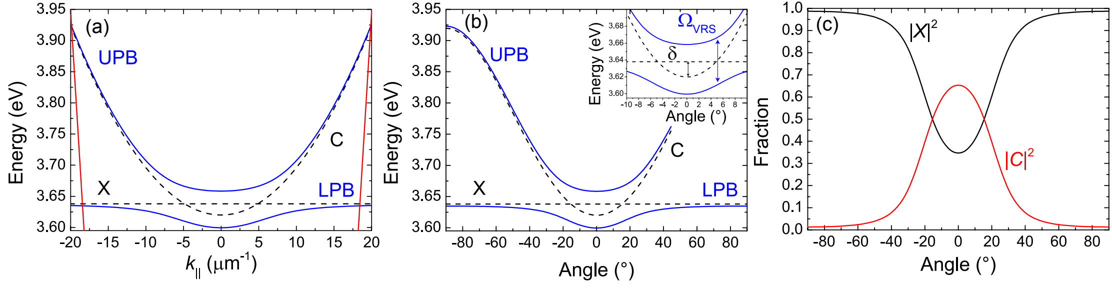

Figure 1.7: (a) Computed dispersions of the upper (UPB) and lower (LPB) polariton branches as a function of in-plane wavevector $k_{||}$ along with the uncoupled cavity (C) and exciton (X) modes for Ω_{VRS} = 56 meV, and m^*_{ph}=5·10^{-5}m_0 (m_0 is the free electron mass). In red the light cone for air is indicated. (b) Polariton modes and uncoupled mode dispersions *versus* external angle. The inset shows a zoom for small external angles in order to illustrate the definition of the detuning δ and the vacuum field Rabi splitting Ω_{VRS}. (c) Corresponding exciton $|X|^2$ and photon $|C|^2$ fractions of the lower polaritons *versus* external angle.

At this stage, it is useful to give a simplified expression for the coupling constant g [91]:

$$g \approx \hbar \left(\frac{2\Gamma_0 c N_{QW,eff}}{n_c L_{eff}} \right)^{1/2}, \tag{1.37}$$

where L_{eff} is the effective cavity length, given in equation 1.25, and $N_{QW,eff}$ is the number of QWs coupled to the cavity light field. The effective number of QWs $N_{QW,eff}$ can be obtained by summing the normalized squared electric field at the QW positions [92]. $\hbar\Gamma_0$ is the radiative width of the free exciton and can be expressed in terms of the exciton oscillator strength per unit area (f_{osc}/A):

$$\hbar\Gamma_0 = \frac{\pi}{n_c} \frac{e^2}{4\pi\epsilon_0} \frac{\hbar}{m_0 c} \frac{f_{osc}}{A}. \tag{1.38}$$

Thus in order to increase the coupling constant g, the number of QWs has to be increased and QWs have to be placed at the cavity light field antinodes in order to enhance the overlap of the exciton wavefunction with the electric field. Furthermore, the effective cavity length has to be kept as short as possible. This can be achieved by choosing DBRs with quarter-wave pairs that present a high refractive index contrast, e.g., dielectric DBRs (dDBRs).

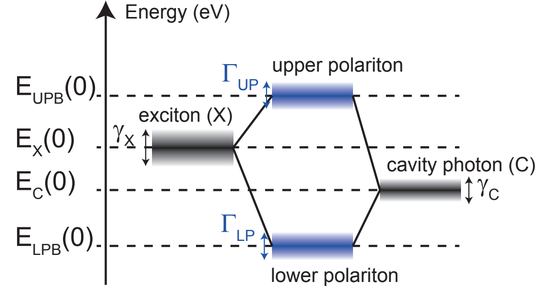

Figure 1.8: Schematic representation of the coupling between the two uncoupled modes (exciton X and cavity photon C) giving rise to two new eigenmodes: the upper and the lower polariton states. Γ_{UP}, Γ_{LP}, γ_C, and γ_X are the upper polariton, lower polariton, cavity photon, and exciton broadenings.

Impact of exciton and photon mode broadening

The previous model describing the strong coupling regime does not take into account the broadenings of the exciton and the photon modes. We have sources of homogeneous and inhomogeneous broadenings for the exciton mode, as already mentioned in section 1.1.3, and as well the photon mode suffers from broadening. The main sources of broadening of the cavity photon mode are the non-zero transmission of the Bragg mirrors, in-plane photonic disorder, and residual absorption. They will be discussed in detail in section 3. In Fig. 1.8 a schematic representation of the real case, where we have a non-zero linewidth for the exciton (γ_X), the cavity photon (γ_C), the upper polariton (Γ_{UP}) and the lower polariton (Γ_{LP}), is displayed.

The SCR in presence of dissipation can be modeled using the analogy with two damped oscillators. The vacuum Rabi splitting for the absorption line splitting in this case becomes equal to (in the case of sources of homogeneous broadening only) [92]:

$$\hbar\Omega_{VRS} = 2\sqrt{g^2 - \frac{1}{2}(\gamma_X^2 + \gamma_C^2)}. \tag{1.39}$$

Thus the absorption line splitting can be observed as long as $g^2 > (\gamma_X^2+\gamma_C^2)/2$, i.e., the system is in the strong coupling regime. Note however that while $(\gamma_X - \gamma_C)^2/4 < g^2 < (\gamma_X^2+\gamma_C^2)/2$ the system remains in a non perturbative regime, whereas no mode splitting is observed. The latter is the so-called intermediate coupling regime [93]. The weak coupling regime occurs for $g^2 < (\gamma_X - \gamma_C)^2/4$.

The effect of inhomogeneous excitonic broadening onto the mode splitting can be modeled in the framework of the transfer matrix formalism using a slight variation of the *linear dispersion model*, as described by Zhu *et al.* [94]. The latter showed that mode splitting can be observed using a completely classical model where each QW is treated as a local Lorentz oscillator. Note however that a more sophisticated model should rely on the nonlocal semiclassical theory [92, 95]. The local fully classical theory provides results close to the latter provided the homogeneous linewidth of the exciton γ_X is sufficiently large, otherwise it can yield nonphysical results. In the case of inhomogeneous broadening the response of each QW is not treated by identical Lorentz oscillators anymore, but rather by a set of nonidentical Lorentz

oscillators, i.e., the dielectric function $\epsilon(E)$ of the QWs is replaced by [96]:

$$\epsilon(E) = \epsilon_\infty + \int_{-\infty}^{\infty} g(E')L(E-E')dE', \tag{1.40}$$

where $g(E')$ is the distribution function of the individual Lorentz oscillators $L(E) \sim 1/(E_0^2 - E^2 - i\gamma_X E)$, associated to each excitonic transition, and ϵ_∞ is the background dielectric constant. The distribution function $g(E')$ can be taken as Gaussian.

Demonstration of the strong coupling regime with bulk GaN and GaN/AlGaN MQW microcavities

The first demonstration of cavity polaritons in III-nitride based cavities goes back to 2003 and has been achieved for a bulk GaN microcavity grown on a silicon substrate with a top dielectric DBR at cryogenic temperature (T = 5 K) [97]. Only two years later the same group reported strong light-matter coupling at RT with a vacuum Rabi splitting up to 60 meV for a bulk GaN microcavity with a top metallic mirror [98]. They further pursued their studies on bulk GaN microcavities by studying the influence of the mirrors on the strong coupling regime [99]. However, the quality factor of those structures remained too low (ranging from 50 to 190 depending on the samples [99]) for the observation of nonlinear properties, such as polariton lasing. Parallel to this group, Alyamani and coworkers reported in 2007 the observation of the strong coupling regime at low and room temperature for a hybrid GaN microcavity based on $Al_xGa_{1-x}N/Al_yGa_{1-y}N$ DBRs [100]. However, big improvements considering the quality factor of III-nitride based cavities are related to the pioneering work at the EPFL of Carlin and coworkers who developed the growth of crack-free InAlN based DBRs [101]. Thus, RT polariton luminescence from a bulk GaN microcavity based on a bottom lattice-matched $Al_{0.85}In_{0.15}N/Al_{0.2}Ga_{0.8}N$ DBR and a top dielectric DBR was reported in 2006 [102] followed by the first observation of polariton lasing at RT in 2007 [54].

Furthermore, polariton lasing under non-resonant optical pumping was reported one year after in a III-nitride based quantum well structure [55]. The latter structure grown on a c-plane sapphire substrate consists of a strain relieving template, followed by a 35 pair bottom lattice-matched $Al_{0.85}In_{0.15}N/Al_{0.2}Ga_{0.8}N$ DBR. Then the $5\lambda/2$ active region consisting of a 67 period GaN (1.2 nm) / $Al_{0.2}Ga_{0.8}N$ (3.6 nm) MQW structure sandwiched between two $\lambda/4$ $Al_{0.2}Ga_{0.8}N$ layers. The 3λ-cavity layer is finally completed by a 13 pair top SiO_2/Si_3N_4 DBR (cf. Fig. 1.9(a)) [55, 70]. In Fig. 1.9(b) the RT experimental dispersion curves deduced from angle-resolved PL measurements are shown, highlighting the anticrossing behavior showing a large vacuum Rabi splitting Ω_{VRS} of 56 meV. In Fig. 1.9(c) and 1.9(d) the nonlinear behavior of the PL-emission is shown, i.e., the demonstration of low-threshold lasing dubbed as polariton lasing.

In the meantime polariton lasing was achieved as well in all-dielectric microcavities based on

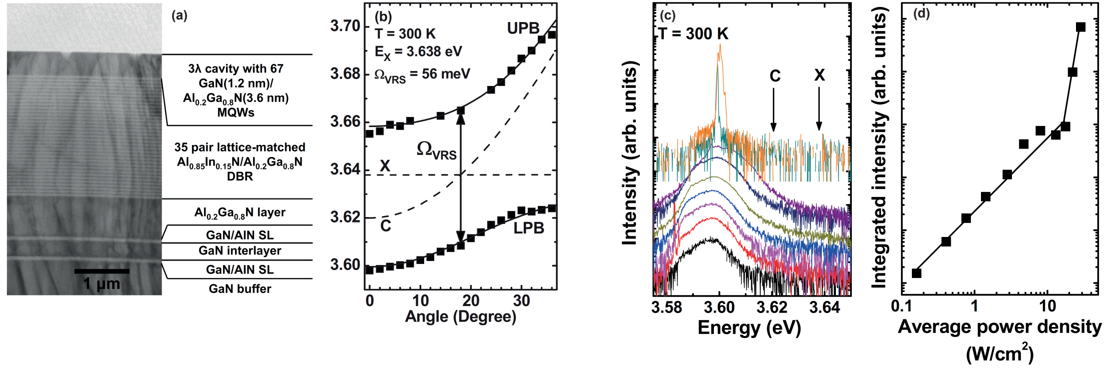

Figure 1.9: (a) Cross-section transmission electron micrograph of a GaN/AlGaN MQW half-microcavity structure together with experimental evidence for polariton lasing (c)-(d). (b) RT experimental dispersion curve deduced from PL spectra (black squares) and fits of the LPB and the UPB (black lines). The position of the uncoupled cavity mode (C) and the uncoupled exciton (X) is also reported (dashed lines). (c) RT emission spectra at average pump power densities ranging from 0.16 to 28.8 W/cm^2 at $k_{||}$=0, shifted for clarity. C and X are also reported (arrows). (d) Integrated output intensity. The line is a guide for the eyes. (a)-(d) Taken from G. Christmann *et al.* [55, 70].

bulk GaN [103]. Furthermore, the strong coupling regime together with nonlinear emission has been recently observed in a non-polar microcavity based on a GaN/AlGaN MQW active region, taking advantage of the increased oscillator strength in non-polar QWs due to the absence of the QCSE [104, 105].

Strong coupling with InGaN/GaN quantum wells? Motivation and state of the Art

As mentioned in the previous section the observation of polariton lasing under nonresonant optical pumping at RT is well established in both bulk GaN and GaN/AlGaN MQW based planar microcavity structures. However, for electrical-injection purposes they seem not to be suitable due to (i) the difficulties related to *p*-type doping and (ii) the availability of a transparent conductive oxide (TCO) layer in the corresponding wavelength region. *P*-type doping becomes progressively more difficult when increasing the Al content, as increasing the Al content of AlGaN layers strongly raises the activation energy of the deep Mg acceptor level [106]. Conventional TCOs such as indium tin oxide (ITO) and ZnO are not transparent in the near-UV spectral region due to their small energy band gap (~ 3.2 eV). Furthermore, materials with a wider band gap tend to exhibit a smaller conductivity. The most promising material for UV TCOs seems to be Ga_2O_3. Conductivities up to ~ 1 S·cm^{-1} have been reported for Sn doped thin layers [107]. Note that in general TCO thin films used as electrodes present conductivities of the order of 10^3 S·cm^{-1} [108]. In order to circumvent this problem deep-UV LEDs are backside emitting devices, i.e., the LED is grown on an AlN templates on a transparent sapphire substrate, using a top *p*-GaN contact or recently even a *p*-AlGaN one to a highly reflective metallic electrode [109, 110]. Unfortunately this approach is not well suited for

the GaN/AlGaN MQW microcavity structure described above as the DBR growth has been optimized on an absorbing GaN template.
Thus, when speaking about electrical-injection, microcavities with embedded InGaN/GaN MQWs have to be considered [25]. However, III-nitride based electrically-driven VCSELs based on InGaN/GaN MQWs[5] are far from being conventional since the report of lasing action at RT in such structures is very recent [14, 18].[6]

Note that the SCR has been reported in 2004 by Tawara and coworkers for $In_{0.15}Ga_{0.85}N$ /$In_{0.02}Ga_{0.98}N$ QWs inserted in an $Al_{0.07}Ga_{0.93}N$ cavity layer sandwiched between two dielectric (SiO_2/ZrO_2) distributed Bragg reflectors [111]. However, those latter results have not been recognized by the III-nitride and the cavity polariton communities, due to an unconsistent ratio of inhomogeneous exciton broadening to vacuum Rabi splitting (VRS) [112–114]. Actually, they reported a VCR of 6 meV and 17 meV for two samples with a different quantum well number, whereas their inhomogeneous exciton broadening is by far larger, typically ~ 200 meV.

Only recently the first RT current injected polariton LED based on $In_{0.15}Ga_{0.85}N$/GaN MQWs was reported by T.-C. Lu *et al.* [115]. The claim for strong coupling observation is not free of any doubts mainly because their interpretation is based on an exciton inhomogeneous linewidth broadening of 7 meV. No absorption-like measurements are shown to prove the latter, particularly because the state of the art broadening of such QWs is increased by at least a factor of 5 (cf. chapter 4). In conclusion the strong coupling regime with InGaN/GaN QWs remains to be proven.

[5] No electrically-driven VCSELs based on GaN/AlGaN MQWs have been reported so far due to the above-mentioned challenges.
[6] By design, those devices are not optimized for strong coupling applications.

2 Theoretical study of emission properties of III-nitride polariton laser diodes

In this chapter the main emission characteristics of electrically-driven polariton LDs based on planar GaN microcavities with embedded InGaN QWs are studied theoretically. The modeling of the steady state properties of two experimentally relevant pumping geometries has been performed by Ivan Iorsh at Durham University, Durham, UK, in close interaction with our group.
The chapter is organized as follows: first the reader is provided with the present status of electrically-driven polariton sources. Then, the most promising material systems, including III-nitride compounds, for the realization of RT electrically driven polariton lasers are discussed. In a second part two experimentally relevant pumping geometries of polariton LDs are presented. A generic description of polariton LDs is given in a third section. In a next section, using a quasi-analytical model the steady-state, high-speed current modulation and the RIN features, which are all figures of merit of polariton LDs, are derived. Eventually, in the last section of this chapter the emission properties of III-nitride polariton LDs are summarized and compared to those of VCSELs.

2.1 Introduction

Since Imamoğlu *et al.* [33] suggested in 1996 the use of non-equilibrium polariton condensates to produce a low threshold coherent light source, experimentalists were challenged with the realization of the first polariton LD. Prior to the realization of the first diodes the possibility of nonresonant electrical injection of excitons had to be proven. In 2007 Bajoni and coworkers showed that at low current density, the emission spectra of a *p*-*i*-*n* diode with an embedded InGaAs QW were dominated by exciton emission at low temperature [116]. The latter was paving the way for the first realizations of polariton LEDs by two different groups simultaneously only one year later [48, 49]. Structures were GaAs-based microcavities and anticrossing behavior was observed at cryogenic temperatures (up to 100 K). In the same year a third group realized the first polariton LED based on a GaAs-microcavity operating at RT [50].

Lately, hints for polaritonic nonlinearities under electrical injection have been observed in the latter system at cryogenic temperatures [51, 52]. However, in practice these were shown to lase not only at low temperatures but as well under strong magnetic fields.

Despite the fact that the strong coupling regime is preserved at high temperatures under electrical injection, GaAs-based microcavities are not expected to operate as polariton lasers at RT due to the limited robustness of QW excitons in this material system. Indeed, Saba and coworkers showed through experiments carried out under resonant excitation that the cut-off temperature of parametric gain, i.e., of polaritonic nonlinearities, scales linearly with the exciton binding energy [53].

When searching for material systems defined by larger values of the exciton binding energy, a strong interest has been directed towards wide bandgap semiconductors like GaN or ZnO [117] and organic molecules, like polystyrene films doped with the molecular dye tetraphenylporphyrin zinc [118], J-aggregates [45], or anthracene [119]. Considering organic semiconductor microcavities, RT polariton lasing under optical pumping has only been demonstrated recently [119, 120] mainly due to difficulties in building-up a macroscopically occupied ground state due to the low scattering rate of reservoir excitons with phonons compared to their radiative recombination rate. Having a look at ZnO, it appears as a promising candidate as polariton lasing can be achieved up to RT together with a large Vacuum Rabi splitting under optical pumping [117]. However, ZnO-based microcavities present some drawbacks considering the practical realization of a polariton LD: the fabrication of ZnO-based planar microcavities remains challenging as they are fully hybrid structures, i.e., they consist of a top dielectric DBR and an epitaxial ZnO layer deposited either on a dielectric DBR or on a III-nitride DBR. Fully hybrid cavities are preferred to cavities using ZnMgO-based DBRs due to the narrow stopband of the latter and the presence of eventual cracks. Another limiting factor when considering electrical injection stems from the fact that *p*-type conductivity in ZnO remains to be unambiguously demonstrated.

Thus, for the realization of polariton LDs able to operate at RT III-nitrides emerge as the main contender. They exhibit highly stable excitons up to RT and polariton lasing has been thoroughly investigated under nonresonant optical pumping at RT in both bulk GaN and GaN/AlGaN MQW based microcavity structures (cf. section 1.2.2). Very recently Bhattacharya *et al.* [24] observed electrically-injected polariton lasing from a bulk GaN-based microcavity diode. The sample design requirements to achieve polariton lasing under electrical injection in planar III-nitride microcavities are high and described in the next section.

2.2 Design of III-nitride polariton laser diodes

The experimental observations of polariton lasing under non-resonant optical pumping in bulk GaN and GaN/AlGaN MQW based microcavities [54, 55] triggered a few interesting the-

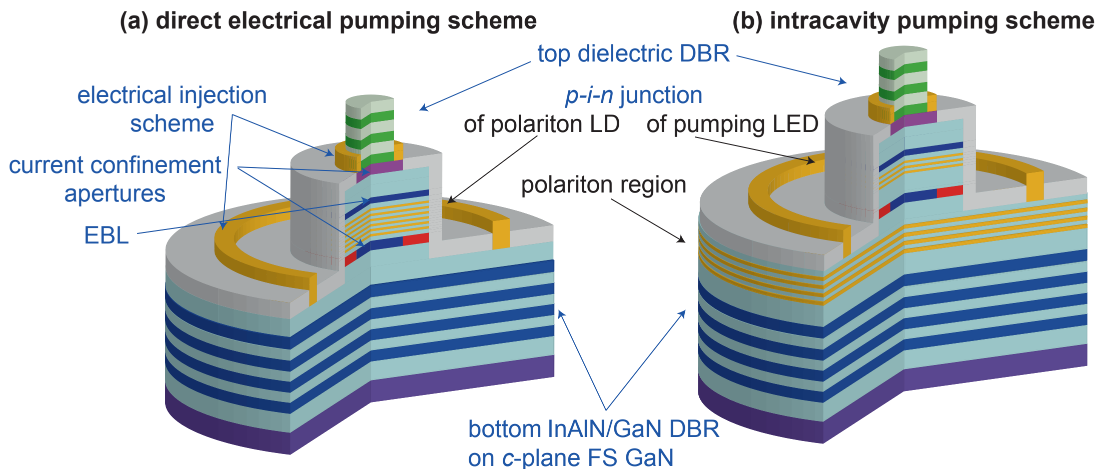

Figure 2.1: Schematic 3D cross-section of two experimentally relevant pumping geometries. In blue the shared key building blocks with a semi-hybrid III-nitride VCSEL are indicated, whereas in black the crucial elements of polariton LDs are highlighted. In the direct electrical pumping scheme (a) a high number of InGaN/GaN multiple QWs lies in the middle of the *p*-*i*-*n* junction, whereas in the intracavity optical pumping scheme (b) only a few QWs lie in the *p*-*i*-*n* junction region. The latter act as an internal pump (pumping LED) for the underlying InGaN/GaN multiple QWs (polariton region).

oretical proposals for an electrically injected polariton laser based on the latter material system [121–123]. For instance a J_{thr} of ~ 50 A/cm^2 at RT is predicted for an electrically injected bulk GaN-microcavity [122]. Note that Bhattacharya *et al.* [24] measured a J_{thr} of ~ 200 A/cm^2 at RT with a specific design: a *c*-plane bulk GaN diode is etched into mesas and subsequent DBRs are sputtering onto the side walls. Though such a structure has the advantage of simplicity, it should be noted that a structure based on QWs is necessary to further reduce J_{thr}. Furthermore, a patent has been deposited suggesting a polariton laser design based on an intracavity pumping geometry as described hereafter [123].

The design of a polariton laser diode is similar to the one of a VCSEL, based on an intracavity contact scheme. One possible design, the direct electrical pumping scheme, is depicted in Fig. 2.1(a). The key building blocks of the latter, actually corresponding to the one of a semi-hybrid III-nitride VCSELs, are listed hereafter [124]:

- a top dielectric DBR,
- an efficient current injection scheme, especially regarding hole spreading,
- current confinement apertures,
- an InGaN/GaN QW-based active region,
- a bottom InAlN-based epitaxial DBR grown on *c*-plane FS-GaN.

Each element has to be chosen with great care. A top dielectric DBR with a short penetration depth (L_{DBR}, cf. equation 1.28) can be achieved by the SiO_2/TiO_2 bilayer system since it exhibits a very large refractive index contrast (cf. section 3.1). To compensate for the relatively poor lateral hole spreading into the *p*-type GaN layer, which is mainly due to current crowding-a detrimental effect whose impact is enhanced by the annular contact geometry-and thus to get light emission from the active region sandwiched between the DBRs, various approaches can be implemented. An efficient current injection scheme to improve the lateral spreading of the hole current is based on a TCO, such as ITO or ZnO, sandwiched between the *p*-type GaN layer and the top dielectric DBR (cf. Fig. 2.1(a)). Note that so far all III-nitride based electrically-driven VCSELs rely on an ITO layer [13–19]. Recently developed buried tunnel junctions could provide an interesting alternative [125]. Furthermore, current confinement apertures have to be used: on the *n*-side a buried oxidized InAlN interlayer can be inserted and/or on the *p*-side the current confinement can be achieved via surface treatment or a dielectric aperture [18, 126]. Note that the approach based on a buried oxidized InAlN interlayer proved to be less reliable than surface treatment using a CHF_3/Ar reactive-ion etching (RIE) plasma for the achievement of an electrically-driven VCSEL [18]. Then the use of an electron-blocking layer (EBL) located on top of the electrically pumped region is intended to avoid an excess of electrons on the *p*-type side and thus limit unwanted electron-hole recombination [127]. Furthermore, the suggested structure is based on a bottom lattice-matched InAlN/GaN epitaxial DBR grown on *c*-plane FS-GaN (cf. section 3.2). Note that, due to the difficulty to obtain high-quality highly-reflective nitride-based DBRs many groups working on III-nitride VCSELs focused on a fully-hybrid approach [14, 16, 17]. However, the semi-hybrid approach is the preferred one due to a much more challenging process flow of the full-hybrid approach (cf. chapter 5).
The main difference between III-nitride polariton laser diodes and VCSELs lies in the InGaN/-GaN QW-based active region.[1] Indeed, it is known that the optimum threshold current density required for conventional lasing is achieved for a small number of QWs (N_{QW}). With increasing N_{QW}, the gain increases and the losses in the laser medium are compensated with greater ease. On the other hand, J_{thr} increases proportionally to N_{QW}. Therefore, some optimal N_{QW}, typically ranging between 1 and 3, results from the opposite trends [128]. The limitation in N_{QW} also originates from the non-uniform carrier injection when this number becomes too large, mainly due to the limited hole transport properties in III-nitride devices. Because of the different physics at play, in polariton LDs designed for RT operation the optimum N_{QW} value will be much larger than 3. Actually, the light-matter coupling scales with $\sqrt{N_{QW,eff}/L_{eff}}$ (cf. equation 1.37). Thus the suggested polariton LD depicted in Fig. 2.1(a) is based on an active region with a large N_{QW} value, which is directly electrically-injected.

However, a way to circumvent the conflicting requirements presented by a structure where N_{QW} should be large for strong coupling regime purposes and small for electrical injection

[1] For efficient electrical injection, the most appropriate choice of active medium would be to switch from GaN/AlGaN QWs to InGaN/GaN QWs (cf. section 1.2.2). Other critical aspects considering InGaN/GaN QWs are discussed in chapter 3.

ones would be to use an intracavity pumping geometry (cf Fig. 2.1(b)). Within such a pumping scheme, a small number of QWs sandwiched in the intrinsic region of a *p*-*i*-*n* diode would be electrically pumped (cf. Fig. 2.1(b) *p*-*i*-*n* junction of pumping LED). This QW subset, *a priori* not taking part in the formation of polaritons, would act as a pumping LED. As such it would emit photons at an energy greater than the absorption edge of a MQW region located underneath (denoted as polariton region[2] in Fig. 2.1(b)). Thus, this MQW region would be in the strong coupling regime and act as a low threshold coherent light source.

2.3 Polariton condensation phase diagram

In this section first the phase transitions that cavity polaritons can undergo are described and a comparison to Bose-Einstein condensation is drawn. Then the polariton condensation phase diagram (δ, T, P_{thr}) of the two experimentally relevant pumping geometries, described in the previous section, calculated from coupled semiclassical Boltzmann equations are derived and discussed.

2.3.1 Polariton Bose Condensation

Cavity polaritons are two-dimensional weakly interacting bosons. Furthermore, contrary to the bulk case, the in-plane cavity polariton dispersion (cf. Fig. 1.7(a)) exhibits a well-defined minimum at $k_{||} = 0$. This makes polaritons good candidates for Bose-Einstein condensation.

Bose-Einstein Condensation

In 1925 Einstein made the following prediction: as bosons tend to accumulate in unlimited quantity in a degenerate state, an ideal Bose gas, such as an atomic gas of non-interacting bosons, should exhibit, below a finite temperature, a new kind of phase transition [34]. Bosons are distributed in energy according to the Bose-Einstein distribution:

$$f_{BE}(\mathbf{k}, T, \mu) = \frac{1}{\exp(\frac{E(\mathbf{k})-\mu}{k_B T}) - 1}, \tag{2.1}$$

where $E(\mathbf{k})$ is the dispersion relation of the bosons in the d-dimensional k-space, T is the temperature, μ is the chemical potential, which is fixed by the total number of particles in the system $N(T,\mu)=\sum_{\mathbf{k}} f_{BE}(\mathbf{k}, T, \mu)$. The number of particles can be separated into two terms, one accounting for the ground state and one for the excited states:

$$N(T,\mu) = \frac{1}{\exp(\frac{-\mu}{k_B T}) - 1} + \sum_{\mathbf{k}, k\neq 0} f_{BE}(\mathbf{k}, T, \mu). \tag{2.2}$$

[2] Note that polaritons are basically delocalized over the whole cavity, even though the excitons giving rise to their formation are localized in the QW planes [129].

If we assume $E(\mathbf{k}=0)=0$, μ has negative values and is an increasing function of the density. In the thermodynamic limit[3] the density is given by:

$$n(T,\mu) = \lim_{L\to\infty}\frac{N(T,\mu)}{L^d} = \lim_{L\to\infty}\frac{1}{L^d}\frac{1}{\exp(\frac{-\mu}{k_B T})-1} + \frac{1}{(2\pi)^d}\int_{k\geq 2\pi/L}^{\infty} f_{BE}(\mathbf{k},T,\mu)d\mathbf{k} \tag{2.3}$$

The striking feature of the density is that when $\mu \to 0$ the ground state density does not vanish anymore, as this is the case for $\mu \neq 0$, and the integral, accounting for the excited states, converges for $d > 2$, but diverges for $d \leq 2$. It means that in higher dimensions a phase transition occurs only when $\mu = 0$. In this case the density of the excited states is clamped and at higher densities the extra particles collapse into the ground-state. This saturation of the excited states and the macroscopic occupation of the ground state is the phase transition called the Bose-Einstein condensation (BEC). Note that the experimental observation of BEC in diluted gases of alkali atoms in 1995 has been awarded by the Nobel prize in Physics in 2001 [35, 36].

Quasi Bose-Einstein Condensation

Thus since cavity polaritons are two-dimensional quasiparticles, they cannot undergo a strict BEC transition, even when taking into account weak interactions, as the number of particles which can be fitted into all the excited states is divergent for any μ (the integral in equation 2.3 diverges for $d \leq 2$). However, in a finite system a quasi-BEC can take place at a finite temperature: whenever the ground state occupancy exceeds unity, stimulated relaxation towards the later occurs followed by coherent emission of photons, due to the spontaneous radiative decay of the short-lived polaritons in the condensate. The latter losses imply that the condensate has to be continuously pumped and as such the system represents an intrinsically open system. However, a quasi-BEC contains all specific ingredients of a true BEC: (i) above some critical density, condensation takes place in the ground state, out of a thermalized Bose gas, (ii) spatial coherence, and (iii) a macroscopic polarization which is an evidence for spontaneous symmetry breaking[4] across the entire condensate build up. Quasi-BEC of cavity polaritons has been experimentally demonstrated for the first time in a CdTe-based microcavity in 2006 at LT [37].

The theoretical polariton phase diagram including structural disorder is given for a CdTe microcavity in Fig. 2.2. When realistic structural disorder, for example due to DBR fluctuations leading to photonic disorder, is taken into account, polaritons first undergo a quasiphase transition toward a Bose glass:[5] the system contains an assembly of strongly populated localized states, all with the same μ. Increasing further the polariton density results in an

[3]The thermodynamic limit is the process by which the system volume L^d and the number of particles N increase indefinitely whereas the density n remains constant.

[4]Note that spontaneous symmetry breaking is considered to be a *smoking gun* for BEC ever since the pioneering work of Goldstone [130].

[5]In the weak interaction limit the latter phase is an Anderson glass phase [132].

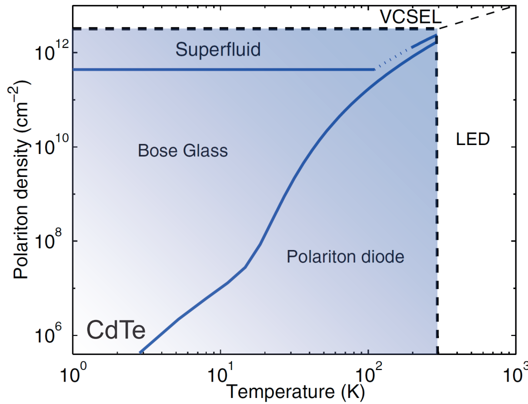

Figure 2.2: Calculated polariton phase diagram for a CdTe microcavity containing 16 QWs. In the blue region the strong coupling holds and the three different phases of cavity polaritons are shown: the polariton diode regime, i.e., the linear regime, the Bose glass phase, corresponding to a quasi-BEC, and the superfluid phase. Adapted from Ref. [131].

increasing μ and whenever μ corresponds to the localization energy, a delocalization of the condensate occurs and the so-called Kosterlitz-Thouless (KT) phase transition toward superfluidity takes place [133]. Rising further the polariton density results in a bleaching of the excitonic transition and thus into a transition from the strong to the weak coupling regime (labeled as VCSEL region in Fig. 2.2). The strong coupling regime can also be lost due to exciton thermal dissociation with increasing temperature (labeled as LED region in Fig. 2.2). Note that in III-nitride based microcavities strong in-plane spatial photonic disorder cannot be avoided and thus a similar polariton phase diagram is expected [134].

Thermodynamic versus Kinetic Regime

In the case of polariton condensation one can distinguish between a kinetic condensation regime, in which the distribution is not thermal and the threshold is governed by the relaxation kinetics, and a thermodynamic regime, where the threshold is governed by the thermodynamic parameters of the system. A polariton laser can operate in both regimes, whereas the quasi-BEC, defined as an equilibrium phase transition, of polaritons is associated with the thermodynamic regime only. The two different regimes have been identified experimentally in several microcavity systems.

The first experimental investigation has been done by Kasprzak *et al.* [135] in 2008 on a CdTe microcavity system and is displayed in Fig. 2.3(a). They measured the threshold power density (P_{thr}) for polariton lasing (polariton condensation) as a function of detuning δ for two different lattice temperatures (T_{latt}). In the case of the GaN/AlGaN MQW microcavity mentioned in section 1.2.2 experimental values for P_{thr} have been measured that cover a wide range of detunings and temperatures, cf. Fig. 2.3(e) [137]. In Fig. 2.3(e) the optimum detuning δ_{opt} corresponds to the balance between the mean polariton relaxation time and the mean polariton lifetime [135, 138]. As the minimum in P_{thr} for a given temperature is reported for δ_{opt}, any low threshold polariton laser device should be preferably driven at δ_{opt}. For the above-mentioned non-resonant optically pumped GaN-based microcavity δ_{opt} decreases from 0 to -55 meV, with temperature increasing from cryogenic to RT [138]. As can be seen in Fig. 2.3(a) and Fig. 2.3(c) in the case of CdTe- and GaAs-based microcavities δ_{opt} is close to

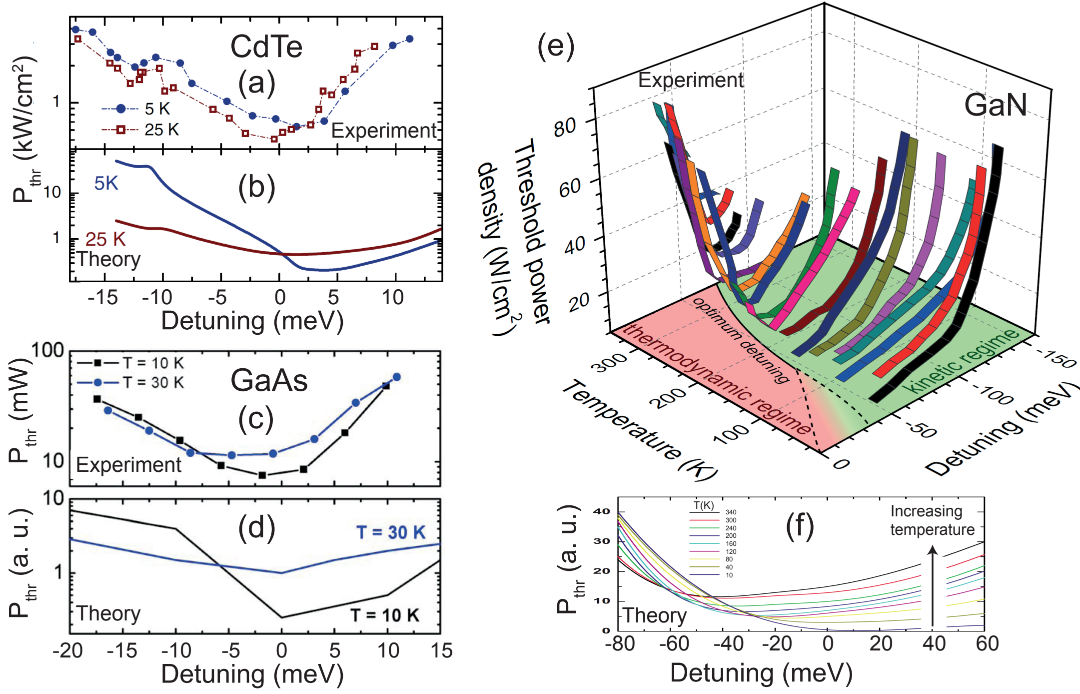

Figure 2.3: Measured and calculated P_{thr} as a function of the detuning δ for (a)-(b) CdTe at T_{latt} = 5 K (solid blue circles) and 25 K (open brown squares). Adapted from Ref. [135]; (c)-(d) GaAs at T_{latt} = 10 K (black squares) and 30 K (blue circles). Adapted from Ref. [136]; (e)-(f) GaN from cryogenic to room temperature. Adapted from Ref. [137] and Ref. [138].

zero: δ_{opt}^{CdTe}(5 K) ~ 3 meV [135] and δ_{opt}^{GaAs}(10 K) ~ -3 meV [136].[6]

On the road toward a polariton laser diode, the knowledge of δ_{opt} is indispensable. Thus, the next section is devoted to the theoretical derivation of the polariton phase diagram (δ, T, P_{thr}) in the framework of a semi-classical Boltzmann approach for devices relying on the two geometries given in section 2.2. Note that a satisfactory qualitative agreement between experimental results and simulations, shown in Fig. 2.3(b), 2.3(d), and 2.3(f) for CdTe, GaAs, and GaN, respectively, was found when using the latter, even without considering structural disorder.

2.3.2 Coupled semiclassical Boltzmann equations for III-nitride polariton laser diodes

The theoretical model based on semi-classical Boltzmann equations used for the investigation of the dynamics of cavity polaritons, respectively of the polariton relaxation kinetics, has been introduced for the first time by F. Tassone *et al.* [140, 141]. As mentioned above it has been successfully used to describe the relaxation dynamics of polaritons along the lower polariton

[6]Similar results have been recently reported by J. Schmutzler *et al.* [139], who systematically studied the phase transition to polariton condensation in a GaAs-based microcavity covering a larger temperature range, i.e., from 10 to 90 K.

branch (including the exciton reservoir) in optically pumped microcavities:

$$\frac{dn_{\boldsymbol{k}}}{dt} = P_{\boldsymbol{k}} - \frac{n_{\boldsymbol{k}}}{\tau_{\boldsymbol{k}}} + \sum_{\boldsymbol{k}' \neq \boldsymbol{k}} \left(W_{\boldsymbol{k}'\boldsymbol{k}} n_{\boldsymbol{k}'} \left(n_{\boldsymbol{k}} + 1 \right) - W_{\boldsymbol{k}\boldsymbol{k}'} n_{\boldsymbol{k}} \left(n_{\boldsymbol{k}'} + 1 \right) \right), \tag{2.4}$$

where $n_{\boldsymbol{k}}$ is the concentration of exciton-polaritons with in-plane wavevector $\boldsymbol{k}$, and $P_{\boldsymbol{k}}$ describes the pumping rate. $\tau_{\boldsymbol{k}}$ is the polariton radiative lifetime, $W_{\boldsymbol{k}\boldsymbol{k}'}$ is the total scattering rate between quantum states indicated by $\boldsymbol{k}$ and $\boldsymbol{k}'$ with $\boldsymbol{k} = \left(k_x, k_y\right)$, $k_{x,y} = \pm\frac{2\pi j}{L}, j = 0,1,2,...,$ and $|\boldsymbol{k}| < \frac{\omega}{c}$, where L is the lateral size of the system, and ω is the frequency of the exciton resonance. Note that the polariton lifetime can be calculated using the Hopfield coefficients given in equation 1.35 and the lifetime of exciton τ_x and cavity photons τ_{cav}:

$$\frac{1}{\tau_p(\boldsymbol{k}_{||})} = \frac{|X_{\boldsymbol{k}_{||}}|^2}{\tau_x} + \frac{|C_{\boldsymbol{k}_{||}}|^2}{\tau_{cav}}. \tag{2.5}$$

The scattering rates are treated perturbatively and encompass all the interactions polaritons can undergo with their environment, namely exciton(-polariton)-phonon, exciton(-polariton)-exciton(-polariton) and exciton(-polariton)-free electron interactions. These scattering rates can be obtained using the formalism developed in Ref. [142]. Note that the model we use differs from the system of rate equations initially proposed by Tassone and Yamamoto for optically pumped microcavities [141]. In particular, it explicitly accounts for the electron-hole plasma and introduces the exciton(-polariton)-electron scattering as one of the important mechanisms of exciton(-polariton) relaxation into the condensate.

Differences regarding the above-mentioned formalism have to be identified for the two pumping geometries described in section 2.2. The intracavity optical pumping geometry essentially differs from the direct electrical pumping geometry due to the following reasons:

- The pumping rate $P_{\boldsymbol{k}}$ in equation 2.4 strongly depends on the pumping geometry. However, for both geometries we neglect the temperature dependence of $P_{\boldsymbol{k}}$. Note that for III-nitride based devices the large activation energy (E_A) of Mg, which acts as a deep acceptor ($E_A \in$ 110-190 meV) [143], leads to a reduced p-type conductivity and a concomitant decrease in hole mobility when lowering the temperature.
- The internal quantum efficiency (IQE, called hereafter η_{int}) of the pumping LED has to be taken into account. This latter quantity is taken equal to 90%, which corresponds to the best commercial devices. At shorter wavelengths an efficiency droop is generally observed. However, between 390 and 400 nm the latter amounts to less than 10% [144].
- The density of free carriers (electrons) in the polariton region (cf. Fig. 2.1(b)) is constant since free carriers are located in the n-type region, whereas this density is current-

dependent in the previous injection scheme and will have an impact on the injection dependence of the exciton(-polariton)–electron scattering term.

- While one can assume that for the intracavity optical pumping scheme, free electrons in the n-doped region are thermalized and obey Fermi statistics with an effective temperature (T_{eff}) close to T_{latt}; for the direct electrical pumping scheme electrons are not thermalized to the lattice temperature. In this latter situation, we consider a Boltzmann carrier distribution with $T_{eff} > T_{latt}$.

Pumping rate $P_{\boldsymbol{k}}$ for the two geometries

Direct electrical pumping geometry: We consider an electrically injected electron-hole pair density n_{e-h} given by the following rate equation:

$$\frac{dn_{e-h}}{dt} = \frac{J}{e} - \frac{n_{e-h}}{\tau_{e-h}} - Wn_{e-h}, \tag{2.6}$$

where J is the electric pumping rate, τ_{e-h} is the decay rate of the electron-hole plasma, and W is the exciton formation rate. Equation 2.6 can be solved analytically, which yields, assuming the following initial condition, $n_{e-h}(t=0)=0$, a simple dependence:

$$n_{e-h}(t) = \frac{J}{e}\frac{\tau_{e-h}}{1+W\tau_{e-h}}\left[1-\exp\left(-Wt-\frac{t}{\tau_{e-h}}\right)\right]. \tag{2.7}$$

Excitons are formed out of this electron-hole plasma and relax along the lower polariton branch $E_{\boldsymbol{k}}$ such that $P_{\boldsymbol{k}}$ can be written as:

$$P_{\boldsymbol{k}} = \begin{cases} 0 & \text{for } E_{\boldsymbol{k}} - E_X < E_{B,2D} \\ \frac{Wn_{e-h}}{\widetilde{N}} & \text{for } E_{\boldsymbol{k}} - E_X \geq E_{B,2D}, \end{cases} \tag{2.8}$$

where $\widetilde{N}$ is the number of states within the light cone fullfilling the condition $E_{\boldsymbol{k}} \geq E_X + E_{B,2D}$.

Intracavity pumping geometry: For the intracavity optical pumping geometry we consider that strongly-coupled quantum wells are indirectly optically pumped with an energy-dependent pump intensity which reads:

$$P_{\boldsymbol{k}} = \frac{\eta_{int}J}{\sqrt{2\pi}(\delta E)}e^{-\frac{(E_{\boldsymbol{k}}-E_{pump})^2}{2(\delta E)^2}}, \tag{2.9}$$

where E_{pump} is the central energy of the LED which is set equal to the exciton energy and δE

is the linewidth of the LED which is set to 90 meV and is considered temperature-independent as a first approximation.

In the numerical calculations the set of parameters given in Table 2.1 has been used. The threshold current density (J_{thr}) dependence as a function of temperature and detuning is displayed in Figs. 2.4(a) and 2.4(b) for the two pumping geometries. In this way, one obtains the polariton condensation phase diagram (δ, T, J_{thr}) under electrical pumping, which is analogous to that derived under optical pumping for GaN/AlGaN MQW microcavities (cf. Fig. 2.3(e)) [137, 138]. One can see that at room temperature the lowest threshold current density ($J_{thr,min}$) is obtained for a negative detuning of -19 meV and amounts to ~5 A cm^{-2} for the direct electrical pumping geometry, while a $J_{thr,min}$ value of ~6 A cm^{-2} at a negative detuning of -32 meV is derived for the intracavity pumping geometry. Those values are in good agreement with that predicted in previous work [25, 151].

	Pumping geometry	
	Intracavity	Electrical
Exciton lifetime (τ_x) (ns) [145]	1	
Cavity lifetime (τ_{cav}) (ps)[a]	1	
Electron-hole pair lifetime (τ_{e-h}) (ns)[b]	5	
Vacuum Rabi splitting (Ω_{VRS}) (meV) (section 3.3.4)	45	
Device size (S) (μm^2)	50×50	
Number of QWs (N_{QW})	65 + 1-3	65
Exciton energy (E_X) (eV)	2.987	
Exciton binding energy ($E_{B,2D}$) (meV) (section 1.1.1)	45	
Central LED energy (E_{pump}) (eV)	3.138	-
IQE (η_{int})	0.9	-
Exciton formation rate (W) (ps^{-1})	-	0.01
Effective electron temperature (T_{eff}) (K)	800	-
n_d (cm^{-2})	2×10^{12}	-
	III-nitride material parameters	
Electron effective mass (m_e^*) [60]	$0.2m_0$	
Heavy hole effective mass (m_h^*) [60]	$1.1m_0$	
LO-phonon energy (E_{LO}) (meV)	92	
Deformation potential (D) (eV) [149]	11.1	
Mass density (ρ) (kg/m^3)	6150	
Speed of sound in [0001] direction (c_s) (m/s) [150]	7960	
Exciton Bohr radius ($a_{B,3D}$) (nm)	3.2	

Table 2.1: List of parameters adopted in this work to compute the polariton phase diagram for the two pumping geometries.

[a] $\tau_{cav} = \frac{Q\hbar}{E_0}$, where E_0 is the lower polariton mode energy and Q is the quality factor of the cavity, taken equal to ~ 5000.

[b] In violet standard edge-emitting LDs, τ_{e-h} amounts to 2 -3 ns at threshold [146]. Knowing that in the present case the polariton devices operate at lower carrier densities, a longer lifetime is expected due to reduced Auger recombinations [147, 148].

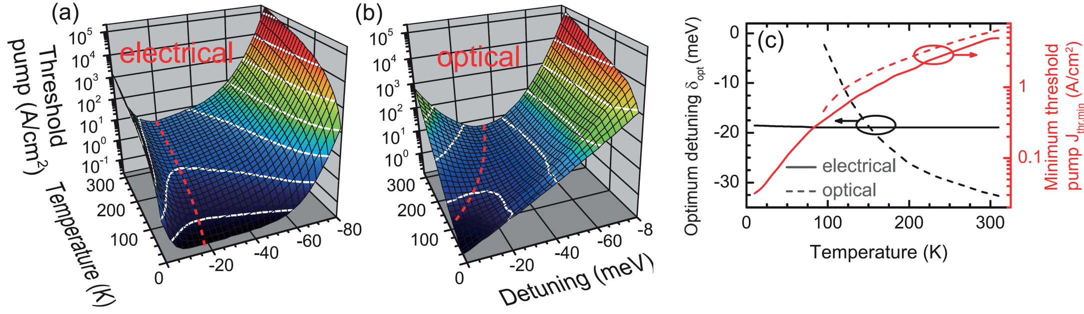

Figure 2.4: Polariton condensation phase diagram (δ, T, J_{thr}) for (a) the direct electrical and (b) the intracavity optical pumping schemes. The red dashed line in each plot corresponds to δ_{opt}, respectively to the evolution of $J_{thr,min}$ with temperature. (c) δ_{opt} (black solid and black dashed lines) and $J_{thr,min}$ (red solid and red dashed lines) evolution at the optimum detuning as a function of lattice temperature for the direct electrical (solid lines) and the intracavity (dashed lines) pumping schemes. Adapted from Ref. [26].

The switching from the kinetic to the thermodynamic regime at a given temperature provokes J_{thr} first to decrease with increasing detuning (decreasing δ in absolute value) because of the enhancement of the total scattering rate to the ground state, before inducing an increase of J_{thr} concomitantly with δ due to the combined effects of the increasing polariton effective mass (which leads to a larger value of the critical density for polariton condensation, $n_{2D,crit}$, as predicted by the thermodynamic theory) and thermal detrapping from the ground state.[7] It is also noticeable that the temperature dependence of δ_{opt} significantly differs from one geometry to the other (cf. Figs. 2.4(a)–2.4(c)). This is attributed to the difference in the efficiency of the free electron scattering mechanism as a function of temperature [153]. For the direct electrical pumping geometry, the electron distribution does not depend on T_{latt} since electrons are not thermalized, thus leading only to slight changes in the free electron scattering rate with temperature and thereby explaining the weak $\delta_{opt}(T)$ variation displayed in Figs. 2.4(a) and 2.4(c). For the intracavity optical pumping geometry, electrons are thermalized to T_{latt}, which leads to a behavior closer to that reported for GaN/AlGaN MQW MCs under nonresonant optical pumping (cf. Figs. 2.4(b) and 2.4(c)) [138]. However, it should be recognized that assuming an electron temperature equal to T_{latt} is a crude approximation. We should also point out that, for the sake of simplicity, we did not account for the large activation energy of the Mg acceptor in GaN compounds, which would most likely degrade the electrical characteristics and thus lead to an increase in J_{thr} at low temperatures.

The low threshold values reported for the intracavity pumping geometry can probably be explained by the broad spectral distribution of the pump $P_{\boldsymbol{k}}$. In the direct electrical injection geometry, excitons characterized by high energies and large in-plane wave vectors are created from the electron-hole plasma, which requires a comparatively long time to relax to the $k = 0$ state. However, in the case of intracavity optical pumping, a broad distribution of excitons centered at E_{pump}, but also covering lower energy states, is created. Those excitons which

[7] An in-depth study of the crossover form the kinetic to the thermodynamic regime for the optically pumped GaN/AlGaN MQW microcavities is given in Ref. [152].

occupy lower energy and lower k states compared with the direct electrical pumping geometry quickly relax to the lower polariton branch ground state and enhance polariton relaxation, which results in the lower threshold for this geometry. However, if the intracavity emission line is strongly blueshifted from the polariton modes, the ratio between the polariton lasing thresholds for the two pumping configurations is expected to be modified. One would then expect a higher threshold for the intracavity pumping geometry due to the IQE of the internal pump, which is less than 100%.

2.4 Figures of merit of polariton laser diodes

The data communications (datacom) transceiver market has experienced tremendous growth over the last fifteen years, mainly attributed to improvements related to the high-speed characteristics of VCSELs. The progression of datacom interconnects as a function of time is compelling: high-speed devices (current VCSEL transceivers are offered at speeds up to 12.5 Gb/s [154]) are achieved with ever decreasing costs (~ 10 $/Gb ps [154]). Over 18 million 850 nm wavelength VCSEL-based datacom transceivers were sold resulting in revenues of almost US$ 500 million in 2009. Rather suited for free-space than for optical fiber communication short wavelength-devices based on III-nitrides are steps behind: a major breakthrough was achieved in 2008 with the first cw RT operation of a GaN-based VCSEL at about 414 nm wavelength [14]. However, the latter is based on a challenging hybrid design and far from any low-cost commercial realization. Note that recently lasing has been achieved in semi-hybrid structures [15, 18]. Such structures would make the process flow much easier and would likely increase the mass production yield.
Due to their potentially low lasing threshold and similarities to VCSELs (cf. section 2.5), polariton LDs emerge as interesting candidates for future high-speed devices. For any commercial offering of such devices besides liability a range of specifications must be met with high-yield: threshold current density, modulation bandwidth, RIN, linewidth, series resistance, etc. For the two experimentally relevant pumping geometries described in section 2.2, the threshold current density as a function of detuning and temperature has already been derived in section 2.3. The present section deals with the high-speed current modulation of the latter, which is ruled by the modulation bandwidth. The RIN features of the latter are also derived; all those properties being obtained using a quasi-analytical model, described hereafter.

2.4.1 Simplified rate equations and their steady-state solutions

To obtain a qualitative understanding of the functionality of polariton laser diodes, we compare the modeling results obtained with the full set of semiclassical Boltzmann equations with a simplified quasi-analytical model based on a two level system [141, 155]. The first level, the so-called exciton reservoir, consists of exciton states with large k, lying energetically close to the uncoupled exciton, whereas the second level includes the ground state polaritons, the

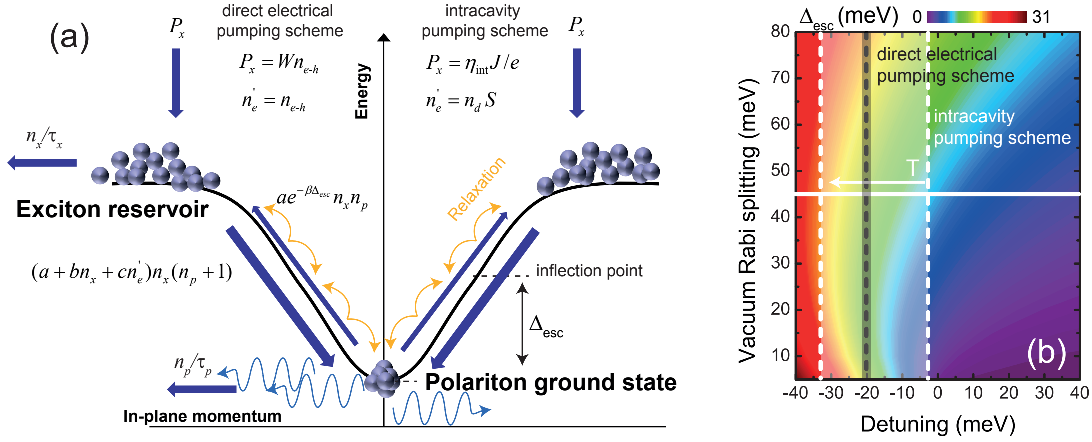

Figure 2.5: (a) Flowchart reservoir model depicting the flow of particles per unit time based on the rate equations 2.10 and 2.11. (b) Characteristic energy splitting between the bottom of the lower polariton branch and the inflection point (Δ_{esc}) as a function of detuning and vacuum Rabi splitting. The optimal detuning range ($\delta_{opt}(T)$) of both pumping geometries are indicated.

so-called condensate:

$$\frac{dn_x}{dt} = P_x - \frac{n_x}{\tau_x} - an_x(n_p+1) + ae^{-\beta\Delta_{esc}} n_p n_x - bn_x^2(n_p+1) - cn_e' n_x(n_p+1), \tag{2.10}$$

$$\frac{dn_p}{dt} = -\frac{n_p}{\tau_p} + an_x(n_p+1) - ae^{-\beta\Delta_{esc}} n_p n_x + bn_x^2(n_p+1) + cn_e' n_x(n_p+1), \tag{2.11}$$

where n_e', n_x, and n_p are the concentrations of free carriers, excitons and exciton-polaritons, respectively. a accounts for the acoustic and optical phonon relaxation rates, β is equal to $1/(k_B T)$ with k_B being the Boltzmann constant, Δ_{esc} is the characteristic energy splitting between the bottom of the LPB and states beyond the inflection point of the LPB where zero in-plane wavevector polaritons are scattered, which is a quantity sensitive to the detuning. The evolution of Δ_{esc} as a function of detuning and vacuum Rabi splitting is depicted in Fig. 2.5(b). The shaded areas correspond to $\delta_{opt}(T)$ for the two pumping geometries. b is the exciton-exciton scattering rate and c is the rate of exciton relaxation mediated by free carriers. For the sake of illustration, the two-level model with the rates into and out of those reservoirs is displayed in Fig. 2.5(a). Furthermore, we have to distinguish the two geometries. Specificities related to each pumping geometry are contained in P_x and n_e'. Thus for the electrical pumping geometry we have to add the rate equation describing the electron-hole plasma (namely equation 2.6) as $P_x = Wn_{e-h}$ and $n_e' = n_{e-h}$, whereas in the case of the intracavity pumping geometry P_x is given by $\eta_{int}J/e$ and $n_e' = n_d S$ with S the emitting surface

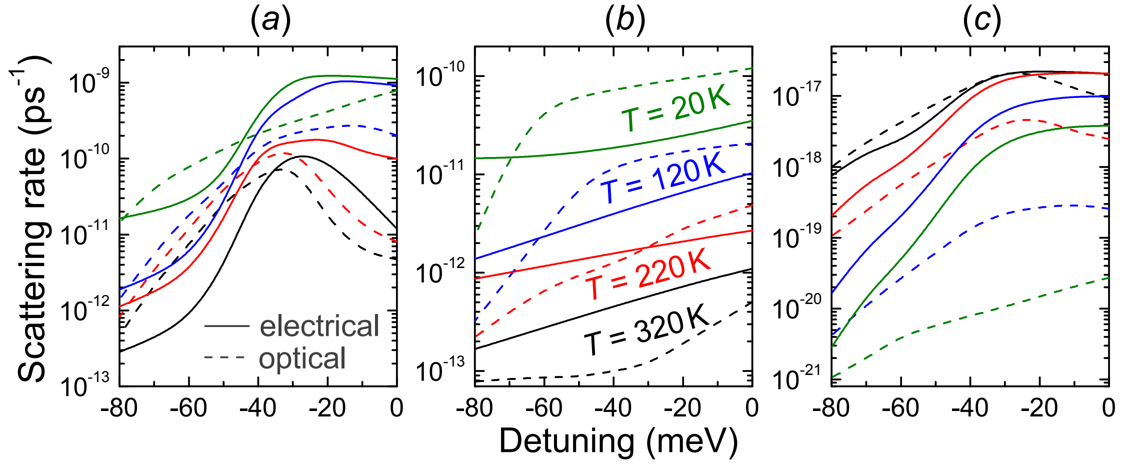

Figure 2.6: Averaged scattering rates a, b, and c as a function of detuning obtained by fitting the full semiclassical Boltzmann system of equations at various temperatures for the two pumping schemes: electrical (solid lines) and intracavity (dashed lines) pumping. Adapted from Ref. [26].

area and n_d the density of free-carriers per unit surface obtained from the doping level in the polariton region.[8] The solid (dashed) curves in Fig. 2.6 show the detuning dependence of the fitting parameters a, b, and c at various temperatures for the electrical and intracavity pumping scheme, respectively. They have been deduced by a fitting procedure, in which they figure as fitting parameters of the rate equation model when the latter is compared to the full semiclassical Boltzmann model. Note that the latter procedure has been done at the condensation threshold. Thus, the scattering rates a, b, and c correspond to rates evaluated at the condensation threshold.

One can see in Fig. 2.6 that—overall—all the scattering mechanisms that contribute to populate the polariton lasing mode become less efficient when going towards more negative detunings (in absolute value). It stems from the reduced exciton fraction of polariton states at large negative detuning (cf. equation 1.35), so that all interactions involving polaritons become weaker than at zero or positive detuning. In some cases, the detuning dependence of the scattering rates is nonmonotonic and it is also sensitive to the pumping scheme. This is due to the complexity of the lower polariton branch dispersion. The average scattering rates are therefore sensitive to both the shape of the polariton dispersion and the excitation spectrum profile. Above threshold, the $(1 + n_p)$ terms appearing in the rate equations can be approximated as n_p. Note that the omission of the spontaneous relaxation term is easily justified as $n_p \gg 1$. After some algebra, the steady-state solutions (i.e., for $t = \infty$) for the electron-hole pair, exciton, and polariton populations for the direct electrical pumping geometry are given

[8] W, η_{int}, S, and n_d are given in Table 2.1.

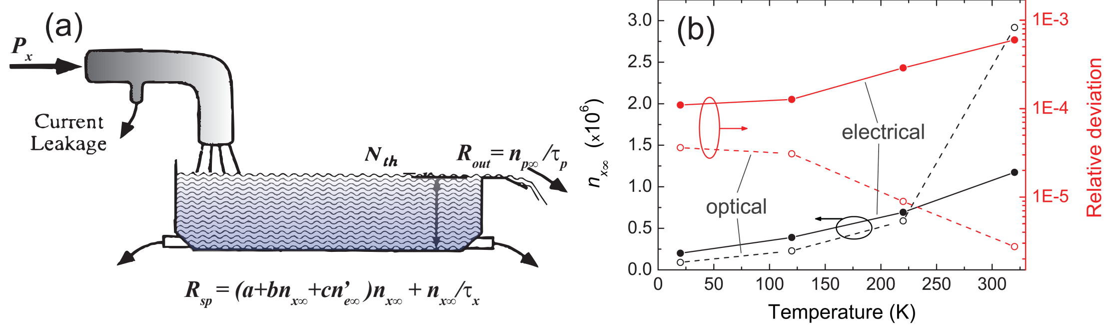

Figure 2.7: (a) Reservoir analogy above threshold where water level has risen to the spillway so that an increased input results in an increased output (R_{out}) but no increase in water level (carrier density $N_{thr} = n_{x\infty}$). Adapted from Ref. [156] to the rate equations given in 2.10 and 2.11. (b) Left-hand side vertical scale: evolution of $n_{x\infty}$ as a function of temperature calculated at the optimum detuning using the exact expressions for the electrical (connected black dots) and the intracavity (connected black circles) pumping geometries. Right-hand side vertical scale: relative deviation between the exact and the approximated expressions for the electrical (connected red dots) and the intracavity (connected red circles) pumping geometries. Adapted from Ref. [26].

by:

$$n_{x\infty} = \frac{-cn_{e-h\infty} + a(e^{-\beta\Delta_{esc}} - 1) + \sqrt{(-cn_{e-h\infty} + a(e^{-\beta\Delta_{esc}} - 1))^2 + \frac{4b}{\tau_p}}}{2b}, \tag{2.12}$$

$$n_{p\infty} = \tau_p(Wn_{e-h\infty} - \frac{n_{x\infty}}{\tau_x}), \tag{2.13}$$

$$n_{e-h\infty} = \frac{J\tau_{e-h}}{e(1+\tau_{e-h}W)}. \tag{2.14}$$

Note that for the intracavity optical pumping geometry, slight changes occur since $n_{e-h\infty}$ in equation 2.12 has to be replaced by n_d , and $Wn_{e-h\infty}$ in equation 2.13 has to be replaced by P_x.

We should emphasize that for this latter geometry, the carrier population, which acts as a reservoir for the stimulated relaxation process (here the excitons), gets clamped once it crosses the condensation threshold, which is expected due to the similarities of the above-mentioned rate equations with those describing conventional LDs [156]. Actually the stimulated relaxation term uses up all additional carrier injection and brings them into the condensate, where coherent light emission occurs due to the finite lifetime of the latter. Corzine and Coldren [156]

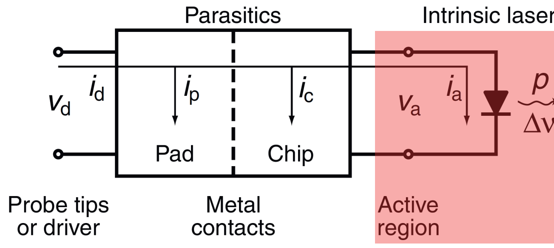

Figure 2.8: The cascaded two-port model for VCSELs can be applied as well to the case of polariton LDs. In this work only the intrinsic laser response (shaded area) is treated. Adapted from Ref. [154].

compare the carrier dynamics in conventional LDs to a water reservoir. Thus we can use the same analogy for the clamping of the exciton population above threshold (cf. Fig. 2.7(a)): the water level has reached the spillway and any further increase in input (P_x) does not increase the water level ($N_{thr} = n_{x\infty}$) but the output (R_{out}). A similar treatment can be used for the direct electrical pumping geometry since $4b/\tau_p \gg (-cn_{eh\infty} + a(e^{-\beta\Delta_{esc}} - 1))^2$. Thus, for both cases, we obtain $n_{x\infty} \sim 1/\sqrt{b\tau_p}$. The evolution of $n_{x\infty}$ as a function of temperature at the optimum detuning is shown in Fig. 2.7(b) using both the exact expression and the approximate one for the two pumping geometries. The validity of the approximation for $n_{x\infty}$ is confirmed by the close correspondence between the two quantities independent of the temperature. Considering its approximate expression, the increase with temperature of $n_{x\infty}$ can be directly inferred from the results displayed in Fig. 2.6, which show a decrease in the exciton-exciton scattering rate b with increasing T_{latt}, and it is also fully consistent with the overall temperature dependence of the analytical expression for b derived by Tassone and Yamamoto [141]. Note that one also expects a decrease in $n_{x\infty}$ with increasing detuning likely due to the concomitant increase in the relaxation process from the excitonic reservoir (which coincides with the decrease or even the disappearance of the relaxation bottleneck) and that of τ_p [141].

2.4.2 High-speed current modulation treatment: determining the modulation bandwidth

The modulation bandwidth characterizes the dynamic response of a LD to some small perturbation to the system such as a modulation of the current above threshold. The latter is determined by the intrinsic laser response as well as the extrinsic parasitic response. Note that for high-frequency devices parasitics are always a concern. In Fig. 2.8 the cascaded two-port model for a LD (valid for standard LDs and polariton LDs) is shown, indicating the currents i_p and i_c entering into the pad and the chip parasitics, respectively. In order to achieve the intrinsic modulation bandwidth, those currents have to be minimized. Hereafter we will derive the intrinsic modulation bandwidth for the two polariton LDs described in section 2.2.

Unfortunately, exact analytical solutions to the full rate equations 2.10 and 2.11 cannot be obtained. Thus we will perform a differential analysis of the rate equations as described in Ref. [156] for the case of conventional LDs. The differential of the rate equations can be written in compact matrix form:

Electrical pumping geometry

$$\frac{d}{dt}\begin{bmatrix} dn_x \\ dn_p \end{bmatrix} = \begin{bmatrix} -\gamma_{xx} & -\gamma_{xp} \\ \gamma_{px} & -\gamma_{pp} \end{bmatrix} \begin{bmatrix} dn_x \\ dn_p \end{bmatrix} + \begin{bmatrix} dn_{eh}(W - cn_{x\infty}n_{p\infty}) \\ dn_{eh}(cn_{x\infty}n_{p\infty}) \end{bmatrix}, \tag{2.15}$$

where

$$\gamma_{xx} = \frac{1}{\tau_x} + an_{p\infty} + 2bn_{x\infty}n_{p\infty} + cn_{eh\infty}n_{p\infty} - an_{p\infty}e^{-\beta\Delta_{esc}}, \tag{2.16}$$

$$\gamma_{pp} = \frac{1}{\tau_p} - an_{x\infty} - bn_{x\infty}^2 - cn_{eh\infty}n_{x\infty} + an_{x\infty}e^{-\beta\Delta_{esc}}, \tag{2.17}$$

$$\gamma_{xp} = an_{x\infty} + bn_{x\infty}^2 + cn_{eh\infty}n_{x\infty} - an_{x\infty}e^{-\beta\Delta_{esc}}, \tag{2.18}$$

$$\gamma_{px} = an_{p\infty} + 2bn_{x\infty}n_{p\infty} + cn_{eh\infty}n_{p\infty} - an_{p\infty}e^{-\beta\Delta_{esc}}. \tag{2.19}$$

Intracavity pumping geometry

$$\frac{d}{dt}\begin{bmatrix} dn_x \\ dn_p \end{bmatrix} = \begin{bmatrix} -\gamma_{xx} & -\gamma_{xp} \\ \gamma_{px} & -\gamma_{pp} \end{bmatrix} \begin{bmatrix} dn_x \\ dn_p \end{bmatrix} + \begin{bmatrix} \frac{\eta_{int}}{e}dJ \\ 0 \end{bmatrix}, \tag{2.20}$$

where

$$\gamma_{xx} = \frac{1}{\tau_x} + an_{p\infty} + 2bn_{x\infty}n_{p\infty} + cn_d n_{p\infty} - an_{p\infty}e^{-\beta\Delta_{esc}}, \tag{2.21}$$

$$\gamma_{pp} = \frac{1}{\tau_p} - an_{x\infty} - bn_{x\infty}^2 - cn_d n_{x\infty} + an_{x\infty}e^{-\beta\Delta_{esc}}, \tag{2.22}$$

$$\gamma_{xp} = an_{x\infty} + bn_{x\infty}^2 + cn_d n_{x\infty} - an_{x\infty}e^{-\beta\Delta_{esc}}, \tag{2.23}$$

$$\gamma_{px} = an_{p\infty} + 2bn_{x\infty}n_{p\infty} + cn_d n_{p\infty} - an_{p\infty}e^{-\beta\Delta_{esc}}. \tag{2.24}$$

To obtain the small-signal response of the exciton and the polariton concentration, dn_x and dn_p respectively, to a sinusoidal current modulation dJ, we assume $dJ = J_1 \exp(i\omega t)$, $dn_{eh} = n_{eh1} \exp(i\omega t)$, $dn_x = n_{x1} \exp(i\omega t)$, and $dn_p = n_{p1} \exp(i\omega t)$. The linear systems 2.15 and 2.20 can be solved for the small-signal polariton concentration by simply applying Kramer's theorem:

Electrical pumping geometry

$$n_{p1}(\omega) = \frac{\gamma_{px}[W - cn_{x\infty}n_{p\infty}] + (i\omega + \gamma_{xx})cn_{x\infty}n_{p\infty}}{(\gamma_{px}/\tau_p - \omega^2 + i\omega\gamma_{xx})} \frac{J_1/e}{i\omega + W + 1/\tau_{eh}} = n_{p1}(0)H(\omega), \tag{2.25}$$

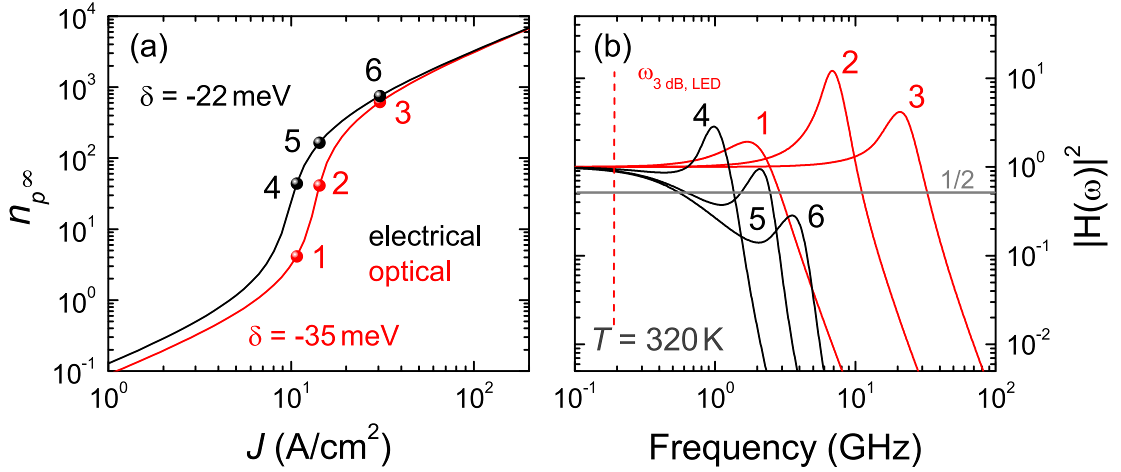

Figure 2.9: (a) Polariton condensate occupation number vs current density for the electrical (black line) and intracavity (red line) pumping geometries determined at 320 K and at the optimum detuning. (b) Frequency dependence ($\nu = \omega/2\pi$) of the square modulus of the modulation transfer function, $|H(\omega)|^2$. Each curve corresponds to one of the steady-state solutions indicated in Fig. 2.9(a). Furthermore, corresponding cutoff frequencies ω_{3dB} can be deduced by intersection of the gray line with $|H(\omega)|^2$ and the one of the pumping LED $\omega_{3dB,LED}$ is indicated. Adapted from Ref. [26].

where $H(\omega)$ is the modulation transfer function:

$$H(\omega) = \frac{\gamma_{px}/\tau_p(W+1/\tau_{eh})}{\gamma_{px}[W - cn_{x\infty}n_{p\infty}] + \gamma_{xx}cn_{x\infty}n_{p\infty}} \frac{\gamma_{px}[W - cn_{x\infty}n_{p\infty}] + (i\omega + \gamma_{xx})cn_{x\infty}n_{p\infty}}{(\gamma_{px}/\tau_p - \omega^2 + i\omega\gamma_{xx})(i\omega + 1/\tau_{eh} + W)}. \tag{2.26}$$

Intracavity pumping geometry

$$n_{p1}(\omega) = \frac{\gamma_{px}\eta_{int}J_1/e}{(\gamma_{px}/\tau_p - \omega^2 + i\omega\gamma_{xx})} = n_{p1}(0)H(\omega), \tag{2.27}$$

where $H(\omega)$ is the modulation transfer function:

$$H(\omega) = \frac{\gamma_{px}/\tau_p}{(\gamma_{px}/\tau_p - \omega^2 + i\omega\gamma_{xx})}. \tag{2.28}$$

The general behaviour of $|H(\omega)|^2$ is shown in Fig. 2.9(b) for the two pumping geometries at room temperature and at the optimum detuning δ_{opt} for different values of the input current J (cf. Fig. 2.9(a)).

It is essentially a second order low-pass filter for the intracavity pumping geometry and a third order low-pass filter for the electrical pumping geometry.[9] However, for both pumping

[9] Second or third order filters are filters with a denominator polynomial that is of second or third order, respec-

geometries a *relaxation resonance frequency* $\omega_{R,polLD} = \sqrt{\gamma_{px}/\tau_p}$ and a damping factor γ_{xx} can be defined. The intensity modulation can follow the current modulation at frequencies near $\omega_{R,polLD}$, with an enhancement at $\omega_{R,polLD}$ before the response drops off drastically. The resonance frequency can be greatly simplified since the term $2bn_{x\infty}n_{p\infty}$ in the expression of γ_{px} (equations 2.19 and 2.24) dominates independently of the detuning and the temperature. Consequently, the square of the resonance frequency reduces to:

$$\omega^2_{R,polLD} \approx \frac{2bn_{x\infty}n_{p\infty}}{\tau_p} \approx 2n_{p\infty}\sqrt{\frac{b}{\tau_p^3}}. \tag{2.29}$$

Therefore, within this theoretical framework, the resonance frequency for polariton LDs is directly proportional to the square root of the polariton population in the condensate and inversely proportional to the square root of the polariton lifetime (keeping in mind that the exciton population of the reservoir $n_{x\infty}$ is clamped above threshold). In this respect, such a dependence is similar to the dependence of ω_R in conventional LDs above threshold, since in this latter case [156]:

$$\omega^2_R \approx \frac{v_g a_{diff} N_p}{\tau_{cav}}, \tag{2.30}$$

where v_g is the group velocity, a_{diff} is the differential gain, N_p is the average photon density in the cavity, and τ_{cav} is the cavity photon lifetime already defined in Table 2.1.
The damping factor can be rewritten using equations 2.16 and 2.21 as:

$$\gamma_{xx} = \frac{1}{\tau_x} + \gamma_{px} = \frac{1}{\tau_x} + \omega^2_{R,polLD}\tau_p. \tag{2.31}$$

It is thus seen that for large resonance frequencies, the damping of the response is ruled by the polariton lifetime. On the other hand, the inverse of the exciton lifetime acts as a damping factor offset, which is important for small polariton condensate populations where the resonance frequency is small.
At this stage, we should point out that the validity of the previous treatment for the intracavity pumping scheme might be limited by the actual response of the pumping LED. Therefore, it is necessary to determine the LED *cutoff frequency* $\omega_{3dB,LED}$, i.e., the frequency at which the input power, i.e., its dc value, is attenuated by half or 3 dB,[10] and compare it to $\omega_{R,polLD}$.
Following the theoretical approach described in the previous sections, the rate equations governing the emission of the LED are given by equation 2.6 and:

$$\frac{dn_x}{dt} = -\frac{n_x}{\tau_x} + Wn_{e-h}, \tag{2.32}$$

tively, usually presenting complex roots. In general, the higher the order the faster the transition from pass-band to stop-band.

[10] Note that the frequency response in decibels is given by $10\log_{10}|H(\omega)|^2$. Thus if the input power is attenuated by half $|H(\omega)|^2 = 1/2$ and $10\log_{10}(1/2) \sim -3$ dB.

from which one can deduce the modulation transfer function $H_{LED}(\omega)$ using harmonic analysis:

$$H_{LED}(\omega) = \frac{\frac{1}{\tau_x}\left(\frac{1}{\tau_{e-h}} + W\right)}{\left(i\omega + \frac{1}{\tau_x}\right)\left(i\omega + \frac{1}{\tau_{e-h}} + W\right)}. \tag{2.33}$$

The corresponding relaxation resonance frequency $\omega_{R,LED}$ and the damping factor γ_{LED} can be written as:

$$\omega_{R,LED} = \sqrt{\frac{1}{\tau_x}\left(\frac{1}{\tau_{e-h}} + W\right)} \approx 3.2 \text{ GHz} \tag{2.34}$$

and

$$\gamma_{LED} = \frac{1}{\tau_x} + \frac{1}{\tau_{e-h}} + W \approx 11.2 \text{ GHz}, \tag{2.35}$$

respectively. As we deal with a large damping ($\gamma_{LED}>\omega_{R,LED}$), the response drops below the 3 dB cutoff at a frequency less than $\omega_{R,LED}$. The frequency cutoff $\omega_{3dB,LED}$ can be determined by setting $|H_{LED}(\omega_{3dB,LED})|^2 = 1/2$:

$$\omega_{3dB,LED} = \sqrt{\omega_{R,LED}^2 - \frac{\gamma_{LED}^2}{2} + \sqrt{\left(\omega_{R,LED}^2 - \frac{\gamma_{LED}^2}{2}\right)^2 + \omega_{R,LED}^4}} \approx 1 \text{ GHz}. \tag{2.36}$$

Much larger values are predicted for the intracavity pumping geometry when using equation 2.28 (up to $\omega_{3dB} \sim 200$ GHz cf. Fig. 2.9(b)). However, in this regime the modulation transfer function of the device is limited by the frequency response of the pumping LED, which has a cutoff frequency given by equation 2.36. However, for the electrical pumping case (equation 2.26) with current densities in the range 10–20 A cm^{-2}, the peak frequency ω_P lies in the range 6-12 GHz and the cutoff frequency ω_{3dB} is expected to be ~ 16 GHz (Fig. 2.9(b)).

The analysis of the intrinsic modulation transfer function, derived from the dynamical response of polariton LDs to a small modulation of the current above threshold, demonstrates the interesting potential of the direct electrical pumping scheme, since a cutoff frequency ω_{3dB} up to ~ 16 GHz is predicted, whereas for the intracavity optical pumping scheme, the cutoff frequency is shown to be limited by the frequency response of the pumping LED, for which $\omega_{3dB} \sim 1$ GHz. As already mentioned before, devices characteristics can be considerably changed due to parasitic effects, i.e., the overall modulation transfer function is given by [154]

$$H(\omega) = H_{ext}(\omega) H_{int}(\omega), \tag{2.37}$$

with

$$H_{ext}(\omega) = \frac{A_c}{1 + i\omega/\omega_0}, \tag{2.38}$$

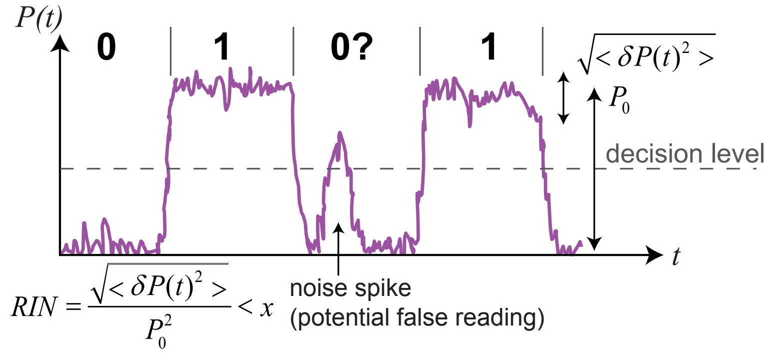

Figure 2.10: Noise in modulated laser signals for digital applications illustrating the definition of RIN assuming a mean-squared noise distribution $< \delta P(t)^2 >$ at 0 and P_0 output power. Adapted from Ref. [156].

where A_c is a proportionality constant and ω_0 is the parasitic roll-off frequency. This gives the commonly used equation, which is squared for fitting the frequency response to extract ω_R, γ, and ω_0. Furthermore, thermal management is also an important issue. For example, the first VCSEL to demonstrate a bandwidth in excess of 20 GHz was achieved with a GaAs/AlGaAs MQW active region emitting at 850 nm in 1997. This is still the highest reported bandwidth for the common 850-nm VCSELs, whose operation is neither limited by parasitics nor by its intrinsic response but by thermal effects [157].

2.4.3 Relative intensity noise

Conventional LDs suffer from random temporal fluctuations in the carrier and photon densities, even in the absence of current modulation. For digital applications one can define the *bit-error-rate* (BER). The BER measures the probability to record a noise spike, i.e., a potential false reading, as illustrated in Fig. 2.10. If the noise spike exceeds the decision level, then a false recording might be made. Such a noise floor can eventually have a detrimental impact for both analog and digital applications and thus it is useful to quantify the RIN of a laser:

$$RIN = \frac{< \delta P(t)^2 >}{P_0^2}, \tag{2.39}$$

where P_0 denotes the laser output power and $< \delta P(t)^2 >$ is the mean-squared noise distribution. However, LDs are often driven at a specific frequency, which depends on the application and thus it is common to define the RIN per unit bandwidth (in dB/Hz), (RIN/Δf). Note that the full RIN can be found by integrating the RIN per unit bandwidth over the detection bandwidth of the system of practical interest. Now, we would like to derive the expressions of the RIN/Δf for polariton LDs. To compute this quantity, we first derive the expression of the spectral density of the output power $S_{\delta P}(\omega)$ using the simplified differential rate equations given in section 2.4.1 written in a compact matrix form in a way similar to that developed by Coldren and Corzine [156]. The relevant Langevin noise source spectral densities or correlation strengths have to be evaluated. The latter is done in Appendix A.2.1. Eventually, the RIN/Δf is obtained for the two pumping geometries described in section 2.2 at RT and at δ_{opt}.

The Langevin approach

Because the subsequent analysis is restricted to polariton devices operating above the lasing threshold, the terms of spontaneous origin can be omitted. In other words the $(1+n_p)$ terms appearing in the rate equations 2.10 and 2.11 can be approximated as n_p. To determine $\frac{RIN}{\Delta f}$, we introduce the time-dependent Langevin noise sources $F_{n_x}(t)$ and $F_{n_p}(t)$ as the *ac* driving sources for the exciton reservoir and ground state polariton populations, respectively. The usual assumption of white noise is made for those sources, which allows to make use of the differential rate equations. The whole treatment is considered for a constant drive current (i.e., $dI = 0$) so that the differential rate equations written in compact matrix form in the frequency domain become:

$$\begin{bmatrix} \gamma_{xx} + j\omega & \gamma_{xp} \\ -\gamma_{px} & \gamma_{pp} + j\omega \end{bmatrix} \begin{bmatrix} n_{x1}(\omega) \\ n_{p1}(\omega) \end{bmatrix} = \begin{bmatrix} F_{n_x}(\omega) \\ F_{n_p}(\omega) \end{bmatrix}, \tag{2.40}$$

where n_{x1}, n_{p1}, F_{n_x}, and F_{n_p} correspond to the components of the noise that fluctuate at frequency ω. The expressions for γ_{xx}, γ_{pp}, γ_{xp}, and γ_{px} are pumping geometry dependent and are given in equations 2.16-2.24. Once again using Kramer's theorem expression for $n_{x1}(\omega)$ and $n_{p1}(\omega)$ can be obtained. The exciton and the ground state polariton spectral densities $S_{n_x}(\omega)$ and $S_{n_p}(\omega)$, respectively, are defined as:

$$S_{n_{x,p}}(\omega) = \frac{1}{2\pi}\int < n_{x1,p1}(\omega) n_{x1,p1}(\omega')^* > d\omega'. \tag{2.41}$$

Hereafter we are only interested in the expression of $S_{n_p}(\omega)$. The latter can be obtained using the expression of $n_{p1}(\omega)$ derived from the complex matrix form 2.40:

$$S_{n_p}(\omega) = \frac{|H(\omega)|^2}{\omega_R^4}\left[(\gamma_{xx}^2 + \omega^2) < F_{n_p} F_{n_p} > + 2\gamma_{xx}\gamma_{px} < F_{n_p} F_{n_x} > + \gamma_{px}^2 < F_{n_x} F_{n_x} >\right], \tag{2.42}$$

where $H(\omega)$ is the pumping geometry dependent modulation transfer function (cf. equations 2.26 and 2.28) and ω_R is the relaxation resonance frequency equal to $\sqrt{\gamma_{px}/\tau_p}$. The Langevin noise correlation strengths $< F_{n_p} F_{n_p} >$, $< F_{n_p} F_{n_x} >$, $< F_{n_x} F_{n_x} >$ are given in Appendix A.2. Furthermore, as the compact matrix form 2.40 is identical to that of a conventional semiconductor LD [156], we can readily express $S_{\delta P}(\omega)$:

$$S_{\delta P}(\omega) = \left(\frac{\eta_0 h\nu}{\tau_p}\right)^2 S_{n_p}(\omega) + 2Re\left[\left(\frac{\eta_0 h\nu}{\tau_p}\right) < n_{p1} F_0 >\right] + < F_0 F_0 >, \tag{2.43}$$

where η_0 is the optical efficiency of the laser taken equal to 0.6, and F_0 is the Langevin noise

source for the stream of output photons resulting from the spontaneous decay of ground state polaritons.
Note that the optical efficiency defined here multiplied by the injection efficiency (η_i) yields the differential quantum efficiency also called slope efficiency, $\eta_d = \eta_i \cdot \eta_0$. The injection efficiency is defined as the fraction of current above threshold which results in stimulated emission and the differential quantum efficiency is proportional to the slope of the PI curve (output power vs current curve). The optical efficiency depends as well on the transmission of the top and bottom DBR (T_t and T_b), i.e., $\eta_0 = \hat{\eta}_0 \cdot \eta_{ut}$ with $\eta_{ut} \approx T_t/(T_t + T_b)$ [154]. For $\hat{\eta}_0$, values of 0.6 - 0.8 can be found in the literature [154, 156] and thus taking $\eta_{ut} \approx (1-0.99)/(2-(0.99+0.996)) \approx 0.71$[11] results in an optimistic value of ~ 0.6 for η_0. F_0 is accounting for the fact that the partition noise of photons transmitted outside the cavity differs from that of photons reflected back in. Note that the output power P_0 is given by:

$$P_0 = \eta_0 \frac{n_{p\infty}}{\tau_p} h\nu. \tag{2.44}$$

Together with the correlation strengths associated with the partition noise (cf. Appendix A.2), we can now evaluate $S_{\delta P}(\omega)$ given by equation 2.43 for the two pumping geometries. For the intracavity pumping geometry, we obtain:

$$S_{\delta P,intra}(\omega) = h\nu P_0 \left[1 + \frac{|H(\omega)|^2}{\omega_R^4} [a_1 + a_2\omega^2] \right], \tag{2.45}$$

where

$$a_1 = \frac{2\eta_0}{\tau_p} \left[\frac{1}{2n_{p_\infty}} \left(\gamma_{xx}^2 < F_{n_p} F_{n_p} > + 2\gamma_{xx}\gamma_{px} < F_{n_p} F_{n_x} > + \gamma_{px}^2 < F_{n_x} F_{n_x} > \right) - \gamma_{xx}\omega_R^2 \right], \tag{2.46}$$

and

$$a_2 = \frac{< F_{n_p} F_{n_p} > P_0}{h\nu n_{p_\infty}^2} = \frac{2\eta_0}{\tau_p} \left(\frac{1}{\tau_p} + a n_{x_\infty} e^{-\beta\Delta_{esc}} \right). \tag{2.47}$$

Once the expression of $S_{\delta P}(\omega)$ is known, we can readily determine $\frac{RIN}{\Delta f}$ since both quantities

[11] If mirror losses are neglected $T_{t,b}$ =1-$R_{t,b,max}$. Furthermore, a $R_{b,max}$ of 99.6% can be achieved for LM InAlN/GaN DBRs [158] and a $R_{t,max}$ of 99% for SiO_2/TiO_2 DBR when using 4 quarter-wave pairs (cf. equation 1.27).

are linked by:

$$\frac{RIN_{intra}}{\Delta f} = \frac{2S_{\delta P,intra}(\omega)}{P_0^2} = \frac{2h\nu}{P_0}\left[1 + \frac{|H(\omega)|^2}{\omega_R^4}[a_1 + a_2\omega^2]\right]. \tag{2.48}$$

For this pumping geometry, we can point out the close similarity of the RIN expression with that of conventional LDs that only differs by the a_1 and a_2 coefficients.

For the direct electrical pumping geometry, the determination of the expression of the spectral density of the output power $S_{\delta P}(\omega)$ and hence that of $\frac{RIN}{\Delta f}$ are more tedious because of the form of the modulation transfer function, which is more complex. We finally derive for $\frac{RIN}{\Delta f}$:

$$\frac{RIN_{elec}}{\Delta f} = \frac{2h\nu}{P_0}\left[1 + \frac{|H(\omega)|^2}{\omega_R^4}\left[a_1 + a_2\omega^2 - A' + \frac{2\eta_0}{\tau_p}\gamma_{xx}\omega_R^2\right]\right], \tag{2.49}$$

where

$$\begin{aligned} A' \quad = \quad & -2\frac{\eta_0}{\tau_p}\omega_R^2[C_1(C_2^2 + c^2 n_{x_\infty}^2 n_{p_\infty}^2\omega^2)]^{-1}[cn_x n_p\gamma_{xx}\omega^4 + (C_2C_3 - C_2\gamma_{xx}^2 + C_2C_4\gamma_{xx} \\ & - C_3C_4cn_{x_\infty}n_{p_\infty} + C_3cn_{x_\infty}n_{p_\infty}\gamma_{xx} + C_4cn_{x_\infty}n_{p_\infty}\gamma_{xx}^2)\omega^2 + C_2C_3C_4\gamma_{xx}], \end{aligned} \tag{2.50}$$

and

$$|H(\omega)|^2 = \frac{C_1^2(C_2^2 + c^2 n_{x_\infty}^2 n_{p_\infty}^2\omega^2)}{(C_3^2 + \gamma_{xx}^2\omega^2)(C_4^2 + \omega^2)}. \tag{2.51}$$

where the expression of the C_i coefficients with $i \in \{1,4\}$ are given in the Appendix A.2.2.

The polariton laser RIN is plotted in Figs. 2.11(a) and 2.11(b) for the intracavity and the electrical pumping geometries, respectively, based on the parameters listed in Table 2.1 and using the expressions given in section 2.4.1 for n_{e-h_∞}, n_{x_∞}, and n_{p_∞}. It can be readily seen that as for conventional semiconductor LDs, the expected minimum RIN of polariton LDs – whatever the pumping geometry – is equal to $\frac{2h\nu}{P_0}$, i.e., to the standard quantum limit, also called shot noise floor. This is the case for the high-frequency range, i.e., for frequencies well above the relaxation resonance frequency. However contrary to conventional LDs where

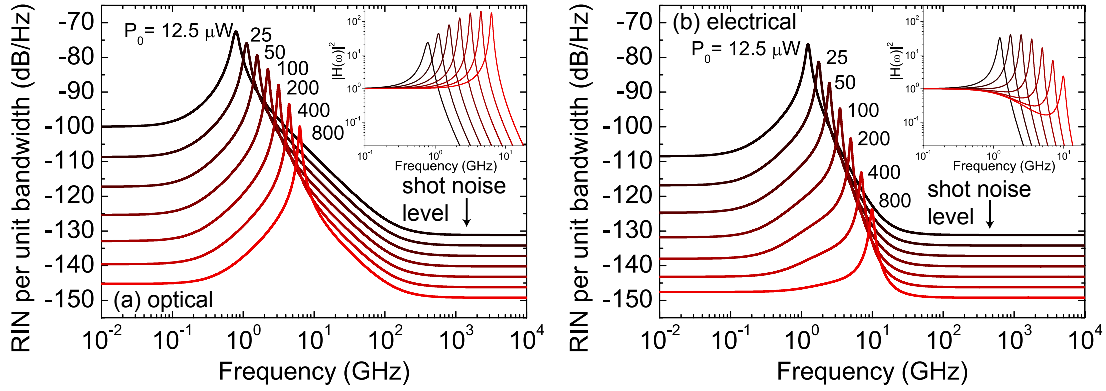

Figure 2.11: Calculated relative intensity noise as a function of frequency ($\nu = \omega/2\pi$) at different optical output power levels at RT and at δ_{opt} for an InGaN/GaN MQW polariton LD with (a) the intracavity optical pumping and (b) the direct electrical pumping geometries, based on the parameters given in Table 2.1. The insets display the corresponding modulation transfer functions for the same output powers as in the corresponding main figures. Adapted from Ref. [159].

the excess intensity noise is mostly dominating in the vicinity of ω_R at high output powers, an excess noise is still present at low frequencies ($\omega < 0.1\omega_R$), whose origin will be briefly commented hereafter. For the electrical pumping geometry it can also be seen that for high optical output power levels, a shoulder (i.e., extra-noise) is present on the low-frequency side of the resonance, which is inherited from the non-conventional lineshape of the modulation transfer function (cf. inset of Fig. 2.11(a)). In this latter geometry, the peculiar lineshape of $H(\omega)$ is also responsible for a sharp decrease in the RIN above ω_R – whose slope increases with output power – leading to a much faster convergence toward the shot noise level than under the intracavity pumping geometry, which exhibits a behavior closer to that of conventional semiconductor LDs with a RIN that falls off at high frequencies at 20 dB/decade before reaching the shot noise level. Note also that the damping of the RIN peak is much more pronounced for polariton LDs having the direct electrical pumping geometry than for the intracavity one. Finally unlike conventional LDs, the RIN peak gets narrower with increasing optical output power, which is likely due to the absence of an equivalent gain suppression factor in our modeling [156, 160]. Indeed in order to model properly the operating behavior of this former type of devices, the damping factor, which enters in the expression of the modulation transfer function, includes a phenomenological expression for the gain accounting for saturation phenomena via a gain suppression factor [156]. This decrease in the gain with increasing current induces a broadening of $|H(\omega)|^2$ and hence of the RIN peak as can be directly inferred from equations 2.48 and 2.49, which is, as we pointed out, fairly similar to that of conventional LDs. The main underlying physical phenomenon responsible for saturation is usually ascribed to intraband carrier relaxation, which leads to a sublinear increase in the intracavity photon density for large currents [128]. In the case of the modeling of polariton LDs, intraband carrier relaxation is at the heart of the semi-classical Boltzmann equations that are computed to derive the evolution of the carrier densities along polariton branches as a function of the

pumping rate. Such an effect is thus phenomenologically included in the rate equations 2.10 and 2.11 but contrary to the case of conventional LDs it does not induce a broadening of the lineshape of the RIN peak with increasing optical output power. However, at this stage we cannot fully discard the contribution of other phenomena that could also induce a behavior similar to that observed for conventional LDs. In particular, it was highlighted by Tassone and Yamamoto that heating of excitons in the reservoir above threshold would decrease the exciton-exciton scattering efficiency, which would subsequently induce an incomplete clamping of n_x [161]. Such an effect could manifest itself in polariton LDs in a way similar to gain suppression in conventional LDs.

In order to get more insights into $\frac{RIN}{\Delta f}$, we should notice that the expression for the RIN derived for the intracavity pumping geometry can be further simplified when considering the power dependence of the a_1 and a_2 terms (cf. equation 2.48). This simplification step is much easier to perform for this latter pumping geometry compared with the electrical one because the modulation transfer function is identical to that of conventional LDs. In this latter case when only keeping terms in a_1 and a_2 that depend on P_0, we obtain:

$$\frac{RIN_{intra,approx}}{\Delta f} = \frac{2h\nu}{P_0} + \frac{|H(\omega)|^2}{\omega_R^4} < F_{n_p} F_{n_p} > \frac{2}{n_{p_\infty}^2}\left(\frac{1}{\tau_x^2} + \omega^2\right). \tag{2.52}$$

The suitability of this simplified expression for the RIN in polariton LDs having the intracavity pumping geometry is illustrated in Fig. 2.12(a) where an excellent agreement is observed between equations 2.48 and 2.52 at low output power levels. When setting $\omega = 0$ in equation 2.52, we obtain:

$$\frac{RIN_{intra,approx}}{\Delta f}(\omega = 0) = \frac{2h\nu}{P_0} + \frac{2h\nu}{P_0}\left[\frac{2}{\omega_R^4}\left(\frac{1}{\tau_p} + a n_{x_\infty} e^{-\beta \Delta_{esc}}\right)\frac{\eta_0}{\tau_p \tau_x^2}\right], \tag{2.53}$$

where the second term on the right-hand side decreases as $1/P_0^3$ since $\omega_R^4 \propto P_0^2$. Consequently, this term will rapidly drop below the shot noise floor with increasing power. From equation 2.53, we therefore expect a low-frequency $\frac{RIN}{\Delta f}$ converging toward the shot noise level. Obviously this is not the case, as can be seen in Figs. 2.11 and 2.12(a), because of an irreducible offset introduced by the terms contained in the expression of a_1 (equation 2.46). All of them being of similar weight, except for the very last one ($\propto \omega_R^2$) that can be neglected, a tractable analytic expression of the RIN at large optical output powers cannot be readily derived from equations 2.46-2.48. Finally let us recall that for this specific geometry, the reported high-frequency behavior of the RIN should likely be affected by the cutoff frequency of the pumping LED, which was shown to amount to 1 GHz for the set of considered parameters (cf. equation 2.36).

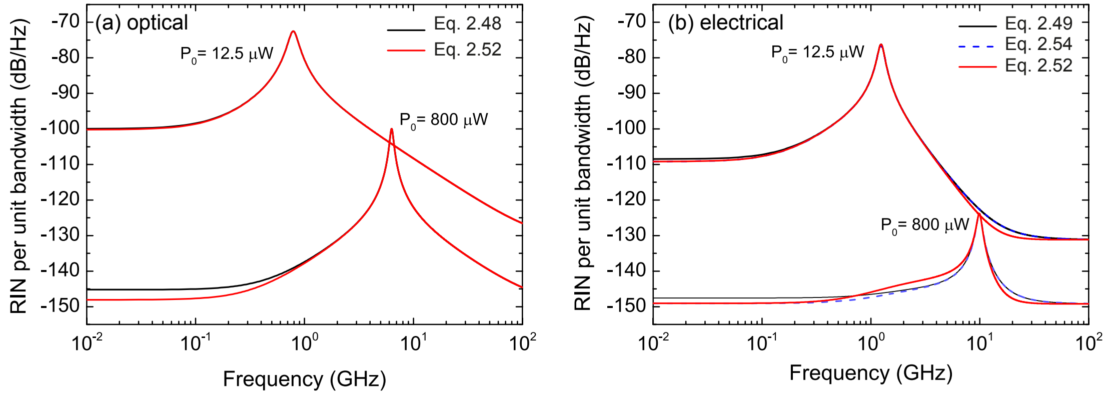

Figure 2.12: Calculated RIN as a function of frequency ($\nu = \omega/2\pi$) at two different optical output power levels (low and high) at RT and at δ_{opt} for an InGaN/GaN MQW polariton LD for (a) the intracavity optical pumping geometry using equations 2.48 (black lines) and 2.52 (red lines) (b) for the direct electrical pumping geometry using equations 2.49 (black lines), 2.52 (red lines) and 2.54 (blue dash-dotted lines). Adapted from Ref. [159].

As briefly mentioned above, at first sight such a simplified treatment cannot be easily carried out for the electrical pumping geometry due to the complexity of the modulation transfer function. However, when applying equation 2.52 to this geometry with the proper set of parameters, a reasonable agreement is achieved between the exact and the simplified expressions for $\frac{RIN}{\Delta f}$ – especially at low output power – as can be seen in Fig. 2.12(b); meaning thereby that the qualitative evolution of the latter is, as could be anticipated, governed by the same parameters. Contrary to the intracavity pumping scheme a slight difference can be noticed for the high-frequency tail of the RIN peak whatever the output power level. In fact it can be shown that it arises from an extra term that is given in the following improved expression for $\frac{RIN}{\Delta f}$ under direct electrical pumping that is also displayed in Fig. 2.12(b):

$$\frac{RIN_{elec,approx}}{\Delta f} = \frac{2h\nu}{P_0}\left[1+\frac{|H(\omega)|^2}{\omega_R^4}\left(<F_{n_p}F_{n_p}>\frac{\eta_0}{\tau_p n_{p_\infty}}\left(\frac{1}{\tau_x^2}+\omega^2\right)\right.\right.$$
$$\left.\left.-\frac{2\eta_0}{\tau_p}\frac{C_4(\omega_R^2-\omega^2)\omega^2\omega_R^4}{\omega_R^4C_4^2+\omega^2C_1^2(cn_{x_\infty}n_{p_\infty})^2}\right)\right]. \tag{2.54}$$

In summary, we have carried out an analysis of the relative intensity noise per unit bandwidth in polariton LDs for two relevant pumping geometries, namely, the direct electrical and the intracavity ones (cf. section 2.2), in the framework of a theoretical treatment adapted from that applied to conventional semiconductor LDs using rate equations including Langevin noise sources. The resulting general expressions can be applied to all inorganic semiconductor polariton LDs, but numerical calculations have been performed in the specific case of III-nitride devices. It was shown that in the high-frequency range the expected minimum RIN

of polariton LDs—whatever the pumping geometry—is equal to the standard quantum limit $2h\nu/P_0$. The general line shape of the RIN as a function of frequency and optical output power has been discussed for the two geometries and approximate (simplified) expressions for the RIN have been given.

2.4.4 Emission linewidth

Unless great care is taken, conventional LDs and VCSELs do have laser linewidths much greater than the MHz. It results from phase fluctuations in their output, mainly arising from spontaneous emission and carrier density fluctuations. However, for many applications, such as sensor or communication systems, it is advantageous to have submegahertz linewidths [162]. Thus, achieving a precise understanding of the emission linewidth of any practical devices, such as future polariton LDs, is of great importance.
An accurate calculation of the emission linewidth (γ_{polLD}) of a polariton LD would require a proper quantum optics treatment, which is clearly beyond the scope of the present work. However, in this section we wish to point out the critical parameters that will likely affect γ_{polLD} and to derive the modified Schawlow-Townes linewidth for the two pumping geometries given in section 2.2. In the case of conventional LDs the modified Schawlow-Townes linewidth only considers spontaneous emission noise. In the very same way as it is done for conventional semiconductor LDs, using the rate equation 2.11, i.e., including the terms of spontaneous origin, we can extract the expression of the effective polariton lifetime τ'_p:

$$\frac{1}{\tau'_p} = \frac{1}{\tau_p} - \left[a(1 - e^{-\beta\Delta_{esc}}) + cn'_{e_\infty} + bn_{x_\infty} \right] n_{x_\infty}, \tag{2.55}$$

where the second term on the right-hand side of equation 2.55 is obviously the equivalent for polariton LDs to the product of the confinement factor (Γ_{cf}) with the group velocity (v_g) and the material gain per unit length (g) in VCSELs or conventional LDs (the effective cavity lifetime (τ'_{cav}) is then given by: $1/\tau'_{cav} = 1/\tau_{cav} + \Gamma_{cf} g v_g$ [156]). It describes the increase in the ground state polariton lifetime resulting from the efficient relaxation of excitons from the reservoir that will compensate for polariton losses. The below-threshold linewidth, accurate for amplified spontaneous emission, namely the famous Schawlow-Townes linewidth is given by $h/2\pi\tau'_p$. However, M. Lax showed that above threshold the nonlinear coupling between the rate equations resulted in a factor of 2 reduction in the linewidth [163]. Thus, the *modified* Schawlow-Townes linewidth formula when accounting for the 1/2 correction factor [156] is then such that:

$$\gamma_{ST} = \frac{h}{4\pi\tau'_p}. \tag{2.56}$$

Figure 2.13: Evolution of the modified Schawlow-Townes linewidth of polariton LDs at the optimum detuning as a function of temperature for the electrical (red dots) and the intracavity optical (black dots) pumping geometry. Taken from Ref. [159].

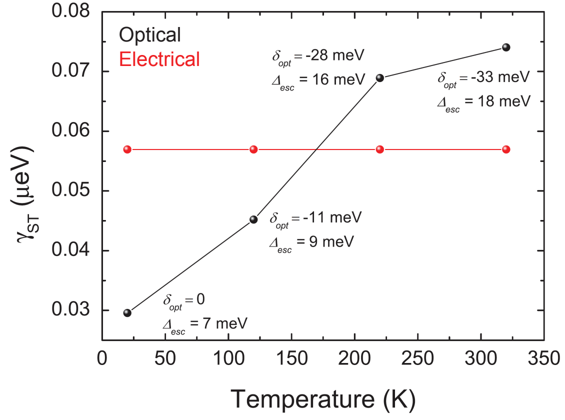

The evolution of γ_{ST} for the two pumping geometries is displayed in Fig. 2.13 at the optimum detuning as a function of temperature. Note here that the exact behavior reported for temperatures below 200 K should only be considered as indicative because electrically-injected devices become progressively less efficient with decreasing temperature due to the reduced $p-$type conductivity.

Note that for conventional LDs $\gamma_{ST,LD} = \Gamma_{cf} R_{sp}/4\pi n$, where R_{sp} is the spontaneous emission rate, and n is the photon density (or output power) [156]. One central conclusion of this formula is that the LD linewidth varies inversely with the output power, leading to a linewidth collapse at high current densities. Note that equation 2.56 is not independent of the polariton density as a, b, and c all depend on n_p. Furthermore, for conventional LDs it can be shown that the linewidth is enhanced by a factor $(1+\alpha^2)$, i.e., $\gamma_{LD} = \gamma_{ST,LD}(1+\alpha^2)$. The 1 represents the spontaneous emission noise ($\gamma_{ST,LD}$) and α^2 represents the carrier noise contribution [156]. Haug and co-workers [164] showed that the polariton linewidth can be expressed in a similar way as to conventional LDs with a linewidth enhancement factor $\alpha^2 = (\Delta\omega/\Gamma)^2$, where $\Delta\omega$ is the frequency shift associated with phase fluctuations, and Γ is the decay rate of the density fluctuations.

In 'early' experiments a net increase in the emission linewidth of optically pumped MCs above threshold with increasing density (P_x) was observed and explained to originate from polariton-polariton interactions [165]. Tassone and Yamamoto [161], and then Porras and Tejedor [166], suggested that a self-phase modulation term, not present in conventional LDs, should lead to an increased γ_{polLD} with increasing P_x. However, those 'early' measurements suffered from intensity noise fluctuations of the pump laser. The 'true' emission linewidth associated with polariton condensates was only made accessible thanks to the use of semiconductor LDs free from intensity fluctuations on the ns time scale, leading to a coherence time of 120–150 ps in a CdTe MC at cryogenic temperatures, i.e., corresponding to a linewidth of ~ 10 μeV [167]. In Fig. 2.14(a) the corresponding first-order coherence function $g^{(1)}(\tau)$ versus delay time τ for a polariton condensate above threshold is shown. Note that the spectral

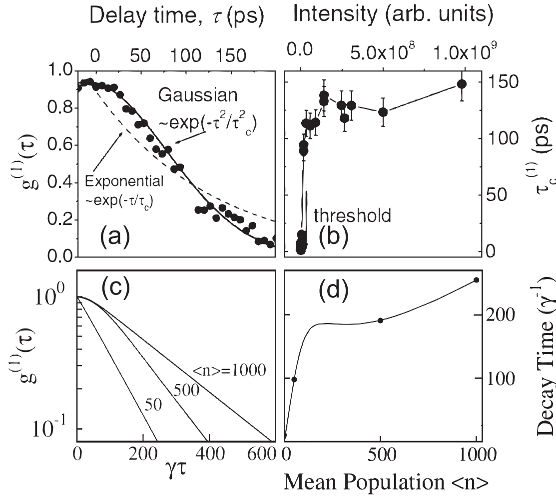

Figure 2.14: Coherence properties of a polariton condensate. Experimentally determined (a) first-order coherence function $g^{(1)}(\tau)$ above threshold and (b) dependence of the coherence time on pumping intensity. Calculated (c) decay of $g^{(1)}(\tau)$ for populations $\langle n \rangle$ = 50, 500, 1000 and (d) decay time ($\gamma^{-1} = \tau_{cav}/2$) for $g^{(1)}(\tau)$ as a function of the population obtained applying the Kubo statistic lineshape theory. Experimental and calculated results adapted from Refs. [167] and [168], respectively.

shape of emission is obtained by taking the Fourier transform of $g^{(1)}(\tau)$ [168] and thus the linewidth is proportional to $1/\tau_c$, where τ_c is the coherence time. In Fig. 2.14(b) the variation of the coherence time is plotted as a function of the emission intensity, which is proportional to the mean number of particles in the condensate state ($\langle n \rangle$). Close to threshold when $\langle n \rangle$ is small the Schawlow-Townes decay is responsible for the increase of τ_c. Whittaker and Eastham attributed the observed plateau in the variation of τ_c with condensate occupation (Fig. 2.14(b)) to a critical slowing down of number fluctuations [168]. Note that the same trend is observed in conventional LDs close to threshold and Haken [169] showed a close analogy of this behavior with the critical slowing down of number fluctuations in the vicinity of an equilibrium phase transition. In Figs. 2.14(c) and 2.14(d) the results of Whittaker's and Eastham's theoretical quantum model, which is based on the Kubo statistic lineshape model and self-phase modulation, are shown. Those authors show that the available experimental results (Figs. 2.14(a) and 2.14(b)) are well explained by their model describing a MC polariton condensate as a pumped dissipative system where the main decoherence process is the combined effect of number fluctuations and inter-particle interactions. However, their model predicts a regime of motional narrowing at higher pump powers, which has not been observed so far, possibly due to the disorder limited size of the condensates.

Provided linewidth enhancement effects do not play a significant role, which should be the case at least at cryogenic temperatures according to the most recent theories [164, 167, 168], it is predicted that the linewidth of III-nitride polariton LDs γ_{polLD} should be equal to γ_{ST} at least close to threshold [168]. Thus, γ_{polLD} can be deduced directly from Fig. 2.13. The slightly narrower linewidth predicted for the direct electrical pumping geometry, 5.7×10^{-2} (14 MHz) vs 7.3×10^{-2} μeV (18 MHz) for the intracavity one, is likely inherited from the strong dependence of the effective ground-state polariton lifetime given by equation 2.55 on the term proportional to the exciton-exciton scattering rate. The latter is slightly larger for the direct electrical pumping geometry compared with the intracavity one, which is inherited from the δ_{opt} value that is closer to zero detuning with this geometry (cf. Fig. 2.4(c)). Qualitatively we

	Microcavity Laser	
	VCSEL	Polariton LD
Reservoir	unbound e-h pairs	excitons
Stimulation condition	population inversion	ground state occupancy > 1
Emission wavelength	λ_{cav}	$\lambda_{pol} = hc/E_{LPB}(0)$
lifetime	τ_{cav}	$\tau_p(\delta)$
Equilibrium	None	δ-dependent
J_{thr} (kA/cm^2)	1 - 10	10^{-1}-10^{-3}
δ_{opt} (meV)	0	< 0
Above threshold clamping of	carriers (e and h)	excitons
ω_R^2	$v_g a_{diff} N_p / \tau_{cav}$	$2n_{p\infty}\sqrt{b/\tau_p^3}$
Linewidth	$\gamma_{LD} \propto 1/\tau'_{cav}$	$\gamma_{polLD} \propto 1/\tau'_p$

Table 2.2: Comparison between VCSELs and polariton LDs at RT for III-nitride based devices.

can understand that when going toward more positive detunings, the critical density leading to condensation increases [138], hence $n_{x\infty}$, which subsequently implies an overall decrease in $1/\tau'_p$ and thus in γ_{ST}.

2.5 Polariton laser vs. VCSEL

The main differences between VCSELs and polariton LDs are given in Table 2.2, which summarizes partly the results of sections 2.3.2, 2.4.2 and 2.4.4. Conventional LDs such as VCSELs are ruled by fermionic statistics, i.e., they form a class of coherent light-emitting devices where the Bernard-Duraffourg condition is fulfilled, which is for the bulk case [30]:

$$E_{Fc} - E_{Fv} \geq \hbar\omega \geq E_g, \tag{2.57}$$

where E_{Fc} and E_{Fv} are the quasi-Fermi levels describing the band filling of the semiconductor with bandgap energy E_g out of equilibrium. The latter means that population inversion is reached. Whenever the Fermi-Dirac function describing the electron occupation probability of levels at an energy $\hbar\omega$ in the conduction band $f_c(\hbar\omega)$ exceeds the one in the valence band $f_v(\hbar\omega)$, i.e., $f_c(\hbar\omega) > f_v(\hbar\omega)$, the absorption $\alpha(\omega)$ of the medium becomes negative. In other words the system exhibits gain $g(\omega)$ [128, 170]:

$$\alpha(\omega) = -g(\omega) = \alpha_{2D,3D}(\hbar\omega)(f_v(\hbar\omega) - f_c(\hbar\omega)), \tag{2.58}$$

where $\alpha_{2D,3D}$ depends on the dimensionality of the system (cf. equation 3.12). As already mentioned previously the physics involved in polariton lasing is very different, since it is based on stimulated relaxation of exciton-polaritons from a reservoir to a lower lasing state of the lower polariton branch triggered by final state occupancy exceeding unity (cf. section 2.3.1).

The emission energy (or wavelength) of coherent light in the case of polariton lasers depends

on the detuning and vacuum Rabi splitting, whereas in the case of a VCSEL, the latter is solely determined by the cavity mode. Furthermore, the threshold of the polariton system does not require population inversion and thus the threshold current density (J_{thr}) is clearly lower than that of a VCSEL. Note that in a polariton LD the total lower polariton density at threshold is well below the exciton saturation density, i.e., a polariton LD operates below the Mott transition, whereas a conventional photon laser such as a EELD or a VCSEL operates clearly above it. Hence the exciton saturation density provides an upper limit for the operation of polariton LDs, i.e., the output power can not be increased indefinitely. However, output powers (P_0) up to several hundreds of μW are expected for polariton LDs (cf. section 2.4.3). Note that the threshold of a conventional photon laser lies clearly above the Mott transition, where the onset of gain occurs (semiconductor transparency), as internal losses have to be compensated for.

In the previous section the low lasing threshold of polariton LDs has already been highlighted. Furthermore, δ_{opt} in the case of polariton LDs has been shown to be temperature dependent and different from zero for most of the temperature range (cf. Fig. 2.4). In the case of a VCSEL, the minimum in the threshold current is expected to occur close to zero detuning, when the overlap between the gain band of the active medium and the cavity mode is maximum. In Fig. 2.15(a) the lasing threshold (P_{thr}) of an InGaN/GaN MQW VCSEL measured at RT under non-resonant excitation for several detuning values is plotted and δ_{opt} can be readily identified [171]. In Fig. 2.15(b) the lasing threshold (J_{thr}) with either an electrical or an intracavity optical pumping geometry at RT shows a quite different δ dependence (theory based). Note that besides the negative δ_{opt} value expected for both geometries the strong increase of the threshold current density by several orders of magnitude when departing from the δ_{opt} position is surprising, especially because no such dependence has ever been observed in the case of the optically pumped GaN/AlGaN MQW based MC [137, 138]. Furthermore, the experimentally determined threshold for the latter MC has been found to occur one to two orders of magnitude below the Mott transition [172], whereas the predicted threshold is two

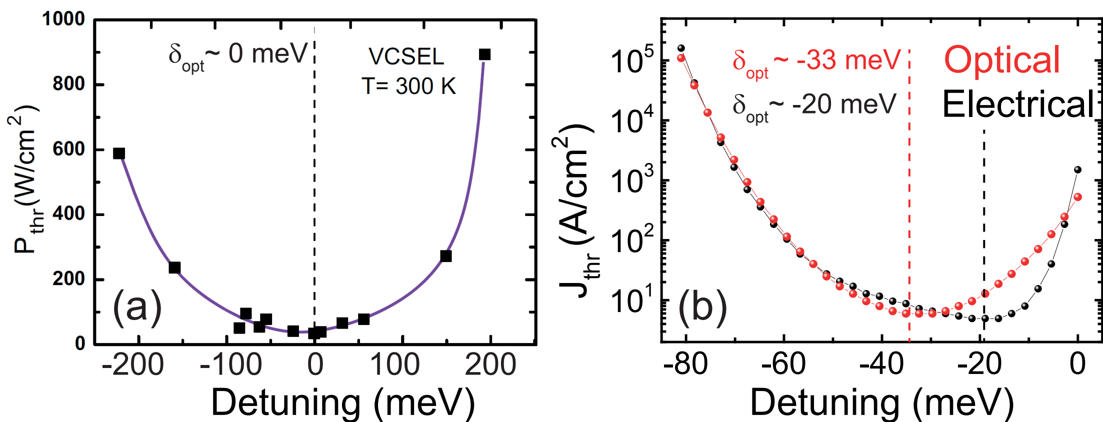

Figure 2.15: Evolution of the nonlinear emission threshold at room temperature versus δ in the case of (a) a VCSEL (experiments), and of (b) polariton LDs with either an electrical or an intracavity optical pumping geometry (theory). (a) Note that the blue line is a guide to the eye. Adapted from Ref. [171].

orders of magnitude lower. Thus, the quantitative validity of the full semiclassical Boltzmann model applied to the two puming geometries remains to be proven.

Using a simplified quasi-analytical model based on a two-level system, i.e., based on two rate equations, provides comparable results to the case of conventional LDs. Indeed, it has been shown (cf. section 2.4.1) that the exciton population, which acts as a reservoir for the stimulated relaxation process, gets clamped once the condensation threshold is crossed, a behavior analogous to what happens in conventional LDs with the carrier density above threshold. Furthermore, an expression for the relaxation resonance frequency (ω_R) for polariton LDs has been derived (cf. Table 2.2 and section 2.4.2). Another important feature of light emitting devices is their emission linewidth (cf. section 2.4.4). In the case of polariton LDs γ_{polLD} is expected to be inversely proportional to the effective polariton lifetime and γ_{polLD} with increasing pump strength is considered to be mainly constant. Note that this is not the case in conventional single mode LDs: at threshold the linewidth (γ_{LD}) is inversely proportional to $\tau_{cav'}$ and above threshold γ_{LD} decreases with increasing pump strength [156].

2.6 Summary of the results

The main emission characteristics of electrically-driven polariton lasers based on planar GaN MCs with embedded InGaN/GaN MQWs were studied theoretically. Two experimentally relevant pumping geometries have been considered, namely the direct injection of electrons and holes into the strongly coupled MC region and intracavity optical pumping via an embedded LED. The minimum threshold current density J_{thr} as a function of lattice temperature and exciton-cavity photon detuning was calculated in the framework of semiclassical Boltzmann equations leading to optimum values two orders of magnitude lower than in equivalent III-nitride based VCSELs (at RT $J_{thr} \sim 5$ A/cm^2 vs 1-10 kA/cm^2). Using a quasi-analytical model the steady-state and the high-speed current modulation including the relaxation oscillation frequency features were derived. Through this analysis it was shown that the exciton population in the reservoir gets clamped above the condensation threshold and is governed by the exciton-exciton scattering rate and the ground state polariton lifetime. Two other important figures of merit, namely the RIN and the modified Schawlow-Townes linewidth were also determined within this theoretical framework, which overall allows establishing a direct comparison with the main emission features of conventional single mode LDs.
For future experiments an interesting aspect to be checked in polariton LDs is their linewidth evolution with pumping strength, which is expected to be mainly constant, whereas for conventional single mode LDs it is known to decrease.

3 Design of microcavities and critical aspects

As already mentioned in section 1.2.1 a microcavity contains the following building blocks: a bottom mirror, an active medium, and a top mirror. First we will consider the optical and structural properties of two kinds of distributed Bragg reflectors, those built from dielectric materials and those from III-nitride-based bilayers. Then a section will be devoted to the design of InGaN/GaN MQW based planar microcavity structures suitable for strong coupling studies under non-resonant optical pumping. We will first detail the requirements in terms of QW absorption features, N_{QW}, and optical cavity length for achieving the strong coupling regime in InGaN/GaN MQW-based MCs by combining envelope function calculations and TMS for to two structure designs: a semi-hybrid and a full-hybrid approach.

3.1 High-quality dielectric Bragg mirrors

3.1.1 Determination of the complex refractive index

The interaction of electromagnetic radiation with electrons of a material affects the propagation of this radiation. As a result, there is a change in wave velocity and intensity described by the complex optical refractive index of the material:

$$\tilde{n} = n_{op} - i k_{op}, \tag{3.1}$$

where n_{op} is the real index of refraction, and k_{op} is the index of absorption, which is also known as the extinction coefficient. The electric field component associated to the propagating wave in the x direction is then expressed by

$$E = E_0 e^{\frac{-i2\pi\tilde{n}x}{\lambda}} = E_0 e^{\frac{-i2\pi n_{op}x}{\lambda}} e^{\frac{-2\pi k_{op}x}{\lambda}}, \tag{3.2}$$

where E_0 is the field amplitude and λ is the wavelength. From the latter the wave velocity v_p can be identified readily using the angular frequency ω and the wave vector $\mathbf{k}$ as $v_p = \omega/|\mathbf{k}| = \frac{2\pi c}{\lambda}\frac{\lambda}{2\pi n_{op}} = c/n_{op}$, whereas in free space the wave velocity is c as n_{op} is equal to unity. The

intensity of the radiation I is proportional to EE^*, thus $I \propto E_0^2 exp(-4\pi kx/\lambda)$. Therefore,

$$I = I_0 e^{-\alpha x}, \tag{3.3}$$

where the absorption coefficient α is defined by $4\pi k/\lambda$, and I_0 is the intensity of the incident radiation. The absorption coefficient can be determined by measuring the reflectivity R and the transmission T of a thin layer. The transmitted intensity T, neglecting interference effects and losses due to scattering is given by [170]:

$$T = (1-R)e^{-\alpha l}, \tag{3.4}$$

where l is the layer thickness. Thus, the absorption coefficient can be found easily:

$$\alpha = -\frac{1}{l} ln\left(\frac{T}{(1-R)}\right). \tag{3.5}$$

A Varian Cary 500 spectrophotometer has been used to measure T and R. The absolute reflectivity has been determined using the V-W configuration, as schematically represented in Fig. 3.1(b). In the V configuration, used for calibration, the measured intensity $I_{m,V}$ depends on the incident intensity I_0 and the reflectivity of the mirrors R_1, R_2 and R_3 via the relationship $I_{m,V} = I_0 R_1 R_2 R_3$, whereas in the VW configuration $I_{m,VW} = I_0 R_1 R_2 R_3 R_{sample}^2$. Thus the reflectivity of the sample can be obtained by $R_{sample} = \sqrt{I_{m,VW}/I_{m,V}}$. Within such a configuration the absolute reflectivity at $\sim 7°$ and with a precision of at best 1% can be obtained. As an illustration the reflectivity and transmission curve measured on a thin TiO_2 layer are shown in the inset of Fig. 3.1(c). The thin TiO_2 layer has been deposited by magnetron sputtering onto a transparent, double side polished sapphire substrate. Furthermore, the extinction coefficient k has been derived using equation 3.5 and is plotted versus wavelength in Fig. 3.1(c).

In order to determine the real index of refraction $n(\lambda)$ the Sellmeier model can be used. The Sellmeier model corresponds to a region where $\epsilon_2 \sim 0$ in the Lorentz model, i.e., $\Gamma \rightarrow 0$ in $L(E)$ $\propto 1/(E_0^2\text{-}E^2\text{-i}\Gamma E)$ using $E = hc/\lambda$ [173]:

$$\epsilon(\lambda) = \epsilon_1(\lambda) = n(\lambda)^2 = A + \sum_j \frac{B_j \lambda^2}{\lambda^2 - \lambda_{0,j}^2}, \tag{3.6}$$

where A and B_j represent analytical parameters used in data analysis. The one-pole Sellmeier dispersion formula, i.e., $j = 1$ in equation 3.6, gives satisfactory results for the dielectric materials under study. In Fig. 3.1(c) the refractive index $n_{op}(\lambda)$ of a TiO_2 layer is derived from the reflectivity and transmission curves shown in the inset using the fact that constructive interference occurs at $\lambda_m = 2l n_{op}(\lambda_m)/m$, with m a positive integer number (the interference maxima (minima) of the reflectivity curve are indicated by red (black) dots in the inset of Fig.

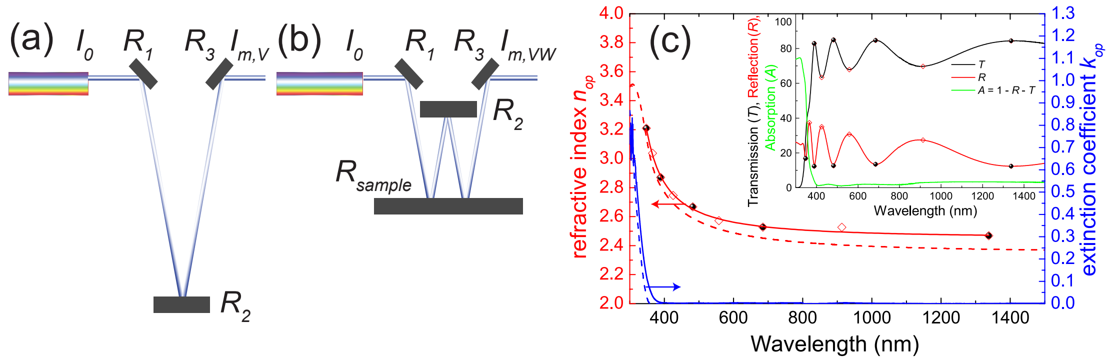

Figure 3.1: Schematic drawing of the (a) V-configuration used for calibration and the (b) V-W configuration used for absolute reflectivity measurements. (c) The blue (red) line corresponds to the imaginary (real) part of the refractive index of a TiO_2 layer derived from the transmission and reflectivity measurements shown in the inset using equations 3.5 and 3.6, respectively. Furthermore, the complex refractive index has been derived from ellipsometry measurements and is shown for comparison in red and blue dashed lines.

3.1(c)). The layer thickness l has been determined from a scanning electron microscope (SEM) image.

The complex refractive index $\tilde{n}$ and the layer thickness l can also be obtained by spectroscopic ellipsometry.[1] A SOPRA GES5E spectroscopic ellipsometer has been used to measure the amplitude ratio ψ and the phase difference Δ between s- and p-polarized light waves reflected on several thin dielectric layers (TiO_2, SiO_2, ZrO_2) deposited on a Si substrate.[2] WinElli II, a data analysis software of SOPRA, is used to model (ψ, Δ) in order to extract n_{op} and k_{op}, whereas for the infrared (IR) spectral range a modified Cauchy law is applied and several Lorentz peaks are added in the UV spectral range. Furthermore, (ψ, Δ) has been modeled by a software written by Georg Rossbach (LASPE-EPFL) and the extracted n_{op}, k_{op} values were in good agreement with those obtained from WinElli II. The experimental results for a thin TiO_2 layer are shown in Fig. 3.1(c) (dashed lines). A slight variation with respect to the values extracted from R and T measurements can be seen, which can be mainly attributed to the precision of the above-mentioned method. However, the former method is preferred to ellipsometric measurements due to impeded access to the ellipsometer (located in the cleanrooms of CMI) and time-consuming modeling.

3.1.2 Improvement of dielectric materials

Most of the dielectric materials employed in the DBRs presented in this work have been deposited by e-beam evaporation using a Leybold – Optics LAB 600 H at the center of Mi-

[1] A complete introduction to spectroscopic ellipsometry is given in Ref. [173].

[2] Si has been chosen as substrate because of its large refractive index n_{op} ~3.3 and the well known wavelength dependence of its complex refractive index.

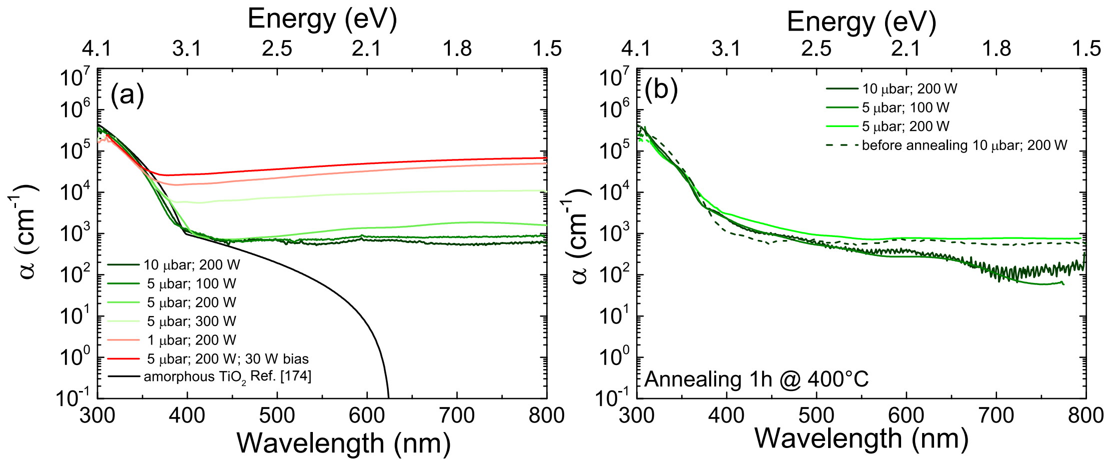

Figure 3.2: (a) Absorption coefficient as a function of the wavelength for TiO_2 layers deposited under different sputtering conditions. (b) The best layers in terms of reduced absorption in the near UV region have been annealed for 1h at 400°C.

croNanoTechnology (CMi) at EPFL. Optimization of materials and subsequent ellipsometric characterization have been done by Gatien Cosendey and Georg Rossbach (LASPE-EPFL), respectively.

Recently, a magnetron sputtering machine has been installed by Kenositec (KS 500 CONFOCAL) in the cleanroom facilities of our Institute. Deposition parameters have been optimized for TiO_2, SiO_2, and ZrO_2 layers to obtain a reduced absorption in the near UV spectral range. Fig. 3.2(a) shows the absorption coefficient, derived using the first method mentioned in section 3.1.1, of thin TiO_2 layers deposited under different conditions. In all cases depositions have been carrried out at RT and under an argon flux of 40 sccm. Different deposition pressures (1-10μbar), and forward powers (100 - 300 W), and the appliance of a RF bias at the substrate have been tested. The best conditions also in terms of deposition rate, which is about

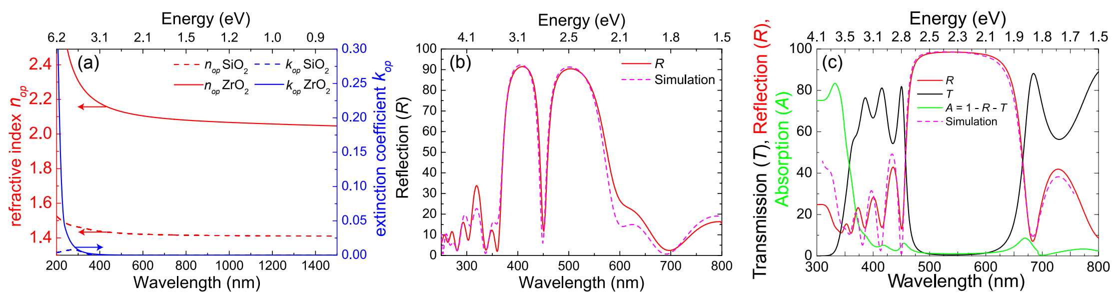

Figure 3.3: The blue dashed (red dashed) line and the blue solid (red solid) line correspond to the imaginary (real) part of the refractive index of SiO_2 and ZrO_2, respectively, derived from ellipsometry measurements. (b) Experimental (red line) and simulated reflectivity curve obtained using TMS (pink dashed line) of a $\lambda/2$ ZrO_2 cavity surrounded by a bottom 3 pair and a top 2 pair SiO_2/ZrO_2 DBR. (c) Reflectivity (R), transmission (T), and absorption (A) measured on a 6-pair SiO_2/TiO_2 DBR. The absorption is obtained through the relation $A = 1 - R - T$ and the simulated reflectivity spectrum by transfer matrix simulation.

0.02 nm/s for TiO_2, are achieved when layers are sputtered at 5 μbar and at a forward power of 200 W. For comparison the absorption coefficient of amorphous TiO_2 given in Ref. [174] is plotted in black. Furthermore, the effect of annealing at 400°C for 1h has also been tested (cf. Fig. 3.2) and improvements in the visible range can be highlighted. However, around 400 nm a slight increase of the absorption has been observed and thus annealing has not been introduced as a standard processing step. High-quality layers have been obtained for SiO_2 and ZrO_2 under the same conditions, i.e., 5 μbar and 200 W, leading to a deposition rate of 0.04 nm/s and 0.035 nm/s, respectively. The complex refractive index of SiO_2 and ZrO_2 layers derived from ellipsometry measurements is shown in Fig. 3.3. It can be seen that SiO_2 layers do not present any relevant absorption and that the absorption edge in ZrO_2 layers is only at ~ 270 nm, whereas in TiO_2 it occurs at around 360 nm. Thus, thanks to their reduced absorption, even in the UV spectral range, SiO_2 and ZrO_2 layers are commonly used as quarter-wave layers in top DBRs of non-resonantly optically pumped microcavities [104]. However, for electrically injected devices the SiO_2/TiO_2 bilayer system is preferred since it exhibits a larger refractive index contrast ($\Delta n_{op}/n_{op}$) of 46% (at 415 nm) with respect to 30% (at 415 nm) for SiO_2/ZrO_2 [18].

3.1.3 Dielectric DBRs

Dielectric DBRs obtained by e-beam evaporation present peak reflectivities over 99.5% when using a minimum number of 7 and 8 pairs for the SiO_2/TiO_2 and the SiO_2/ZrO_2 bilayer system, respectively [124]. A peak reflectivity of 99.3% has been achieved as well for a 7 pair SiO_2/TiO_2 DBR at 440 nm deposited by magnetron sputtering using optimized deposition parameters. However, so far, there was no need to exceed the 99.3% limit as the main goal was the achievement of green LDs (i.e., lasing beyond 500 nm). The latter have been achieved thanks to the deposition of SiO_2/TiO_2 DBRs onto the cleaved facets. For those DBRs a high reflectivity at 500 nm and a minimum at 450 nm was desired. Such requirements were met by a 6 pair SiO_2/TiO_2 DBR exhibiting a peak reflectivity of 98.5% as shown in Fig. 3.3(c). The reflectivity measurements have been performed in the V-W configuration. Note that the slight oscillations visible in the absorption curve, which has been calculated using the relation $A = 1 - R - T$, are due to the fact that transmission measurements are performed at perpendicular incidence, while the reflectivity spectrum is acquired at an incidence angle of ~ 7°.

So far no highly reflective SiO_2/ZrO_2 based DBRs have been achieved by magnetron sputtering. However, to test the material quality a low Q cavity has been deposited onto a double-side polished sapphire substrate. The reflectivity measurement performed in V-W configuration is depicted in Fig. 3.3(b). As it is the case for the SiO_2/TiO_2 DBR (cf. Fig. 3.3 (c)) the simulated reflectivity curve obtained by TMS matches well the measured reflectivity spectrum, which indicates a good knowledge of the optical layer properties and a limited impact of layer roughness.

3.2 High-quality III-nitride Bragg mirrors

3.2.1 An introduction to III-nitride DBRs

Nitride-based DBRs facilitate the fabrication of advanced nitride structures such as (i) RCLEDs, (ii) VCSELs, and (iii) microcavities for fundamental studies (e.g., strong coupling applications, Purcell enhancement,...). Different combinations can be found in the literature for the practical implementation of the latter: AlN/GaN-DBRs [175, 176], AlN-(In)GaN superlattice/GaN-DBRs [177], AlGaN/(Al)GaN-DBRs [178, 179], and InAlN/(Al)GaN-DBRs [101, 180].
The large lattice-mismatch offered by the AlN/GaN quarter-wave combination (~ 2.4%) results in a large build-up of tensile strain with increasing number of pairs, which eventually leads to cracks and threading dislocation generation. However, thanks to the introduction of strain relieving AlN/GaN superlattices into the AlN/GaN DBR, the first cw electrically injected VCSEL has been obtained at 77 K in 2008 [13].[3] This latter VCSEL was based on intracavity contacts as vertical electrical transport through nitride-based DBRs is quite challenging, due to the band offsets in the DBR lattice resulting into 2-dimensional electron gases that enhance the lateral conductivity and degrade largely the vertical one. Recently n-type doped AlGaN/GaN-DBRs based on a corrugated refractive index profile, i.e., on a sinusoidal composition profile, have been realized and a reasonable conductivity was achieved, making such DBRs interesting for electrically-driven devices [181]. Such an approach cannot be easily transposed to the InAlN/GaN system due to the challenges occurring in the growth of the quaternary material AlInGaN, namely non linear flows and strong growth temperature dependence. However, InAlN can be grown lattice-matched to GaN and thus DBRs combining the latter bilayers reveal outstanding results with regard to peak reflectivity and structural quality [101, 177], especially when grown on FS-GaN substrates [158]. Note that only recently the latter have been implemented successfully into a VCSEL structure [18]. In Fig. 3.4 the refractive index contrast ($\Delta n_{op}/n_{op}$) for $In_xAl_{1-x}N$ and $Al_xGa_{1-x}N$ layers deposited on GaN vs the in-plane lattice parameter mismatch is displayed. It can be seen that for nearly LM layers in the case of $In_xAl_{1-x}N$, corresponding to an In composition of ~ 0.2, a $\Delta n_{op}/n_{op}$ of ~ 7% can be achieved at a wavelength of 480 nm, whereas in the case of $Al_xGa_{1-x}N$ only values below 2% are within reach. Note that the values used to calculate $\Delta n_{op}/n_{op}$ for the $In_xAl_{1-x}N$ layers rely on equation 3.8, whereas for the $Al_xGa_{1-x}N$ layers a semiempirical formula, given by equation 3.7, achieved by Brunner *et al.* [182] on thick GaN and $Al_xGa_{1-x}N$ layers with x ranging between 0.11-1, has been used.
Furthermore, the LM system $In_{0.15}Al_{0.85}N/Al_{0.2}Ga_{0.8}N$ has been proven to provide crack-free highly reflective UV-DBRs exhibiting a peak reflectivity higher than 99% at a wavelength as short as ~ 340 nm [180]. The latter has been achieved thanks to a strain engineering solution relying on a short period GaN/AlN superlattice grown underneath a thick $Al_{0.2}Ga_{0.8}N$ layer. Considering microcavities, an $In_{0.15}Al_{0.85}N/Al_{0.2}Ga_{0.8}N$ DBR grown underneath an active medium based on bulk GaN or GaN/AlGaN MQWs proved to be a key element in III-nitride

[3]Note that cw operation at RT for almost the same VCSEL structure besides some improvements has been reported by the same group only 2 years later [15].

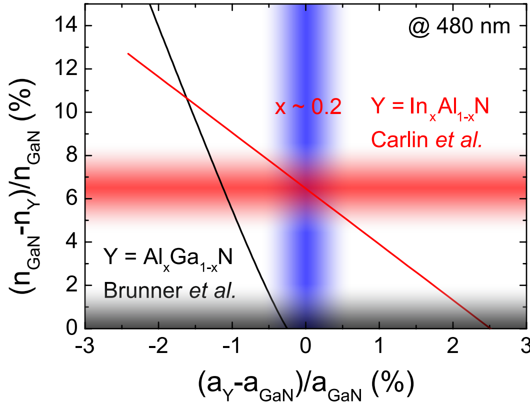

Figure 3.4: Refractive index contrast $(n_{\mathrm{GaN}} - n_Y)/n_{\mathrm{GaN}}$ vs in-plane lattice parameter mismatch $(a_{\mathrm{Y}} - a_{\mathrm{GaN}})/a_{\mathrm{GaN}}$ for Y = $\mathrm{In}_x\mathrm{Al}_{1-x}\mathrm{N}$ layers (red curve) [101] and Y = $\mathrm{Al}_x\mathrm{Ga}_{1-x}\mathrm{N}$ (black curve) [182] at a wavelength of 480 nm. The shaded areas correspond to the refractive index contrast of InAlN or AlGaN layers nearly LM to GaN, i.e., $|(a_{\mathrm{Y}} - a_{\mathrm{GaN}})|/a_{\mathrm{GaN}} < 0.5\%$.

microcavities to achieve polariton lasing [54, 55].

3.2.2 Optical properties of GaN and InAlN layers

The optical constants for GaN are well known thanks to experimental techniques such as transmission, photothermal deflection spectroscopy [182], and spectroscopic ellipsometry [183]. The real index of refraction of MBE grown $\mathrm{Al}_x\mathrm{Ga}_{1-x}\mathrm{N}$ layers in the entire range of composition ($0 \leq x \leq 1$) have been extracted from transmission and photothermal deflection spectroscopy below their bandgap energy by Brunner *et al.* [182]:

$$\begin{aligned}
&n_{op}(y) = (C(x) + A(x)y^{-2}(2 - (1+y)^{1/2} - (1-y)^{1/2})^{1/2}, \text{ where}\\
&C(x) = -2.2x + 2.66,\\
&A(x) = 3.17x^{1/2} + 9.98,\\
&y = h\nu / E_{g,Al_xGa_{1-x}N}, \text{ and}
\end{aligned} \tag{3.7}$$

$E_{g,Al_xGa_{1-x}N}$ is the bandgap energy of the alloy given in equation 1.8.[4] Experimentally-determined optical constants for InAlN layers LM to GaN are extremely scarce. The first report made by Carlin and Ilegems [101] when demonstrating the successful fabrication of highly reflective crack-free InAlN/GaN Bragg mirrors showed that the refractive index contrast ($\Delta n_{op}/n_{op}$) of $\mathrm{In}_x\mathrm{Al}_{1-x}\mathrm{N}$ to GaN is well fitted by a linear dependence with indium content within the 6-21% explored range, according to

$$\frac{\Delta n_{op}}{n_{op}} = 0.127 - 0.35x. \tag{3.8}$$

Furthermore, it was highlighted that the wavelength dependence of the refractive index of LM $\mathrm{In}_{0.17}\mathrm{Al}_{0.83}\mathrm{N}$ follows closely that of $\mathrm{Al}_{0.46}\mathrm{Ga}_{0.54}\mathrm{N}$, which is as well the AlGaN alloy having the same bandgap energy than $\mathrm{In}_{0.17}\mathrm{Al}_{0.83}\mathrm{N}$ [185]. Thus, its dispersion is given for $x = 0.46$ by equation 3.7.
Note that the lack of information on the optical constants and their wavelength dependence,

[4] Furthermore, the anisotropic dielectric function has been determined for AlN and GaN by spectroscopic ellipsometry in Ref. [184].

especially considering the extinction coefficient k_{op}, for InAlN layers in the region up to 25% of indium has been overcome only recently by variable-angle spectroscopic ellipsometry [186, 187].

3.2.3 LM InAlN/GaN DBRs grown onto different substrates

The growth of LM InAlN films on GaN is possible only under specific growth conditions. The main challenge arises from the huge difference in the growth temperature between AlN (~ 1100°C) and InN (~ 600°C). A typical growth temperature of ~ 800°C is chosen, which is a compromise between the reduced surface diffusion length of Al adatoms at lower growth temperatures and the increased In desorption at higher growth temperatures. The growth temperature is actually the key parameter in order to tune the indium content in the InAlN layers. In order to achieve LM conditions an In content of 17% is targeted for structures grown on *c*-plane sapphire substrates [188], whereas for structures grown on FS-GaN substrates a slightly higher In content of 18% is suited [189]. This discrepancy is ascribed to the different residual strain state of GaN buffer layers grown on the two types of substrate.

InAlN/GaN DBRs grown on *c*-plane sapphire are deposited on top of a 2 μm thick GaN buffer layer with a threading dislocation density (TDD) of the order of ~ 8-10 × 10^8 cm^{-2} using trimethyl-indium (TMIn) and trimethyl-aluminum (TMAl) as metal precursors for InAlN, triethyl-gallium (TEGa) as metal precursor for GaN, and NH_3. The InAlN and GaN growth temperature (rate) is 835°C ($T_{sapphire}$) (~ 140 nm/h) and 1065°C (~ 700 nm/h), respectively. N_2 is used as carrier gas for both GaN and InAlN layers. The growth rates are calibrated in a separate run performed prior to the DBR growth using $insitu$ reflectivity measurements to determine the thicknesses of thick InAlN and GaN layers. Such structures are well-suited for RC-LED applications [190]. However, the low thermal conductivity of the sapphire substrate together with large TDDs and an increased surface roughness (cf. Fig. 3.5) with respect to DBRs grown on FS-GaN substrates, make such structures suboptimal for the realization of VCSEL devices despite the achievement of a peak reflectivity above 99%.

The DBR growth parameters on *c*-plane FS-GaN substrates are exactly the same than those of DBRs grown on sapphire, except for a tuning of the InAlN growth temperature setpoint, due to the above-mentioned slight difference in the residual strain state of the buffer layer and the different thermal conductivity of the substrate. The latter has to be considered with great care, as the growth temperature is measured on the susceptor and thus is not the actual sample temperature. As a rule of thumb, InAlN layers LM to GaN have to be grown at $T_{sapphire}$ + 30°C ($T_{sapphire}$ + 40°C) onto single-side polished FS-GaN substrates (onto double-side polished FS-GaN substrates). They are deposited onto a 1 μm thick GaN buffer grown on two different kinds of FS-GaN substrates. The first substrate type exhibits a dislocation density of 4 × 10^7 cm^{-2} and is hereafter referred to as intermediate quality FS-GaN substrate. The second

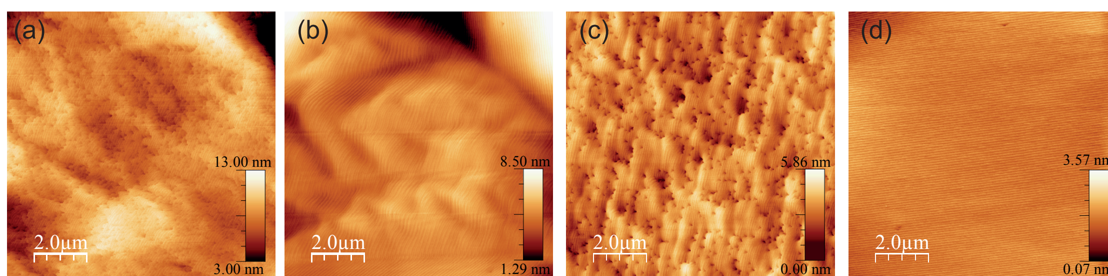

Figure 3.5: 10×10 μm^2 AFM scans of the final top GaN layer of LM InAlN/GaN DBRs grown onto a *c*-plane (a) sapphire substrate (courtesy of Nils A. K. Kaufmann (LASPE-EPFL)), (b) intermediate quality FS-GaN substrate (courtesy of Gatien Cosendey (LASPE-EPFL)), (c) and (d) high-quality FS-GaN substrate under slightly different growth conditions.

substrate, the so-called high-quality FS-GaN substrate, was achieved through epitaxial-growth with inverse-pyramidal pits and shows a reduced dislocation density amounting to 1×10^6 cm^{-2}.

In Figs. 3.5(a) - 3.5(d) 10×10 μm^2 AFM scans of the final top GaN layer of LM InAlN/GaN DBRs grown onto a *c*-plane sapphire substrate, an intermediate quality FS-GaN substrate, and two high-quality FS-GaN substrates are shown. Note that a slightly too high growth temperature (by only 10°C) might result into a high TDD which can be seen in Fig. 3.5(c) with respect to Fig. 3.5(d). A growth temperature rise of 10°C reduces the In content by about 2% and thus results in an increased tensile strain in the InAlN layers [191]. However, the rms roughness of the final top GaN layer is clearly reduced for DBRs grown onto high-quality FS-GaN substrates (0.65 nm for Fig. 3.5(c) and 0.24 nm for Fig. 3.5(d)) with respect to DBRs grown onto sapphire or intermediate quality FS-GaN substrates (1.49 nm for Fig. 3.5(a) and 1.1 nm for Fig. 3.5(b), respectively).

Probing the photonic disorder

In addition to standard structural characterization tools (namely AFM, scanning and transmission electron microscopies) the following characterization method has been used: on top of two 42 pair InAlN/GaN DBRs, one grown onto an intermediate quality FS-GaN substrate and the other onto a high-quality FS-GaN substrate (corresponding AFM images of the top GaN surface are shown in Figs. 3.5(b) and 3.5(c), respectively) a seven-pair ZrO_2/SiO_2 Bragg mirror has been deposited by electron beam evaporation resulting in $\lambda/2$ GaN-ZrO_2 cavities. Note that identical growth conditions were employed for the two DBRs except for a slight variation in the layer thicknesses resulting in a stopband shift of ~20 nm. However, the latter is not expected to affect the following analysis. The in-plane disorder of those test-microcavities, which is directly linked to the DBR structural and optical properties, has been probed through RT two-dimensional micro-transmission mappings using the continuous spectrum of a xenon lamp as incident light source. The light was focused down to a spot size ~2 μm in diameter

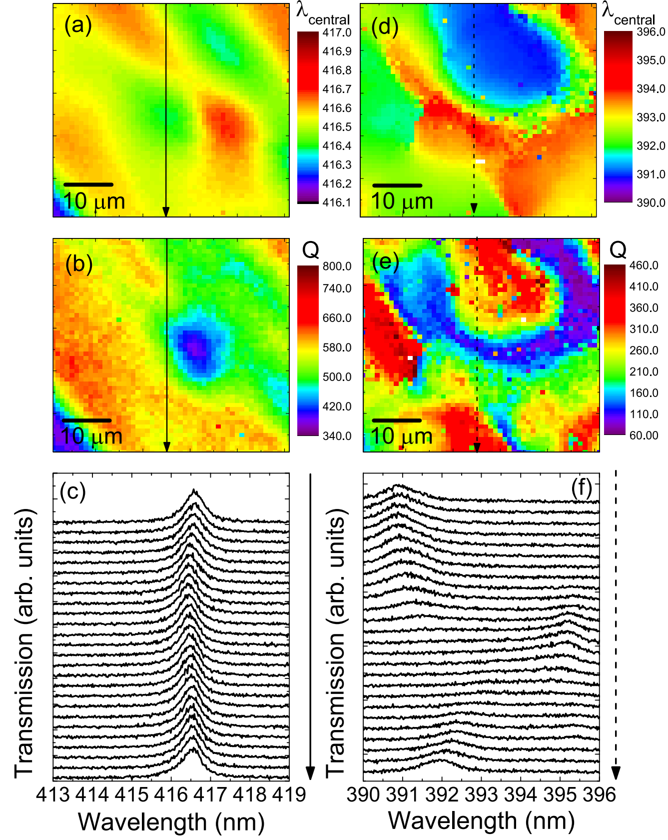

Figure 3.6: (a) and (d) micro-transmission mappings (50×50 μm^2) of the cavity mode wavelength, (b) and (e) corresponding cavity quality factor Q, and (c) and (f) transmission spectra recorded every 2 μm along the continuous and the dashed arrow on a cold GaN/ZrO_2 cavity formed on top of a DBR structure grown on a high-quality FS-GaN substrate (left-hand side column) and on an intermediate quality FS-GaN substrate (right-hand side column), respectively. Adapted from Ref. [191].

on the sample using a long working distance near UV microscope objective (× 100) with a numerical aperture (N.A.) of 0.5. The transmitted light was then collected by a UV optical fiber in far-field configuration ensuring an angular selection of ~ 0.6°. Transmission spectra of the cavities have been acquired every micron over a 50 × 50 μm^2 area (Fig. 3.6). For the DBR structure grown onto the low dislocation density substrate (Fig. 3.6, left-hand side column) a low photonic disorder is evidenced. The cavity mode position is fluctuating by ~ 0.45 nm (~0.1%) and can be related to cavity thickness changes of ~ 1 nm (cf. Fig.3.7(c)). The cavity mode radius a_p can be expressed using the FWHM of the beam divergence angle θ_{FWHM} [192]

$$a_p \approx \frac{\lambda_0}{2\theta_{FWHM}} = \frac{\lambda_0\sqrt{Q}}{4n_c}. \tag{3.9}$$

Q for the microcavity grown onto the high-quality FS-GaN substrate reaches values up to 800 (cf. Fig. 3.6(b)) matching those deduced from TMS (cf. Fig. 3.7(c)). Using equation 3.9 the cavity mode for the lowest Q factor (340) has a spatial extension of a_p ~ 830 nm, whereas a spatial extension a_p ~ 330 nm has been deduced from the measured beam divergence angle below threshold in the case of a VCSEL based on a LM InAlN/GaN DBR [18]. Thus, in the following the cavity mode is approximated by a square of lateral dimension of ~ 1 μm and the AFM map can be used to calculate the mean height map felt by the cavity mode (cf. Fig. 3.7(b)). Over an area of 10×10 μm^2 the mode feels changes in height by ~ ± 1 nm.

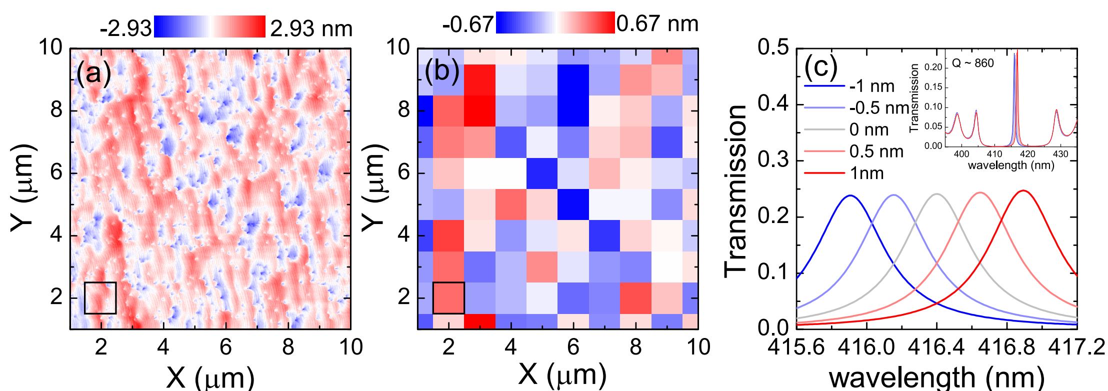

Figure 3.7: (a) 10×10 μm^2 AFM scans of the final top GaN layer of a 42 pair LM InAlN/GaN DBR grown onto a *c*-plane high-quality FS-GaN substrate and (b) the derived mean height map as felt by a cavity mode with a lateral extension of ∼ 1 μm indicated as black square. (c) Transmission spectra of the $\lambda/2$ GaN-ZrO_2 cavity obtained using transfer matrix simulation for thickness changes in the $\lambda/4$ GaN layer of 0, ± 0.5, and ± 1 nm. In the inset the demagnified transmission spectra are shown.

On the other hand, for the DBR structure grown onto the intermediate quality FS-GaN substrate, the photonic disorder is considerably increased. For the second test-microcavity structure, the Q factor only amounts to half that of the former one whereas an identical value is expected. Such an analysis clearly demonstrates that the dislocation density measured on the final top GaN layer does not play a major role for the achievement of samples characterized with a low photonic disorder. However, the dislocation density plays a crucial role for electrically driven devices. It was reported that the reduction in the TDD was essential for obtaining long-lived blue-violet EELDs [193]. The observed difference might originate from different polishing procedures used for the two kinds of substrates. For the intermediate quality FS-GaN substrate local offcut variations are present as can be seen by 10×10 μm^2 AFM scans (cf., e.g., Fig. 3.5(b)).
Note that the success in imaging dislocations by AFM, especially etch-type ones, is highly dependent on the tip used [194]. In order to conclude on the TDD of those DBRs efforts should be made to increase the size of these pits in order to be probed easily by AFM.

Further improvements

For information, the highest quality factor value obtained in our laboratory with a III-nitride microcavity has been observed in a 5λ cavity containing 3 $In_{0.15}Ga_{0.85}N$/GaN QWs based on a 50 pair bottom LM InAlN/GaN DBR grown on sapphire and a 20 pair top SiO_2/Si_3N_4 DBR. Using microphotoluminescence (μ-PL) a Q value of 6400 has been measured [114]. However, for practical applications such as VCSELs and polariton LDs such a high quality factor is not required and has even a detrimental impact considering the outcoupling of the emission. Thus, if a differential efficiency of 50% is desired, the output mirror transmission must be about equal to 0.5% [87].

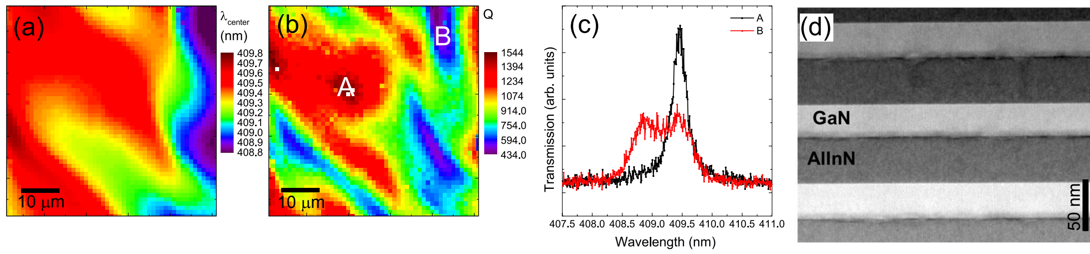

Figure 3.8: (a) Micro-transmission mappings (50×50 μm^2) of the cavity mode wavelength, (b) corresponding cavity quality factor Q, and (c) the transmission spectra of regions A and B. (d) Detailed HAADF STEM cross-section view of InAlN/GaN interfaces in DBRs (courtesy of Dr. Guillaume Périllat-Merceroz (LASPE-EPFL)).

In Figs. 3.8(a)-3.8(c) the results of the micro-transmission mapping, acquired under the above described conditions on a $\lambda/2$ GaN-TiO_2 cavity are shown. The $\lambda/2$ GaN-TiO_2 cavity is based on a bottom 42 pair InAlN/GaN DBR (the corresponding AFM image of the top GaN surface is shown in Fig. 3.5(d)) grown onto a high-quality FS-GaN substrate and a top seven-pair TiO_2/SiO_2 Bragg mirror. Note that such a mirror configuration has been successfully used to achieve the first InAlN-based VCSEL [18]. As for the $\lambda/2$ GaN-ZrO_2 cavity the mode position is fluctuating by only ~ 0.5 nm (0.1%) thanks to the small rms surface roughness of the top GaN surface (Fig. 3.5(d)). However, the increased $\Delta n/n$ value with respect to the SiO_2/ZrO_2 bilayer system, leads to higher quality factors (cf. Fig. 3.8(b)). Although, regions with low quality factor are observed as well. In the transmission spectra corresponding to such regions typically two cavity modes are observed (cf. Fig. 3.8(c)). However, those region are outnumbered by large regions exhibiting high quality factors up to ~ 1500. Note that we do not reach a value up to 3800 as expected from transfer matrix simulations. The latter might be due to rough InAlN/GaN interfaces leading to layer thickness fluctuations. In Fig. 3.8(d) a high angle annular dark field scanning transmission electron microscope (HAADF STEM)[5] cross section view of an InAlN-based DBR clearly shows the presence of dark lines at the InAlN/GaN interfaces, suggesting the presence of thin indium poor layers. Phase separation of the InAlN and uncontrolled desorption of material might occur when growing GaN at a temperature (~ 1050°C) above the thermal stability of LM InAlN, which is about 960°C [195]. To circumvent this drawback, Sadler *et al.* proposed two solutions for the growth of GaN layers used in DBRs [196]. The GaN layer can be grown at the growth temperature of InAlN but this results into a top surface with large undulations unsuitable for DBRs. The second approach relies on the low temperature growth of a thin GaN sublayer followed by a temperature ramp and the subsequent growth of GaN at high temperature. This latter method seems much more promising since it should not alter the GaN surface morphology (smooth layers as shown in Fig. 3.5(d) are expected) while preventing the InAlN desorption at each InAlN/GaN interface. Thus, the overall quality of InAlN-based DBRs is expected to be improved. The implementation of this technique has not yet been realized in our laboratory but is foreseen for the growth of forthcoming DBR samples.

[5]An annular dark field image sampled in a STEM is highly sensitive to variations in the atomic number of atoms in the sample (Z-contrast images).

3.3 Design of microcavities

This section is devoted to the design of InGaN/GaN MQW based planar MC structures suitable for strong coupling studies under non-resonant optical pumping. We first detail the requirements in terms of QW absorption features, N_{QW} value per antinode, and optical cavity length for achieving the strong coupling regime in InGaN/GaN MQW-based semi-hybrid and full-hybrid MCs by combining envelope function calculations and TMS, which leads to two corresponding optimum structure designs. Note that we will not consider monolithic MC designs due to disadvantages like time-consuming growth, narrow stopband width of the III-nitride based DBRs and consequent difficult spectral alignment of the top DBR with respect to the bottom one. Furthermore, high absorption occurring in such top DBRs at the pump wavelength of the excitation laser is highly detrimental.

3.3.1 Semi-hybrid and full-hybrid approach

In order to properly design an InGaN/GaN MQW based planar MC suitable for strong coupling studies, the requirements resulting from envelope function calculations, TMS and fabrication challenges should all be considered. Among the first straightforward elements to consider, we can cite the bottom and the top DBRs, as well as the central wavelength of the targeted MC structure.

Crack-free high-quality nearly LM InAlN/GaN DBRs grown on *c*-plane FS-GaN substrate constitute an ideal template for the growth of the active region. On the other hand dielectric DBRs are usually preferred as top DBR because they are much less time-consuming than epitaxial mirrors in terms of fabrication while presenting a large stopband, low residual absorption at the pump wavelength of the excitation laser (typically 244, 266, and 355 nm) and a high peak reflectivity, typically well in excess of 99%, for a limited number of pairs due to the large refractive index contrast of the bilayer constituents. With respect to the low residual absorption at the pump wavelength of the excitation laser the SiO_2/ZrO_2 combination is preferred whereas for structures based on electrical intracavity contacts one might rather consider the SiO_2/TiO_2 bilayer system since it exhibits a very large refractive index contrast (cf. section 3.1.2).

The nature and the geometry of the MQW active region are obviously critical when it comes to RT strong coupling applications due to the stringent requirements the former should fulfill to ensure that cavity polaritons are still robust quasiparticles. Because RT residual absorption in the LM InAlN/GaN DBR is expected to significantly increase for energies larger than 3.3 eV due to the subbandgap absorption occurring in the bilayer constituents (cf. Fig. 3.9), the $In_xGa_{1-x}N$/GaN QWs should be designed such that their excitonic QW absorption lies well below this value. A 300 meV safety margin appears as a reasonable trade-off, hence leading to a maximum value for the absorption peak of ~ 3.0 eV, i.e., ~ 413 nm. Thus in order to minimize the impact of the QCSE, 2 nm thick $In_{0.1}Ga_{0.9}N$ wells surrounded by 3 nm thick GaN barriers have been chosen since their emission energy also closely matches that of a cavity mode centered at 3.0 eV.

Table 3.1: Comparison between the semi-hybrid and the full-hybrid approach.

	Bottom DBRs		
	LM InAlN/GaN	SiO_2/ZrO_2	SiO_2/TiO_2
L_{DBR} at 3 eV (nm)	473	81	53
Absorption edge (eV)	3.29	4.59	3.31

Such a geometry is much easier to handle than full-hybrid MC structures for which the required extra processing steps, like substrate removal and flip-chip, are known to affect the fabrication yield. However, a full-hybrid approach presents also some advantages with respect to the above-described semi-hybrid approach: (i) the mirror penetration depth (L_{DBR}) is much shorter and (ii) very low In content QWs can be chosen as absorption in the near UV spectral region is not an issue for dielectric Bragg mirrors (i.e., SiO_2/ZrO_2 DBRs). The bottom mirror penetration depth L_{DBR} given by equation 1.28 for the semi-hybrid approach is increased by a factor 6 or 9 with respect to the full-hybrid approach relying on a SiO_2/ZrO_2 or a SiO_2/TiO_2 bottom DBR, respectively (cf. Table 3.1). We can estimate the maximum reflectivity (R_{max}) achievable with Bragg mirrors using the relationship [197]:

$$R_{max}(E) = 1 - \alpha(E) L_{DBR}(E). \tag{3.10}$$

For strong coupling regime and VCSELs it is desirable to have mirrors characterized by a $R_{max} > 98.5\%$ [87]. Thus, using equation 3.10 one can calculate the limit of the admitted DBR absorption (cf. red lines in Fig. 3.9). As long as the DBR absorption stays below this limit, highly reflective mirrors can be obtained. From Fig. 3.9 it can be deduced that below a wavelength of 377 nm (375 nm) this is not anymore the case for the LM InAlN/GaN DBR (SiO_2/TiO_2 DBR, respectively). The latter values are listed in Table 3.1 under absorption edge. Consequently, for UV applications requiring high reflectivity mirrors, the development of LM AlGaN–InAlN reflectors is a better option, whereas in the case of the full-hybrid approach the bottom DBR has to be exchanged with a SiO_2/ZrO_2 one.

In order to bring useful insights into the way to achieve the strong coupling regime with InGaN-based MC structures, TMS have been performed for the semi-hybrid and the full-hybrid approach (cf. section 3.3.4). Note that for both approaches, in order to compare the latter, the same QW structure has been chosen, i.e., 2 nm thick $In_{0.1}Ga_{0.9}N/GaN$ QWs

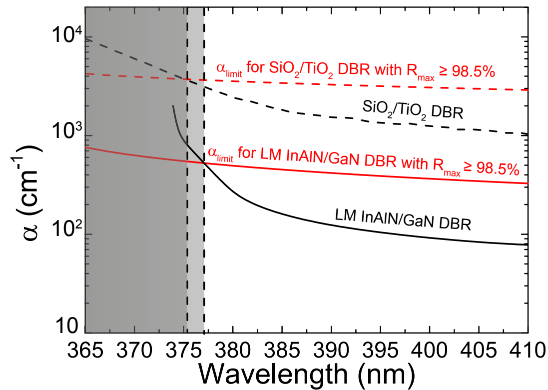

Figure 3.9: Absorption vs. wavelength in a 40-pair LM InAlN/GaN DBR (adapted from Ref. [197]) and in a 7-pair SiO_2/TiO_2 DBR only taking into account the absorption occurring in the TiO_2 layers (black lines). α_{limit} (red lines) indicates the wavefunction dependent limit in which highly reflective mirrors with $R_{max} \geq 98.5\%$ can be obtained, as long as the DBR absorption stays below it.

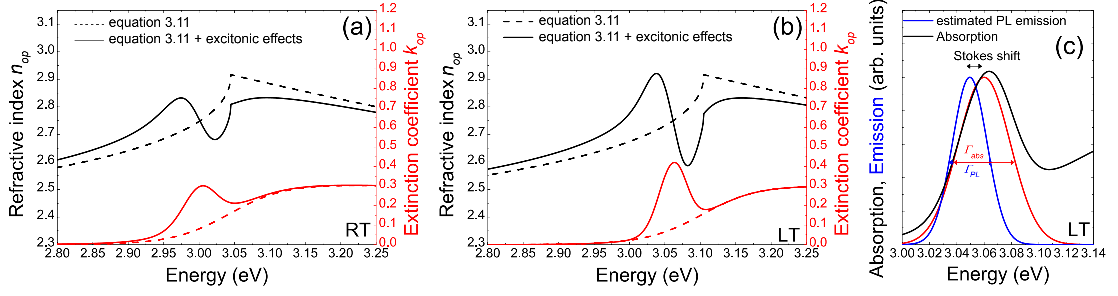

Figure 3.10: (a) The black (red) dashed line corresponds to the real (imaginary) part of the refractive index of an $In_{0.1}Ga_{0.9}N$ layer at RT approximated by shifting the refractive index of GaN according to the band-gap energy of the alloy as proposed by Bergman and Casey [198] (cf. equation 3.11). For the black (red) line excitonic effects are included and the latter refractive index dispersion is used in TMS. (b) Same as (a) for the LT case (T = 10 K). (c) The absorption (black line) of the InGaN layer is deduced from the extinction coefficient k shown in (b) and the corresponding excitonic emission lineshape (blue line) is estimated using the approach developed by F. Yang *et al.* [199]. Adapted from Ref. [200].

surrounded by 3 nm thick GaN barriers. TMS *a priori* require reliable optical constants for all the materials at play. The optical constants for selected dielectric materials (SiO_2, TiO_2, and ZrO_2) and the III-nitride compounds GaN and InAlN have been given in the previous sections (cf. sections 3.1.2 and 3.2.2, respectively). However, so far we have not discussed the optical constants of InGaN QWs.

3.3.2 Optical properties of InGaN layers

Experimentally-determined optical constants for InGaN layers are extremely scarce or even not existing in the case of InGaN layers grown on FS-GaN substrates due to the lack of thick high-quality layers. In order to determine the dielectric function of the latter by ellipsometry sufficiently thick layers need to be grown. The heteroepitaxial nature of those epilayers (InGaN layers grown on GaN) implies a trade-off between the layer thickness and its quality. Indeed, the latter should significantly decrease beyond a certain critical thickness, as pseudomorphic growth could not hold anymore and relaxation of misfit strain via plastic deformation, mainly generating misfit dislocations, inevitably occurs (cf. section 4.2.1).

The refractive index dispersion of the $In_xGa_{1-x}N$ alloy is approximated by shifting the refractive index of GaN (cf. equation 3.7) according to the bandgap energy of the alloy such as proposed by Bergman and Casey [198]:

$$n_{In_xGa_{1-x}N}(E) \sim n_{GaN}(E - (E_{g,In_xGa_{1-x}N} - E_{g,GaN})), \tag{3.11}$$

where $E_{g,In_xGa_{1-x}N}$ is the bandgap energy of the $In_xGa_{1-x}N$ alloy given in equation 1.8.

For direct bandgap semiconductors the absorption coefficient $\alpha(E)$ at zero temperature is

derived from the joint density of states and thus depends on the dimensionality of the system. Using the effective-mass approximation [170]:

$$\begin{aligned}\alpha_{2D}(E) &= \frac{e^2}{2\epsilon_0 c n_{op}\hbar}\left(\frac{\mu^*}{m_0}\right) f_{osc}\Theta(E-E_g) = \alpha_{0,2D}\Theta(E-E_g-e_1-hh_1),\\ \alpha_{3D}(E) &= \frac{e^2\sqrt{m_0}}{\sqrt{2}\pi\epsilon_0 c n_{op}\hbar^2}\left(\frac{\mu^*}{m_0}\right)^{3/2} f_{osc}\sqrt{E-E_g}\Theta(E-E_g) = \alpha_{0,3D}\sqrt{E-E_g}\Theta(E-E_g),\end{aligned} \tag{3.12}$$

where $\Theta(E)$ corresponds to the step function and the oscillator strength of the optical transition f_{osc} is determined by the momentum matrix element P_{CV}, i.e., [170]

$$f_{osc} = \frac{2|P_{CV}|^2}{m_0 E}. \tag{3.13}$$

The momentum matrix element can be written as a function of the Kane element P [170]:

$$|P_{CV}|^2 = \frac{m_0^2 P^2}{3\hbar^2} = m_0 \frac{m_0/m_e^* - 1}{6}\frac{E_g + \Delta}{1 + \frac{2\Delta}{3E_g}}, \tag{3.14}$$

where Δ is the split-off hole energy. Note that in those expressions excitonic effects are not taken into account. Moreover, the absorption is modified at finite temperatures by the Fermi-Dirac distribution (cf. equation 2.58). Hereafter, we will only consider small displacements from the equilibrium of the semiconductor, i.e., the two quasi-Fermi levels lie within the bandgap, and the modification of the absorption coefficient can be considered as a first approximation independent of energy [128]. However, once the energy separation between the two quasi-Fermi levels exceeds the bandgap, photon amplification takes place (the Bernard-Duraffourg condition is fulfilled) and thus the absorption is strongly modified.
In order to account for the band-to-band absorption (α_{BB}) a broadened sigmoid profile is commonly convoluted to the α_{2D} given by equation 3.12 [201, 202]:

$$\alpha_{BB}(E) = \frac{\alpha_0}{1 + \exp(\frac{E_{g,In_xGa_{1-x}N} - E}{\Delta E})}, \tag{3.15}$$

where the broadening parameter ΔE is equivalent to the Urbach tail energy. We display in Figs. 3.10(a) and 3.10(b) the complex refractive index dispersion of a low In content two dimensional InGaN layer at RT and LT (dashed lines), respectively. As the bandgap changes with temperature the dispersions are blueshifted by ~ 60 meV (cf. Table 1.2). For the band-to-band absorption the broadened sigmoid profile given by equation 3.15 is used with a broadening parameter ΔE of 40 meV taken from the values found by R. W. Martin *et al.* [202] for low In content InGaN epilayers emitting at 3.0 ± 0.1 eV.[6]

[6] A similar broadening parameter is found for 100 nm thick InGaN bulk layers grown on FS-GaN substrates emitting at ~ 3 eV (cf. section 4.3.6).

3.3.3 Optical properties of InGaN layers including excitonic effects

In order to include excitonic effects, the dispersion of the refractive index given in the previous section is modified in the following way: an excitonic transition at RT might be represented by a Voigt profile superimposed to the band-to-band absorption edge and energetically separated by the exciton binding energy. The Voigt profile of the excitonic transition is the convolution of a homogeneous line ($\epsilon_{hom}(\omega)$ = Lorentzian) of a given FWHM Γ_h and an inhomogeneous line ($g(\omega')$ = Gaussian) of FWHM Γ_{inh} [96, 102]:

$$\begin{aligned}
&\epsilon(\omega) = (n_{op}(\omega) - ik_{op}(\omega))^2 = \int \epsilon_{hom}(\omega-\omega')g(\omega')d\omega', \\
&\text{with } \epsilon_{hom}(\omega) = \epsilon_\infty + \frac{f_{osc}^{QW}}{S}\frac{e^2\hbar^2}{[(l_W\epsilon_0 M)(\omega_0^2-\omega^2+i\omega\Gamma_h/2)]} \text{ in the 2D case,} \\
&\text{and } \epsilon_{hom}(\omega) = \epsilon_\infty + \frac{f_{osc}^{bulk}}{V}\frac{e^2\hbar^2}{[(\epsilon_0 M)(\omega_0^2-\omega^2+i\omega\Gamma_h/2)]} = \epsilon_\infty + \frac{4\pi\alpha_{X_A}\omega_0^2}{[\omega_0^2-\omega^2+i\omega\Gamma_h/2]} \text{ in the 3D case ,}
\end{aligned} \tag{3.16}$$

where $\epsilon_\infty = n_{op}^2(\omega)$ (i.e., the dispersion without excitonic effects given by equation 3.11) is the background dielectric constant, M is the exciton effective mass equal to $m_e^* + m_h^*$, ω_0 is the pulsation of the excitonic resonance, f_{osc}^{QW}/S is the excitonic QW oscillator strength per unit surface, and f_{osc}^{bulk}/V is the excitonic bulk oscillator strength per unit volume. Note that f_{osc}^{bulk}/V can be shown to be $f_{osc}/\pi a_{B,3D}$ [203]. In the 2D case depending on the wave-function overlap the oscillator strength is expected to be enhanced with repect to the 3D case [203]:

$$\frac{f_{osc}^{QW}}{S} = \frac{4|P_{CV}|^2\mathscr{P}_{QW}^2}{m_0 E}\frac{1}{\pi a_{B,3D}}, \tag{3.17}$$

where $\mathscr{P}_{QW}$ is the overlap integral between electron and hole envelope wave-functions. Note that using such an approach, we do not take into account the Sommerfeld or Coulomb enhancement factor, which increases the absorption coefficient $\alpha_{3,2D}$ given by equation 3.12 even above the band edge [170, 201].

The excitonic Voigt profile separated by an exciton binding energy of ~ 45 meV deduced from envelope function calculations (cf. Fig. 1.3(b)) is superimposed to the band-to-band absorption edge. For the homogeneous line broadening a value of 25 meV, corresponding to the RT case [113], and an inhomogeneous line broadening of 45 meV have been chosen.[7] Thus, in Figs. 3.10(a) and 3.10(b) the complex refractive index dispersion of a low In content two dimensional InGaN layer including an excitonic transition is displayed for the RT and LT case (solid lines), respectively.

3.3.4 Modeling: Transfer matrix simulations

As already mentioned the light-matter coupling strength scales like $\sqrt{N_{QW}^{eff}/L_{eff}}$ (cf. equation 1.37) [92]. Therefore, it is of interest to map the evolution of Ω_{VRS} by TMS for different

[7] We emphasize that the value of 45 meV has been derived following the approach reported by F. Yang *et al.* [199], as explained in the section, by considering the FWHM of the emission line of a single $In_{0.1}Ga_{0.9}N$/GaN QW acquired at LT and under low excitation, which amounts to ~ 32 meV (cf. section).

geometries of the active medium for the semi-hybrid and the full-hybrid approach (cf. section 3.3.1). Ω_{VRS} has thus been calculated for a given number of QWs ($N_{QW/AN}$), ranging from 1 to 14, which is repeated at each cavity light field antinode, the latter also ranging from 1 to 14 (N_{max}) (Figs. 3.11(a) and 3.11(b)). We point out that except for the QWs the imaginary part of all the remaining optical layers has been neglected as the operating wavelength of the microcavity is targeted at an energy located about 500 meV below the absorption edge of GaN (even more in the case of LM InAlN layers).

Simulations are first performed for a negligibly small inhomogeneous broadening Γ_{inh} (< 1 meV) of the QWs, a homogeneous broadening Γ_h of 25 meV and an oscillator strength $f_{osc} \sim 1.3\times10^{13}$ cm^{-2}. Note that for narrow GaN (1.2 nm)/$Al_{0.2}Ga_{0.8}N$ (3.6 nm) MQWs a value of $f_{osc} \sim 2.1\times10^{13}$ cm^{-2} has been previously determined [70]. As can be seen in Fig. 1.3(b), the wavefunction overlap in a 2 nm thick $In_{0.1}Ga_{0.9}N$/GaN SQW is reduced by almost a factor of 2 compared to the 1.2 nm thick GaN/$Al_{0.2}Ga_{0.8}N$ SQW. However, for the 2 nm thick $In_{0.1}Ga_{0.9}N$/GaN MQW structure the reduction in the wavefunction overlap is less drastic and amounts to a factor of ~ 1.26 (cf. Fig. 1.3(b)). Thus employing a value of ~ 1.3×10^{13} cm^{-2} for f_{osc} in TMS appears as a reasonable choice for the present MQW geometry. At this stage, it is worth pointing out that MC structures with $N_{QW} \geq 35$, i.e., structures corresponding to the upper right part in Figs. 3.11(a) and 3.11(b) (cf. white dashed lines), are expected to suffer from strain relaxation. Indeed in section 4.2.2 we highlight that in the case of $In_{0.12}Ga_{0.88}N$ (2 nm)/GaN (3 nm) MQWs grown on FS-GaN beyond a critical number of QWs of ~ 30, a pronounced increase in the inhomogeneous linewidth broadening was observed by means

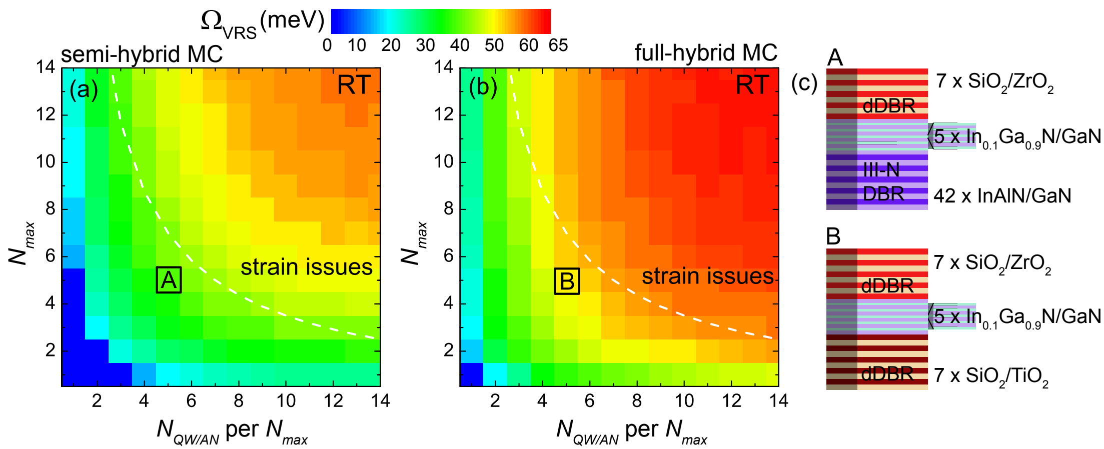

Figure 3.11: Normal mode splitting Ω_{VRS} calculated by TMS for microcavities based on a bottom (a) 42 pair InAlN/GaN DBR (semi-hybrid approach) and (b) 7 pair SiO_2/TiO_2 (full-hybrid approach). For both approaches a 7 pair SiO_2/ZrO_2 top DBR, and different geometries for the active medium assuming a homogeneous broadening $\Gamma_h = 25$ meV and an oscillator strength $f_{osc} = 1.3\times10^{13}$ cm^{-2} have been considered. N_{max} is the number of cavity light field antinodes, which is proportional to the physical cavity length L_{cav}, whereas $N_{QW/AN}$ is the number of InGaN(2 nm)/GaN(3 nm) QWs positioned at each antinode. (c) A schematic drawing of the most adapted structures surrounded by black squares in (a) and (b) is shown.

of microphotoluminescence (μ-PL) measurements. As a result, for both approaches and for a negligibly small Γ_{inh} value the most adapted structure deduced from our TMS in terms of Ω_{VRS} value would be composed of 5 antinodes with 5 QWs. In such a case, a normal mode splitting of 36 meV (49 meV) is obtained for the semi-hybrid MC (full-hybrid MC, respectively). The increased mode splitting in the full-hybrid MC structure can be readily explained by a reduced effective cavity length ($L_{eff,FH}$ ~ 624 nm)[8] with respect to the semi-hybrid MC structure ($L_{eff,SH}$ ~ 1044 nm). Note that for a $L_{eff,SH}/L_{eff,FH}$ ratio of ~ 1.7 a VRS ratio of ~ 0.77 is expected when using a simple proportionality rule $\Omega_{VRS,SH}/\Omega_{VRS,FH} \sim (L_{eff,SH}/L_{eff,FH})^{-1/2}$. However, a VRS ratio of 0.73 is found from TMS. The difference might be attributed primarily to the dependence of the mode splitting on Γ_h and γ_c (cf. equation 1.39). Furthermore, the expression of the mirror penetration depth has been derived for an infinite number of quarter-wave pairs.
Now, in order to derive the expected features of a cavity having a realistic active region, the impact of the inhomogeneous broadening of the excitonic transition on the absorption has to be accounted for. Previously, such calculations performed for a GaN/AlGaN MQW based MC led to a good agreement with experimental data [113]. The evolution of the cavity absorption spectrum at zero cavity photon - exciton detuning as a function of Γ_{inh} for the two most adapted structures depicted in Fig. 3.11(c) has been calculated in a similar fashion and are displayed in Figs. 3.12(a) and 3.12(b). As mentioned above, for low Γ_{inh} values compared to Ω_{VRS}, the normal mode splitting remains almost unaffected and is equal to 36 meV (49 meV). Once Γ_{abs} matches Ω_{VRS}, which occurs for Γ_{inh} = 19 meV (Γ_{inh} = 34 meV) when using equation 4.4, a progressive collapse of the normal mode splitting with increasing Γ_{inh} values is observed until it is completely lost. To be more quantitative two absorption peaks can still be resolved, i.e., there is a well defined minimum between the peaks up to a Γ_{inh} value equal to ~ 46 meV (region III in Fig. 3.12(a)) (~ 65 meV (region III in Fig. 3.12(b))). Note however that the corresponding PL spectra show hardly separable peaks for Γ_{inh} values larger than 36 meV (49 meV) (cf. horizontal white dashed line in Fig. 3.12(a) and Fig. 3.12(b), respectively) as depicted in Fig. 3.12(c). To obtain those PL spectra, we assumed that they possess a thermal lineshape and hence they are given by the absorption spectra multiplied by a Boltzmann occupancy factor [113, 204].

From the previous analysis, the following conclusion can be drawn: considering the semi-hybrid approach the strong coupling regime might be observable at RT up to a Γ_{inh} value of 46 meV by means of linear spectroscopy techniques such as absorption, reflectivity or transmission measurements, whereas for the full-hybrid approach the latter observation might be possible up to a Γ_{inh} value of 65 meV. Switching now to PL measurements, the discrimination of the upper polariton branch (UPB) might not be possible anymore for Γ_{inh} values larger than 36 meV (49 meV). However, the mode coupling is not yet completely lost at this point and polaritonic features such as non-parabolic mode dispersion and polariton lasing might still be observable by means of RT PL measurements. Thus we estimate that the critical value for Γ_{inh} that would still be compatible with the observation of the strong

[8] Equation 1.25 has been used to calculate the effective cavity length.

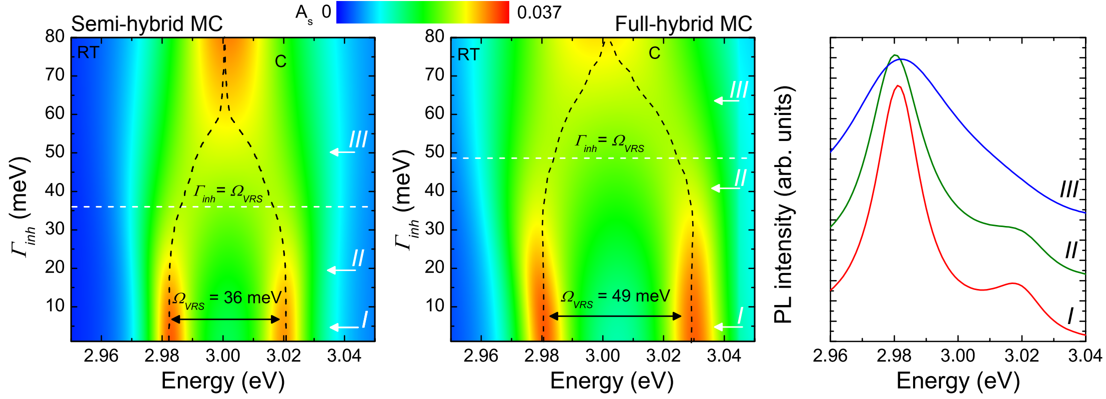

Figure 3.12: (a) and (b) Simulated absorption spectra at zero cavity photon - exciton detuning as a function of Γ_{inh} for the structures surrounded by the black square in Figs. 3.11(a) and 3.11(b), respectively, i.e., 3λ cavities containing 5 QWs at each antinode. (b) RT PL spectra deduced from absorption spectra, corresponding to the arrows I–III shown in (a), by using a Boltzmann occupancy factor.

coupling regime amounts to 46 meV for the semi-hybrid approach and to 65 meV for the full-hybrid approach. In conclusion, the critical value for Γ_{inh} of a full-hybrid MC structure with respect to a semi-hybrid MC structure is increased by a factor of 1.41. Thus, in the next chapter we will have a closer look at InGaN/GaN MQWs with the aim to estimate Γ_{inh}, the inhomogeneous absorption line broadening.

3.4 Summary of the results

The optical and structural properties of dielectric and III-nitride based Bragg mirrors have been discussed. A new kind of characterization method for III-nitride Bragg mirrors has been implemented: a dielectric DBR has been deposited directly on top of the latter resulting in a passive MC. Probing the photonic disorder of such a MC provides information about the crystalline quality of the III-nitride DBR. For mirrors grown on high-quality FS-GaN substrate a low photonic disorder has been measured. Note that such a low photonic disorder is crucial for both strong coupling applications and VCSELs.
Using envelope function calculations and TMS, the requirements in terms of QW absorption features (Γ_{inh}), N_{QW} per antinode, and the optical cavity length for achieving the strong coupling regime in InGaN/GaN-based MCs have been investigated for two structure designs: a semi-hybrid and a full-hybrid approach. For the semi-hybrid MC a critical value of Γ_{inh} equal to 46 meV has been found to maintain the SCR, while 65 meV is the limit for the full-hybrid MC.

4 Active medium: Low In content InGaN/GaN QWs and InGaN bulk layers

Since the first realization of an efficient blue LED based on InGaN/GaN QWs in the mid-nineties by S. Nakamura and co-workers [7] the number of publications related to the InGaN alloy is increasing continuously. Even though several technical breakthroughs such as the commercialization of blue LEDs and LDs have seen the light of day, their most crucial component, the active medium, remains not fully understood. One of the main questions preoccupying the III-nitride LED and LD communities nowadays is related to the nature of the carrier localization process in such QWs.
However, before addressing this issue, growth and strain relaxation aspects have to be considered. In particular, strain accumulation and consequent relaxation processes prove to be detrimental for strong coupling applications. In addition, the relationship existing between absorption linewidth, emission linewidth, and localization energy is crucial for these latter applications but for conventional LDs as well. Therefore, an absorption-like technique, namely the photoreflectance (PR) spectroscopy, has been introduced, allowing to probe intrinsic electronic properties from cryogenic to RT. Furthermore, comparisons to the GaN/AlGaN QW system are drawn in order to conclude on the stringent requirements for the observation of the strong coupling regime as deduced from TMS in the previous section.
Complementary, InGaN bulk layers grown on high-quality FS-GaN substrates have also been characterized in order to better understand some of the observed features in temperature-dependent PR spectra acquired on InGaN/GaN MQWs. These layers allow investigating in a careful way the localization mechanisms. Eventually, experimental results are compared to a model based on a stochastic distribution of indium atoms at the atomic scale.

4.1 Low indium content InGaN/GaN QWs grown onto different substrates

Over the past two decades various growth conditions of MOVPE grown InGaN/GaN QWs have been investigated. The very high equilibrium vapor pressure of nitrogen over InN which is several orders of magnitude higher than that over AlN or GaN, prohibits any In incorporation

under typical GaN growth conditions (~ 1000°C, ~ 200 mbar) [205]. Note that the same incorporation efficiency may be obtained at about 500°C for In and Ga [206]. Unfortunately, the crystalline quality of layers grown at such a low temperature is limited. Furthermore, the NH_3 cracking efficiency becomes small. Therefore, InGaN/GaN QWs are typically grown between 700 and 900°C. Several studies have been done on the effect of the barrier temperature growth. Kumar *et al.* [207] reported that GaN barriers grown at temperatures below 800°C exhibit defects and In inclusions. Thus, temperature ramp-ups for the barrier growth have shown to improve the maximum output power of green LEDs [208] and to sharpen the interfaces of capped $In_{0.1}Ga_{0.9}N$/GaN SQWs [209].[1] However, the latter SQWs exhibit a broad RT PL linewidth (FWHM) of > 27 nm (195 meV) at 414 nm (3 eV) and to our knowledge such studies have not yet been published for QWs emitting at the same wavelength but with a state of the art linewidth broadening of ~ 11 nm (80 meV). Furthermore, if no In droplets are present such temperature ramps are not expected to improve considerably the homogeneity of the QWs and thus the FWHM of the absorption line, which is one of the parameters of interest to achieve the SCR [211]. Note that In droplets might form even for low In content MOVPE grown InGaN layers under particular growth conditions [212, 213] and in this case temperature ramps might help evaporating them.

The effect of growth interruptions on the light emission and indium clustering of InGaN/GaN MQWs was investigated by H. K. Cho *et al.* [214]. In order to achieve homogeneous MQWs, they concluded in favor of growth interruption, as for no growth interruption they observed clear indium clustering in energy-filtered TEM images. However, no special care was taken in order to prevent indium clustering by the exposure of the MQWs to the electron beam in TEM, as only about two years later T.M. Smeeton *et al.* [215] pointed out that *false* indium cluster detection in TEM might occur.

Actually, LEDs with QWs presenting gross well width fluctuations (WWFs) exhibit better performance due to a reduction of defect-related nonradiative recombinations by providing an additional barrier to carrier diffusion to defect sites [211]. Note that the LED's performance is not directly related to the FWHM of the absorption line contrary to the case of LDs, where an increased absorption line might be detrimental to the lasing threshold [216].

In our case, low indium content QWs and GaN barriers are grown at an equal temperature of ~ 855°C at a growth rate of ~ 160 nm/h.[2] The precursors are TEGa, TMIn, and NH_3 and nitrogen is used as carrier gas. The V/III ratio corresponds to ~ 1300 and growth interruptions of 30 seconds are used before and after each QW interface.

InGaN/GaN QWs in this work are mainly grown on *c*-plane FS-GaN substrates. As for LM InAlN/GaN DBRs (cf. section 3.2.3) the growth parameters of InGaN/GaN QWs on *c*-plane FS-GaN substrates are exactly the same than that of InGaN/GaN ones grown on *c*-plane sapphire, except for a tuning of the growth temperature. Furthermore, similar PL linewidths have been

[1] Note that growth interruptions proved to smooth out the interface roughness of GaAs-based QWs, leading to a drastic sharpening of the PL spectra by a factor of 4-5 [210].

[2] As a rule of thumb, an increase of 10 °C translates into a reduction in indium incorporation followed by a blue shift of the emission wavelength by about 10 nm.

observed for 5 $In_{0.1}Ga_{0.9}N$ (2 nm)/GaN (3 nm) QWs when grown on FS-GaN or sapphire (not shown hereafter). However, as already mentioned, FS-GaN substrates are favored as the reduction in TDD is essential for obtaining long-lived blue-violet LDs [193].

Probing excitonic disorder

Two nominally identical $In_{0.1}Ga_{0.9}N$ (2nm)/GaN SQWs capped with a 20 nm thick GaN layer, one grown onto a high-quality FS-GaN substrate (substrate 1) and the other one onto an intermediate quality FS-GaN substrate (substrate 2), were characterized by LT μ-PL mappings and AFM measurements. For both structures, $10 \times 10\ \mu m^2$ AFM scans revealed a dislocation density similar to that of the substrate indicating that no additional dislocations are formed during the growth. However, in the case of the SQW grown onto the intermediate quality FS-GaN substrate local offcut variations similar to the ones seen in Fig. 3.5(b) are present.

LT μ-PL experiments, performed in the backscattering configuration, relied on the frequency-doubled line of a cw Ar^+-laser ($\lambda = 244$ nm) as excitation source focused down to a spot size of $\sim 1\ \mu$m. The μ-PL setup includes a high N.A. (0.55) UV microscope objective, a low mechanical drift cryostat, and a closed-loop piezo-stage for performing spatially-resolved mappings.

LT μ-PL mappings ($T = 10$ K, $50 \times 50\ \mu m^2$) of the peak energy of the two InGaN/GaN SQW are displayed in Figs. 4.1(a) and 4.1(b), respectively. The homogeneity of the SQW sample grown onto substrate 1 is highlighted by the standard deviation of the emission energy, centered at 3.030 eV, which only amounts to 0.8 meV and by a narrow mean linewidth of 33.6 meV. Furthermore, the peak to valley energy difference ($\Delta E_{peak-valley}$), i.e., the maximal emission energy difference occurring on the LT μ-PL mapping, amounts to only 8 meV.

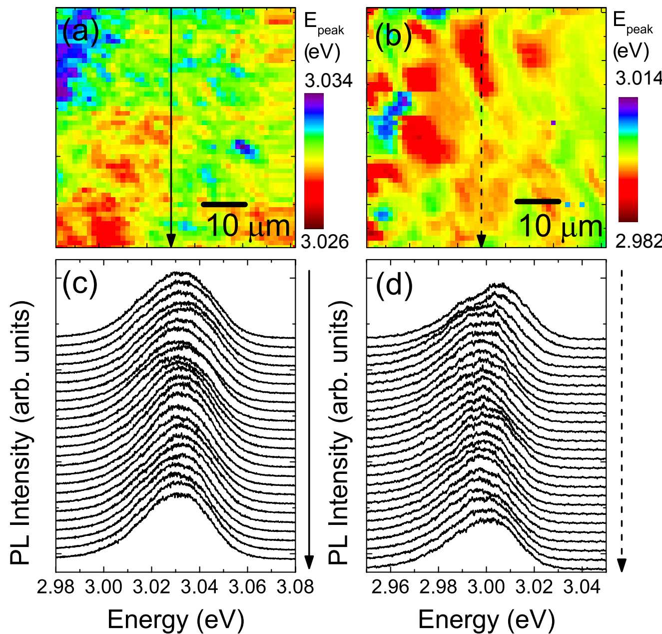

Figure 4.1: (a) and (b) LT (10 K) μ-PL mapping ($50 \times 50\ \mu m^2$) and (c) and (d) corresponding spectra recorded every 2 μm along the continuous and dashed arrow of an InGaN/GaN SQW grown on a high-quality FS-GaN substrate (left-hand side column) and on an intermediate quality FS-GaN substrate (right-hand side column), respectively.

Table 4.1: Mean values μ and standard deviations σ of the energy-peak position and the emission FWHM extracted from the LT μ-PL mappings (T = 10 K, 50 × 50 μm^2) shown in Fig. 4.1. Furthermore, the maximal difference in the energy-peak position over such a mapping is given by $\Delta E_{peak-valley}$.

Sample grown on	Substrate 1		Substrate 2	
	μ	σ	μ	σ
E_{peak} (meV)	3030	0.8	2998	3.3
FWHM (meV)	33.6	0.6	33.3	3.1
$\Delta E_{peak-valley}$ (meV)	8		32	

The average FWHM extracted from those mappings acquired every micron does not seem to depend on the sample substrate as for both QWs a LT FWHM of ~ 33 meV is measured (cf. Table 4.1). However, the homogeneity does depend on the choice of the substrate, as can be inferred from the standard deviation σ of the energy-peak position, which increases from 0.8 meV for substrate 1 up to 3.3 meV for substrate 2, and from $\Delta E_{peak-valley}$, which increases to 32 meV (cf. Table 4.1). Furthermore, from the spectra displayed in Figs. 4.1(c) and 4.1(d) it can be seen that in the case of the SQW grown on substrate 1 the spectra preserve a Gaussian lineshape over 50 μm whereas in the case of the SQW grown on substrate 2 an asymmetrical lineshape is observed over the same distance. Nonetheless, we can conclude that the role played by excitonic disorder is marginal for the $In_{0.1}Ga_{0.9}N$/GaN SQWs grown on the present FS-GaN substrates. Moreover, in contrast to the photonic disorder (cf. section 3.2.3), local offcut variations only slightly affect the excitonic disorder. Note that a slight difference is observed for the energy-peak position (E_{peak}) of the two InGaN/GaN SQWs even though exactly the same growth conditions have been used. The latter might originate from a small variation in the In content (originating from a weak temperature difference and/or offcut variations) and/or a variation in the QW thickness. Note that it has been shown that the In incorporation strongly depends on the offcut orientation of the GaN substrate [217, 218].

4.2 Relaxation issues for InGaN/GaN MQW structures and InGaN bulk layers

4.2.1 Strain relaxation of heterostructures of (0001) InGaN on GaN

Strain relaxation is a well-known, undesired phenomenon in heteroepitaxy, as it results in the generation of misfit dislocations (MDs), which are detrimental to device performance. Therefore, the understanding of the relaxation mechanisms and of the conditions favorable for the relaxation onset is of primary importance. Thus, several models have been introduced to calculate the critical thickness h_{crit} for relaxation of pseudomorphically grown layers. Most commonly used is the formula of Matthews and Blakeslee [219], initially introduced to calculate h_{crit} in cubic III-V heterostructures. In contrast, the mechanism responsible for relaxation in III-nitride compounds having the wurtzite structure differs from the latter and have been addressed by several authors [220, 221]. In Fig. 4.2 frequently used models are compared to experimental values of InGaN on GaN (0001). The recently suggested formula for

$In_xGa_{1-x}N$ on GaN by Pristovsek *et al.* [222]

$$h_{crit}(x) = \frac{1}{2G_x}\left(\frac{1-\nu_x}{1+\nu_x}\right)\frac{E_{crit}}{f^2(x)}, \tag{4.1}$$

where G_x is the shear modulus, ν_x the Poisson ratio, E_{crit} the critical energy given by the formation of dislocations at the onset of relaxation, and $f(x)$ the misfit $\frac{a(x)-a_{sub}}{a_{sub}}$, with $a(x)$ the in-plane lattice parameter of the alloy with composition x, fits the best the experimental values (cf. black line in Fig. 4.2 issued from Ref. [223]).

The critical thickness such as shown in Fig. 4.2 is only valid for single layers and not for MQWs. A. D. Bykhovski *et al.* [233] calculated the elastic strain relaxation for III-nitride superlattices (SLs). In the case of $(GaN)_n/(AlN)_m$ SLs, where n and m are the corresponding numbers of atomic layers, they showed that the critical thickness for such SLs ($h_{crit,SL}$) with arbitrary n/m ratio can be estimated as follows:

$$h_{crit} < h_{crit,SL} < 1.45 h_{crit}, \tag{4.2}$$

where the upper limit corresponds to the case of a symmetrical SL, i.e., $n = m$.

4.2.2 Relaxation issues in the case of MC structures based on InGaN/GaN MQWs

In polar III-nitride cavities containing a GaN/AlGaN MQW region, polariton lasing was reported for a 3λ MC containing 67 GaN/AlGaN QWs homogeneously distributed across the cavity region leading to a vacuum Rabi splitting Ω_{VRS} = 56 meV in the low density regime [55]. Thus, as a first attempt a similar approach has been considered to demonstrate the SCR when using an InGaN/GaN MQW active region. A MC was therefore grown on a *c*-plane sapphire substrate. The structure consists of a bottom LM 42 pair InAlN/GaN DBR followed by a 3λ cavity containing 62 $In_{0.12}Ga_{0.88}N$ (2 nm)/GaN (3 nm) QWs. For such a structure when completed with a 7 pair SiO_2/ZrO_2 DBR a vacuum Rabi splitting at negligible Γ_{inh} of ~ 50 meV is

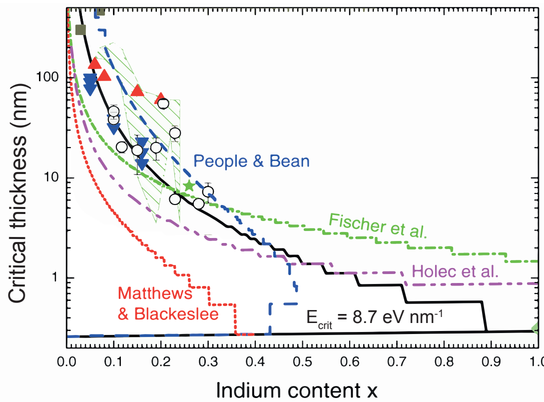

Figure 4.2: $In_xGa_{1-x}N$ layer thickness for relaxation on GaN (0001) as a function of indium content (○ (see, e.g., Ref. [222]), ■ (e.g., Ref. [224]), ▲ (e.g., Ref. [225]), ▼ (e.g., Ref. [226]), ★ (e.g., Ref. [227]), ♦ (e.g., Ref. [228]), hatched area is between last strained and first relaxed (Ref. [229])). The critical thickness was calculated (in quantities of strained ML in [0001]) by People and Bean [230] (blue line), by Matthews and Blakeslee [219] (red line), by Fischer et al. [231] (green line), and by Holec *et al.* [232](violet line). The thick solid line is calculated from equation 4.1 using E_{crit} = 8.7 eV nm^{-2}. Adapted from Ref. [223].

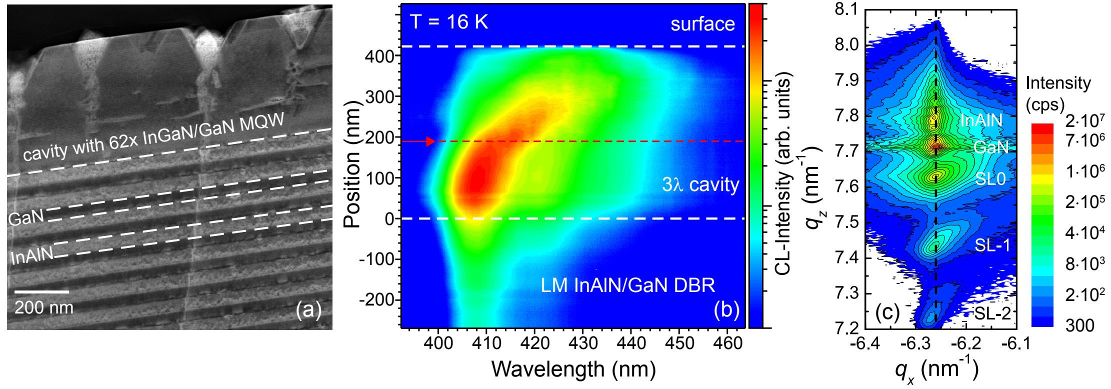

Figure 4.3: (a) Detailed HAADF STEM cross-section view of an InGaN/GaN MQW based half-cavity grown onto LM InAlN/GaN DBR , (b) LT STEM-CL linescan over the cavity region where white dashed lines mark the DBR/cavity and cavity/surface interfaces, respectively. The red dashed line marks the onset of strain relaxation. (c) Reciprocal space map of the asymmetric GaN (11-24) reflex. The GaN, InAlN, and QW SL (SL0, SL-1, SL-2) are identified. ((a) and (b) courtesy of G. Schmidt [234] and (c) courtesy of Dr. F. Bertram, Otto-von-Guericke-University Magdeburg.)

predicted (cf. Fig. 3.11(a) for $N_{max} = 5$ and $N_{QW/AN} = 12$). However, such a structure presents a poor material quality as can be seen in the HAADF STEM cross-section view displayed in Fig. 4.3(a) (courtesy of G. Schmidt, Otto-von-Guericke-University, [234]). Threading dislocations (TDs) that pass through the DBR layers and the active region can be identified. Within the InGaN/GaN MQWs these TDs are the origin of pit formation in the upper part of the cavity (cf. Fig. 4.3 (a)). From SEM and AFM images the density of those pits, also called V-defects, has been estimated to 2×10^9 cm^{-2}. Such pits considerably increase the PL line broadening (hence Γ_{inh}) and are therefore detrimental to the achievement of SCR. In Fig. 4.3(b) a STEM cathodoluminescence (CL) linescan over the cavity region, acquired at 16 K, is displayed. From the bottom of the cavity to the surface the QW emission exhibits a redshift (from 407 to 429 nm) accompanied by a decrease in intensity. At about 190 nm from the cavity/DBR interface, indicated by a red dashed line and an arrow in Fig. 4.3(b), the CL signal reveals a step of 30 meV in its peak position, an increased FWHM, and a considerably decreased intensity. Thus, when $In_{0.12}Ga_{0.88}N$ (2 nm)/GaN (3 nm) MQWs are grown on a LM InAlN/GaN DBR on c-plane sapphire, above 30 QWs (corresponding to the above-mentioned 200 nm or to a $h_{crit,SL} = 160$ nm after substracting a quarter-wave layer of GaN (~ 40 nm)) the material quality is considerably affected, i.e., plastic strain relaxation occurs.

Furthermore, a X-ray diffraction (XRD) reciprocal space map of the asymmetric GaN (11-24) reflex indicates gradual relaxations (cf. Fig. 4.3(c), courtesy of Dr. F. Bertram, Otto-von-Guericke-University). The latter can be seen from the asymmetric peak distribution of the QW reflections denoted by (SL0, SL-1, SL-2). The QW reflections are broadened along the relaxation line. However, the relaxation is less than 50%.

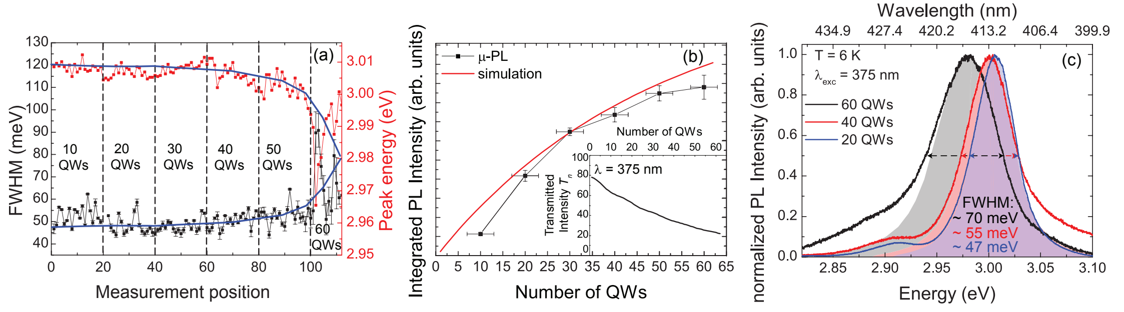

Figure 4.4: LT μPL measurements on InGaN/GaN MQWs carried out at various etching depths. (a) Peak position (red dots) and peak broadening, i.e., its FWHM (black dots) are deduced from μPL linescan measurements taken every 5 μm. Note, that every 100 μm a step of about 50 nm, i.e., 10 InGaN/GaN QWs, occurs. The blue lines are guides to the eye. (b) Mean integrated PL intensity vs QW number compared to TMS results. The transmitted intensity T_n as a function of the QW number deduced from TMS is shown in the inset. (c) μ-PL spectra of the first 20, 40 and 60 QWs are shown. Adapted from Ref. [235].

Furthermore, the same active medium has been grown on a FS-GaN substrate. For GaN epilayers grown on such substrates a slightly different basal strain is expected, i.e., they are expected to be more relaxed than GaN epilayers grown on sapphire. Thus, strain relaxation in InGaN/GaN SLs is expected to occur at a slightly increased $h_{crit,SL}$ value. Indeed, from AFM scans the pit density is estimated to *only* 2×10^7 cm^{-2} (cf. Fig. 4.5(a)). To further investigate the origin of such a relaxation, a series of 100 μm wide terraces each separated by 50 nm high steps was realized using conventional photolithography and dry etching techniques, which leads to a staircase profile allowing to probe buried QWs from the surface (whole set of QWs) down to the substrate (no QW), each step corresponding to the removal of ~10 QWs. μPL linescan measurements were performed at 6 K with a cw 375 nm LD, for which one spectrum was taken every 5 μm along the staircase profile. In Fig. 4.4(a), the peak position and the broadening deduced from the μPL spectra vs the measurement position are displayed. A slight redshift of the PL peak can be seen with increasing QW number together with a considerable linewidth broadening (cf. blue guides to the eye). Furthermore, the mean integrated PL intensity per step can be deduced. The result is compared to TMS in Fig. 4.4(b). From the normal incident laser light only a small fraction (~ 20%) penetrates through all the 62 InGaN/GaN QWs due to absorption occurring mainly in the QWs. In the inset of Fig. 4.4(b) the transmitted intensity T_n, starting from $I_0 = 100$, is shown as a function of the penetration depth, i.e., the number of QWs. Note that QWs have been considered to be all identical and the complex refractive index dispersion of excitonic InGaN given in section 3.3.3 has been used for TMS. A residual absorption in the GaN barriers corresponding to $\alpha = 900$ cm^{-1} has also been taken into account. Then, identical absorption and losses due to scattering are assumed and thus the emission (N_{ph}) vs number of QWs is proportional to the sum of the transmitted intensities, i.e.,

$$N_{ph}(N_{QW}) \propto \sum_{n=1}^{N_{QW}} T_n \cdot A, \tag{4.3}$$

where A is a constant corresponding to the number of photons collected per QW. Indeed, in such a simple model photon reabsorption is neglected, which is reasonable considering the significant Stokes shift present in such samples (cf. section 4.3.4). However, the mean integrated PL intensity shown in Fig. 4.4(b) follows closely the predicted behavior, i.e., it does not quench considerably for a high number of QWs. The latter is a sign of improved material quality with respect to the active medium grown onto the LM InAlN/GaN DBR on c-plane sapphire, which is further confirmed by a comparison of XRD measurements (not shown hereafter). The asymmetric peak distribution of the QW reflections in the reciprocal space map of the (11-24) reflex is less pronounced. Furthermore, the broadening of the QW reflections is reduced. However, when having a look at typical μPL spectra, those corresponding to the first 20, 40, and 60 QWs starting from the substrate are shown in Fig. 4.4(c), it can be seen that the FWHM for the PL emission originating from 60 MQWs is equal to 70 meV, i.e., it is increased by a factor of ~ 1.5 with respect to 20 MQWs. If one makes the hypothesis that the present MQW active region undergoes marginal thickness and In composition fluctuations, the observed changes in μPL spectra could be ascribed to plastic strain relaxation. For our MQW sample, changes in the μPL spectra are seen beyond a $h_{crit,SL}$ value of 160-200 nm (i.e., the change in linewidth occurs for a QW number ranging between 30 and 40 starting from the substrate).

In conclusion, $h_{crit,SL}$ for an $In_{0.12}Ga_{0.88}N$ (2 nm)/GaN (3 nm) MQW structure has been estimated using two different approaches to exceed 160 nm, i.e., it corresponds to a critical QW number of ~ 30. Using equation 4.2 h_{crit} for a bulk $In_{0.12}Ga_{0.88}N$ layer deposited on GaN is estimated to amount to ~ 110 nm. Note that with such a value we are above all theoretical predictions (cf. Fig. 4.2) but only slightly above the reported experimental results (Ref. [229]). Anyhow, the very onset of misfit strain relief can hardly be seen by means of PL [232] nor by CL. Indeed, changes might only be visible in CL and PL spectra when the plastic strain relaxation occurring through MD formation is significant. Furthermore, note that we cannot discard dislocation climbing downwards to the MQW structure/GaN interface [221]. Thus, in order to properly deduce $h_{crit,SL}$, a series of layers with an increasing QW number should be grown and analyzed, which is well beyond the scope of this work.

4.2.3 A promissing solution: MCs based on interlayers

Not only the number of QWs is problematic, but as well the top interface roughness has to be considered with great care. In Fig. 4.5(a) a 10×10 μm^2 AFM scan of a 68 $In_{0.1}Ga_{0.9}N$ (2 nm)/GaN (3 nm) MQW region grown onto a FS-GaN substrate reveals a so-called finger-like morphology. Such a morphology is typical for thick layers (GaN or InGaN with low In content) when grown at conventional QW growth temperatures, i.e., at 840 °C, and with N_2 carrier gas [236]. In Fig. 4.5(c) the 10×10 μm^2 AFM scan of the final top GaN layer of a 4×5 $In_{0.1}Ga_{0.9}N$ (2 nm)/GaN (3 nm) MQW structure shows a very smooth morphology without any V-defects. Such a morphology has been obtained thanks to the introduction of high temperature (HT) GaN layers. About 30 nm of HT GaN has been inserted between the four sets of 5 MQWs positioned

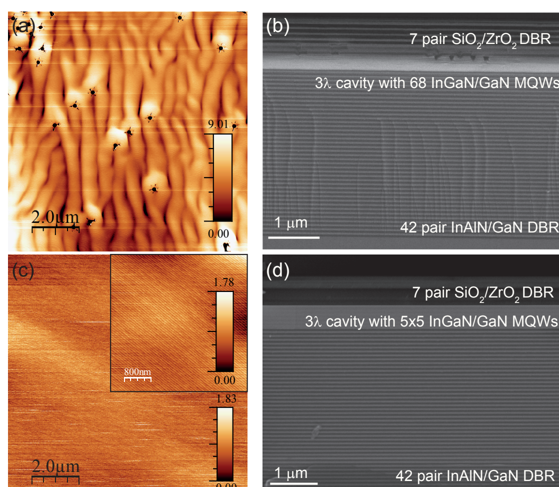

Figure 4.5: (a) and (c) 10×10 μm^2 AFM scans of the final top GaN layer of a 68 (4×5, respectively) InGaN/GaN MQW sample grown on a FS-GaN substrate and (b) and (d) corresponding SEM images when such an active medium is deposited on top of a LM InAlN/-GaN DBR grown on a FS-GaN substrate. The inset in (c), a 4×4 μm^2 AFM scan, highlights the regular staircase morphology.

at cavity light field antinodes. The growth conditions used for GaN quarter-wave layers in LM InAlN/GaN DBRs have been applied, i.e., a growth temperature of 1065°C (cf. section 3.2.3). In Figs. 4.5(b) and 4.5(d) SEM images of MCs based on a high number of InGaN/GaN MQWs and on a reduced number of MQWs including HT GaN interlayers, respectively, are shown. V-defects are clearly visible at the top cavity-DBR interface in the first case (Fig. 4.5(b)).

4.3 On the nature of localization in InGaN/GaN QWs and InGaN bulk layers

4.3.1 Carrier localization mechanism

The startling success of InGaN-based LEDs has been attributed to carrier localization occurring in the QWs. As III-nitride based QW structures present relatively high dislocation densities compared to their III-arsenide counterpart, nonradiative recombinations at dislocations were first thought to be detrimental for the achievement of efficient light emitting devices. Fortunately, the latter proved not to be an issue as in InGaN/GaN QWs carrier localization is an efficient barrier against carrier diffusion toward nonradiative defect sites [237]. Note that a few reports suggested that the high efficiency of light emitting devices might also arise from dislocation screening by different microstructures such as (i) V-defects formed around dislocation cores providing an energy barrier due to the thinner QWs at the V-defect walls [238], (ii) step-pinning by dislocations leading to locally thinner QWs [239, 240], and (iii) 'gappy' QWs consisting of interlinked dislocation-free InGaN stripes separated by dislocation-rich GaN troughs [241]. However, dislocation screening is unlikely to be the main mechanism influencing carrier nonradiative recombinations and thus it is essential to understand carrier localization mechanism. The precise nature of those localization centers is still a matter of debate. Three possible causes of carrier localization occurring at different scales have been mostly considered in the literature, namely: (i) random alloy fluctuations at the atomic scale involving In-N-In chains [242, 243], (ii) WWFs [244, 245], and (iii) indium clustering [246]. D. Watson-Parris *et al.* [247] recently reported via simulations that fluctuations in the alloy

concentration originating from a random distribution of indium atoms in the GaN matrix together with an electron localization occurring at a larger scale on WWFs can satisfactorily reproduce localization features of InGaN/GaN QWs. According to their model, holes are strongly localized in regions of above average indium content (cf. section 4.3.6 for further elucidations), whereas electrons mainly feel WWFs. Thus, the commonly observed inhomogeneous PL linewidth broadening is mainly attributed to the hole localization.
Besides the presence of such localization centers, there is another important effect that has a strong impact on the optical properties and therefore on the device functionality of nitride heterostructures: the internal electric field. Having these two effects in mind, the optical properties of an InGaN/GaN SQW grown on a high-quality FS-GaN substrate are examined carefully in the next section.

4.3.2 Optical properties of InGaN/GaN SQWs at low temperature

$In_{0.1}Ga_{0.9}N$ (2nm)/GaN (3nm) SQWs grown onto FS-GaN substrates exhibit very homogeneous LT μ-PL mappings (cf. section 4.1), a proof of high structural homogeneity. In order to gain further insights into the properties of such SQW samples, further LT μ-PL measurements (using the same experimental conditions as mentioned in section 4.1), amongst others with subwavelength lateral resolution, have then been performed on the InGaN/GaN SQW grown onto the high-quality FS-GaN substrate mentioned in section 4.1.

Probing individual localization centers

To probe the eventual signature of individual localization centers the SQW was patterned using electron beam lithography and subsequently etched using a chlorine-based inductively coupled plasma into pillars of ~ 60 nm in height and down to 100 nm in diameter. In the optical microscope image shown in Fig. 4.6(a) the position of the 2000 - 500 nm size mesas can be seen readily. The 200 nm mesa can be guessed but the 100 nm mesa cannot be seen at all and its position is indicated by a lithographically defined arrow at the left hand side. Note also that the pillars were covered by a ~ 100 nm thick layer of SiO_2 in order to passivate surface states. Such a procedure allows one to reach subwavelength lateral resolution for the smallest mesas. The corresponding spectra, obtained in the low-excitation power density regime, are shown in Fig. 4.6(b). When decreasing the mesa size, the PL signal progressively splits into individual, spectrally narrow emission lines, which are tentatively ascribed to the recombination of electron-hole pairs occurring in single localization centers [248]. We can notice that despite the presence of those individual lines, the Gaussian-like character of the emission is preserved down to a mesa diameter of 200 nm. Transitions with a narrow linewidth down to 3.5 meV can be observed for the 100 nm mesa together with the corresponding first LO-phonon replica located 92 meV below the zero-phonon-line transition. Such a linewidth remains larger than the 0.8 meV reported by Schömig and co-workers for a similar InGaN/GaN SQW grown on *c*-plane sapphire substrate, [248] which might likely be due to a different sensitivity to the local environment, hence leading to a larger spectral diffusion in the present

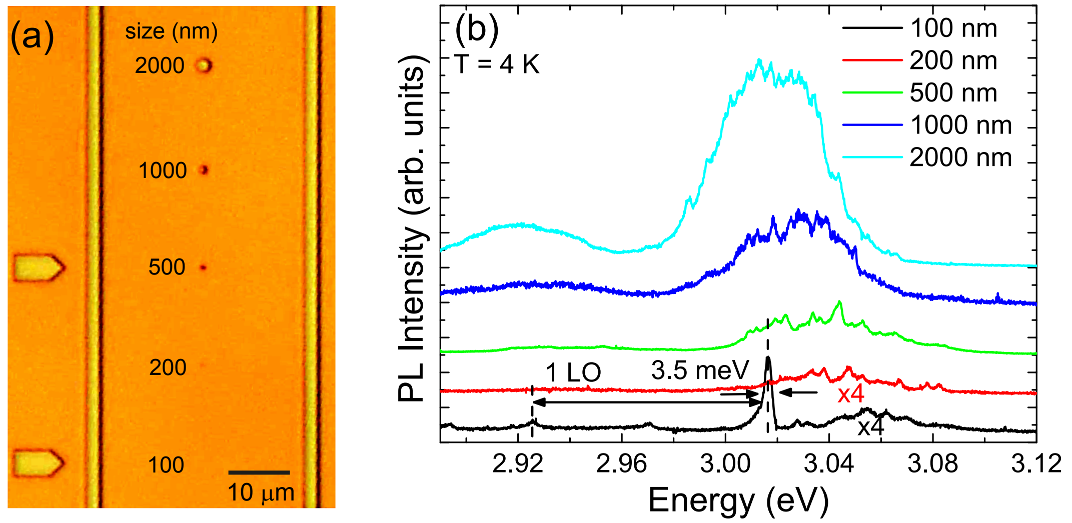

Figure 4.6: (a) Optical microscope image of the patterned InGaN/GaN SQW. (b) LT μ-PL measurements taken for different sizes of the lithographically defined mesas shown in (a).

sample. In particular, the presence of surface states on the mesa sidewalls could potentially explain this larger value since in the sample investigated by Schömig and co-workers a metal mask with nanoapertures down to 100 nm in diameter was deposited on the sample surface to limit the probed area.

LT excitation power-dependent μ-PL measurements performed on the unpatterned SQW are reported in Fig. 4.7. At low injection power density several individual emission lines emerge from the Gaussian background. When increasing the power density, they remain at the same energy position (cf. red dashed lines in Fig. 4.7(a)) whereas the Gaussian background slightly blueshifts while gaining in importance. A similar power dependence was observed in the above-mentioned InGaN/GaN SQW by Schömig *et al.* [248] as well as in InGaN/GaN nanowire heterostructures [249]. Such a counterintuitive behavior for III-N heterostructures grown along the c-axis can be ascribed to the following qualitative picture: at the initial stage individual localization centers remain occupied at most by a single electron-hole pair when increasing the excitation power density (cf. region I in Fig. 4.7(b) corresponding to a maximum excitation power density of ~ 600 W/cm^2), which is supported by a linear increase in the emitted light in this region, while keeping the charge configuration of the nanoenvironment of the localization centers unmodified. The overall blueshift of the emission is then ascribed to the progressive filling of multiple individual localization centers of higher energy. For excitation power densities larger than ~ 600 W/cm^2, individual emission lines cannot be distinguished anymore and the QW Gaussian-like emission linewidth starts to increase. Above a certain excitation power density one can expect the nanoenvironment of the localization centers to be affected. Note, however, that such an effect will likely depend on the size, shape, and strain state of the localization centers [250], which makes a quantitative estimate of the interaction of carriers with the local polarization field leading to a screening of the QCSE in indium-rich localization centers relatively challenging. In the present QW sample such a screening likely

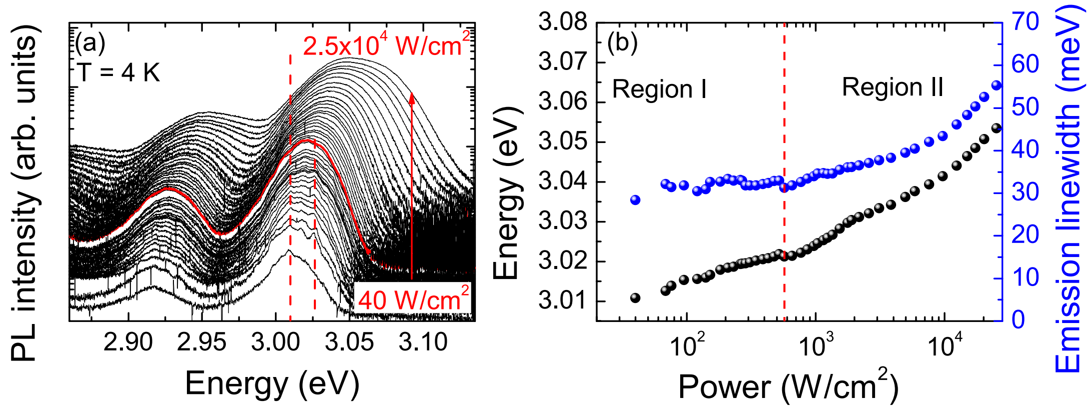

Figure 4.7: (a) Excitation power-dependent PL emission spectra taken on the InGaN/GaN SQW sample at 4 K. (b) QW emission linewidth and energy-peak position deduced from a Gaussian profile analysis. Taken from Ref. [200].

occurs in region II (see Fig. 4.7(b)), in which the QW emission linewidth increases and is accompanied by a more pronounced blueshift than in region I, the latter amounting to ~ 43 meV at ~ 2.5×10^4 W/cm^2. This increase in the linewidth is likely due to a combination of several mechanisms such as band-filling effects, i.e., the successive population of localized and delocalized states, collisional broadening and spectral diffusion. The QW emission lineshape asymmetry and the flattening of QW spectra toward the high energy side observed for the highest excitation power densities for this SQW sample are also a hint for the transition from an exciton population toward an electron-hole plasma one, i.e., the signature of the Mott transition [251]. Note however that a precise understanding of this effect for the present sample would require a careful and quantitative analysis that lies beyond the scope of the present work.

4.3.3 On the suitability of the envelope function formalism for optical transitions in InGaN/GaN SQWs

Based on the above-mentioned results, it is legitimate to wonder whether we should account for a breakdown of the conventional 2D picture to describe the present InGaN/GaN SQW. Indeed, recent studies performed on InGaN QW heterostructures showed that to theoretically account for their spectral features modeling based on a so-called quantum dot- or nanodisk-like picture is employed, which includes lateral confinement [252]. In addition, we could also question the suitability of our envelope function formalism since it is a simple continuum-based theoretical model, which does not account for alloy or built-in field fluctuations at the microscopic level. Note that numerical solutions of the effective mass Schrödinger equation have been calculated including such fluctuations in Ref. [247]. To check the robustness of our approach, we can therefore focus on the computed value for the LT transition energy of the ground state including excitonic effects for a single QW corresponding to the nominal growth conditions: a 2 nm-thick $In_{0.1}Ga_{0.9}N$ well pseudomorphically grown on GaN subjected

to a built-in field of 1.5 MV/cm (cf. section 1.1.1). The obtained value of 3.127 eV differs from the 3.030 eV reported in Tab. 4.1. However, it is important to notice that the value derived from simulations does not account for the Stokes shift which amounts to 46 meV (cf. section 4.3.4 and Tab. 4.3) for the QW of interest. When including such a correction, the energy difference between theory and experiment is reduced to 51 meV. Such a difference can easily be accounted for by considering the very same well except for: (i) an increased thickness of 1 monolayer, or (ii) an increased indium content of 1% (and hence of the built-in field). Indeed when subtracting the measured SS value transition energies of (i) 3.036 and (ii) 3.041 eV are then obtained, which are reasonably close to the measured one. It therefore means that the energy position of the intrinsic ground state of this InGaN/GaN SQW can be well reproduced using a standard 2D-picture. This aspect is of prime importance as it indicates that in such a case the in-plane wave vector is a good quantum number and that such heterostructure is compatible with the formation of 2D cavity polaritons. Obviously one could argue that such an agreement is purely fortuitous and that the combination of local strain and alloy compositions could lead to an assembly of zero-dimensional emitting regions whose emission energy corresponds to the experimentally measured one. However, we also pointed out that WWFs are likely limited in those wells, which is supported by the reasonable inhomogeneous broadenings and Stokes shift values (cf. section 4.3.4). Hence, it is fair to say that for such a low indium-content QW, the appropriateness of the conventional 2D-picture is plausible.

4.3.4 Estimation of Γ_{inh}: absorption-like measurements at low temperature

The preservation of a narrow absorption linewidth (Γ_{abs}) in InGaN/GaN QWs is a key issue for (i) the realization of efficient III-nitride blue to green EELDs and (ii) strong coupling applications. Indeed, inhomogeneous gain broadening is known to have a detrimental impact on the general properties of EELDs including the threshold current density. In section 3.3.4 the effect of Γ_{inh} onto the mode splitting is illustrated by TMS. Note that considering a Voigt profile for the excitonic transition (cf. section 3.3.3) Γ_{abs} can be related to the inhomogeneous and homogeneous broadening through the approximate formula given by Oliviero and Longbothum [253]:

$$\Gamma_{abs} \sim 0.5346\Gamma_h + \sqrt{0.2166\Gamma_h^2 + \Gamma_{inh}^2}, \tag{4.4}$$

for which $\Gamma_h \sim 0$ at LT, hence leading to $\Gamma_{abs} = \Gamma_{inh}$. Furthermore, theoretical attempts have been made to relate the optical absorption to emission spectra of excitons in disordered two-dimensional semiconductors. Thus, F. Yang *et al.* [199] developed a model linking the Stokes shift (SS),[3] the absorption and the excitonic emission linewidth in terms of statistical properties of a Gaussian random function. Their approach can be used as a basis to derive the excitonic absorption features in two-dimensional semiconductors at LT. They found that Γ_{abs}

[3]The Stokes shift is defined as the energy difference between the maximum of the emission and absorption spectrum of the same optical transition.

is connected to SS and the FWHM of the emission line (Γ_{PL}) through the relationship

$$\Gamma_{abs} \sim 1.81 \cdot SS \sim 1.42 \cdot \Gamma_{PL}. \tag{4.5}$$

Thus, the emission lineshape corresponding to the absorption spectrum calculated from the extinction coefficient k_{op} presented in Fig. 3.10(b) (red line) is estimated and plotted as a function of energy in Fig. 3.10(c) (blue line). As a consequence if the absorption linewidth Γ_{abs} amounts to 45 meV as this is the case in Fig. 3.10(b), the corresponding emission spectrum is expected to occur slightly redshifted, by a SS value of ~ 25 meV, and to exhibit a narrower linewidth of ~ 32 meV.
In order to test the validity of the latter relationship for III-nitride QW structures, an adapted experimental technique has to be chosen. Note that optical properties related to electronic states of semiconductors can be studied by various spectroscopic methods such as photoluminescence excitation spectroscopy (PLE), spectroscopic ellipsometry, Raman scattering, photocurrent spectroscopy, absorption, reflectivity, and transmission spectroscopy, modulation spectroscopy, etc. In contrast to PL measurements, the above-mentioned spectroscopic methods allow accessing the intrinsic properties of the investigated samples. However, since its inception in 1964, it has been recognized that, with respect to sharp, highly structured spectra, modulation spectroscopy is unsurpassed. It is the only experimental technique that enables the direct measure of derivatives of $\epsilon(\omega)$ with respect to some modulation parameters. One distinguishes between *external* and *internal* modulation. In the case of *internal* modulation the modulation is applied to the measuring system itself (e.g., wavelength modulation spectroscopy), whereas in the case of *external* modulation, the properties of the sample itself are directly altered (e.g., in electroreflectance (ER), thermoreflectance, or piezoreflectance spectroscopy).

Photoreflectance

Photoreflectance (PR) belongs to the external modulation techniques where the varying parameter is the internal (built-in) electric field, i.e., the depletion layer field is screened by absorbed carriers of the modulated laser beam. In this case PR can be considered as an electromodulation technique. However, the optical features can also be related to screening of the exciton interaction by the induced carriers modulated by the laser beam [254] and/or the partial screening of the QCSE.

Line shape considerations

Differential changes in the reflectivity can be written as:

$$\frac{\Delta R}{R} = \alpha_s(\epsilon_1, \epsilon_2)\Delta\epsilon_1 + \beta_s(\epsilon_1, \epsilon_2)\Delta\epsilon_2, \tag{4.6}$$

Range	Intraband	Interband	Spectral characteristics
High	$\lvert\hbar\Theta\rvert \geq \gamma_{PR}$	$e\mathscr{E}a_0 \sim E_g$	Stark shifts and modified selection rules
Intermediate		$e\mathscr{E}a_0 \ll E_g$	FKOs (equation 4.8)
Low	$\lvert\hbar\Theta\rvert \leq \gamma_{PR}/3$		Third-derivative or first-derivative dependence of $\epsilon_{1,2}$ and equation 4.9 or 4.10 does apply

Table 4.2: The three ranges of ER spectra depending on the relative strength of the perturbation ($\mathscr{E}$).

where α_s and β_s are the Seraphin coefficients, related to the unperturbed dielectric function, and $\Delta\epsilon_1$ and $\Delta\epsilon_2$ are the changes induced in the complex dielectric function due to the perturbation. In ER and in PR the relative strength of the perturbation with respect to characteristic quantities of the semiconductor under consideration affects the recorded spectra. As most of the theoretical considerations have been done for ER (cf. Aspnes [255]), in the following mainly ER is mentioned. However, the same formalism is commonly used for the interpretation of PR. One distinguishes between three different regimes: (i) high, (ii) intermediate, (iii) and low field regime (cf. Table 4.2). In the high-field regime the electro-optic energy ($\lvert\hbar\Theta\rvert$), given by [256]

$$: \lvert\hbar\Theta\rvert = \left(\frac{e^2\mathscr{E}^2\hbar^2}{8\mu^*}\right)^{1/3}, \tag{4.7}$$

where $\mathscr{E}$ is the relative strength of the perturbation, is much greater than the broadening parameter of the transition (γ_{PR}) but $e\mathscr{E}a_0 \sim E_g$ (a_0 beeing the lattice parameter) so that Stark shifts are produced and selection rules are modified. When $e\mathscr{E}a_0 \ll E_g$ the band structure is not modified but Franz-Keldysh oscillations (FKOs) above the band edge might be observable [255]:

$$\frac{\Delta R}{R}(E) \propto \frac{1}{E^2(E-E_g)} \exp\left(\frac{-2\sqrt{E-E_g}\gamma_{PR}}{(\hbar\Theta)^{3/2}}\right) \cos\left(\frac{4}{3}\left(\frac{E-E_g}{\hbar\Theta}\right)^{3/2} + \phi\right). \tag{4.8}$$

In the low field regime $\lvert\hbar\Theta\rvert \leq \Gamma/3$ holds in addition. FKOs disappear from the spectrum and the lineshape can be fitted using equation 4.9 or 4.10.

Aspnes developed a formalism for third-derivative ER spectra where the normalized differential reflectivity $\frac{\Delta R}{R}(E)$ is given by [256]:

$$\frac{\Delta R}{R}(E) = Re[Ce^{i\theta}(E-E_0+i\gamma_{PR})^{-m}], \tag{4.9}$$

where C and θ are the amplitude and phase factors that determine the amplitude and the asymmetry of the lineshape, respectively. E_0 and γ_{PR} determine the energy location and width of the transition and m depends on the dimensionality of the critical point. Note that equation 4.9 can be derived from equation 4.6 for a Lorentzian form of the dielectric function assuming a parabolic band approximation.

However, the situation is different for bound states, including excitons, because the particle (electron or hole) and its wavefunction are localized in space. The formalism derived by Aspnes is no longer valid and the change in the dielectric function induced by the modulation is *first derivative* and can be expressed as [257, 258]:

$$\Delta\epsilon = \left[\frac{\delta\epsilon}{\delta E_g}\frac{\delta E_g}{\delta F} + \frac{\delta\epsilon}{\delta\Gamma}\frac{\delta\Gamma}{\delta F} + \frac{\delta\epsilon}{\delta I}\frac{\delta I}{\delta F}\right]\Delta F, \tag{4.10}$$

where ΔF is the change in the field, I the intensity of the optical transition, and Γ the broadening of the latter. Equation 4.10 has been developed for a dielectric function of either Lorentzian or Gaussian form and satisfactory fits have been obtained for several MQW systems, e.g., for a GaAs/AlGaAs MQW structure [259]. However, equation 4.9 with parameter $m = 3$ is sometimes used to reflect the first derivative functional form in the case of a Gaussian broadened transition [260, 261]. Note that for QW structures FKOs are not expected, as QW structures do not suffer from the Franz-Keldysh effect but rather from the QCSE when subject to an electric field, even though reports on FKOs in QWs can be found in the literature [262].

Evaluation of the Stokes shift

In order to evaluate the Stokes shift of InGaN/GaN MQWs, PR spectra are compared to PL ones. Note that such a comparison might result into the extraction of a *quasi*-Stokes shift when dealing with InGaN/GaN MQWs suffering from a strong built-in electric field (strong QCSE). The latter separates the electron and hole wavefunctions and reduces strongly the oscillator strength of the fundamental transition without necessarily affecting higher order transitions whose confinement is given by a rectangular potential. Thus, the latter might prime over the fundamental transition and the difference between PL and any absorption-like measurement will result into a *quasi*-Stokes shift (cf. Fig. 4.8 adapted from Ref. [263]). Note that we expect the latter effect to be marginal in the InGaN/GaN QW samples considered hereafter (i.e., our QWs are too thin and the In content is too small).

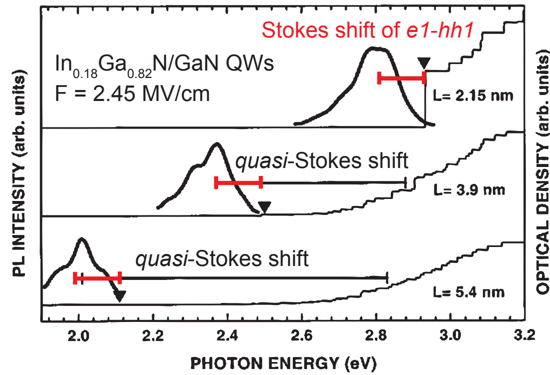

Figure 4.8: PL spectra are compared to interband absorption spectra calculated for InGaN QWs with $x = 0.175$, for the three corresponding well widths. The Stokes shift of the $e1$-$hh1$ transition resulting from the disorder-induced fluctuations was kept constant and equal to 120 meV (red horizontal segments). The black horizontal segments indicate the experimental *quasi*-Stokes shift occurring in thicker QWs due to an absorption onset made of transitions between excited levels. Adapted from Ref. [263].

Sample	Γ_{PL} (meV)	γ_{PR} (meV)	SS (meV)	Γ_{abs} (meV)
(a) $In_{0.1}Ga_{0.9}N$/GaN SQW	32	44	46	45
(b) 5 $In_{0.1}Ga_{0.9}N$/GaN MQWs	45	43	58	63
(c) 4×5 $In_{0.1}Ga_{0.9}N$/GaN MQWs	55	48	60	77
(d) GaN/$Al_{0.15}Ga_{0.85}$ SQW	15	23	8	21
(e) 67 GaN/$Al_{0.2}Ga_{0.8}N$ MQWs	10	24	10	14

Table 4.3: Spectroscopic features deduced from LT measurements performed on the three different InGaN/GaN QW samples and the two GaN/AlGaN ones. Γ_{PL} is the PL linewidth, γ_{PR} is the PR linewidth. The other parameters are defined in the main text.

We will consider the above-mentioned SQWs, 5 MQWs, and four sets of 5 MQWs separated from each other by 30 nm of GaN. They are nominally identical $In_{0.1}Ga_{0.9}N$ (2 nm)/GaN (3 nm) QWs capped with a 20 nm thick GaN layer in the case of the SQW and the 5 MQW sample. Note that growth conditions have been described in sections 4.1 and 4.2.3 and all the samples revealed a dislocation density, determined by AFM, similar to that of the FS-GaN substrate ($\sim 1 \times 10^6$ cm^{-2}) indicating that no additional dislocations are formed during the growth. In Fig. 4.5(c) 4×4 and 10×10 μm^2 AFM scans of the final top GaN layer of the 4 × 5 MQW sample are presented.
To help estimating the absorption linewidth of the above-mentioned InGaN/GaN QWs two different GaN/AlGaN QW samples were considered as a reference. The first sample consists of a 1.5 nm thick GaN SQW deposited on a barrier composed of a 10 nm thick $Al_{0.3}Ga_{0.7}N$ layer followed by 50 nm of $Al_{0.15}Ga_{0.85}N$ grown on a FS-GaN substrate. It was then capped with a 30 nm thick $Al_{0.15}Ga_{0.85}N$ layer followed by 10 nm of $Al_{0.3}Ga_{0.7}N$. A detailed description of the growth process and optimization of the interfaces for such QWs can be found in Ref. [264]. A 67 GaN (1.2 nm)/$Al_{0.2}Ga_{0.8}N$ (3.6 nm) MQW sample grown on c-plane sapphire was also considered, which was deposited during the same run as a reference microcavity structure for which RT polariton lasing was demonstrated several years ago [55, 70].

The LT PL linewidth of the 5 InGaN/GaN MQW in the low injection regime is increased to a value of 45 meV compared to 32 meV for the SQW (cf. Fig. 4.9(b) and Table 4.3). This increase can certainly be partly attributed to the sample geometry, i.e., to the inhomogeneous redistribution of the polarization fields among wells and barriers. Indeed, the two external QWs of the 5-QW set are expected to experience a larger built-in field than the three inner ones, which most likely leads to slightly different emission energies. In addition, QW and barrier thickness fluctuations as well as In content variations cannot be fully excluded. A further increase in the LT PL linewidth to 55 meV is observed for the 4 × 5 InGaN/GaN MQW sample. In this case the linewidth increase might originate from a slight strain accumulation and some unwanted In diffusion effects for the first sets of QWs as they must undergo several temperature ramps up to 1065°C for the growth of the GaN interlayers.

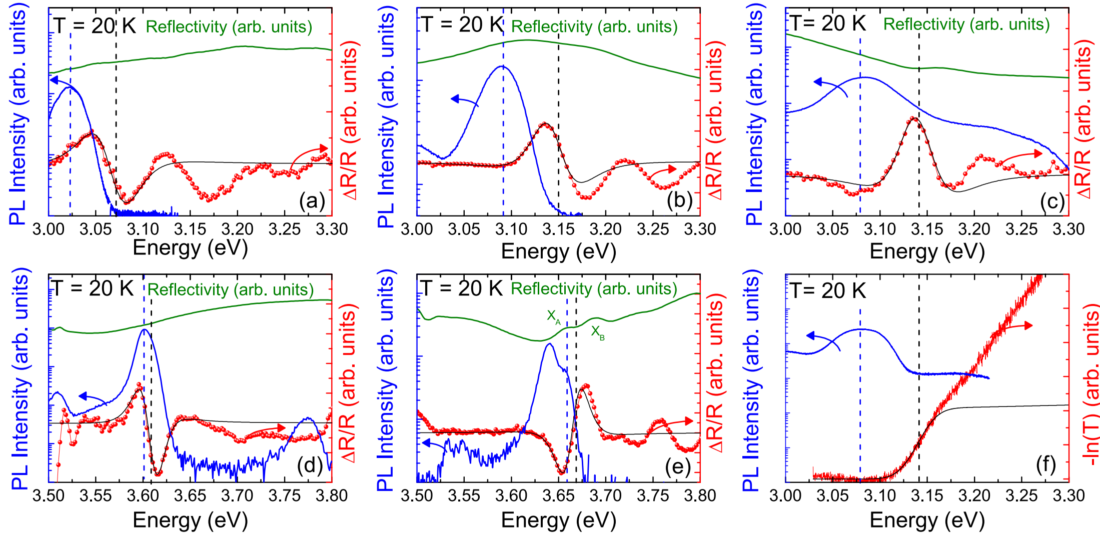

Figure 4.9: LT ER, PR signal (red dots) compared with the PL spectrum (blue) measured at the same position on a series of QW samples: (a) $In_{0.1}Ga_{0.9}N/GaN$ SQW, (b) 5 $In_{0.1}Ga_{0.9}N/GaN$ MQWs, (c) 4 × 5 $In_{0.1}Ga_{0.9}N/GaN$ MQWs, (d) $GaN/Al_{0.15}Ga_{0.85}N$ SQW, and (e) 67 $GaN/Al_{0.2}Ga_{0.8}N$ MQWs. For each sample, the LT reflectivity spectrum (dark green) measured at the same sample position is also shown. The blue vertical dashed lines and the black vertical dashed lines indicate the position of the excitonic resonance deduced from PL and ER, PR measurements, respectively. The energy difference between those resonances leads to the Stokes shift values that are listed in Table 4.3. In (f) an absorption measurement of the same sample as shown in (c) together with PL is displayed. Taken from Ref. [200].

We point out that in the specific case of the InGaN/GaN SQW PR measurements were not successful, which is likely due to a combination of (i) the lower oscillator strength compared to its GaN/AlGaN counterpart, (ii) the inhomogeneous broadening that blurs the transition, and (iii) the small amount of absorbing material at play. However, the fundamental transition of this SQW could be resolved using the semi-contactless ER technique (cf. Fig. 4.9(a)). For comparison, the LT PR linewidth measured on the two GaN/AlGaN QW samples lies well below 30 meV (Figs. 4.9(d) and 4.9(e)). Note that with GaN SQWs even narrower spectroscopic features (PL and reflectivity linewidths) can be observed when choosing a slightly different sample geometry. The best GaN SQWs in terms of narrow spectroscopic features are surrounded by low Al content AlGaN barriers (typically with 5% Al content) and have a slightly larger well thickness [264, 265]. As such QWs are energetically closer to the transition of bulk GaN, our reference GaN/AlGaN SQW sample is more compliant with our request, i.e., it is characterized with well resolved PR spectra with a resonance occurring far enough from the bulk transition. In each case, the fundamental PR QW resonance has been fitted using equation 4.9 with $m = 3$ as we consider Gaussian-broadened excitonic transitions due to inhomogeneities such as composition and thickness fluctuations. The reference baseline for those fits was taken on the low energy side of each InGaN/GaN QW ER/PR spectrum as it allows avoiding uncertainties related with higher energy QW resonances. The PR linewidth of the 67 GaN/AlGaN MQW sample, which encompasses the A and B excitons, amounts to 24 meV and in the reflectivity

spectrum the A and B exciton transitions X_A and X_B can be clearly identified (cf. Fig. 4.9(e)). Note that for this sample a smaller Γ_{PL} than for the GaN/AlGaN SQW has been measured. This might be due to the higher carrier densities present in the SQW with respect to the MQW sample.
For the InGaN/GaN QWs the PR linewidth is significantly increased by more than a factor of 2 (cf. Figs. 4.9(a)-4.9(c), and Table 4.3). Furthermore, the SS value has been derived for all the investigated samples from both PL and ER/PR spectra (cf. Table 4.3). Thus SS values are about four to six times larger for InGaN/GaN QWs compared with GaN/AlGaN ones. We point out that when considering the corresponding LT reflectivity spectra the determination of the fundamental QW optical transition is hardly possible for the InGaN/GaN SQW sample and the 5 InGaN/GaN MQW sample. However, for the 4 × 5 InGaN/GaN MQW sample a weak optical transition feature can be identified both in the reflectivity and the transmission spectra shown in Figs. 4.9(c) and 4.9(f), respectively. For this latter sample the analysis of the PR spectrum (lineshape fitting) can be validated by the transmission measurement as the same SS value is deduced (cf. vertical dashed lines in Figs. 4.9(c) and 4.9(f)). Here we used the fact that the relative absorption coefficient can be computed from the natural logarithm of the transmission (cf. equation 3.5). The spectral position of the resonance was then obtained using equation 3.12, i.e., the QW absorption edge is just modeled by a sigmoid profile as no excitonic features can be resolved. Note that the height of the plateau is set by the kink observed in the transmission spectrum. In the absence of available transmission measurements for samples (a) and (b) due to the above-mentioned experimental issues, we can further make use of the consistency between the PR and transmission results obtained for the 4 × 5 InGaN/GaN MQW sample to confirm the position of the transition deduced from the PR fits performed for those low QW number samples since a similar approach was used for the PR lineshape fitting of all the samples. The precision in the SS values amounts to about 10 meV, which is reasonable given the involved broadenings. These results clearly show that with InGaN/GaN QWs the absorption linewidth is significantly increased compared to GaN/AlGaN ones (cf. Table 4.3). The Γ_{abs} values are estimated from LT PL linewidth measurements using the relation 4.5. Note that the larger Γ_{PL} value compared to γ_{PR} for the 5 InGaN/GaN and the 4 × 5 InGaN/GaN MQW samples could be explained by the fact that not all the QWs are probed via PR, which is a technique known to be mostly sensitive to the region close to the sample surface. Such an assumption is consistent with the fact that the difference between Γ_{PL} and γ_{PR} is larger for the 4 × 5 InGaN/GaN MQW sample. Here we wish to point out that even though the parameter C appearing in equation 4.9 is related to the oscillator strength of an optical transition, it is hazardous to compare its value from one sample to another. Indeed, it is extremely sensitive to: (i) the lateral extent of the modulation (spot size), (ii) the cap thickness which will affect the modulation depth, (iii) undesired PL collected by the photodiodes, which is not necessarily originating from the QWs, (iv) the thickness of barriers and/or interlayers that will affect the number of effectively probed QWs, (v) the surface roughness that can be responsible for parasitic light scattering. All those considerations indicate that any quantitative estimate of f_{osc} to draw a comparison between the present heterostructures would most likely be entailed by too large uncertainties, which explains why such an information is not given. As

a consequence, when combining the lower oscillator strength of the fundamental excitonic transition of InGaN/GaN QWs compared to that estimated for GaN/AlGaN ones (cf. section 3.3.4) and the significantly broader absorption lineshape, it appears that the SCR should prove much more challenging to achieve with the former active region.

4.3.5 Temperature-dependent studies of InGaN/GaN MQWs and bulk InGaN layers

In every semiconductor an increase in temperature results in a reduction of its bandgap (cf. section 1.1.2) and more energetic carriers. However, in the case of strongly disordered alloys such as InGaN based structures (MQWs or bulk ones) carrier localization leads to a particular temperature dependent behavior. As the absorption strength of the above-mentioned InGaN/GaN SQW is not sufficient to induce an optical signature when measuring PR spectra whatever the temperature, we will compare the above-mentioned 5 $In_{0.1}Ga_{0.9}N$ (2 nm)/GaN (3 nm) MQW sample to a bulk GaN layer and GaN/AlGaN QWs.

Temperature-dependence of 5 InGaN/GaN MQWs

From Fig. 4.10 the evolution of the Stokes shift as a function of temperature of a bulk GaN layer and of 5 InGaN/GaN MQWs, both grown onto high-quality c-plane FS-GaN substrates, can be deduced. In the case of the bulk GaN sample no Stokes shift is measured. In addition reflectivity (R) measurements reveal clear excitonic transitions. Note that the resolution of R spectra is improved with respect to that of PR spectra due to limitations of the PR setup (cf. Appendix A.3). However, two transitions can be readily identified in PR and R measurements corresponding to the fundamental A exciton ($X_A^{n=1}$) and the B exciton ($X_B^{n=1}$) transition. A third feature corresponding most probably to a mixture of three transitions, namely the C exciton ($X_C^{n=1}$) transition and the first excited states of the A exciton ($X_A^{n=2}$) and B exciton ($X_B^{n=2}$), can be identified [83]. However, the extraction of the exact position of the particular transitions from R measurements is only possible within an exciton-polariton model including spatial dispersion [266], which is beyond the scope of this work.

If one considers the best GaN/AlGaN SQWs in terms of narrow spectroscopic features, the observation of $X_A^{n=1}$ and $X_B^{n=1}$ transitions has been reported in low-temperature (T = 10 K) reflectivity and PL spectra [267, 268].
The situation is quite different for InGaN/GaN QWs. To our knowledge no sufficiently narrow spectroscopic features in order to distinguish between $X_A^{n=1}$ and $X_B^{n=1}$ have been reported yet in the latter material system. Furthermore, R measurements do not allow the extraction of any intrinsic transition related to the 5 InGaN/GaN MQWs under study.

Thus, in Fig. 4.10 temperature-dependent PL and PR measurements *only* are shown for the 5 MQW sample. In Figs. 4.10(e) and 4.10(g) the typical S-shaped temperature-dependent emission shift measured on the 5 InGaN/GaN MQW sample can be seen [269], which is com-

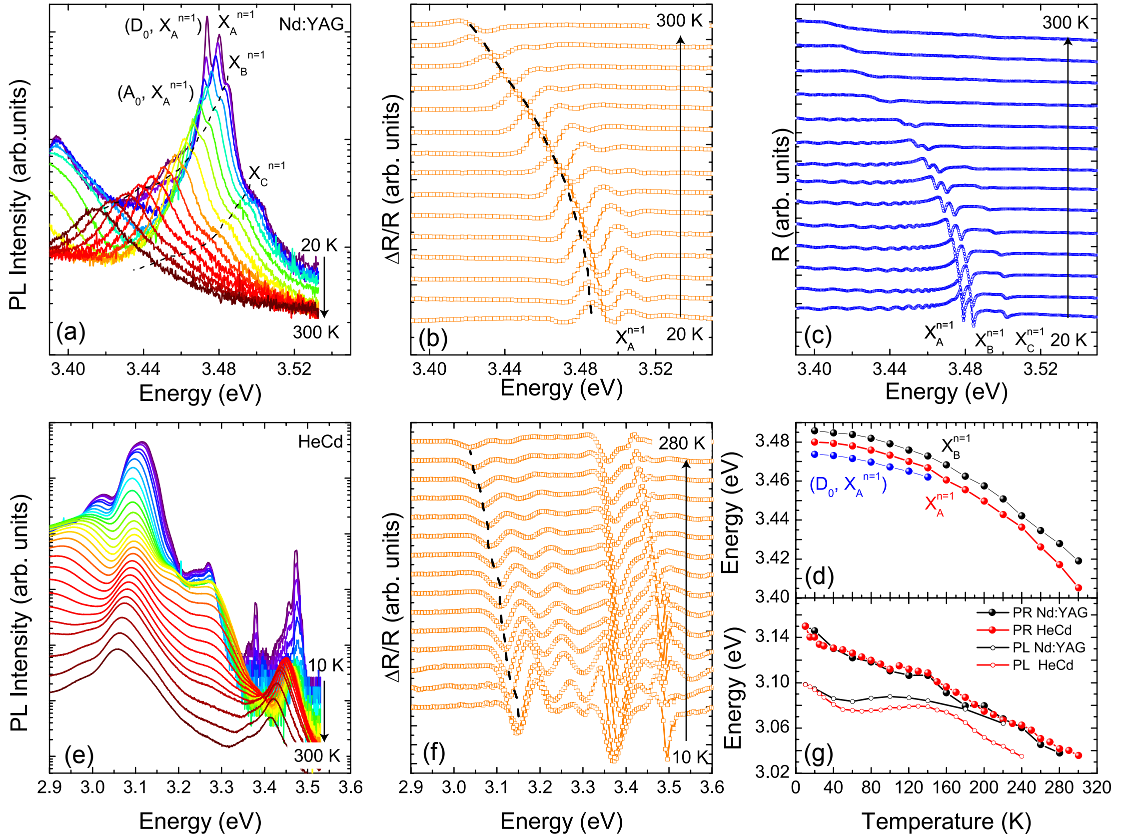

Figure 4.10: Temperature-dependent PL and PR measurements done on a bulk GaN layer (top row) and on 5 $In_{0.1}Ga_{0.9}N$ (2 nm)/GaN (3 nm) MQWs (bottom row): PL in (a) and (e), PR ($\Delta R/R$) in (b) and (f), and of reflectivity (R) in (c). (d) A exciton ($X_A^{n=1}$), B exciton ($X_B^{n=1}$), and the donor-bound (D_0,$X_A^{n=1}$) transition energy extracted from (a). (g) PR measurements shown in (f) are compared to PL measurements acquired under the same excitation conditions (not shown here).

monly attributed to a temperature-dependent carrier distribution among different localized states, also referred to as exciton hopping [243,270]. Note that such a PL behavior related to exciton hopping was initially revealed in InGaAs/InP and ZnCdSe/ZnSe QWs [271,272] and was accounted for in terms of incomplete thermalization of localized excitons at LT. The latter is also observed for bulk InGaN layers. Thus, the carrier dynamics occurring in such layers are further discussed in section 4.3.6.

We point out that in Fig. 4.10(g) PL measurements have been acquired under modulation conditions, i.e., under very low injection conditions using two different laser sources, namely a pulsed frequency-quadrupled Nd:yttrium aluminum garnet (Nd:YAG) laser (λ = 266 nm), providing a pulse length of 500 ps, a repetition rate of 8.52 kHz and a cw HeCd laser (λ = 325 nm). Beyond 240 K, nonradiative recombinations prevent the acquisition of PL spectra in this excitation regime. Furthermore, PL measurements acquired with the Nd:YAG laser do not overlap with those acquired with the HeCd likely due to different excitation conditions.

Power-dependent studies have also been performed on this 5 InGaN/GaN MQW sample and a behavior similar to that of the InGaN/GaN SQW sample (cf. section 4.3.2) has been found. In the temperature-dependent PR spectra of the 5 InGaN/GaN MQW sample several features are worth being mentioned: (i) the temperature dependence of the signature of the GaN bandgap (mainly due to the cap and barrier material) follows the conventional trend, as observed for bulk GaN (cf. Fig. 4.10(d)) and GaN/AlGaN QWs (not shown here), (ii) the fundamental QW transition probed in PR exhibits an anomalously large shift with temperature (~ 115 meV over the 10 to 300 K range) whatever the modulated laser type (either the pulsed Nd:YAG laser or the cw 325 nm HeCd laser) (cf. Fig. 4.10(g)), (iii) even at 300 K, there is no overlap between the PL and PR spectrum of the fundamental QW transition, contrary to the GaN/AlGaN QW case (not shown here). (iv) Several excited QW transitions appear between the fundamental QW transition and the signature of the bulk GaN layer. Their temperature dependence bears a resemblance to the fundamental transition for lower excited states and switches to a more or less conventional trend for the higher excited ones.

Using the empirical Varshni formula 1.9 we find a shift of 72 (24) meV for a temperature change from 10 to 300 K in GaN (InN). Thus, InGaN layers are expected to exhibit an intermediate value, which is not the case. An alternative explanation might be a significant change in the built-in field over temperature due to a different thermal expansion of the GaN barriers with respect to one of the $In_{0.1}Ga_{0.9}N$ QW layer. The variation in transition energy due to a change in the piezoelectric polarization[4] for an $In_{0.1}Ga_{0.9}N$/GaN SQW has been calculated using equation 1.5 but only between 50 and 300 K due to the accessible range for the temperature-dependent lattice parameters [273, 274]. A value of ~ 0.9 meV has been found and since a very small increase is expected between 10 and 50 K, this alternative explanation has to be withdrawn.

The observed shift might be ascribed to a screening of the QCSE by the injected carriers. Note however that, the injected carrier density (N_{2D}), given by:

$$N_{2D} = \frac{(1-R)AI_p\tau_x}{\pi r^2 h\nu}, \tag{4.11}$$

amounts to 3.2×10^7 cm^{-2}. The latter has been calculated using a reflectivity at the air-sample interface (R) equal to ~ 0.2, an absorption of the excitation source A equal to ~ 1, a τ_x value equal to that quoted in Table 2.1, an excitation spot radius r equal to 500 μm, and an excitation source (cw the HeCd laser with $h\nu = 3.81$ eV) intensity I_p equal to 200 μW . Note that such a low carrier density should not affect the transitions of the QW, as carrier densities above ~ 10^{11} cm^{-2} are expected to induce partial screening of the built-in electric field of such QWs [275]. However, it is possible that locally strongly inhomogeneous carrier densities are present, due to carrier localization, and shift the fundamental QW transition measured in PR spectra. Since

[4] We expect the change in spontaneous polarization with temperature to be negligible (cf. section 1.1.1).

with increasing temperature nonradiative channels start to play an important role, the carrier density in the QW is reduced, thus mitigating the effect on the PR spectra.

Franz-Keldysh oscillations

The latter explanation can be further supported by temperature-dependent PR measurements performed on thick InGaN layers. Several 100 nm thick InGaN layers with In contents in the 2-18% range have been grown onto high-quality FS-GaN substrates. As an illustration, in Fig. 4.11 temperature-dependent PR measurements done on a 100 nm thick $In_{0.07}GaN_{0.93}N$ layer are shown. Above the $In_{0.07}GaN_{0.93}N$ band edge strong FKOs are observed. At the InGaN/air interface the Fermi-level pinning by surface states of intrinsic origin (dangling bonds) and/or extrinsic origin (e.g., presence of a native oxide on the surface) and the presence of surface charges can result in a band bending. The origin of the surface charges is related to the total polarization of the InGaN layer, its impurity concentration, or rather its doping. The composition dependence of the Fermi-level pinning at the oxidized surfaces of n-type $In_xGa_{1-x}N$ films has been investigated by X-ray photoemission spectroscopy. The band bending magnitude, i.e., the barrier height (Φ_B) was estimated to be composition-dependent as follows [276]:

$$\Phi_B = 0.53 - 2.1x + 0.95x^2. \tag{4.12}$$

Note that a positive Φ_B value corresponds to an upward band bending and a positive surface charge density. Thus, ionized impurities are distributed over a depletion width (w):

$$w = \sqrt{\frac{2|\Phi_B|\epsilon_r\epsilon_0}{eN_d}}, \tag{4.13}$$

where N_d is the donor concentration. Furthermore, from Poisson's equation an electric field whose magnitude varies linearly with the distance from the surface (z) is deduced:

$$F(z) = -\frac{eN_d}{\epsilon_r\epsilon_0}(w - z). \tag{4.14}$$

PR and ER spectra allow the extraction of a mean value for the latter, i.e., [277]:

$$F_{FKO} = \frac{eN_d w}{2\epsilon_r\epsilon_0} = \frac{\Phi_B}{w} = \sqrt{\frac{|\Phi_B|eN_d}{2\epsilon_r\epsilon_0}}. \tag{4.15}$$

The magnitude of this electric field can be derived from the oscillatory behavior of the PR or ER spectra observed above the bandgap (FKOs). A commonly used method is illustrated in Fig. 4.11(b), in which the Franz-Keldysh extremum position $4/(3\pi)\cdot(E_j\text{-}E_g)^{3/2}$ is plotted over its index (j). The extracted positions follow approximately a straight line with a slope S, which is

related to the electric field by:

$$S = (\hbar\Theta)^{3/2} = \frac{\hbar e F_{FKO}}{(2\mu^*)^{1/2}}. \quad (4.16)$$

A more convenient method is based on the fitting of equation 4.9 with $m = 3$ to account for Gaussian broadened excitonic transitions and equation 4.8 to account for FKOs above the band edge to the experimental spectra. The two methods give consistent results: the field increases with temperature by almost a factor two. This effect might be related to an enhanced screening by injected carriers at low temperatures, as already advanced to account for the particular temperature-dependent behavior observed in the PR measurements of the 5 InGaN/GaN MQW sample. Note that at RT the extracted field (F_{FKO}) amounts to ~ 100 kV/cm. It has the same magnitude than the one extracted from contactless electroreflectance (CER) studies performed on non-intentionally doped GaN layers [277]. For non-intentionally doped GaN the electron background concentration is about ~ 10^{17} cm^{-3} [278]. Indeed, using

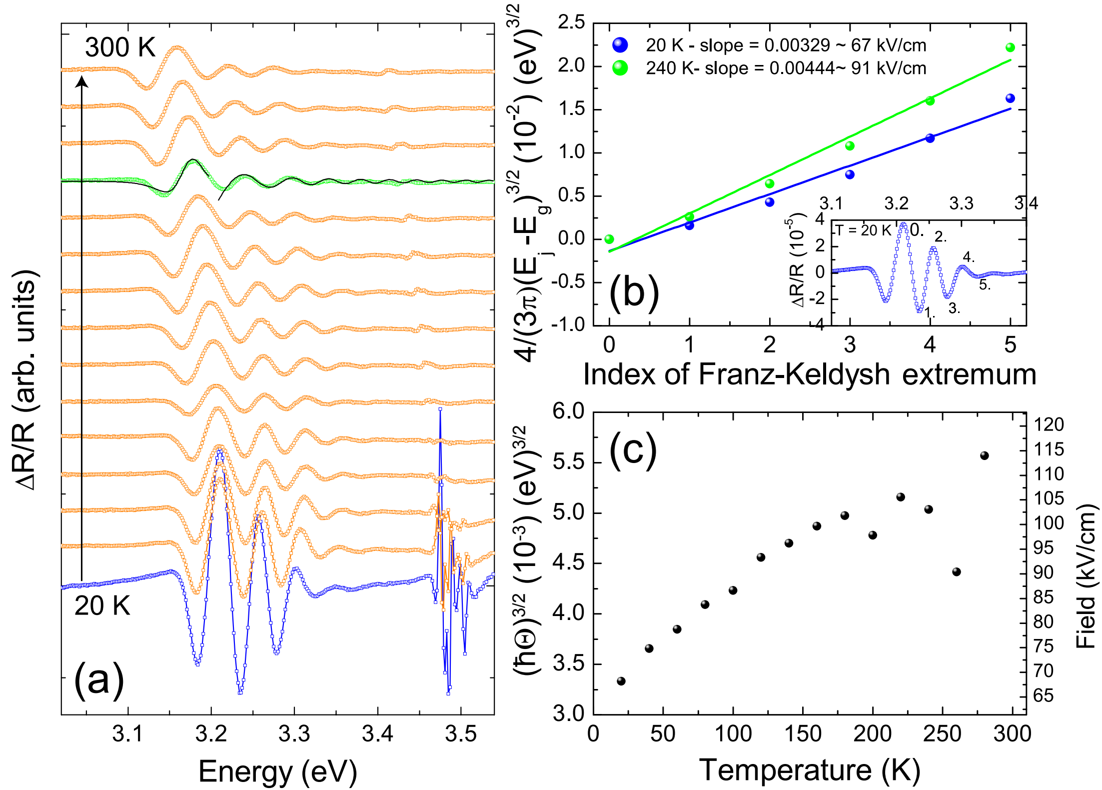

Figure 4.11: (a) Temperature-dependent PR measurements performed on a 100 nm thick $In_{0.07}Ga_{0.93}N$ layer. (b) Analysis of PR extrema according to Aspnes [255, 256] for two different temperatures (20 and 240 K): The position of FKO-extrema ($(E_j$-$E_g)^{3/2}$) extracted as illustrated in the inset over its index results in a straight line, whose slope is proportional to the electric field (cf. equation 4.16). (c) Temperature-dependent field (electro-optic energy $\hbar\Theta$) originating from surface charges extracted from fitting using equations 4.9 with $m = 3$ and 4.8 to experimental spectra. An example of such a fit is given for $T = 240$ K in (a).

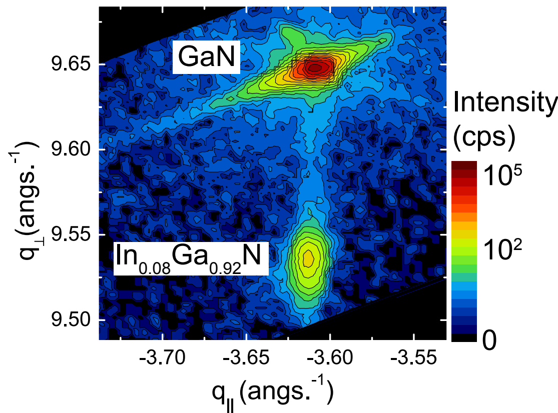

Figure 4.12: Reciprocal space map of the asymmetric GaN (10-15) reflex of a 100 nm thick InGaN layer grown on FS-GaN substrate. Courtesy of Dr. Lise Lahourcade (LASPE-EPFL).

equations 4.12 and 4.15 a value of ~ 2×10^{17}cm^{-3} is found for the carrier concentration of our $In_{0.07}Ga_{0.93}N$ layer. Note that the interpretation of C-V measurements performed on low In content layers ($x \lesssim 0.1$) proved to be difficult. However, a carrier concentration of ~ 3×10^{18}cm^{-3} was deduced for a 100 nm thick $In_{0.2}Ga_{0.8}N$ layer.
Note that PR measurements acquired under the same modulation conditions (i.e., the same I_p) have been performed on all 100 nm thick InGaN layers. However, FKOs have not been systematically observed including the case of bulk GaN (cf. Fig. 4.10(b)). The latter might be explained by the dependence of w ($w \propto \sqrt{\Phi_B}$, cf. equation 4.13) with In content. For layers without In or with a low In content w is relatively large and the amount of injected carriers is not sufficient to achieve PR spectra in the intermediate regime (cf. section 4.3.4). However, if the In content is increased w decreases and the depletion layer field is screened more efficiently by the same amount of injected carriers. Thus, PR spectra can be recorded in the intermediate regime and FKOs above the band edge are visible. Note that I_p cannot be arbitrarily chosen, as PR spectra are acquired under modulation conditions allowing for an optimal signal to noise ratio (cf. Appendix A.3). For a more systematic study of the electric field in such layers CER seems a more suitable technique [277] but it is more time-consuming to implement.

Temperature-dependence of InGaN bulk layers

Several 100 nm thick InGaN layers with different In contents ranging between 2 and 18% have been grown on FS-GaN substrates. In a first attempt the In content has been determined by XRD measurements. A detailed analysis of reciprocal space mappings of such layers has been done by my colleague Dr. Lise Lahourcade (LASPE-EPFL) and will not be presented hereafter. However, in Fig. 4.12 a reciprocal space map of the asymmetric GaN (10-15) reflex of a 100 nm thick InGaN layer grown on FS-GaN substrate is shown, indicating no strain relaxation. Its In content is approximatively 8%. Furthermore, energy-dispersive X-ray (EDX) spectroscopy measurements have been performed to get rid of strain issues in the determination of the In content. A brief discussion about the determination of the In content is given later and in a first attempt reference is made to the In contents determined by EDX measurements.

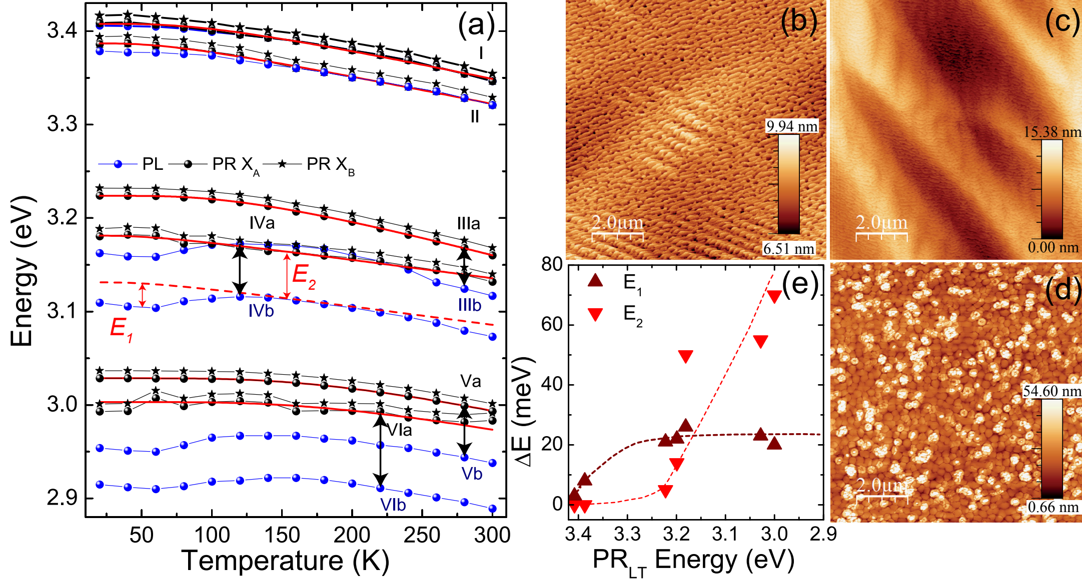

Figure 4.13: (a) Temperature-dependent behavior of the bandgap of 100 nm thick InGaN layers with six different In contents ranging between 2 and 12% deduced from PL and PR measurements. It is best accounted for when using equation 1.10 (red lines) and the corresponding fitting parameters are listed in Table 4.4. (b)-(d) 10×10 μm^2 AFM scans of InGaN layers with 2, 10, and 18% of In, respectively. (e) Localization energies versus E_g deduced from PR measurements (PR$_{LT}$). Note that the brown and red lines are a guide to the eye.

The temperature-dependent behavior of the bandgap of such layers deduced from PL and PR measurements are shown in Fig. 4.13(a). It is best accounted for when using equation 1.10 instead of the usual Varshni formula (cf. red lines in Fig. 4.13(a)). The corresponding parameters $E_g^{PR}(T = 0$ K), a_{BE}^{PR}, and Θ_{BE}^{PR} are listed in Table 4.4 together with the In content determined by EDX measurements. On every sample complementary temperature-dependent transmission measurements have been performed and the corresponding parameter set ($E_g^T(T = 0$ K), a_{BE}^T, Θ_{BE}^T) is listed as well in Table 4.4. Note that equation 1.10 has been successfully applied to the case of AlGaN alloys. Brunner *et al.* [182] showed that the temperature-dependent bandgap reduction was independent of the Al content. Such a situation does not occur in InGaN alloys: θ_{BE} seems to increase with the In content, whereas a_{BE} fluctuates around a value of 0.35 ± 0.08. Even though care was taken to probe the same sample region in PR and in transmission measurements, the parameter sets ($E_g(T = 0$ K), a_{BE}, Θ_{BE}) do not overlap completely. This can be easily understood, as for layers with increasing In content spatial fluctuations in the In incorporation cannot be neglected anymore, as discussed further below. However, the difference in the parameter set of GaN with respect to the one of sample I (2% InGaN layer) and the anomalous parameter set deduced from PR measurements for sample IV remain open questions.

Note that for layers with an In content below 4% very sharp excitonic transitions were measured at LT (≤ 20 K). Excitonic features related to X_A and X_B have been clearly resolved in LT

PR, PLE and transmission spectra. The LT PLE spectrum of an InGaN layer with 2% of In is shown in Fig. 4.14(a). Furthermore, the biexciton (XX) transition is seen in the corresponding LT PL spectrum achieved under high injection PLE excitation conditions using an optical parametric oscillator system operating at 350 nm and 1.5 kW cm^{-2}. The latter has been validated through power dependent studies (not shown here). In agreement with LT PR measurements a Stokes shift of ~ 7 meV is revealed from the comparison of the X_A transition observed in PL and in PLE. Furthermore, the S-shaped temperature-dependent emission shift is not observed for such low In content layers and the Stokes shift at RT (labeled E_2 in Fig. 4.13(a)) is equal to 0 (cf. sample I and II in Fig. 4.13(a)). However, with increasing indium content the Stokes shift increases. For layers with an In content above ~ 7% a significant Stokes shift is measured at RT (cf. sample IV in Fig. 4.13(a)). In Fig. 4.13(a) the Stokes shift observed between PR and PL spectra of sample IV is tentatively attributed to two different localization effects characterized by two different localization energies (E_1 and E_2). E_1 corresponds to the minimum in the S-shaped emission shift located between 20 and 150 K. E_2 determines the localization above ~ 150 K. Comparing the experimental results of samples V and VI presented in Fig. 4.13(a), it can be seen that they are characterized by a similar value of E_1, whereas E_2 is clearly increased for sample VI. In Fig. 4.13(e) E_1 and E_2 versus decreasing LT PR energy, i.e., increasing In content, are plotted. E_1 saturates above ~ 3.2 eV, corresponding to an In content of ~ 10%. On the other hand E_2 starts to strongly increase above the latter In content. Before providing an interpretation for the particular behavior of E_1 and E_2 with increasing indium content (cf. section 4.3.6), the crystalline quality of such layers has to be investigated.

When increasing the indium content, a progressive degradation of the surface quality is clearly seen on 10×10 μm^2 AFM scans (Figs. 4.13(b) to 4.13(d)). For In contents ≥ 15% an even stronger degradation is expected as the critical thickness for relaxation is clearly crossed. According to M. Pristovsek [223] (cf. Fig. 4.2) the critical In content for 100 nm thick InGaN layers grown on GaN leading to relaxation is ~ 6%. Indeed, a pronounced wavelike (or valley-hill)

Sample	In content (EDX)	E_g^{PR} (T = 0 K)	a_{BE}^{PR} (meV/K)	Θ_{BE}^{PR} (K)	E_g^{T} (T = 0 K)	a_{BE}^{T} (meV/K)	Θ_{BE}^{T} (K)
GaN	0	3.503	0.53	437	-	-	-
I	0.02	3.408	0.31	290	3.408	0.32	220
II	0.03	3.387	0.31	203	3.387	0.32	203
III	0.08	3.224	0.44	390	3.186	0.44	397
IV	0.09	3.181	0.2	168	3.144	0.44	376
V	0.11	3.029	0.39	635	3.032	0.29	422
VI	0.12	3.003	0.35	650	2.946	0.44	493

Table 4.4: Parameters related to Fig. 4.13(a) ($E_g^{PR}(T = 0$ K), a_{BE}^{PR}, Θ_{BE}^{PR}) and to temperature-dependent transmission measurements ($E_g^{T}(T = 0$ K), a_{BE}^{T}, Θ_{BE}^{T}) . The parameters a_{BE} and Θ_{BE} of equation 1.10 characterize the temperature-dependent bandgap reduction. The parameters for the GaN layer are obtained from the experimental data displayed in Fig. 4.10(e).

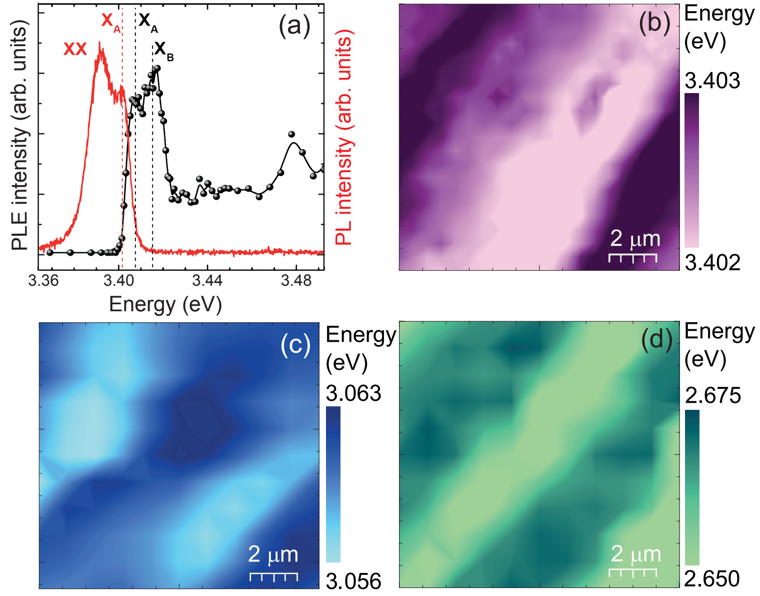

Figure 4.14: (a) LT PLE (black dots) and PL (red line) spectra measured on an InGaN layer with 2% of In. The vertical dashed lines indicate the position of the various excitonic resonances. (b)-(d) LT μ-PL mapping (10×10 μm^2) of InGaN layers with 2, 8, and 15% of In, respectively. Courtesy of Dr. Lise Lahourcade (LASPE-EPFL).

morphology is observed in 10×10 μm^2 AFM scans of InGaN layers above such an In content (see e.g., Fig. 4.13(c)). Another interesting aspect of such layers is that their spatial emission pattern is found to be strongly dependent on their surface morphology. In Figs. 4.14(b) to 4.14(d) LT μ-PL mappings (10×10 μm^2) measured on the InGaN layers, whose AFM scans are presented in Figs. 4.13(b) to 4.13(d), are shown. As seen in the AFM scan of Fig. 4.13(c) the mappings reveal a periodic modulation of the emitted light. The magnitude of the latter increases with the In content of the layer. Such a behavior is not surprising knowing that the In incorporation strongly depends on the offcut orientation given here by the wavelike morphology [217, 218].

4.3.6 Discussions: intrinsic and extrinsic properties of InGaN alloys

In order to elucidate the spectroscopic measurements of this chapter the intrinsic and the extrinsic properties of InGaN alloys have to be discussed. Hereafter we mean by intrinsic properties those of a perfect InGaN alloy, characterized by a random distribution of cations, free from any defect states. We relate extrinsic properties to carrier dynamics including localization and diffusion within such a perfect alloy.

The ideal InGaN alloy: random distribution of cations

If a stochastic distribution of indium atoms at the atomic scale is considered, the InGaN alloy might be treated in the following way: indium atoms are distributed randomly on cation sites of the InGaN alloy, as suggested by Galtrey *et al.* [245]. A binomial distribution can be used to estimate composition fluctuations, which depend on the standard deviation of a random variable. Let us take as random variable the composition $X = N/n$, where N is the number

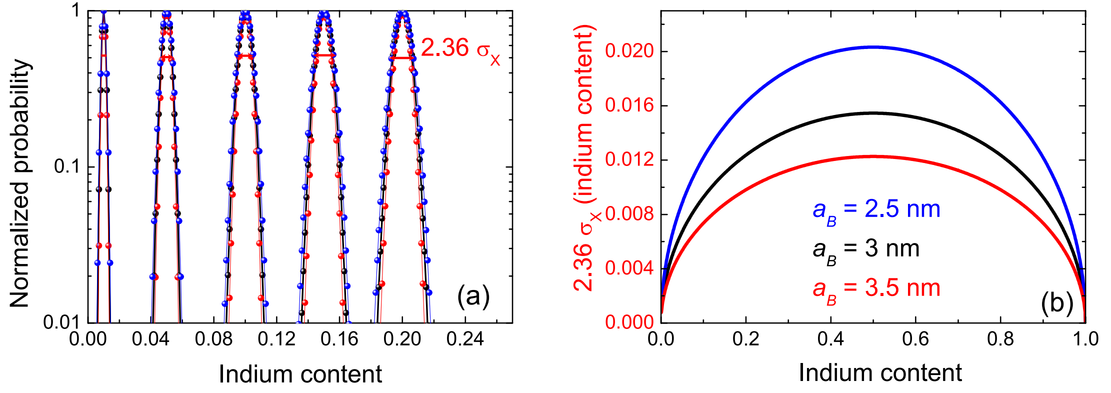

Figure 4.15: Random InGaN alloys following a binomial distribution: (a) composition fluctuations in the In content are calculated for a nominal In content of 1, 5, 10, 15, and 20% using bins of 4603, 5800, and 7624 atoms corresponding to a_B of 2.5, 3, and 3.5 nm (blue, black, red). For all contents the distribution is normalized. (b) Corresponding FWHM (2.36·σ_x) of the distributions plotted against the nominal In content.

of indium atoms within a bin of n cations (trials) and by itself a random variable [279]. The mean alloy composition (nominal indium content) is expressed as p, the fraction of group III sites occupied by In atoms rather than Ga ones. The probability to find k indium atoms among n cations is:

$$P(N=k) = \binom{n}{k} p^k (1-p)^{n-k}. \tag{4.17}$$

Note that the standard deviation of N is given by $\sigma_N = \sqrt{np(1-p)}$. Thus, the standard deviation of X (σ_X) is given by:

$$\sigma_X = \sqrt{\frac{p(1-p)}{n}}. \tag{4.18}$$

From equation 4.18 one can see that σ_X increases with increasing nominal indium content, as illustrated in Fig. 4.15(a) for $n = 4603$, 5800, and 7624 . Note that n corresponds to an average number of cations within the excitonic volume V_{exc}. V_{exc} is approximated as a sphere with a radius equal to the exciton Bohr radius, which is taken equal to 2.5, 3, and 3.5 nm.[5]
The absorption line broadening is expected to increase with the indium content, i.e., $\Gamma_{abs} \propto 2\sqrt{2ln2}\sigma_X = 2.36\sigma_X$, up to a content of 0.5 (cf. Fig. 4.15(b)). Note, that an increase of Γ_{abs} with indium content has been predicted as well in a recent theoretical work, due to numerous possible configurations for the indium atoms within a 16-atom supercell, each of them being characterized with a different energy gap [280].

[5]Note that the volume of an elementary cell in wurtzite GaN is about $V_{ec} \sim 0.3 \cdot 0.3 \cdot \sin(60°) \cdot 0.5 \sim 0.039$ nm^3. V_{ec} contains 2 cations and as $V_{exc} \sim 113$ nm^3 for $a_B = 3$ nm, the exciton is sensitive to ~ 5800 cations.

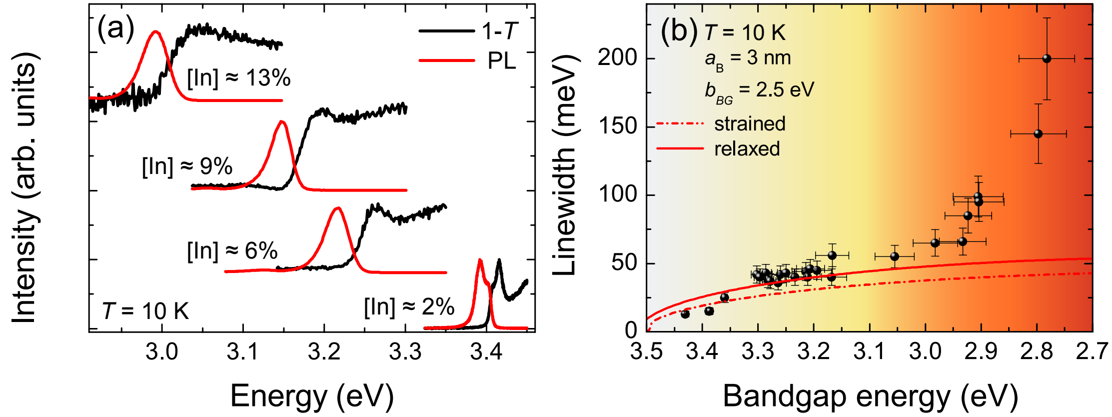

Figure 4.16: (a) LT transmission vs PL measurements of 100 nm thick InGaN layers with In contents ranging between 2 and 13% and (b) the corresponding LT FWHM of the transmission spectra plotted against E_g deduced from the latter (absorption energy). Courtesy of Dr. Lise Lahourcade (LASPE-EPFL).

LT transmission measurements performed on 100 nm thick InGaN layers together with corresponding PL measurements recorded on the same spot are displayed in Fig. 4.16(a). The linewidth of LT transmission measurements, which is proportional to Γ_{abs}, has been extracted and its value versus the deduced E_g, i.e., the In content, is plotted in Fig. 4.16(b). Note that for all transmission measurements the same fitting procedure has been used: two Gaussians separated by 8 meV, accounting for the X_A and X_B transition, are convoluted with a sigmoid profile of the same broadening and shifted in energy by the exciton binding energy. For the exciton binding energy a linear interpolation between the GaN and InN values has been used. The transmission linewidth (black dots) increases with the In content. Furthermore, the transmission linewidth (Γ_T) might be compared to [281]:

$$\Gamma_T(x) = 2.36 \left| \frac{\partial E_g}{\partial x} \right| \sigma_X, \tag{4.19}$$

where $|\partial E_g / \partial x| = |E_{g,InN} - E_{g,GaN} - b_{BG}(1-2x)|$. Therefore, in Fig. 4.16(b) equation 4.19 is plotted using bandgap values reported in Table 1.2, $b_{BG} = 2.5$ eV, and $a_B = 3$ nm (red lines). $K.p$ calculations performed by Georg Rossbach (LASPE-EPFL) allow to distinguish relaxed from strained layers (solid vs dashed lines, respectively). Note that the low In content layers (2-3%) are fully strained, whereas those at $\sim 4\%$ do show partial relaxation in reciprocal space mappings. Furthermore, their Γ_T fits not too badly the strained line (red dashed line). For intermediate In content layers experimental data rather follows the relaxed line (red solid line), whereas a clear deviation from the binomial approximation is seen for layers with increasing In content, i.e., their linewidth lies above the red solid line. The latter already occurs at an In content of $\sim 12\%$, where strong degradation of the crystalline quality of such layers is expected.

Hereafter the choice of the values of a_B and b_{BG} is discussed. Note that the experimental

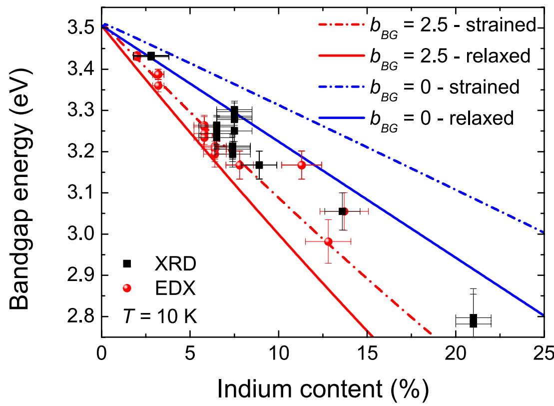

Figure 4.17: Bandgap energy as determined by LT (T = 10 K) transmission measurements vs In content deduced from reciprocal space mappings (black squares) and EDX measurements (red dots) compared to situation of bandgap bowing $b_{BG} = 0$ and $b_{BG} = 2.5$ eV for the relaxed and strained case.

determination of a_B in InGaN layers is far from being trivial. A change with the In content is generally expected. However, in a first attempt a constant value of 3 nm has been taken as quoted for GaN layers by S. F. Chichibu *et al.* [84].
The bandgap energy deduced from LT transmission measurements vs the In content deduced from reciprocal space mappings and EDX measurements is plotted in Fig. 4.17. The experimental data are compared to $k.p$ calculations of the bandgap evolution at 0 K for b_{BG} equal to 0 and 2.5 eV for the strained and the relaxed case (dashed and solid lines, respectively). From this comparison it is challenging to conclude on the value of b_{BG} and the layers' strain state. Note that in our EDX measurements the probed region ($\sim 50 \times 50\ \mu\text{m}^2$) is much smaller than the one probed by XRD ($\sim 1 \times 1$ mm^2) or transmission measurements ($\sim 0.5 \times 0.5$ mm^2). Thus, it would be more relevant to perform a statistical analysis of EDX measurements. On the other hand, segregation or composition gradients, which occur in high In content layers (starting from ~ 10%), complicate the interpretation of XRD measurements. Thus, it would be also interesting to investigate strained layers over the same composition range. Such a study would provide a more representative value for b_{BG}.
Note that the energy-gap bowing parameter b_{BG} of $In_xGa_{1-x}N$ is as well a matter of debate in the literature. In a recent theoretical paper composition-dependent bowings of the gaps were found [282]. The authors estimate the bowing to range from 1.7 (large x) to 2.8 eV (small x) and being equal to 2.1 eV for $x = 0.5$ in the case of a uniform, i.e., a non 'clustered', $In_xGa_{1-x}N$ alloy.

In conclusion, the simple model based on a stochastic distribution of indium atoms within InGaN layers suggests a steep absorption linewidth increase in the UV region but a more moderate one in the visible spectral range. On this basis, the following suggestion might be forwarded: gain dilution in green laser diodes should not be much higher than in blue laser diodes provided that the In content within the QWs is homogeneous and abrupt interfaces are present. This is confirmed by a constant material gain reported lately at the SPIE Photonics West conference (February, 2014) by OSRAM between 450 and 520 nm. Note that a strong inhomogeneity in the In content within the QWs might drastically increase the absorption linewidth and thus it has to be avoided.

Carrier dynamics

According to Fig. 4.15(a) the exciton in low In content layers does not feel large composition fluctuations. However, localization is observed over the whole composition range (only at LT for low In content layers). Kent and Zunger [284] predicted strong hole localization on randomly formed In-N-In-N-In-N zigzag atomic chains along the [110] direction in cubic InGaN and along the [11$\bar{2}$0] one for the hexagonal case. Chichibu *et al.* [243] concluded using monoenergetic positron annihilation spectroscopy that localization of holes (positrons) occurs at atomic condensates of In-N of spatial extent smaller than 4 nm. In Fig. 4.18 three different situations of positron localization in a defect-free statistically homogeneous InGaN alloy are schematically represented: (a) slight localization due to trapping by a single In atom, (b) localization occurring on an In-N-In-N-In-N zigzag chain, and (c) strong localization by a randomly formed atomic condensate of In-N (Adapted from Chichibu *et al.* [243]). Furthermore, the authors measured the positron diffusion length (L_+) at RT for InGaN layers with different In contents, e.g., for a 200-nm-thick nearly strain-relaxed (0001) $In_{0.05}Ga_{0.95}N$ film grown on GaN/(0001) Al_2O_3 a value of ~ 4 nm is found for L_+. As a positron is positively charged, positrons and holes suffer from similar Coulomb potential environments and thus the hole diffusion length ($L_{diff,h}$) might be of the order of L_+. If the latter is indeed the case, excitonic diffusion occurs at a nanometric scale and thus no interdiffusion between the valleys and hills observed in AFM (cf. Figs. 4.13(b)-4.13(d)) is possible. However, the morphology does have an influence on the measured transmission and PL spectra due to the diffraction

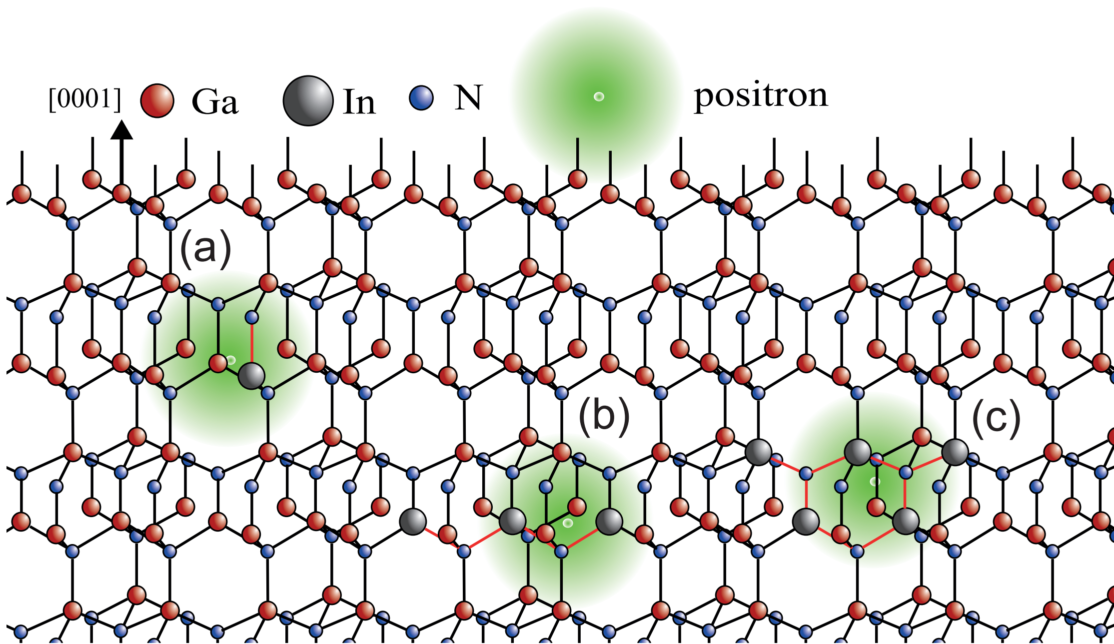

Figure 4.18: A positron in defect-free statistically homogeneous InGaN alloy might be trapped by (a) a single In atom [283], (b) an In–N-In–N–In– zigzag chain [242, 284] spontaneously formed along the [11$\bar{2}$0] direction, or (c) by atomic condensates of In–N whose size is larger than the chain in (b). Adapted from Chichibu *et al.* [243].

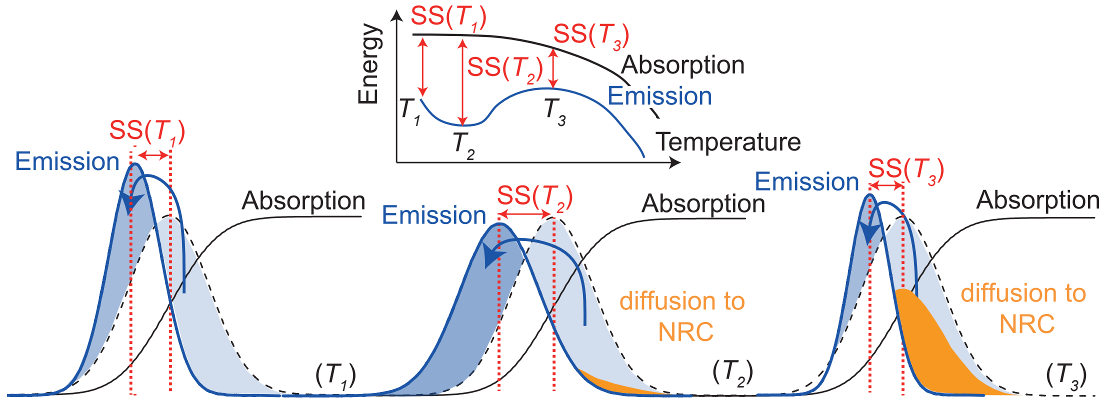

Figure 4.19: Illustration of the S-shaped temperature-dependent emission shift: (T_1) the black dashed line corresponds to the initial distribution. Thermally activated carriers (light blue area) diffuse to lower energy band-tail states (dark blue area) producing a slight Stokes shift (SS(T_1)). (T_2) Further increasing the temperature results in an increased diffusion enabling carriers to reach energetically deep trapping states. (T_3) Diffusion to nonradiative recombination centers (NRC) starts to play a role. Thus, $L_{diff,h}(T_3)$ is reduced and the lowest trapping states cannot be reached anymore.

limited size of the spot, having an averaging effect.

When performing temperature-dependent PL measurements several interdependent parameters have to be considered: the carrier diffusion length (respectively, $L_{diff,h}$),[6] the diffusion constant (D), the carrier lifetime (τ), and thermally activated detrapping and tunneling. Note that those parameters are temperature-dependent and related to each other by $L_{diff,h}(T) = \sqrt{D(T) \cdot \tau(T)}$. The common explanation of the S-shaped temperature-dependent emission shift is the following [269]: (i) the diffusion constant D increases with temperature [286] without strongly affecting the carrier lifetime. Thus, $L_{diff,h}(T)$ increases and thermally activated carriers are able to reach lower energy band-tail states (or trapping states), i.e., randomly formed atomic condensates of In–N, before recombining. The latter, depending on the In content of the alloy, results in a pronounced redshift of the emission, as illustrated in Fig. 4.19 from T_1 to T_2. (ii) D further increases but due to the increased temperature nonradiative processes become important, i.e., the carrier lifetimes decrease greatly with increasing temperature. Thus, $L_{diff,h}(T)$ decreases and these carriers recombine before reaching the lower energy band-tail states. The latter, depending on the In content of the alloy, results in a pronounced blueshift of the emission as illustrated in Fig. 4.19 from T_2 to T_3. Simply put, the observed blueshift is based on the onset of thermalization, i.e., carriers rise to their thermal average [270, 281].

The two localization energies E_1 and E_2 observed in the previous section (cf. section 4.3.5) are parameters related to carrier dynamics and as well to intrinsic material properties (e.g., Γ_{abs}). When using a macroscopic probe the observed S-shaped temperature-dependent emission

[6] Carrier diffusion is mainly due to hole diffusion [243, 285].

shift reflects an averaged situation. However, carrier dynamics take places at a nanometric scale. The increase of E_2 with In content is a commonly observed behavior as well observed in QW structures related to an increasing number of energetically deep trapping states (cf. Fig. 4.15(a)). However, the saturation of E_1 is staggering and not observed in QW structures. Note that the localization mechanisms are likely different in QWs as they further suffer from strong built-in electric fields. The saturation of E_1 might be related to the crystalline quality of the layers. A possible explanation might be an increase of nonradiative recombinations, reducing the carrier lifetime and the probability to reach lower energy tail states. The increase in nonradiative recombinations is supported by a decreasing internal quantum efficiency η_{int} above an In content of ~ 10%. Note that η_{int} is approximated as the spectrally integrated PL intensity at 300 K divided by that at 20 K (Ref. [145]). However, in order to elicit the latter, temperature-dependent time-resolved measurements are indispensable. Note that such measurements are foreseen in our laboratory in a near future.

4.4 Summary of the results

Aiming a reduced inhomogeneous broadening, which limits gain dilution in III-nitride MQW EELDs and which is also a prerequisite for strong coupling applications, the optimal growth conditions for various thin low In content $In_xGa_{1-x}N(x \sim 0.1)$/GaN QWs grown on FS-GaN substrates have been investigated. Furthermore, a low excitonic disorder has been measured at the microscopic scale for such SQWs. The critical thickness for relaxation for an $In_{0.12}Ga_{0.88}N$ (2 nm)/GaN (3 nm) MQW structure has been estimated using two different approaches (LT CL and LT μ-PL linescans) to exceed 160 nm, i.e., a thickness corresponding to a critical QW number of ~ 30. In order to circumvent this problem a promising solution for the active region based on GaN interlayers has been implemented.

The nature of localization in InGaN/GaN MQWs and InGaN bulk layers has been critically discussed and individual localization centers of an $In_{0.1}Ga_{0.9}N$/GaN SQW have been probed by LT μ-PL measurements, amongst others with subwavelength lateral resolution. LT absorption-like (PR and ER) measurements have been performed on various $In_{0.1}Ga_{0.9}N$/GaN QWs, ranging from the SQW case to a set of several MQWs, and a comparison has been drawn with their GaN counterparts. For InGaN/GaN QWs, the PR linewidth has been found to be significantly increased by more than a factor of 2. Furthermore, a systematic increase in the inhomogeneous linewidth (of emission and absorption) with increasing number of wells was revealed. Various possible reasons for this degradation such as inhomogeneous built-in field distribution among the QWs and a large sensitivity to strain fluctuations have been identified.

The intrinsic and extrinsic properties of $In_{0.1}Ga_{0.9}N$/GaN MQWs have been probed by temperature-dependent absorption-like (PR) and PL spectroscopy,

respectively. A particular temperature-dependent behavior has been found, which could be explained by a large sensitivity of such QWs to a few injected carriers. The latter explanation has been further supported by temperature-dependent absorption-like (PR) measurements performed on thick InGaN layers. Various 100 nm thick InGaN layers with In contents ranging between 2 and 18% have been compared to a model based on a stochastic distribution of indium atoms at the atomic scale. The model failed for layers with In contents above ~ 12% as such layers suffer from detrimental strain relaxation. For low In content layers ($x < 12\%$) the model holds. On this basis, the follwing suggestion is forwarded: gain dilution in green laser diodes should not be much higher than in blue laser diodes provided that the In content within the QWs is homogeneous and abrupt interfaces are present.
Furthermore, two localization energies have been identified and attributed to originate from carrier dynamics taking place at the nanometric scale.

5 Light-matter interaction in InGaN-based microcavities

In this chapter the light-matter interaction in $In_xGa_{1-x}N$/GaN MQWs and $In_xGa_{1-x}N$ bulk layers with $x \sim 0.1$ when inserted in III-nitride based MCs are analyzed. First the MC structures are designed, carefully fabricated, then their material quality is assessed by means of XRD, AFM and SEM, and finally spectroscopic measurements allow to determine their coupling regime (weak or strong coupling).
In a last section various mechanisms leading to stimulated emission in InGaN based electrically- or optically- pumped structures are critically discussed.

5.1 Semihybrid MC structures

The optimum semi-hybrid MC structure design as deduced from TMS (cf. section 3.3.1), i.e., the 3λ MC structure based on 5×5 $In_{0.1}Ga_{0.9}N$ (2 nm)/GaN (3 nm) MQWs is schematically drawn in Fig. 5.1(a).[1] In addition, a $3\lambda/2$ semi-hybrid MC based on a thick $In_{0.12}Ga_{0.88}N$ (73 nm) layer positioned at a cavity light field antinode will be considered (cf. Fig. 5.1(b)). With a thickness of 73 nm, the layer does not suffer from the detrimental QCSE normally present in QW structures with thick QWs. In Table 5.1 the two MC structures are compared. Note that as for bulk material the oscillator strength ($4\pi\alpha_{X_A}$ or $4\pi\alpha_{X_A}\omega_0^2$) is commonly given as dimensionless quantity or in $(eV)^2$, respectively [98, 102, 287] (cf. equation 3.16). In order to compare f_{osc} of the two structures, it is convenient to calculate f_{osc} in $(eV)^2$: for the QW case

[1] A schematic drawing and a SEM image of this structure have already been shown in Figs. 3.11(c) and 4.5(d), respectively.

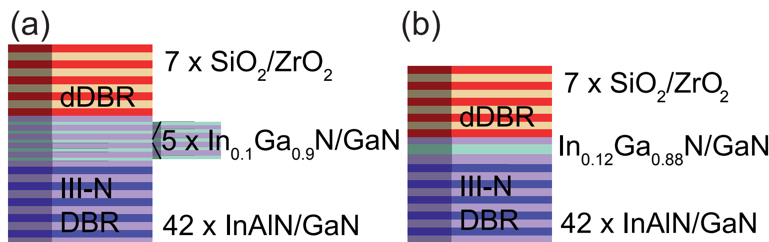

Figure 5.1: Schematic drawings of (a) a 5×5 InGaN/GaN MQW based semi-hybrid and (b) an thick InGaN layer based semi-hybrid MC structure.

MC	MQW based SH	bulk based SH
optical cavity thickness	3λ	$3\lambda/2$
N_{QW}	5×5	-
L_{eff} (nm)	1044	794
f_{osc}	slightly reduced	~ bulk GaN
	$f_{osc}^{QW} \sim 1.3\times10^{13}$ cm^{-2}	$4\pi\alpha_{X_A} \sim 13\times10^{-3}$ [102]
	(0.08 eV^2)	(0.12 eV^2)
$\Omega_{VRS}(T = 300$ K, $\Gamma_{inh} = 0)$ (meV)	36	39

Table 5.1: Relevant parameters for the achievement of the SCR for the 5×5 InGaN/GaN MQW based semi-hybrid (MQW based SH) and the thick InGaN layer based semi-hybrid MC structure (bulk based SH).

we deduce a value of 0.08 (eV)^2 and for the bulk case of 0.12 (eV)^2. In the 2D case depending on the wave-function overlap the oscillator strength is expected to be enhanced with repect to the 3D case (cf. equation 3.17): if a wave-function overlap of 1 is taken a value of 0.15 (eV)^2 is found which is clearly above the bulk value. Note that for the bulk much lower values (by more than a factor of 2) are quoted in Ref. [287]. Using the f_{osc} values of Table 5.1 similar vacuum Rabi splittings at RT and negligible inhomogeneous broadening ($\Gamma_{inh} = 0$) are deduced from TMS for the two structures.

5.2 Experimental features of semi-hybrid cavity structures

Note that a common protocol to characterize III-nitride based MC structures includes the following measurements performed on the half cavity (HC) and on the full cavity (FC) structure:

- μ-PL mapping of HC giving access to excitonic disorder
- μ-Transmission mapping of FC giving access to photonic disorder
- LT absorption-like measurements of HC
- Fourier-PL and Fourier-R at different sample positions and temperatures
- Power-dependent studies

A common way to demonstrate SCR is to reveal an anticrossing behavior in temperature-dependent PL, transmission, reflectivity or absorption measurements [288, 289]. The latter arises from a change in the detuning between exciton mode and cavity photon mode with increasing temperature. Starting with a moderate negative detuning at LT the exciton redshifts due to bandgap reduction whereas the cavity mode position is only slightly affected by temperature changes. Thus, at a finite temperature a crossing, i.e., a change in the sign of the detuning, is expected. In the case of strong exciton cavity photon mode coupling, instead of a mode crossing an anticrossing of the lower and upper polariton mode with temperature is

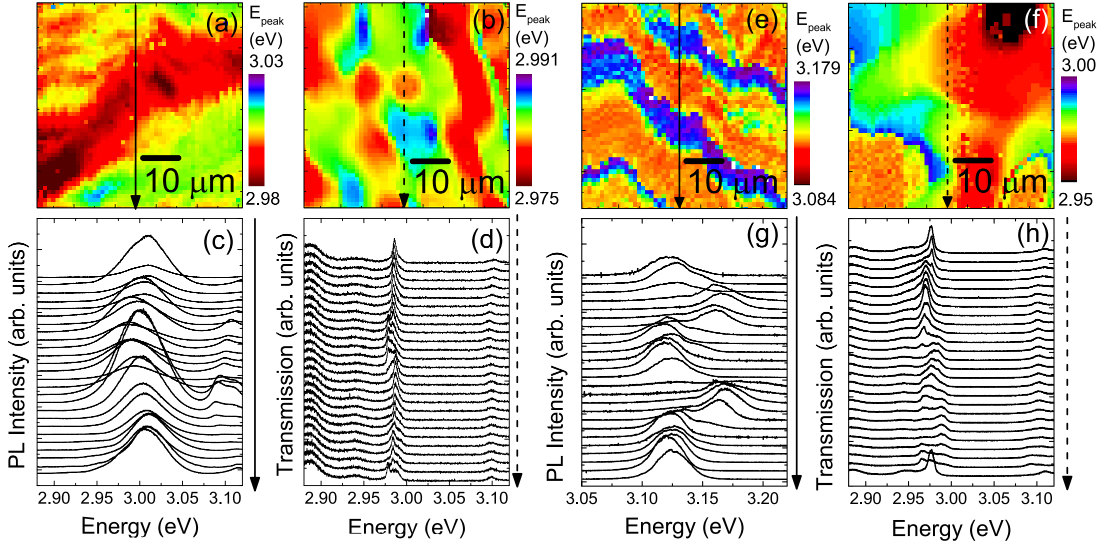

Figure 5.2: Excitonic and photonic disorder probed on (a)-(d) an InGaN/GaN MQW based and (e)-(h)a thick InGaN layer based semi-hybrid MC structure. (a) and (e) LT (4 K) μ-PL mappings (50×50 μm^2) of the corresponding HC structures. (b) and (f) RT micro-transmission mappings (50×50 μm^2) of the full semi-hybrid MC structures. The spectra in (c), (g), (d), and (h) are recorded every 2 μm along the continuous and dashed arrows in (a), (e), (b), and (f), respectively.

observed. However, such measurements require either homogeneous samples or a possibility to correct for the temperature-dependent sample drift in the cryostat.

Excitonic and photonic disorder

The homogeneity of a MC is given by its excitonic and photonic disorder. Thus, the excitonic disorder of the HC structures (without top DBR) is deduced from 50×50 μm^2 μ-PL mappings acquired at 4 K every 1 μm with a frequency-doubled line of a cw Ar^+-laser (λ= 244 nm) and the photonic disorder of the FC structures from 50×50 μm^2 micro-transmission mappings performed at RT. The LT 50×50 μm^2 μ-PL mappings of the InGaN/GaN MQW and the bulk InGaN based half cavities (structures shown in Figs. 5.1(a) and 5.1(c), respectively) are shown in Figs. 5.2(a) and 5.2(e), respectively. Note that for both structures the excitonic disorder is increased with respect to the SQW case as the standard deviation (σ) of the mappings amounts to 9.4 and 18.6 meV (cf. Table 5.2) instead of 0.8 meV (cf. Table 4.1). This might be ascribed to different underlying layers (LM InAlN/GaN DBR instead of GaN buffer) and the stacking of QWs. However, the situation is different for the bulk InGaN cavity, as such an emission pattern is also observed when directly grown on a FS-GaN substrate (cf. Fig. 4.14(c)).
The corresponding photonic disorder of the full semi-hybrid MCs can be deduced from the micro-transmission mappings shown in Figs. 5.2(b) and 5.2(f). With respect to the empty cavity case we do observe an increase of the photonic disorder for both structures (cf. Table 5.2

	MQW based SH		bulk based SH	
	μ	σ	μ	σ
Excitonic disorder: E_{peak} of HC (meV)	2999.6	9.4	3137.9	18.6
Photonic disorder: E_{peak} of FC (meV)	2982.9	2.5	2973	12.5

Table 5.2: Excitonic and photonic disorder of the 5×5 InGaN/GaN MQW based semi-hybrid (MQW based SH) and the thick InGaN layer based semi-hybrid MC structure (bulk based SH): The mean value μ and standard deviation σ are extracted from LT μ-PL mappings (shown in Figs. 5.2(a) and 5.2(e)) for the HC structures and from RT micro-transmission mappings (shown in Figs. 5.2(b) and 5.2(f)) of FC structures.

σ equal to 2.5 and 12.5 meV, respectively, vs. σ equal to 0.5 meV (extracted from Fig. 3.7(a))). Note that the large value of the bulk InGaN based MC is mainly due to the morphology of the InGaN layer, which is comparable to the one observed in the 10×10 μm^2 AFM scan shown in Fig. 4.13(c).
The quality factor of a microcavity is obviously affected by the exciton-cavity mode detuning. Indeed, the closer the cavity mode position from the absorption edge of the active medium (MQWs or bulk InGaN layer), the lower the measured Q value as previously explained, e.g., by Simeonov *et al.* [290] or Gacevic *et al.* [291] for microdisks and planar MCs, respectively, using both embedded InGaN/GaN QWs as an internal light source. As the detuning is not constant across the whole wafers, Q values ranging from a few hundreds up to 1090 (450) are measured for the InGaN/GaN MQW (thick InGaN layer) based MC. The difference in Q for the two cavities might be related to: (i) the increased thickness of the absorbing medium for the thick InGaN layer based MC (73 nm vs 25×2 = 50 nm) and (ii) an increased absorption due to the deteriorated crystalline quality of the thick InGaN layer with respect to the QW case. Note that 73 nm lies above the critical thickness for relaxation for this In content (x = 0.12) [223]. However, the high Q value measured for the InGaN/GaN MQW based MC supports the high optical quality of this MC.

In conclusion, InGaN/GaN MQW and thick InGaN layer based semi-hybrid MCs suffer from strong excitonic and photonic disorder. Temperature-dependent measurements are subject to a sample drift ranging up to a few mm. As such a drift cannot be easily corrected,[2] temperature-dependent measurements are not well suited to check the (anti)-crossing behavior and to conclude about the coupling regime (strong or weak).
On the other hand, the SCR can be revealed by angle-resolved PL, transmission, reflectivity or absorption measurements, which neither depend on disorder nor suffer from the temperature-dependent sample drift. However, first the spectral features of the HC structures have to be carefully analyzed.

[2]For example, such a drift could be corrected manually in the case of a patterned sample.

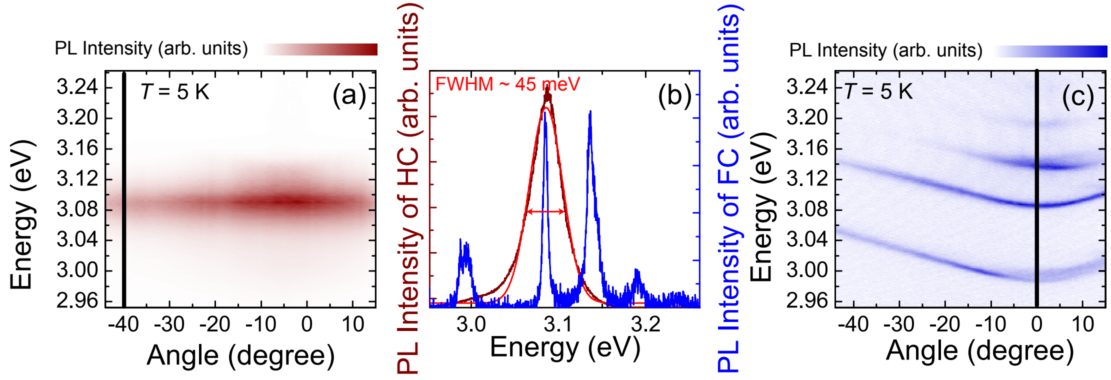

Figure 5.3: Fourier-space images of the thick InGaN layer based (a) HC and (c) MC structure emission spectrum measured at 5 K. (b) The LT HC emission at an emission angle of 40° (brown line) and the LT FC emission at normal incidence. The red line corresponds to a Gaussian fit with FWHM of 45 meV.

LT absorption-like measurements on HC

As already emphasized in chapter 4, the knowledge of intrinsic properties of the investigated samples are indispensable for strong coupling applications. However, absorption-like measurements performed on $In_xGa_{1-x}N$/GaN MQW samples with $x \sim 0.1$ proved to be rather challenging (cf. section 4.3.4). Hereafter LT PL measurements of the HC structures are presented.

Note that LT PL measurements of the HC structures have been acquired either in the same configuration as those of the FC structure (i.e., angular-resolved μ-PL measurements) or using a cw HeCd laser (λ = 325 nm, macro-PL measurements). For angular-resolved PL measurements (Fourier-space imaging of PL) a near UV (NUV) microscope objective and a pulsed 355 nm Nd:YAG laser (τ = 570 ps, f = 7.1 kHz) have been used. By means of two lenses with respective focal lengths of 30 and 20 cm, the back focal plane of the microscope objective (Fourier plane) was directly imaged on the entrance slit of the spectrometer. With the latter, a spectral resolution better than 150 μeV was reached via the combination of a 55 cm focal length monochromator and a liquid-nitrogen cooled CCD (cf. Appendix A.4 for further explanations). In Fig. 5.3(a) a LT Fourier-space image of the thick InGaN layer based semi-hybrid HC PL emission is shown. The FWHM at an emission angle of 40° amounts to ~ 45 meV. A similar result (FWHM = 52 meV) has been measured for the InGaN/GaN MQW based HC (cf. Fig. 5.4).

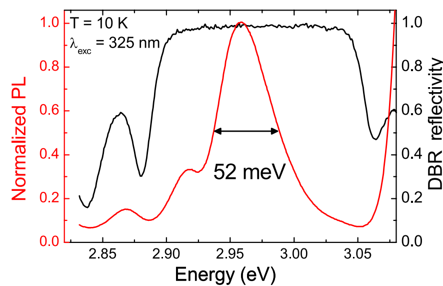

Figure 5.4: LT macro-PL spectrum of the 5×5 InGaN/GaN MQW based HC structure (red line) and reflectivity spectrum of the bottom DBR (black line).

Probing cavity dispersions

Note that for the InGaN/GaN MQW based semi-hybrid MC the requirements for strong coupling applications in terms of QW absorption features have been detailed in section 3.3.4 and the knowledge of Γ_{inh} has been ascertained as a priority. Using the approach of F. Yang *et al.* [199] the PL-linewidth can be related to the absorption one, which leads to $\Gamma_{abs} \sim 74$ meV. Hence, when using equation 4.4 $\Gamma_{inh} \sim 74$ meV as the impact of Γ_h can be neglected at low temperature. If we consider the evolution of the simulated absorption spectra as a function of Γ_{inh} shown in Fig. 3.12(a) with such a Γ_{inh} value, the InGaN/GaN MQW based semi-hybrid MC is expected to operate in the weak coupling regime at RT. When considering the simulated absorption spectra as a function of Γ_{inh} in the LT case (not shown), the system lies only slightly above the crossover from the strong to the weak coupling regime. However, to further check what is expected from TMS results, LT and RT Fourier-space PL measurements were performed (Figs. 5.5(a) and 5.5(b), respectively). The mode dispersion clearly matches that of a parabolic cavity mode using a photon effective mass of $5.2{\cdot}10^{-5} m_0$, hence indicating that the present MC structure operates in the weak coupling regime. The horizontal red line in Figs. 5.5(a) to 5.5(c) is an estimate of the free exciton position (X_A), which should be located ~ 50 meV above the signature of the PL emission assuming the relationship considered between the measured PL linewidth and the Stokes shift holds. The estimate of the free exciton position at RT is positioned at a lower energy due to the temperature-dependent bandgap reduction. In first approximation the parameters characterizing the temperature-dependent bandgap reduction of InGaN bulk layers with a similar In content have been taken (cf. Table 4.4). Note that the LT and RT emission do not result from the same sample point which can be seen clearly by the difference in cavity mode position. A much smaller temperature-dependent cavity mode shift is expected. The same dispersion is found in RT Fourier-space reflectivity measurements (Fig. 5.5(c)). Furthermore, the transmitted PL has been acquired together with the Fourier-space PL measurement (green line in Fig. 5.5(a)). The latter allows to distinguish between cavity and Bragg modes (indicated in blue in Fig. 5.5(a)).

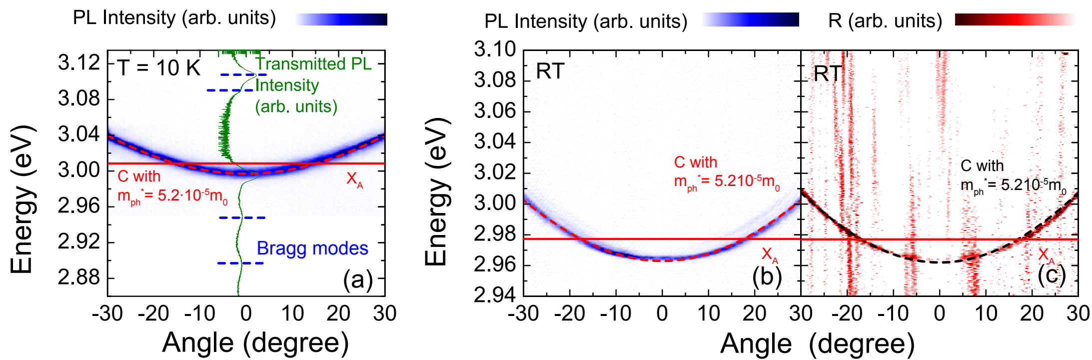

Figure 5.5: (a) Fourier-space image of the 5×5 InGaN/GaN MQW based semi-hybrid MC emission spectrum measured at 10 K and (b) at RT in the low carrier injection regime. (c) Fourier-space image of the microcavity reflectivity at RT at the same sample position as that probed in (b).

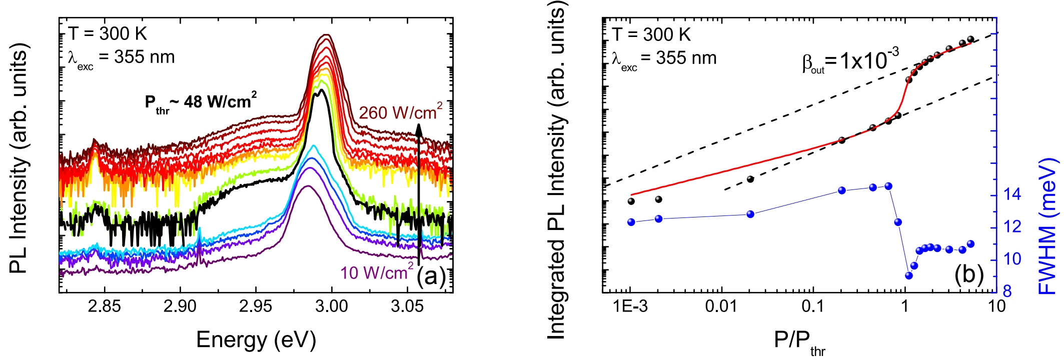

Figure 5.6: (a) Semilogarithmic plot showing the power-dependence of macro-PL spectra, shifted for clarity, taken under normal incidence at RT on the 5×5 InGaN/GaN MQW based semi-hybrid MC structure. (b) Integrated output intensity against normalized incident pump power (black dots) and corresponding fit (red line) as described in the text, the dashed lines are a guide to the eye; and corresponding evolution of the mode linewidth (connected blue dots).

A parabolic mode dispersion has been measured as well for the thick InGaN layer based semi-hybrid MC over a temperature range from 4 K to RT.

Power-dependent studies

The excitation power-dependent measurements acquired on the 5×5 InGaN/GaN MQW based semi-hybrid MC shown in Fig. 5.6(a) show a clear lasing threshold occurring at an average pump power density of ~ 48 W/cm^2. The spectrally integrated input-output characteristic of the MC structure is displayed on a logarithmic scale in Fig. 5.6(a). From such a plot, we can extract the spontaneous emission coupling factor β_{out} using the solution of the standard rate equation model that gives the dependence of the output integrated intensity [292]:

$$I_{out} \propto \frac{r+1-\sqrt{(r-1)^2+4\beta_{out}r}}{2(1-\beta_{out})-(r+1-\sqrt{(r-1)^2+4\beta_{out}r})}, \tag{5.1}$$

where r is the normalized pump rate. The best fit leads to a β_{out} value equal to 1×10^{-3}, which is more than two orders of magnitude larger than the values usually reported for EELDs [128] as expected for a vertical cavity laser with fewer modes supporting spontaneous emission. However, we expect our β_{out} value to be overestimated due to the contribution of several modes in the spontaneous emission below threshold compared to the stimulated emission originating from a smaller number of modes, for which the gain is maximum, above threshold [192]. The signature for coherent light emission is also supported by the decrease in the emission linewidth when crossing the lasing threshold (connected blue dots in Fig. 5.6(b)), which decreases from 14 to ~9 meV. The observed increase in the linewidth with increasing pump power density above threshold is likely due to the contribution of additional lasing modes slightly detuned between each other that progressively switch on, i.e., the coherent

emission originates from a larger area for larger pump power densities. A similar power-dependent behavior has been measured for the thick InGaN layer based semi-hybrid MC (not shown) with a lasing threshold at ~ 130 W/cm^2.

Note that 48 W/cm^2 is a relatively low lasing threshold when compared to the polariton lasing threshold in GaN based MCs (~ 35 and 17.7 W/cm^2 for the GaN bulk layer and the GaN/AlGaN MQW based MC, respectively [114]). The origin of lasing processes in InGaN-based structures is still a matter of debate and will be addressed in section 5.4.

Another peculiar behavior is the observed blueshift of the cavity mode with increasing pumping power below lasing threshold (cf. Fig. 5.6). The latter is commonly observed in III-nitride MCs based on InGaN/GaN as well as GaN/AlGaN QWs [105, 114, 172]. In the case of strong light-matter coupling the blueshift of the lower polariton branch, which is temperature- and detuning-dependent, amounts to a few meV. It is attributed to be primarily governed by exciton saturation effects [172]. However, the situation is different in the case of weak light-matter coupling.
In the case of a non-polar III-nitride MC based on GaN/AlGaN MQWs the coexistence of the two different light-matter coupling regimes (weak and strong) along orthogonal polarization planes is observed and LT power-dependent measurements reveal a blueshift of ~ 4 meV at 50 K for the two directions, respectively for the two coupling regimes [105]. For the above-mentioned low In content InGaN based MCs the blueshift ranges between 6-10 meV at RT.
The blueshift of the cavity mode might be explained by a decreasing n_c (cf. equation 1.23). Note that already for a reduction of 0.01 (0.1) in n_c (n_{op} of the QWs) a blueshift of ~ 10 meV is expected. However, several mechanisms, strongly dependent on the detuning, might affect n_c, leading either to a red- or blueshift of the cavity mode : (i) bandgap renormalization (BGR) induced by many-body interactions is expected to scale with the cubic root of the injected carrier density, (ii) filling of band-tail states, (iii) QCSE screening, (iv) screening of exciton properties such as oscillator strength saturation and renormalization of exciton binding energy.
Note that the cavity mode as observed in PL measurements results from a convolution with the QW emission. Thus, the generally observed strong blueshift of the InGaN/GaN QW emission (cf. section 4.3.2) could also result in a blueshift of the observed cavity mode. However, the present MC Q factor to QW Γ_{PL} ratio provides a blueshift of maximal ~ 3 meV. In conclusion, the blueshift of the QW emission cannot be the main driving force and several of the above-mentioned mechanisms affecting n_c might occur simultaneously depending crucially on the detuning, temperature, and the injected carrier density.

optical cavity thickness	4λ
N_{QW}	5×3
L_{eff} (nm)	824
f_{osc}^{QW} (cm^{-2})	$\sim 1.3\times10^{13}$
$\Omega_{VRS}(T = 300$ K, $\Gamma_{inh} = 0)$ (meV)	33

Table 5.3: Relevant parameters for the achievement of the SCR for the 5×3 InGaN/GaN MQW based hybrid.

5.3 Hybrid MC structures

Note that the optimum hybrid MC design deduced from TMS (cf. section 3.3.1) has not be realized. Instead my colleague Dr. Munise Cobet (LASPE-EPFL) realized a 4λ hybrid MC structure close to the latter. The 4λ hybrid MC structure as schematically drawn in Fig. 5.7(a) is based on a bottom and top 8 pair SiO_2/ZrO_2 DBR and on an active medium of 5×3 $In_{0.1}Ga_{0.9}N$ (2 nm)/GaN (3 nm) MQWs initially grown on c-plane sapphire. Note that due to fabrication issues the optical cavity thickness had to be increased by one λ, consisting in a $\lambda/2$ layer of GaN inserted above and below the active medium. Furthermore, the $N_{QW/AN}$ is reduced to 3 in order to reduce Γ_{inh}. For such a MC structure a VRS of 33 meV is deduced from TMS at RT and at negligible Γ_{inh} (cf. $\Omega_{VRS}(T = 300$ K, $\Gamma_{inh} = 0)$ in Table 5.3 and Fig. 5.7(b)). Note that two absorption peaks can be resolved, i.e., there is a well defined minimum between the peaks, up to a Γ_{inh} value equal to 41 meV. Thus, similar results as for the above-mentioned semihybrid MCs are expected. However, Fourier-space PL measurements (courtesy of my colleague Dr. Munise Cobet) have shown intriguing features that might be compatible with the SCR. This might be indeed possible if the InGaN QWs completely relax their strain when removed from the sapphire substrate without affecting their quality, i.e., keeping the LT PL linewith below ~ 40 meV. In such a case the built-in electric field would consist of a polarization component of spontaneous origin only leading to a much reduced value of ~ 115 kV/cm.[3] Thus, the wave-function overlap would be increased leasing to a $f_{osc}^{QW} \sim 2.4\times10^{13} cm^{-2}$, about twice the value when accounting for the strain induced built-in field (cf. Table 5.3), and a $\Omega_{VRS}(T = 300$ K, $\Gamma_{inh} = 0)$ of ~ 45 meV. Thus, the collapse of the SCR would occur at a much higher value of Γ_{inh}, i.e., at a value of ~ 56 meV. Note however that the complete strain relaxation of thin,

[3] For pseudomorphically grown $In_{0.1}Ga_{0.9}N$/GaN MQWs the built-in electric field is estimated to reach 1520 kV/cm.

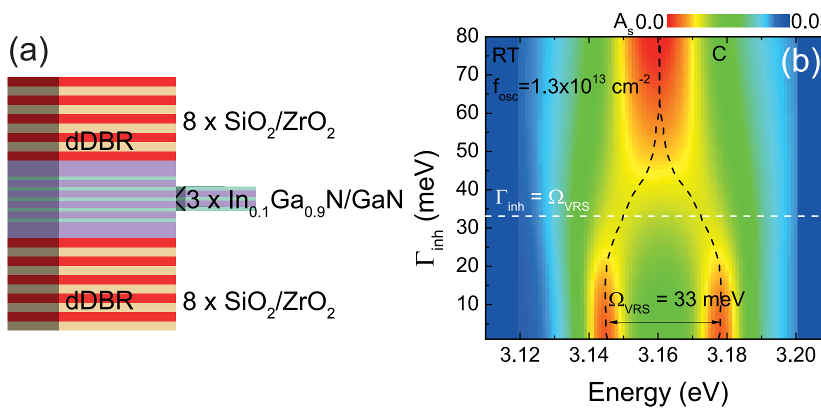

Figure 5.7: Schematic drawings of (a) a 5×3 InGaN/GaN MQW based hybrid MC structure. (b) Corresponding simulated absorption spectra at zero cavity photon-exciton detuning as a function of Γ_{inh}.

low In content InGaN/GaN MQWs when released from the substrate is highly speculative. However, studies regarding such particular strain relaxation would trigger a lot of interest as well for devices, especially for those based on high In content active regions suffering from an even larger, detrimental electric built-in field.

5.4 Origin of lasing processes in InGaN-based structures

In striking contrast to GaInAs, InGaPAs, and GaAsSb based devices, where parameter-free simulations are able to predict their behavior [293], the understanding of group III-nitride devices is far from this level. Moreover, their complex material properties, such as Coulomb interaction effects (excitonic effects are far from being negligible), strong internal spontaneous and piezoelectric fields, and random potential fluctuations resulting in energetically deep trapping states (band-tail states) do play an important role. However, the effect of the band-tail states on the formation and relaxation processes of e-h plasmas and excitons is not yet clear. On the other hand, it is known that those band-tail states influence the material gain and the emission of stimulated light [216, 294–296]. Indeed, Y. K. Song *et al.* [297] showed that the inversion distribution can be easily realized in band-tail states. However, it is not yet clear whether the lasing originates from localized excitons or a localized e-h plasma [295, 298].
Indeed, different possibilities of excitonic stimulated emission in II-VI and III-V semiconductors due to exciton-exciton or exciton-optical phonon scattering processes or precisely because of exciton localization [299] have already been investigated. Excitonic gain due to localization in inhomogeneously broadened QWs (such as InGaN/GaN QWs) has been described in a phenomenological model in the following way: assuming a volume defined by the mean free path (localization site) can be occupied by only one exciton, the population inversion condition for such excitons is given by [299]:

$$f - (1 - f) = 2f - 1 > 0, \tag{5.2}$$

where f is the probability of the state being occupied. Therefore, an occupied site provides gain, whereas an unoccupied one absorption.
Note that in an (In, Al)GaN LD emitting at ~ 3 eV an instability of the exciton transition with increasing carrier density has been observed [295]. The authors attributed lasing to originate from an e-h plasma. However, they observed an excitonic signature in the optical gain spectra at low carrier densities. Thus, for a structure design with reduced losses, the observation of excitonic stimulated emission should be possible. Indeed, in an optically-pumped non-polar III-nitride MC based on GaN/AlGaN MQWs excitonic gain based on saturation of localized states is evaluated to be the most likely mechanism to be at the origin of low threshold lasing along the ordinary polarization direction [105]. Note that the LT lasing threshold amounts to ~ 20 W/cm^2, which is only ~ 1.3 times the polariton lasing threshold in the extraordinary direction. Furthermore, the onset of the Mott transition has been measured to occur clearly above the latter lasing threshold.
Note that for the above-mentioned InGaN-based MCs the determination of the Mott transition

proves to be much more challenging than in their GaN counterpart. The deconvolution procedure of power-dependent PL measurements on GaN/AlGaN QWs provides a fairly accurate estimate of the Mott transition but it cannot be directly adapted to the case of $In_{0.1}Ga_{0.9}N$/GaN QWs (cf. section 4.3.2). Efforts should be made in order to develop a consistent procedure to detect the onset of the Mott transition in such QWs. Possible studies could rely on power-dependent PL measurements on very low In content (1-2%) InGaN/GaN SQWs, thereby reducing the inhomogeneous broadening and the built-in electric field. Furthermore, excitonic stimulated emission could be obtained by further possible studies such as optical gain measurements and/or the search for a second threshold that should occur when the system transits to a degenerate electron-hole plasma above the Mott transition.

5.5 Summary of the results

In conclusion, 5×5 $In_xGa_{1-x}N$/GaN MQW and thick $In_xGa_{1-x}N$ layer (73 nm) based semi-hybrid MCs with $x \sim 0.1$ suffer from strong excitonic and photonic disorder. However, for the $In_xGa_{1-x}N$/GaN MQW based MC Q values up to 1090 are measured supporting the high optical quality of this MC. For the MC based on a thick InGaN layer, the latter is reduced to ~ 450, which is attributed to an increased absorption due to a deteriorated crystalline quality of such layers when compared to a 5×5 InGaN/GaN MQW set. The mode dispersion for both semi-hybrid cavities clearly matches that of a parabolic cavity mode, hence indicating that the present MC structures operates in the weak coupling regime in accordance with TMS. Power-dependent studies reveal a low lasing threshold of ~ 48 (130) W/cm^2 for the InGaN/GaN MQW (thick InGaN layer) based MC. Furthermore, a power-dependent blueshift of the cavity mode is revealed and discussed.
Furthermore, III-nitride based hybrid MCs for strong coupling applications have been considered. Eventually, the origin of lasing processes in InGaN based structures has been addressed and further studies have been suggested.
The results of the present chaptre together with those of section 3.3, suggest that SCR with InGaN-based MCs based on a LM bottom InAlN/GaN DBR is not possible with the current quality of the active medium. However, strongly reducing the In content of the active medium and switching to a fully hybrid design should provide strongly coupled MCs.

6 Conclusion

The theoretical studies of the main emission characteristics of III-nitride based polariton LDs are summarized first. In a second step experimental results achieved on the key elements of polariton LDs, namely DBRs and low In content InGaN/GaN QWs, are reviewed. The relevance of the present work for conventional LDs is then recalled and an outlook on future polariton LD designs is given.

Summary of theoretical results

The main emission characteristics of III-nitride based polariton LDs are studied for two experimentally relevant pumping geometries, namely the direct injection of electrons and holes into the strongly coupled MC region and intracavity optical pumping via an embedded LED. The minimum J_{thr} as a function of lattice temperature and exciton-cavity photon detuning was calculated in the framework of semiclassical Boltzmann equations leading to optimum values two orders of magnitude lower than in equivalent III-nitride based VCSELs (at RT $J_{thr} \sim 5$ A/cm^2 for both geometries vs 1-10 kA/cm^2 for the latter). Then a simplified rate equation modeling treatment was introduced to derive both steady-state and high-speed current modulation solutions. This simplified analysis made it possible to show that the carrier population which acts as a reservoir for the stimulated relaxation process, namely that of excitons, gets clamped once the condensation threshold is crossed. This situation is analogous to the case of conventional LDs. The analysis of the modulation transfer function, derived from the dynamical response of polariton LDs to a small modulation of the current above threshold, demonstrates the interesting potential of the direct electrical pumping scheme, since a cutoff frequency ω_{3dB} up to ~ 16 GHz is predicted, whereas for the intracavity optical pumping scheme, the cutoff frequency is shown to be limited by the frequency response of the pumping LED, for which $\omega_{3dB} \approx 1$ GHz. Furthermore, we have carried out an analysis of the relative intensity noise per unit bandwidth for both structures in the framework of a theoretical treatment adapted from that applied to conventional semiconductor LDs using rate equations including Langevin noise sources. The resulting general expressions can be applied to all inorganic semiconductor polariton LDs, but numerical calculations have been performed in the specific case of the two III-N devices. It was shown that in the high-frequency range the expected minimum RIN of polariton LDs—whatever the pumping geometry—is equal to the standard

quantum limit ($2h\nu/P_0$). The general lineshape of the RIN as a function of frequency and optical output power has been discussed for the two geometries and approximate (simplified) expressions for the RIN have been given. We have then addressed the expected evolution of the emission linewidth of those devices by considering the most advanced theories available to date. The modified Schawlow-Townes linewidth has been estimated from the effective ground-state polariton lifetime at threshold leading to a predicted linewidth as narrow as ~ 15 MHz at RT for the two pumping geometries when using a consistent set of parameters for III-nitride polariton LDs.

Summary of experimental results

The parameters governing the achievement of strong light-matter coupling in planar microcavities with embedded c-plane InGaN/GaN MQWs for polariton LD applications have been analyzed by means of simulations and optical characterizations. Beyond the expected impact of the effective cavity length, the total number of quantum wells and the tradeoff between those two parameters, the inhomogeneous broadening of the InGaN/GaN MQW active region has been clearly identified as the most critical parameter that can prevent reaching the SCR in planar MCs. The combination of absorption-sensitive and PL spectroscopy experiments performed on various thin low indium content ($x \sim 0.1$) $In_xGa_{1-x}N$/GaN QWs, ranging from the SQW case to a set of several MQWs, reveals a systematic increase in the inhomogeneous linewidth with increasing number of wells. In particular, it was shown that despite narrow measured linewidths for the SQW case (~ 33 meV measured at LT in PL and 44 meV using semi-contactless ER), the active region in full MC structures, which necessarily requires a large N_{QW} value to potentially reach the SCR as predicted by TMS, presently undergoes a detrimental increase in the emission/absorption linewidth that drives the system into the weak coupling regime.

Another important parameter for polariton applications is the photonic disorder, which has been shown to depend crucially on the choice of substrate for the LM InAlN/GaN DBR growth. However, low-threshold lasing at RT has been reported for optically pumped InGaN based MCs using a LM InAlN/GaN bottom DBR and a SiO_2/ZrO_2 top DBR, which indicates a good local optical feedback.

Various 100 nm thick InGaN layers with In contents ranging between 2 and 18% have been compared to a model based on a stochastic distribution of indium atoms at the atomic scale. For low In content layers (x<12%) the model holds. Layers with larger In contents cannot be compared to it as they suffer from a strong degradation of their crystalline quality.

Relevance of the present work for conventional LDs

For all microcavity based LDs, whether working in the strong (polariton LDs) or weak coupling regime (VCSELs), the photonic disorder is a crucial parameter. Thus, in the VCSEL fabrication process the new kind of characterization method introduced for III-nitride Bragg mirrors

could be performed systematically to gain information about the degree of photonic disorder. Note that the choice of DBR and its fabrication process is far from being conventional. In the case of LM InAlN/GaN DBRs the introduction of a two-step temperature ramp at each interface could further improve the morphology of those interfaces and result in an increase of the overall quality of the DBR. Furthermore, the development of n- doped DBRs could allow significant simplifications in the processing of such devices.
The simple model based on a stochastic distribution of indium atoms within InGaN layers suggests a steep absorption linewidth increase in the UV region but a more moderate one in the visible spectral range. This means that for green LDs, the gain dilution should not be much higher than for blue LDs provided that the In content within the QWs is homogeneous and abrupt interfaces are present. This is confirmed by a constant material gain reported by OSRAM between 450 and 520 nm. Note that a strong inhomogeneity in the In content within the QWs might drastically increase the absorption linewidth and thus it has to be avoided.

Perspectives

The first polariton LDs based on different semiconductor material systems have been reported over the past two years [24, 51, 52]. Our theoretical framework provides general expressions that can be applied to all inorganic semiconductor polariton LDs. Thus it would be interesting to establish their condensation phase diagram, to drive those devices under high-speed current modulation, and to probe their RIN features and linewidth evolution with pumping strength. Such experiments would allow to further highlight their differences with respect to conventional LDs.

Alternative solutions to achieve the SCR with the InGaN system could rely on studies related to strain management of InGaN/GaN MQW structures. Note that solutions regarding strain management are also of potential interest for conventional LDs, especially for those operating in the green spectral range. A further possibility could be the growth of an active region on high-quality FS-GaN substrates that would be subsequently etched away in order to embed the InGaN-based layer between dielectric DBRs. Such an active region could consist either of a thick low indium content bulk $In_xGa_{1-x}N$ layer or of thin low indium content $In_xGa_{1-x}N$/GaN MQWs ($x \lesssim 6\%$) emitting in the NUV range. This would lead to a full-hybrid MC system combining a low inhomogeneous broadening for the active region and a reduced L_{eff} value compatible with the SCR. The use of UV dielectric DBRs with extremely low residual absorption would allow further decreasing the indium content of the active region, which should prove critical in terms of inhomogeneous linewidth broadening. Such an approach would then certainly allow evaluating the full potential of the InGaN alloy for strong coupling applications.

Another interesting solution to achieve the SCR with the InGaN system could rely on semi-

and non-polar structures, as for such structures the negative effects related to the QCSE are expected to be decreased or even eliminated. However, for those orientations issues related to the substrate size, their availability, cost, and the reduced quality of the overgrown layers due to in-plane lattice-mismatch and the presence of defects such as stacking faults remain to be overcome.

A Appendix

A.1 The transfer matrix formalism

For electromagnetic fields Maxwell equations can be used to derive traveling wave solutions which represent the transport of energy from one point to another. In a non-conducting medium described by spatially constant permeability and susceptibility in the absence of charges the wave equation for the electric field (the same holds for the magnetic field) can be derived from Maxwell equations [300]:

$$\nabla^{\mathbf{2}}\mathbf{E}(\mathbf{r},z)+\frac{\omega^2}{c^2}\epsilon(z)\mathbf{E}(\mathbf{r},z)=0, \tag{A.1}$$

where $\mathbf{r}$ is the in-plane position vector and $\epsilon(z)$ is the dielectric constant profile. A planar structure made of a stack of different layers of given thicknesses and infinite lateral extension (cf. Fig. A.1) is translational invariant along the plane and thus the solutions of equation A.1 are plane waves along the in-plane direction:

$$\mathbf{E}_{\boldsymbol{k}_{||}}(\mathbf{r},z)=\boldsymbol{\epsilon}_{||}U_{\boldsymbol{k}_{||},\omega}(z)e^{i\boldsymbol{k}_{||}z}, \tag{A.2}$$

where $\boldsymbol{k}_{||}$ is the in-plane wave vector, $\boldsymbol{\epsilon}_{||}$ is the polarization vector, and $U_{\boldsymbol{k}_{||},\omega}(z)$ is the sum of a wave traveling to the left (with amplitude E_l) and one to the right (with amplitude E_r) along k_z. If we replace the latter into equation A.1 we get a one dimensional problem:

$$\frac{\partial^2 U_{\boldsymbol{k}_{||},\omega}(z)}{\partial^2 z}+(\frac{\omega^2}{c^2}\epsilon(z)-\boldsymbol{k}_{||}{}^2)U_{\boldsymbol{k}_{||},\omega}(z)=0. \tag{A.3}$$

We do have propagation along z with $k_z=\sqrt{\frac{\omega^2}{c^2}\epsilon(z)-\boldsymbol{k}_{||}{}^2}$ only if $\frac{\omega^2}{c^2}\epsilon(z)>\boldsymbol{k}_{||}{}^2$, otherwise the solution of A.3 is an evanescent wave. As the amplitude reflection and transmission coefficient are dependent on the amplitude of the reflected and transmitted field, respectively, the latter have to be determined by imposing Maxwell boundary conditions at each interface between

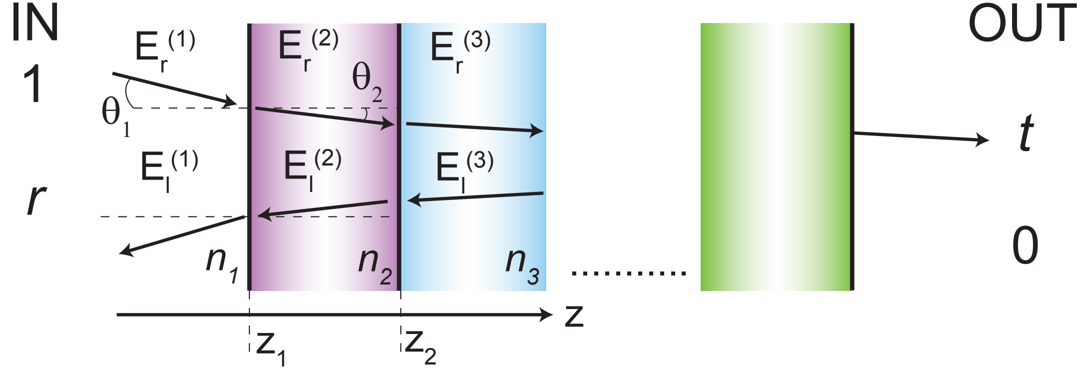

Figure A.1: Schematic representation of left- and right-traveling waves for a homogeneous thin-film multilayer structure. At the incident medium characterized by a refractive index n_1 we have an incoming wave (with amplitude = 1) and a reflected one (with amplitude r), whereas a wave of amplitude t is transmitted from the right boundary of the structure.

two layers. This task is very simple within a transfer matrix approach [85, 301]:

$$\begin{bmatrix} E_r^{(2)} \\ E_l^{(2)} \end{bmatrix} = \begin{bmatrix} M_{11} & M_{12} \\ M_{21} & M_{22} \end{bmatrix} \begin{bmatrix} E_r^{(1)} \\ E_l^{(1)} \end{bmatrix}, \tag{A.4}$$

where $E_r^{(2)}$ and $E_l^{(2)}$ are the amplitudes of the electric field traveling to the right and to the left, respectively, in the purple medium (cf. Fig. A.1) and $E_r^{(1)}$ and $E_l^{(1)}$ are the amplitudes of the electric field traveling to the right and to the left, respectively, in the incoming medium (cf. Fig. A.1).

In the case of a wave arriving onto an interface the two different polarizations TE (transverse electric) and TM (transverse magnetic)[1] have to be considered separately:

$$M_{TE} = \frac{k_z^{(2)} + k_z^{(1)}}{2k_z^{(2)}} \begin{bmatrix} 1 & \frac{k_z^{(2)} - k_z^{(1)}}{k_z^{(2)} + k_z^{(1)}} \\ \frac{k_z^{(2)} - k_z^{(1)}}{k_z^{(2)} + k_z^{(1)}} & 1 \end{bmatrix} = \frac{1}{t_{TE}} \begin{bmatrix} 1 & r_{TE} \\ r_{TE} & 1 \end{bmatrix}, \tag{A.5}$$

$$M_{TM} = \frac{n_2^2 k_z^{(1)} + n_1^2 k_z^{(2)}}{2n_1 n_2 k_z^{(2)}} \begin{bmatrix} 1 & \frac{n_2^2 k_z^{(1)} - n_1^2 k_z^{(2)}}{n_2^2 k_z^{(1)} + n_1^2 k_z^{(2)}} \\ \frac{n_2^2 k_z^{(1)} - n_1^2 k_z^{(2)}}{n_2^2 k_z^{(1)} + n_1^2 k_z^{(2)}} & 1 \end{bmatrix} = \frac{1}{t_{TM}} \begin{bmatrix} 1 & r_{TM} \\ r_{TM} & 1 \end{bmatrix}, \tag{A.6}$$

where $k_z^{(j)} = \sqrt{\frac{\omega^2}{c^2}\epsilon_j - k_{||}^2} = \cos(\theta_j)k_j = \cos(\theta_j)\frac{\omega}{c}n_j$, as $\sqrt{\epsilon_j} = n_j$. From this the following

[1]These two polarizations are also indicated as s and p, respectively.

expressions are obtained:

$$\begin{aligned} r_{TE} &= \frac{n_1\cos\theta_1 - n_2\cos\theta_2}{n_1\cos\theta_1 + n_2\cos\theta_2}, \\ t_{TE} &= \frac{2n_2\cos\theta_2}{n_1\cos\theta_1 + n_2\cos\theta_2} = (1 - r_{TE}), \\ r_{TM} &= \frac{n_2\cos\theta_1 - n_1\cos\theta_2}{n_2\cos\theta_1 + n_1\cos\theta_2}, \\ t_{TM} &= \frac{2n_2\cos\theta_2}{n_2\cos\theta_1 + n_1\cos\theta_2} = \frac{n_2}{n_1}(1 - r_{TM}). \end{aligned} \tag{A.7}$$

For a homogeneous medium the propagation from z_1 to z_2, which corresponds to wave propagation in medium 2 characterized by a refractive index n_2 (cf. Fig. A.1), can be described by the following transfer matrix:

$$M_{hom} = \begin{bmatrix} e^{ik_z^{(2)}(z_2 - z_1)} & 1 \\ 1 & e^{-ik_z^{(2)}(z_2 - z_1)} \end{bmatrix}. \tag{A.8}$$

In order to account for different layers the transfer matrix of the whole structure becomes: $M = ...M_{hom_2} M_2 M_{hom_1} M_1$. If we now consider the situation in which a unitary wave comes from the left-hand side onto the whole structure (cf. Fig. A.1), a wave of amplitude r is reflected back, and a wave of amplitude t is transmitted:

$$\begin{bmatrix} t \\ 0 \end{bmatrix} = \begin{bmatrix} M_{11} & M_{12} \\ M_{21} & M_{22} \end{bmatrix} \begin{bmatrix} 1 \\ r \end{bmatrix}, \tag{A.9}$$

which gives us:

$$r = \frac{-M_{21}}{M_{22}} \quad \text{and } t = \frac{det(M)}{M_{22}}. \tag{A.10}$$

The reflectance is defined by R = $|r|^2$ and the transmittance by T = $|t|^2/\alpha$, [85] where:

$$\alpha_{TE} = \frac{n_{in}\cos(\theta_{in})}{n_{out}\cos(\theta_{out})} \quad \text{and } \alpha_{TM} = \frac{n_{in}\cos(\theta_{in}) n_{out}^2}{n_{out}\cos(\theta_{out}) n_{in}^2}, \tag{A.11}$$

with *in* referring to the input medium and *out* to the output medium. This correction factor α takes into account the ratio of the cross-sectional areas for transmitted and incident beams [173]. The absorptance A is finally given by: $1\text{-}R\text{-}T$. Note that in the literature the following treatment can be found as well [301]:

$$\begin{bmatrix} 1 \\ r \end{bmatrix} = \frac{1}{M_{11}M_{22} - M_{21}M_{12}} \begin{bmatrix} M_{22} & -M_{21} \\ -M_{12} & M_{11} \end{bmatrix} \begin{bmatrix} t \\ 0 \end{bmatrix}. \tag{A.12}$$

A.2 Langevin Noise

A Langevin noise source $F(t)$ is a 'white' noise source, which is a memoryless, stationary process. The best analogy to $F(t)$ is a random number generator that generates uncorrelated numbers between $\pm\infty$ every δt with $\delta t \to 0$. Furthermore the following characteristics are true:[2]

- $< F(t) > = 0$.[3]
- $< F(t)F(t-\tau) > = 0$ except for $\tau = 0$, then $< F(t)F(t) > = \infty$.
- $< F_i(t)F_j(t-\tau)^* > = S_{ij}\delta(\tau)$, where S_{ij} defines the correlation strength between the two noise sources $F_i(t)$ and $F_j(t)$.
- The Langevin noise spectral density is equivalent to the correlation strength, i.e., $S_{ij}(\omega)$ $= S_{ij} = < F_i(t)F_j(t-\tau)^* >$.

A.2.1 The correlation strengths between noise sources: applied to polariton LDs

A method for simplifying the rigourous quantum description of noise in lasers has been suggested by McCumber [302] and others such as Lax [163] based on a shot noise treatment, where the spectral density of shot noise is considered constant and proportional to the average rate of particle flow. Thus the Langevin noise spectral density or the correlation strength (they are interchangeable, i.e., $S_{ij}(\omega) = < F_i(t)F_j(t-\tau)^* >$) between the different Langevin noise sources are given by:

$$< F_i F_i >= \sum R_i^+ + \sum R_i^-, \tag{A.13}$$

$$< F_i F_j >= -\left[\sum R_{ij} + \sum R_{ji}\right], \tag{A.14}$$

where the R_i^+ and R_i^- terms correspond to the rates of particle flow into and out of the reservoir i and reservoir j, respectively. In our case reservoir i can be attributed to the exciton reservoir, whereas reservoir j describes the ground state polariton reservoir. R_{ij} and R_{ji} describe the rate of particle flows between the two reservoirs. For the sake of illustration, the rates into and out of those reservoirs are displayed in Fig. 2.5(a). Using Fig. 2.5(a) neglecting the terms of

[2] The latter are demonstrated in Ref. [156].

[3] The brackets <> refer to a statistical average over many similar systems at the same time t or to a time average as the statistical processes are assumed stationary and ergodic.

spontaneous origin together with equations A.13 and A.14, we obtain:

$$< F_{n_p} F_{n_p} >= \frac{2n_{p_\infty}}{\tau_p} + 2an_{x_\infty} n_{p_\infty} e^{-\beta\Delta_{esc}} \approx \frac{2n_{p_\infty}}{\tau_p}, \tag{A.15}$$

where we used the fact that $\gamma_{pp} = 0$ – which is verified when we neglect the terms of spontaneous origin in the stationary solution of rate equation 2.11. This correlation strength is nearly equivalent to that derived for conventional semiconductor LDs, including VCSELs, except for the second term of the middle expression accounting for thermal escape of ground state polaritons from the condensate, which is inherent to the matter-like character of those bosonic quasiparticles.

$$< F_{n_x} F_{n_x} >= P_x + \frac{n_{x_\infty}}{\tau_x} - \frac{n_{p_\infty}}{\tau_p} + < F_{n_p} F_{n_p} >, \tag{A.16}$$

and

$$< F_{n_p} F_{n_x} >= - < F_{n_p} F_{n_p} > + \frac{n_{p_\infty}}{\tau_p}. \tag{A.17}$$

Furthermore, we also need to know the dependence of $< n_{p1} F_0 >$ and $< F_0 F_0 >$. The latter appear in the expression of the spectral density of the output power $S_{\delta P}(\omega)$. As output power fluctuations are driven by the polariton density fluctuations ($n_{p1}(t)$), they can be expressed as $\delta P(t) = (\eta_0 h\nu/\tau_p) n_{p1}(t) + F_0(t)$, where $F_0(t)$ is the partition noise.[4] As we did in deriving equation 2.41, $\delta P(t)$ can be converted into the frequency domain to obtain:

$$S_{\delta P}(\omega) = \left(\frac{\eta_0 h\nu}{\tau_p}\right)^2 S_{n_p}(\omega) + 2Re\left[\left(\frac{\eta_0 h\nu}{\tau_p}\right) < n_{p1} F_0 >\right] + < F_0 F_0 >, \tag{A.18}$$

where $S_{n_p}(\omega)$ is the ground state polariton spectral density given in equation 2.42. Transposing the development given in Ref. [156] to the present case, we obtain:

$$< n_{p1} F_0 >= \frac{H(\omega)}{\omega_R^2} \left[(\gamma_{xx} + j\omega) < F_{n_p} F_0 > + \gamma_{px} < F_{n_x} F_0 > \right], \tag{A.19}$$

[4] A stream of photons is partly reflected by a mirror, resulting into a random division of transmitted and reflected photons. The latter leads to partition noise in the stream of both transmitted and reflected photons.

Note that the partition noise at the mirror facet creates two additional noise contributions $< F_{n_p} F_0 >$ and $< F_{n_x} F_0 >$. First, there is no correlation between the exciton reservoir noise and the partition noise created by the partially reflecting mirrors, thus:

$$< F_{n_x} F_0 >= 0, \tag{A.20}$$

whereas for the two remaining correlation stengths equations A.13 and A.14 can be used:

$$< F_{n_p} F_0 >= -\eta_0 \frac{n_{p_\infty}}{\tau_p} h\nu = -P_0, \tag{A.21}$$

$$< F_0 F_0 >= h\nu P_0. \tag{A.22}$$

A.2.2 Coefficient related to the transfer function

Hereafter we give the explicit expression of the C_i coefficients appearing in equations 2.50 and 2.51:

$$C_1 = \frac{\frac{\gamma_{px}}{\tau_p}\left(W + \frac{1}{\tau_{e-h}}\right)}{\gamma_{px}(W - c n_{x_\infty} n_{p_\infty}) + \gamma_{xx} c n_{x_\infty} n_{p_\infty}}, \tag{A.23}$$

$$C_2 = \gamma_{px}(W - c n_{x_\infty} n_{p_\infty}) + \gamma_{xx} c n_{x_\infty} n_{p_\infty}, \tag{A.24}$$

$$C_3 = \frac{\gamma_{px}}{\tau_p} - \omega^2 = \omega_R^2 - \omega^2, \tag{A.25}$$

and

$$C_4 = W + \frac{1}{\tau_{e-h}}. \tag{A.26}$$

A.3 Modulation spectroscopy: Photo- and electroreflectance

A.3.1 Principle

Modulation spectroscopy provides information about the intrinsic properties of semiconductor samples. Due to the derivative nature of the modulation spectra, they are highly sensitive to the critical points of the joint density of states. One distinguishes between external and internal modulation. In the case of internal modulation the modulation is applied to the measuring system itself (e.g., wavelength modulation spectroscopy), whereas in the case of external modulation, the properties of the sample itself are directly altered (e.g., in ER, PR, thermoreflectance, or piezoreflectance spectroscopy). The modulation is accomplished in a periodic fashion and the corresponding changes in the optical properties of the semiconductor sample are measured.

A.3.2 Setup specificities

The experimental PR setup in the so-called dark configuration is schematically depicted in Fig. A.2. A Xe-lamp coupled to a monochromator provides monochromatic light. A small part of the monochromatic beam is guided onto a UV enhanced Si-photodiode (the reference photodiode) connected to a digital multimeter (DMM). By means of a beamsplitter (BS) plate the main part (with intensity I_0) is brought into focus on the sample located in a cryostat by means of two lenses with focal length f_2 equal to 20 cm and f_3 equal to 10 cm and two aluminum mirrors (m_1 and m_2). The reflected beam is brought by a mirror (m_3) and a lens with focal length f_4 equal to 7 cm to a second UV enhanced Si-photodiode (the reflectivity photodiode) also connected to a DMM and to a lock-in amplifier. Furthermore, a low-pass filter allows to minimize the impact of scattered laser light. Note that PR measurements might be accomplished as well in the bright configuration. In this case the sample is probed by white light and the second photodiode is placed after a monochromator.[5]

Photoreflectance

In PR, modulation is achieved by photomodulation, i.e., a mechanically chopped laser source is overlapped with the reflectivity beam on the sample. Various laser sources might be used:

- a frequency-quadrupled Nd:YAG laser emitting at 266 nm: 500 ps pulse length and 8.52 kHz repetition rate,
- a frequency-tripled Nd:YAG laser emitting at 355 nm: 570 ps pulse length and 7.1 kHz repetition rate,
- a cw frequency-doubled optically pumped semiconductor laser (OPSL) emitting at 244 nm,

[5] Dark and bright configuration of PR and contactless ER (CER) measurements are compared in Ref. [303].

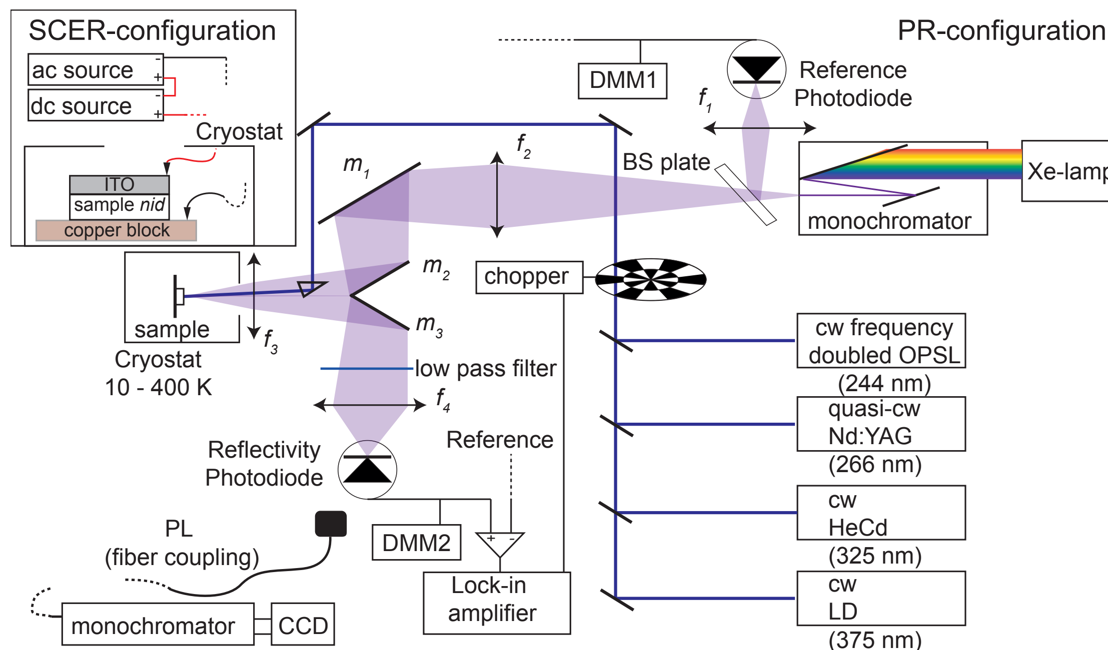

Figure A.2: Schematic view of the PR setup in the so-called dark configuration. In the inset the case of semi-contactless ER (SCER) is illustrated. The pump beam responsible for the photomodulation is replaced by a dc and an ac power supply set up in series.

- a cw HeCd laser emitting at 325 nm,
- or a cw LD emitting at 375 nm.

Note that for most of the PR measurements the photomodulation was achieved with the Nd:YAG laser emitting at 266 nm, mechanically chopped at 170 Hz. A large spot size (~ 1 mm) that matches that of the white light spot was used in order to ensure that the active region is maintained in the low injection regime (no screening of the built-in field).

Semi-contactless electroreflectance

Note that for ER or semi-contactless ER (SCER) the photomodulation is replaced by a direct current (dc) and an alternativ current (ac) power supply set up in series (cf. inset in Fig. A.2). In the case of SCER an ITO layer of ~ 200 nm thickness is sputtered on the sample surface. Then the ITO and a copper block supporting the sample are electrically contacted. A maximum peak-to-peak alternating voltage of ~ 2 V at a frequency of 288 Hz is applied to the sample. The semi-contactless ER technique provides a much better signal to noise ratio than the PR does, which proved really crucial for the characterization of the InGaN/GaN SQW sample.

In PR and SCER the signal measured by the reflectivity photodiode has two components: (i) a dc component, which is proportional to $I_0 R$, and (ii) an ac component, which is proportional

to $I_0 \Delta R$. Note that the DMMs are used to measure the dc part of the signal. The lock-in amplifier is responsible for the ac part. Lock-in amplifiers use a technique known as phase-sensitive detection to single out the ac component (at a specific reference frequency and phase) of a signal.

Furthermore, PL measurements can be done using a fiber connected to the combination of a 32 cm focal length monochromator and a Peltier-cooled CCD.

A.3.3 Critical aspects

Spurious signals such as scattered laser light or PL are a common problem in PR spectroscopy. They distort the PR spectra, and even submerges the PR signal if it is much stronger than the PR signal. Several approaches exist to get rid of spurious signals such as sweeping PR [304], electrical/optical front-end compensation PR [305, 306], employing a subtraction scheme with two detectors [307], using a Fourier transform spectrometer [308], and dual chopped PR [309]. However, none of them has been implemented in our setup instead modulation conditions have been chosen with great care in order to minimize spurious signals. If ever spurious signals are measured as an energy-independent ac component, they simply up-shift PR spectra without distortion.
In Fig. A.3(a) LT (20 K) down-shifted PR spectra acquired at various modulation intensities are displayed. The sample under study is a 5 $In_{0.1}Ga_{0.9}N$ (2 nm)/GaN (3 nm) MQW sample capped with a 20 nm thick GaN layer grown on a c-plane FS-GaN substrate. The photomodulation is acquired with the cw HeCd laser source and the 2D carrier density has been estimated to $3.2 \cdot 10^7$ cm^2 for a modulation intensity of 200 μW (cf. section 4.3.5). Increasing the modulation intensity results in an increased amplitude of the PR resonance until the resonance gets strongly distorted (blue squares) at 200 μW. Note that at higher modulation intensities the PR signal completely submerges. Thus, modulation conditions corresponding to low modulation intensities are generally chosen. Note that for temperature-dependent PR measurements a sufficiently high modulation intensity allowing RT measurements have to be chosen (typically between 20-63 μW depending on the sample).
The normalized spectra of Fig. A.3(a) are shown in Fig. A.3(b). A slight blueshift of ~ 5 meV is observed. The latter might be due to an absorption bleaching of the band-tail states or/and to locally strong inhomogeneous carrier densities, due to carrier localization, affecting the charge configuration of the nanoenvironment of localization centers (cf. section 4.3.2) leading to the observed blueshift. As the modulation intensities are limited due to the increase of spurious signals (mainly PL), in order to further probe the absorption bleaching and an eventual screening of QCSE, a non-modulated pulsed Nd:YAG laser (mentioned above) is superimposed to the HeCd laser spot (pump beam) driven at 20 μW and the monochromatic probe beam. In Fig. A.3(c) the transition energy deduced from the PR spectra shown in the inset blueshifts with increasing intensity of the additional laser source. In this case high peak powers are reached. However, it is difficult to estimate the 2D carrier density per QW as

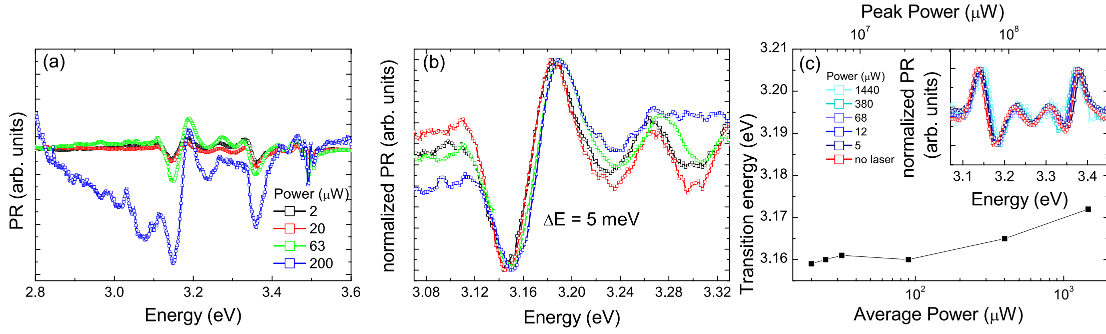

Figure A.3: LT PR spectra of 5 InGaN/GaN MQWs: (a) Increasing the modulation intensity results in an increased amplitude of the PR resonance and an eventual strong distortion of the PR spectra (blue squares). (b) Corresponding normalized PR spectra indicating a slight blue shift (ΔE = 5 meV). Furthermore, a non-modulated Nd:YAG laser is superimposed to the probe and pump beam of PR measurements. (c) Corresponding spectra are displayed in the inset and the transition energy of the fundamental transition is plotted against the power of the non-modulated Nd:YAG laser source.

the carrier redistribution among the five QWs is unknown and furthermore, PR spectra are acquired over several minutes and thus probably governed by an intermediate carrier density (probably not the one present in the QWs just after the rise time). Thus, it is challenging to distinguish screening effects from absorption bleaching. However, as the PR lineshape does not considerably change with increasing carrier densities, screening effects might play a major role.

A.4 Fourier imaging

The energy dispersion of the eigenmodes of a MC (lower and upper polaritons or exciton and cavity photon modes) is experimentally accessible by means of angle-resolved measurements including reflectivity, transmission, absorption or PL. The energy dispersion curve can be recorded either by scanning different emission angles by a fiber-mounted onto one of the arms of a goniometer or by directly imaging the Fourier plane.

A.4.1 Principle

The Fourier plane is the plane on which each point corresponds to the far field emission (θ_e, ϕ_k) of the emitting spot. It is formed at a distance f_{obj}, corresponding to the focal length of the objective, directly on the back of the objective. As the latter amounts to a few mm, two other lenses, with focal length f_1 = 30 cm and f_2 = 20 cm, respectively, are used to image this Fourier plane (FP1) at the entrance of the spectrometer entrance slit (FP2) (cf. Fig. A.4). Simultaneously FP1 is magnified by $\gamma = f_1 / f_2$.

The principle of Fourier spectroscopy is displayed in Fig. A.4(b). A point in the Fourier plane

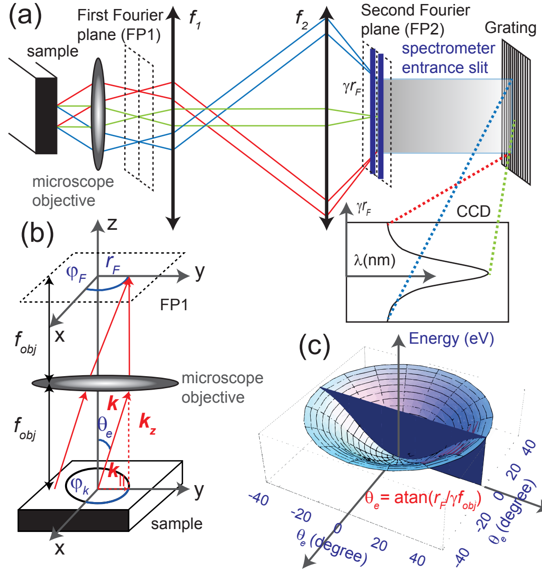

Figure A.4: Fourier imaging spectroscopy principle with one high N.A. microscope objective and two lenses (f_1 and f_2).(a) The sample emits light from two different points into three directions (red, green, blue). The two Fourier planes (FP1 and FP2) are indicated. The energy dispersion curve is monitored on the CCD camera after dispersion on a grating of a section of FP2. The plane FP2 is magnified for clarity. (b) Zoom onto the FP1 formation: Two spatially separated points emitting light with the same angles θ_e and ϕ_k result in one point in the FP1 at (r_F, ϕ_F) situated at a distance f_{obj} from the objective. (c) Formation of the dispersion curve: A narrow spectrometer entrance slit (dark blue plane) selects a line out of the blue emission surface (blue surface).

(in cylindrical coordinates) $\mathbf{r}_F = (r_F,\varphi_F)$ contains all the light emitted from the sample into one direction (θ_e,φ_k). Considering Fig. A.4(b) and using trigonometry, it is straightforward to write the following relation:

$$(r_F, \phi_F) = \left(f_{obj} \tan(\theta_e), \varphi_k\right). \tag{A.27}$$

As there is a relation between θ_e and $k_{||}$ (see equation 1.36), there is also a bijection from the Fourier plane to the plane of the eigenmodes of the MC. We have the following correspondence:

$$(r_F, \phi_F) = \left(f \left(\left(\frac{E(k_{||})}{k_{||}\hbar c} \right)^2 - 1 \right)^{-\frac{1}{2}}, \varphi_k \right). \tag{A.28}$$

A.4.2 Critical aspects

In order to obtain the energy dispersion curves a narrow spectrometer slit is mandatory. An infinitesimal narrow slit corresponds to an intersection of the emission surface with a vertical plane as plotted in Fig. A.4(c). If the center of FP2 does not fall exactly on the center of the entrance slit, the energy dispersion curves are recorded distorted. The latter is illustrated for the cavity mode dispersion of a tilted MC sample.[6] Note that in the case of tilted samples the alignment is more difficult as the maximum of intensity is not in the middle of FP2. In Fig. A.5(a) each ellipse corresponds to a different θ_e, respectively a different emission energy,

[6] In order to access higher emission angles the sample might be tilted.

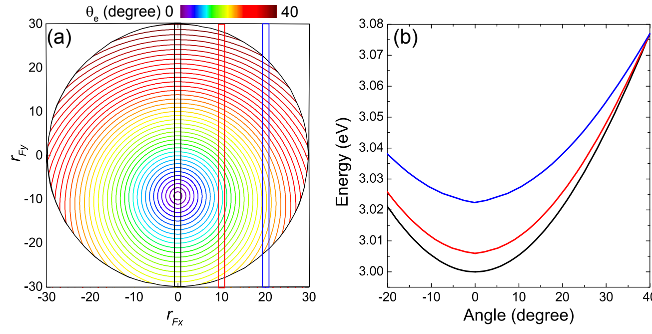

Figure A.5: (a) Fourier plane (FP2) for a sample tilt of 10°. Each ellipse corresponds to a different emission angle (θ_e), respectively, a different emission energy. (b) Corresponding energy dispersion curve in the case of a cavity mode for the three different slit positions indicated in (a).

as seen in FP2. Note that FP2 is limited by N.A. of the objective as indicated by the black line in Fig. A.5(a). Usually, the maximum of intensity is measured at small emission angles, corresponding to the violet-blue circles in Fig. A.5(a), which are clearly off-centered. For FP2 matching the center of the entrance slit (black rectangle), the corresponding energy dispersion curve is plotted in Fig. A.5(b) (black line). Otherwise, the energy dispersion curve is gradually truncated (cf. red and blue lines in Fig. A.5(b)).

A.4.3 Setup specificities

The experimental setup is schematically depicted in Fig. A.6. Various excitation sources might be used:

- a frequency-quadrupled Nd:YAG laser emitting at 266 nm: 500 ps pulse length and 8.52 kHz repetition rate,
- a frequency-tripled Nd:YAG laser emitting at 355 nm: 570 ps pulse length and 7.1 kHz repetition rate,
- a cw frequency-doubled Ar-ion laser at 244 nm,
- an optical parametric oscillator system tunable between 210 and 2300 nm: 7 ns pulse length and 1 kHz repetition rate,
- or a white light source (Xenon lamp) for reflectivity and transmission measurements and real space imaging.

According to the excitation source the objectiv is chosen:

- UV microscope with a N.A. = 0.55 giving access to a maximum detection angle $\theta_{max} \sim$ 33.4° and f_{obj} = 2.5 mm.
- NUV microscope with a N.A. = 0.5 giving access to $\theta_{max} \sim 30$ ° and f_{obj} = 2 mm.

Simultaneously to temperature-dependent PL or reflectivity Fourier spectroscopy (4-400 K) transmission measurements (PL or white light, respectively) might be acquired thanks to a

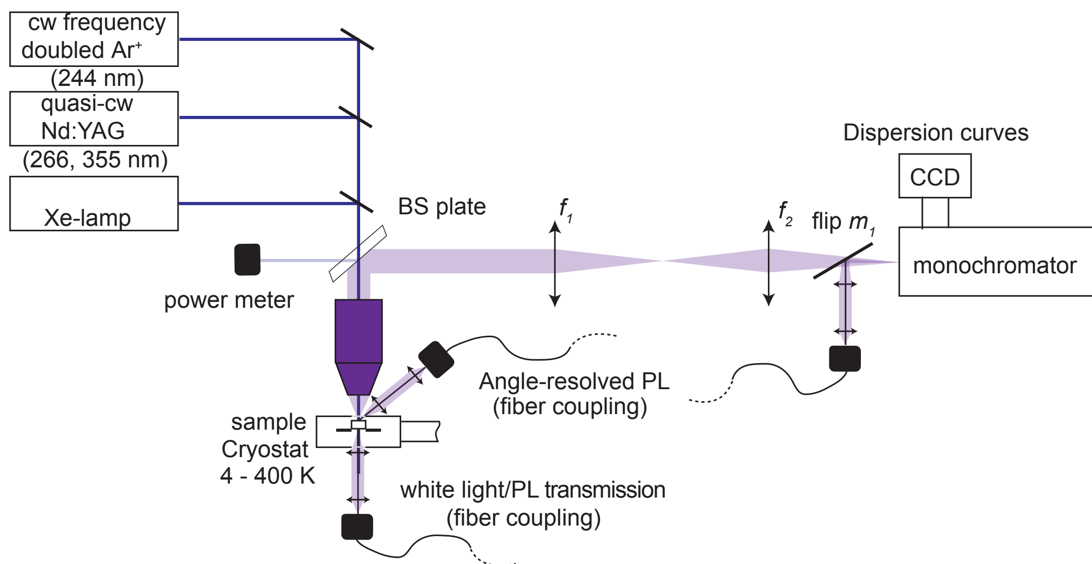

Figure A.6: Schematic representation of the experimental setup including the various excitation sources and the collection lines (1 and 2). Temperature, power, and polarization-resolved studies are possible. The goniometer arm is superimposed to the standard Fourier setup showing the possibility of performing conventional angle-resolved measurements. See text for more details.

fiber coupling and a flip mirror (flip m_1) positioned in front of the spectrometer entrance (cf. Fig. A.6).

As already mentioned previously instead of imaging the Fourier plane different angles might be scanned by a fiber mounted onto an arm of a goniometer as illustrated in Fig. A.6 (angle-resolved PL by fiber coupling). However, the latter is more time-consuming and measurements are limited to relatively large spot sizes as lenses instead of a microscope objectiv are used for the excitation.

Bibliography

[1] McKinsey & Co., *Lighting the Way: Perspectives on the global lighting market* (Press release, 2nd edition, 2012)

[2] N. Holonyak, S. F. Bevacqua, *Coherent (visible) light emission from Ga(As$_{1-x}$P$_x$) junctions*, Appl. Phys. Lett. **1**, 82 (1962)

[3] R. D. Dupuis, *An introduction to the development of the semiconductor-laser*, IEEE J. Quantum Elect. **23**, 651 (1987)

[4] F. Briegleb, A. Geuther, *About MgN and the affinity of nitrogen gas with metals*, Ann. Chem. **123**, 228 (1862)

[5] R. Dingle, K. L. Shaklee, R. F. Leheny, R. B. Zetterstrom, *Stimulated emission and laser action in gallium nitride*, Appl. Phys. Lett. **19**, 5 (1971)

[6] H. Amano, M. Kito, K. Hiramatsu, I. Akasaki, *P-type conduction in Mg-doped GaN treated with low-energy electron-beam irradiation (LEEBI)*, Jpn. J. Appl. Phys. **28**, L2112 (1989)

[7] S. Nakamura, M. Senoh, T. Mukai, *P-GaN/n-InGaN/n-GaN double-heterostructure blue-light-emitting diodes*, Jpn. J. Appl. Phys. **32**, L8 (1993)

[8] S. Nakamura, G. Fasol, *The Blue Laser Diode (The Complete Story)* (Springer-Verlag, Heidelberg, Germany, 1997)

[9] S. Nakamura, M. Senoh, S. Nagahama, N. Iwasa, T. Yamada, T. Matsushita, H. Kiyoku, Y. Sugimoto, *InGaN-based multi-quantum-well-structure laser diodes*, Jpn. J. Appl. Phys. **35**, L74 (1996)

[10] D. Ohnishi, T. Okano, M. Imada, S. Noda, *Room temperature continuous wave operation of a surface-emitting two-dimensional photonic crystal diode laser*, Opt. Express **12**, LEOS (2004)

[11] K. Hirose, Y. Liang, Y. Kurosaka, A. Watanabe, T. Sugiyama, S. Noda, *Watt-class high-power, high-beam-quality photonic-crystal lasers*, Nat. Photon. **8**, 406 (2014)

[12] E. Feltin, A. Castiglia, G. Cosendey, L. Sulmoni, J.-F. Carlin, N. Grandjean, M. Rossetti, J. Dorsaz, V. Laino, M. Duelk, C. Vélez, *Broadband blue superluminescent light-emitting diodes based on GaN*, Appl. Phys. Lett. **95**, 081107 (2009)

[13] T.-C. Lu, C.-C. Kao, H.-C. Kuo, G.-S. Huang, S.-C. Wang, *CW lasing of current injection blue GaN-based vertical cavity surface emitting laser*, Appl. Phys. Lett. **92**, 141102 (2008)

[14] Y. Higuchi, K. Omae, H. Matsumura, T. Mukai, *Room-Temperature cw lasing of a GaN-based vertical-cavity surface-emitting laser by current injection*, Appl. Phys. Express **1**, 121102 (2008)

[15] T.-C. Lu, S.-W. Chen, T.-T. Wu, P.-M. Tu, C.-K. Chen, C.-H. Chen, Z.-Y. Li, H.-C. Kuo, S.-C. Wang, *Continuous wave operation of current injected GaN vertical cavity surface emitting lasers at room temperature*, Appl. Phys. Lett. **97**, 071114 (2010)

[16] D. Kasahara, D. Morita, T. Kosugi, K. Nakagawa, J. Kawamata, Y. Higuchi, H. Matsumura, T. Mukai, *Demonstration of blue and green GaN-based vertical-cavity surface-emitting lasers by current injection at room temperature*, Appl. Phys. Express **4**, 072103 (2011)

[17] C. Holder, J. S. Speck, S. P. DenBaars, S. Nakamura, D. Feezell, *Demonstration of nonpolar GaN-based vertical-cavity surface-emitting lasers*, Appl. Phys. Express **5**, 092104 (2012)

[18] G. Cosendey, A. Castiglia, G. Rossbach, J.-F. Carlin, N. Grandjean, *Blue monolithic AlInN-based vertical cavity surface emitting laser diode on free-standing GaN substrate*, Appl. Phys. Lett. **101**, 151113 (2012)

[19] W.-J. Liu, X.-L. Hu, L.-Y. Ying, J.-Y. Zhang, B.-P. Zhang, *Room temperature continuous wave lasing of electrically injected GaN-based vertical cavity surface emitting lasers*, Appl. Phys. Lett. **104**, 251116 (2014)

[20] U. K. Mishra, L. Shen, T. E. Kazior, Y.-F. Wu, *GaN-Based RF power devices and amplifiers*, Proceedings of the IEEE **96**, 287 (2008)

[21] S. Nagahama, M. Sano, T. Yanamoto, D. Morita, O. Miki, K. Sakamoto, M. Yamamoto, Y. Matsuyama, Y. Kawata, T. Murayama, T. Mukai, *GaN-based laser diodes emitting from ultraviolet to blue-green.*, Proc. SPIE **4995**, 108 (2003)

[22] S. I. Nagahama, Y. Sugimoto, T. Kozaki, T. Mukai, *Recent progress of AlInGaN laser diodes*, Proc. SPIE **5738**, 57 (2005)

[23] T. Onishi, O. Imafuji, K. Nagamatsu, M. Kawaguchi, K. Yamanaka, S. Takigawa, *Continuous wave operation of GaN vertical cavity surface emitting lasers at room temperature*, IEEE J. Quantum Elect. **48**, 1107 (2012)

[24] P. Bhattacharya, T. Frost, S. Deshpande, M. Z. Baten, A. Hazari, A. Das, *Room temperature electrically injected polariton laser*, Phys. Rev. Lett. **112**, 236802 (2014)

[25] R. Butté, N. Grandjean, *A novel class of coherent light emitters: polariton lasers*, Semicond. Sci. Technol. **26**, 014030 (2011)

[26] I. Iorsh, M. Glauser, G. Rossbach, J. Levrat, M. Cobet, R. Butté, N. Grandjean, M. A. Kaliteevski, Richard A. Abram, A. V. Kavokin, *Generic picture of the emission properties of III-nitride polariton laser diodes: Steady state and current modulation response*, Phys. Rev. B **86**, 125308 (2012)

[27] T. H. Maiman, *Stimulated optical radiation in ruby*, Nature **187**, 493 (1960)

[28] Z. I. Alferov, V.M. Andreev, D. Z. Garbuzov, Y. V. Zhilyaev, E. P. Morozov, E. I. Portnoi, V. G. Trofim, *Investigation of influence of AlAs-GaAs heterostructure parameters on laser threshold current and realization of continuous emission at room temperature*, Fiz. Tekn. Poluprovodn. (Sov. Phys. Semicond.) **4**, 1826 (1573 (1970 (1971))

[29] R. Dingle, C. H. Henry, *Quantum effects in heterostructure lasers* (US Patent No 3982207, 1976)

[30] M. G. A. Bernard, G. Duraffourg, *Laser conditions in semiconductors*, Phys. Stat. Sol. **1**, 699 (1961)

[31] Z. Alferov, *Double heterostructure lasers: Early days and future perspectives*, IEEE J. Sel. Top. Quant. Electron. **6**, 832 (2000)

[32] D. G. Deppe, K. Shavritranuruk, G. Ozgur, H. Chen, S. Freisem, *Quantum dot laser diode with low threshold and low internal loss*, Electron. Lett. **45**, 54 (2009)

[33] A. Imamoğlu, R. J. Ram, S. Pau, Y. Yamamoto, *Nonequilibrium condensates and lasers without inversion: Exciton-polariton lasers*, Phys. Rev. A **53**, 4250 (1996)

[34] A. Einstein, *Quantentheorie des einatomigen idealen Gases. Zweite Abhandlung.*, Sitzber. Preuss. Akad. **1**, 3 (1925)

[35] M. H. Anderson, J. R. Ensher, M. R. Matthews, C. E. Wieman, E. A. Cornell, *Observation of Bose-Einstein condensation in a dilute atomic vapor*, Science **269**, 198 (1995)

[36] K. B. Davis, M. O. Mewes, M. R. Andrews, N. J. van Druten, D. S. Durfee, D. M. Kurn, W. Ketterle, *Bose-Einstein condensation in a gas of sodium atoms*, Phys. Rev. Lett. **75**, 3969 (1995)

[37] J. Kasprzak, M. Richard, S. Kundermann, A. Baas, P. Jeambrun, J. M. J. Keeling, F. M. Marchetti, M. H. Szymańska, R. André, J. L. Staehli, V. Savona, P. B. Littlewood, B. Deveaud-Plédran, Le Si Dang, *Bose-Einstein condensation of exciton polaritons*, Nature (London) **443**, 409 (2006)

[38] K. G. Lagoudakis, M. Wouters, M. Richard, A. Baas, I. Carusotto, R. André, Le Si Dang, B. Deveaud-Plédran, *Quantized vortices in an exciton-polariton condensate*, Nature Phys. **4**, 706 (2008)

[39] K. G. Lagoudakis, T. Ostatnický, A. V. Kavokin, Y. G. Rubo, R. André, B. Deveaud-Plédran, *Observation of half-quantum vortices in an exciton-polariton condensate*, Science **326**, 5955 (2009)

[40] A. Amo, D. Sanvitto, F. P. Laussy, D. Ballarini, E. del Valle, M. D. Martin, A. Lemaître, J. Bloch, D. N. Krizhanovskii, M. S. Skolnick, C. Tejedor, L. Viña, *Collective fluid dynamics of a polariton condensate in a semiconductor microcavity*, Nature (London) **457**, 291 (2008)

[41] A. Amo, J. Lefrère, S. Pigeon, C. Adrados, C. Ciuti, R. Houdré I. Carusotto, E. Giacobino, A. Bramati, *Superfluidity of polaritons in semiconductor microcavities,* Nature Phys. **5**, 805 (2009)

[42] S. Utsunomiya, L. Tian, G. Roumpos, C. W. Lai, N. Kumada, T. Fujisawa, M. Kuwata-Gonokami, A. Löffler, S. Höfling, A. Forchel, Y. Yamamoto, *Observation of Bogoliubov excitations in exciton-polariton condensates*, Nature Phys. **4**, 700 (2008)

[43] M. Sich, D. N. Krizhanovskii, M. S. Skolnick, A. V. Gorbach, R. Hartley, D. V. Skryabin, E. A. Cerda-Mendez, K. Biermann, R. Hey, P. V. Santos, *Observation of bright polariton solitons in a semiconductor microcavity*, Nat. Photon. **6**, 50 (2012)

[44] A. Amo, S. Pigeon, D. Sanvitto, V. G. Sala, R. Hivet, I. Carusotto, F. Pisanello, G. Leménager, R. Houdré, E Giacobino, C. Ciuti, A. Bramati, *Polariton superfluids reveal quantum hydrodynamic solitons*, Science **332**, 1167 (2011)

[45] J. R. Tischler, M. S. Bradley, V. Bulovic, J. H. Song, A. Nurmikko, *Strong coupling in a microcavity LED*, Phys. Rev. Lett. **95**, 036401 (2005)

[46] G. H. Lodden, R. J. Holmes, *Electrical excitation of microcavity polaritons by radiative pumping from a weakly coupled organic semiconductor*, Phys. Rev. B **82**, 125317 (2010)

[47] N. Christogiannis, N. Somaschi, P. Michetti, D. M. Coles, P. G. Savvidis, P. G. Lagoudakis, D. G. Lidzey, *Characterizing the electroluminescence emission from a strongly coupled organic semiconductor microcavity LED*, Adv. Opt. Mater. **1**, 503 (2013)

[48] A. A. Khalifa, A. P. D. Love, D. N. Krizhanovskii, M. S. Skolnick, J. S. Roberts, *Electroluminescence emission from polariton states in GaAs-based semiconductor microcavities*, Appl. Phys. Lett. **92**, 061107 (2008)

[49] D. Bajoni, E. Semenova, A. Lemaître, S. Bouchoule, E. Wertz, P. Senellart, J. Bloch, *Polariton light-emitting diode in a GaAs-based microcavity*, Phys. Rev. B **77**, 113303 (2008)

[50] S. I. Tsintzos, N. T. Pelekanos, G. Konstantinidis, Z. Hatzopoulos, P. G. Savvidis, *A GaAs polariton light-emitting diode operating near room temperature*, Nature (London) **453**, 372 (2008)

[51] P. Bhattacharya, B. Xiao, A. Das, S. Bhowmick, J. Heo, *Solid state electrically injected exciton-polariton laser*, Phys. Rev. Lett. **110**, 206403 (2013)

[52] C. Schneider, A. Rahimi-Iman, N. Y. Kim, J. Fischer, I. G. Savenko, M. Amthor, M. Lermer, A. Wolf, L. Worschech, V. D. Kulakovskii, I. A. Shelykh, M. Kamp, S. Reitzenstein, A. Forchel, Y. Yamamoto, S. Hoefling, *An electrically pumped polariton laser*, Nature (London) **497**, 348 (2013)

[53] M. Saba, C. Ciuti, J. Bloch, V. Thierry-Mieg, R. André, Le Si Dang, S. Kundermann, A. Mura, G. Bongiovanni, J. L. Staehli, B. Deveaud-Plédran, *High-temperature ultrafast polariton parametric amplification in semiconductor microcavities*, Nature (London) **414**, 731 (2001)

[54] S. Christopoulos, G. Baldassarri Höger von Högersthal, A. J. D. Grundy, P. G. Lagoudakis, A. V. Kavokin, J. J. Baumberg, G. Christmann, R. Butté, E. Feltin, J.-F. Carlin, N. Grandjean, *Room-temperature polariton lasing in semiconductor microcavities*, Phys. Rev. Lett. **98**, 126405 (2007)

[55] G. Christmann, R. Butté, E. Feltin, J.-F. Carlin, N. Grandjean, *Room temperature polariton lasing in a GaN/AlGaN multiple quantum well microcavity*, Appl. Phys. Lett. **93**, 051102 (2008)

[56] M. Mizuta, S. Fujieda, Y. Matsumoto, T. Kawamura, *Low-temperature growth of GaN and AlN on GaAs utilizing metalorganics and hydrazine*, Jpn. J. Appl. Phys. **25**, L945 (1986)

[57] T. Lei, M. Fanciulli, R. J. Molnar, T. D. Moustakas, R. J. Graham, J. Scanlon, *Epitaxial-growth of zinc blende and wurtzitic gallium nitride thin-films on (001) silicon*, Appl. Phys. Lett. **59**, 944 (1991)

[58] A. L. Allred, *Electronegativity values from thermochemical data*, J. Inorg. Nucl. Chem. **17**, 215 (1961)

[59] P. Waltereit, O. Brandt, A. Trampert, H. T. Grahn, J. Menniger, M. Ramsteiner, M. Reiche, K. H. Ploog, *Nitride semiconductors free of electrostatic fields for efficient white light-emitting diodes*, Nature (London) **406**, 865 (2000)

[60] I. Vurgaftman, J. R. Meyer, L. R. Ram-Mohan, *Band parameters for III-V compound semiconductors and their alloys*, J. Appl. Phys. **89**, 5815 (2001)

[61] F. Bernardini, V. Fiorentini, D. Vanderbilt, *Spontaneous polarization and piezoelectric constants of III-V nitrides*, Phys. Rev. B **56**, 10024 (1997)

[62] F. Bernardini, V. Fiorentini, D. Vanderbilt, *Accurate calculation of polarization-related quantities in semiconductors*, Phys. Rev. B **63**, 193201 (2001)

[63] F. Bernardini, V. Fiorentini, *Nonlinear macroscopic polarization in III-V nitride alloys*, Phys. Rev. B **64**, 085207 (2001)

[64] M. A. Dubois, P. Muralt, *Properties of aluminum nitride thin films for piezoelectric transducers and microwave filter applications*, Appl. Phys. Lett. **74**, 3032 (1999)

[65] M. S. Shur, A. D. Bykhovski, R. Gaska, *Pyroelectric and piezoelectric properties of GaN-based materials*, MRS Internet J. Nitride Semicond. Res. **4**, G1.6 (1999)

[66] V. Fiorentini, F. Bernardini, O. Ambacher, *Evidence for nonlinear macroscopic polarization in III-V nitride alloy heterostructures*, Appl. Phys. Lett. **80**, 1204 (2002)

[67] R. Butté, N. Grandjean edited by C. Wood, D. Jena, *Polarization Effects in Semiconductors: From Ab Initio Theory to Device Applications* (Springer US, New York, 2008)

[68] F. Bernardini, V. Fiorentini, *Spontaneous versus piezoelectric polarization in III-V nitrides: Conceptual aspects and practical consequences*, Phys. Stat. Sol. B **216**, 391 (1999)

[69] N. Grandjean, B. Damilano, S. Dalmasso, M. Leroux, M. Laügt, J. Massies, *Built-in electric-field effects in wurtzite AlGaN/GaN quantum wells*, J. Appl. Phys. **86**, 3714 (1999)

[70] G. Christmann, R. Butté, E. Feltin, A. Mouti, P. A. Stadelmann, A. Castiglia, J.-F. Carlin, N. Grandjean, *Large vacuum Rabi splitting in a multiple quantum well GaN-based microcavity in the strong-coupling regime*, Phys. Rev. B **77**, 085310 (2008)

[71] D. A. B. Miller, D. S. Chemla, T. C. Damen, A. C. Gossard, W. Wiegmann, T. H. Wood, C. A. Burrus, *Electric-field dependence of optical-absorption near the band-gap of quantum-well structures*, Phys. Rev. B **32**, 1043 (1985)

[72] O. Ambacher, J. Majewski, C. Miskys, A. Link, M. Hermann, M. Eickhoff, M. Stutzmann, F. Bernardini, V. Fiorentini, V. Tilak, B. Shaff, L. F. Eastman, *Pyroelectric properties of Al(In)GaN/GaN hetero- and quantum well structures*, J. Phys.: Condens. Matter **14**, 3399 (2002)

[73] Y. P. Varshni, *Temperature dependence of energy gap in semiconductors*, Physica **34**, 149 (1967)

[74] R. Passler, *Parameter sets due to fittings of the temperature dependencies of fundamental bandgaps in semiconductors*, Phys. Stat. Sol. B **216**, 975 (1999)

[75] L. Viña, S. Logothetidis, M. Cardona, *Temperature dependence of the dielectric function of germanium*, Phys. Rev. B **30**, 1979 (1984)

[76] C. D. Thurmond, *Standard thermodynamic functions for formation of electrons and holes In Ge, Si, GaAs, and GaP*, J. Electrochem. Soc. **122**, 1133 (1975)

[77] I. N. Remediakis, E. Kaxiras, *Band-structure calculations for semiconductors within generalized-density-functional theory*, Phys. Rev. B **59**, 5536 (1999)

[78] B. Gil, O. Briot, *Internal structure and oscillator strengths of excitons in strained α-GaN*, Phys. Rev. B **55**, 2530 (1997)

[79] K. Shimada, T. Sota, K. Suzuki, *First-principles study on electronic and elastic properties of BN, AlN, and GaN*, J. Appl. Phys. **84**, 4951 (1998)

[80] M. Suzuki, T. Uenoyama, A. Yanase, *First-principle calculations of effective-mass parameters of AlN and GaN*, Phys. Rev. B **52**, 8132 (1995)

[81] B. Gil, O. Briot, R.-L. Aulombard, *Valence-band physics and the optical properties of GaN epilayers grown onto sapphire with wurtzite symmetry*, Phys. Rev. B **52**, R17028 (1995)

[82] J. Wu, W. Walukiewicz, K. M. Yu, J. W. Ager, E. E. Haller, H. Lu, W. J. Schaff, Y. Saito, Y. Nanishi, *Unusual properties of the fundamental band gap of InN*, Appl. Phys. Lett. **80**, 3967 (2002)

[83] K. Kornitzer, T. Ebner, K. Thonke, R. Sauer, C. Krichner, V. Schwegler, M. Kamp, M. Leszczynski, I. Grzegory, S. Porowski, *Photoluminescence and reflectance spectroscopy of excitonic transitions in high-quality homoepitaxial GaN films*, Phys. Rev. B **60**, 1471 (1999)

[84] S. Chichibu, T. Azuhata, T. Sota, S. Nakamura, *Excitonic emissions from hexagonal GaN epitaxial layers*, J. Appl. Phys. **79**, 2784 (1996)

[85] V. Savona, *Linear optical properties of semiconductor microcavities with embedded quantum wells* (H. Benisty *et al.*, Editors (Springer Verlag, Berlin), p. 173-242, 1999)

[86] D. I. Babic, S. W. Corzine, *Analytic expressions for the reflection delay, penetration depth, and absorptance of quarter-wave dielectric mirrors*, IEEE J. Quantum Elect. **28**, 514 (1992)

[87] C. Wilmsen, H. Temkin, L. A. Coldren, *Vertical-Cavity Surface-Emitting Lasers* (Cambridge University Press, New York, 1999)

[88] H. Benisty, H. De Neve, C. Weisbuch, *Impact of planar microcavity effects on light extraction - Part I: basic concepts and analytical trends*, IEEE J. Quantum Elect. **1612**, 34 (1998)

[89] S. Pau, G. Björk, J. Jacobson, H. Cao, Y. Yamamoto, *Microcavity exciton-polariton splitting in the linear regime*, Phys. Rev. B **51**, 14437 (1995)

[90] J. J. Hopfield, *Theory of the contribution of excitons to the complex dielectric constant of crystals*, Phys. Rev. **112**, 1555 (1958)

[91] M. S. Skolnick, T. A. Fisher, D. M. Whittaker, *Strong coupling phenomena in quantum microcavity structures*, Semicond. Sci. Technol. **13**, 645 (1998)

[92] V. Savona, L. C. Andreani, P. Schwendimann, A. Quattropani, *Quantum well excitons in semiconductor microcavities: unified treatment of weak and strong coupling regimes*, Solid State Commun. **93**, 733 (1995)

[93] R. Houdré, *Early stages of continuous wave experiments on cavity-polaritons*, Phys. Stat. Sol. B **242**, 2167 (2005)

[94] Y. F. Zhu, D. J. Gauthier, S. E. Morin, Q. L. Wu, H. J. Carmichael, T. W. Mossberg, *Vacuum rabi splitting as a feature of linear-dispersion theory - analysis and experimental-observations*, Phys. Rev. Lett. **64**, 2499 (1990)

[95] L. C. Andreani, *Exciton-polaritons in superlattices*, Phys. Lett. A **192**, 99 (1994)

[96] R. Houdré, R. P. Stanley, M. Ilegems, *Vacuum-field Rabi splitting in the presence of inhomogeneous broadening: Resolution of a homogeneous linewidth in an inhomogeneously broadened system*, Phys. Rev. A **53**, 2711 (1996)

[97] N. Antoine-Vincent, F. Natali, D. Byrne, A. Vasson, P. Disseix, J. Leymarie, M. Leroux, F. Semond, J. Massies, *Observation of Rabi splitting in a bulk GaN microcavity grown on silicon*, Phys. Rev. B **68**, 153313 (2003)

[98] F. Semond, I. R. Sellers, F. Natali, D. Byrne, M. Leroux, J. Massies, N. Ollier, J. Leymarie, P. Disseix, A. Vasson, *Strong light-matter coupling at room temperature in simple geometry GaN microcavities grown on silicon*, Appl. Phys. Lett. **87**, 021102 (2005)

[99] F. Réveret, P. Disseix, J. Leymarie, A. Vasson, F. Semond, M. Leroux, J. Massies, *Influence of the mirrors on the strong coupling regime in planar GaN microcavities*, Phys. Rev. B **77**, 195303 (2008)

[100] A. Alyamani, D. Sanvitto, A. A. Khalifa, M. S. Skolnick, T. Wang, F. Ranalli, P. J. Parbrook, A. Tahraoui, R. Airey, *GaN hybrid microcavities in the strong coupling regime grown by metal-organic chemical vapor deposition on sapphire substrates*, J. Appl. Phys. **101**, 093110 (2007)

[101] J.-F. Carlin, M. Ilegems, *High-quality AlInN for high index contrast Bragg mirrors lattice matched to GaN*, Appl. Phys. Lett. **83**, 668 (2003)

[102] R. Butté, G. Christmann, E. Feltin, J.-F. Carlin, M. Mosca, M. Ilegems, N. Grandjean, *Room-temperature polariton luminescence from a bulk GaN microcavity*, Phys. Rev. B **73**, 033315 (2006)

[103] K. S. Daskalakis, P. S. Eldridge, G. Christmann, E. Trichas, R. Murray, E. Iliopoulos, E. Monroy, N. T. Pelekanos, J. J. Baumberg, P. G. Savvidis, *All-dielectric GaN microcavity: Strong coupling and lasing at room temperature*, Appl. Phys. Lett. **102**, 101113 (2013)

[104] G. Rossbach, J. Levrat, A. Dussaigne, G. Cosendey, M. Glauser, M. Cobet, R. Butté, N. Grandjean, H. Teisseyre, M. Bockowski, I. Grzegory, T. Suski, *Tailoring the light-matter coupling in anisotropic microcavities: Redistribution of oscillator strength in strained m-plane GaN/AlGaN quantum wells*, Phys. Rev. B **84**, 115315 (2011)

[105] J. Levrat, G. Rossbach, A. Dussaigne, G. Cosendey, M. Glauser, M. Cobet, R. Butté, N. Grandjean, H. Teisseyre, M. Bockowski, I. Grzegory, T. Suski, *Nonlinear emission properties of an optically anisotropic GaN-based microcavity*, Phys. Rev. B **86**, 165321 (2012)

[106] M. Suzuki, J. Nishio, M. Onomura, C. Hongo, *Doping characteristics and electrical properties of Mg-doped AlGaN grown by atmospheric-pressure MOCVD*, J. Cryst. Growth **189**, 511 (1998)

[107] M. Orita, H. Ohta, M. Hirano, H. Hosono, *Deep-ultraviolet transparent conductive beta-Ga_2O_3 thin films*, Appl. Phys. Lett. **77**, 4166 (2000)

[108] T. Minami, *Transparent conducting oxide semiconductors for transparent electrodes*, Semicond. Sci. Technol. **20**, S35 (2005)

[109] T. Mino, H. Hirayama, T. Takano, N. Noguchi, K. Tsubaki, *Highly-uniform 260 nm-band AlGaN-based deep-ultraviolet light-emitting diodes developed by 2-inchx3 MOVPE system*, Phys. Stat. Sol. C **9**, 749 (2012)

[110] M. Shatalov, W. Sun, A. Lunev, X. Hu, A. Dobrinsky, Y. Bilenko, J. Yang, M. Shur, R. Gaska, C. Moe, G. Garrett, M. Wraback, *AlGaN deep-ultraviolet light-emitting diodes with external quantum efficiency above 10%*, Appl. Phys. Express **5**, 082101 (2012)

[111] T. Tawara, H. Gotoh, T. Akasaka, N. Kobayashi, T. Saitoh, *Cavity polaritons in InGaN microcavities at room temperature*, Phys. Rev. Lett. **92**, 256402 (2004)

[112] J.-Y. Duboz edited by B. Gil, *III-Nitride Semiconductors and Their Modern Devices* (Oxford University Press, Oxford, UK, 2013)

[113] G. Christmann, R. Butté, E. Feltin, J.-F. Carlin, N. Grandjean, *Impact of inhomogeneous broadening on the strong exciton-phonon coupling in quantum well nitride cavities*, Phys. Rev. B **73**, 153305 (2006)

[114] G. Christmann, *III-nitride based microcavities: Towards polariton condensation at room temperature*, PhD Thesis, EPFL (2009)

[115] T.-C. Lu, J.-R. Chen, S.-C. Lin, S.-W. Huang, S.-C. Wang, Y. Yamamoto, *Room temperature current injection polariton light emitting diode with a hybrid microcavity*, Nano Lett. **11**, 2791 (2011)

[116] D. Bajoni, A. Miard, A. Lemaître, S. Bouchoule, J. Bloch, J. Tignon, *Nonresonant electrical injection of excitons in an InGaAs quantum well*, Appl. Phys. Lett. **90**, 121114 (2007)

[117] F. Li, L. Orosz, O. Kamoun, S. Bouchoule, C. Brimont, P. Disseix, T. Guillet, X. Lafosse, M. Leroux, J. Leymarie, M. Mexis, M. Mihailovic, G. Patriarche, F. Réveret, D. Solnyshkov, J. Zuniga-Perez, G. Malpuech, *From excitonic to photonic polariton condensate in a ZnO-based microcavity*, Phys. Rev. Lett. **110**, 196406 (2013)

[118] D. G. Lidzey, D. D. C. Bradley, M. S. Skolnick, T. Virgili, S. Walker, D. M. Whittaker, *Strong exciton-photon coupling in an organic semiconductor microcavity*, Nature (London) **395**, 53 (1998)

[119] S. Kéna-Cohen, S. R. Forrest, *Room-temperature polariton lasing in an organic single-crystal microcavity*, Nature Phot. **4**, 371 (2010)

[120] J. D. Plumhof, T. Stoferle, L. Mai, U. Scherf, R. F. Mahrt, *Room-temperature Bose-Einstein condensation of cavity exciton-polaritons in a polymer*, Nature Mater. **13**, 247 (2014)

[121] G. Malpuech, A. Di Carlo, A. Kavokin, J. J. Baumberg, M. Zamfirescu, P. Lugli, *Room-temperature polariton lasers based on GaN microcavities*, Appl. Phys. Lett. **81**, 412 (2002)

[122] D. Solnyshkov, E. Petrolati, A. Di Carlo, G. Malpuech, *Theory of an electrically injected bulk polariton laser*, Appl. Phys. Lett. **94**, 011110 (2009)

[123] G. Malpuech, D. Solnyshkov, A. Di Carlo, E. Petrolati, *System for light emission in a polariton mode with electrical injection of quantum wells* (WO Patent WO 2010055221, 2010)

[124] G. Cosendey, *(In,Al)N-based blue microcavity lasers*, PhD Thesis, EPFL (2013)

[125] M. Malinverni, $et al.$, *Tunnel junctions*, to be submitted to Appl. Phys. Lett. /J. Appl. Phys.

[126] A. Castiglia, D. Simeonov, H. J. Buehlmann, J. . F. Carlin, E. Feltin, J. Dorsaz, R. Butté, N. Grandjean, *Efficient current injection scheme for nitride vertical cavity surface emitting lasers*, Appl. Phys. Lett. **90**, 033514 (2007)

[127] S. Nakamura, G. Fasol, S. J. Pearton, *The Blue Laser Diode: The Complete Story* (2nd ed., Springer, Berlin, 2000)

[128] E. Rosencher, B. Vinter, *Optoélectronique* (Dunod, Paris, 2002)

[129] J. Keeling, P. R. Eastham, M. H. Szymanska, P. B. Littlewood, *Polariton condensation with localized excitons and propagating photons*, Phys. Rev. Lett. **93**, 226403 (2004)

[130] J. Goldstone, *Field theories with superconductor solutions*, Nuovo Cimento **19**, 154 (1961)

[131] G. Malpuech, D. D. Solnyshkov, H. Ouerdane, M. M. Glazov, I. Shelykh, *Bose glass and superfluid phases of cavity polaritons*, Phys. Rev. Lett. **98**, 206402 (2007)

[132] B. Damski, J. Zakrzewski, L. Santos, P. Zoller, M. Lewenstein, *Atomic Bose and Anderson glasses in optical lattices*, Phys. Rev. Lett. **91**, 080403 (2003)

[133] J. M. Kosterlitz, D. J. Thouless, *Ordering, metastability and phase-transition in 2 dimensional systems*, J. Phys. C Solid State **6**, 1181 (1973)

[134] G. Christmann, D. Simeonov, R. Butté, E. Feltin, J.-F. Carlin, N. Grandjean, *Impact of disorder on high quality factor III-V nitride microcavities*, Appl. Phys. Lett. **89**, 261101 (2006)

[135] J. Kasprzak, D. D. Solnyshkov, R. André, Le Si Dang, G. Malpuech, *Formation of exciton polariton condensate: thermodynamic versus kinetic regimes*, Phys. Rev. Lett. **101**, 146404 (2008)

[136] E. Wertz, L. Ferrier, D. D. Solnyshkov, P. Senellart, D. Bajoni, A. Miard, A. Lemaître, G. Malpuech, J. Bloch, *Spontaneous formation of a polariton condensate in a planar GaAs microcavity*, Appl. Phys. Lett. **95**, 051108 (2009)

[137] R. Butté, J. Levrat, G. Christmann, E. Feltin, J.-F. Carlin, N. Grandjean, *Phase diagram of a polariton laser from cryogenic to room temperature*, Phys. Rev. B **80**, 233301 (2009)

[138] J. Levrat, R. Butté, E. Feltin, J.-F. Carlin, N. Grandjean, D. Solnyshkov, G. Malpuech, *Condensation phase diagram of cavity polaritons in GaN-based microcavities: Experiment and theory*, Phys. Rev. B **81**, 125305 (2010)

[139] J. Schmutzler, F. Veit, M. Assmann, J.-S. Tempel, S. Hoefling, M. Kamp, A. Forchel, M. Bayer, *Determination of operating parameters for a GaAs-based polariton laser*, Appl. Phys. Lett. **102**, 081115 (2013)

[140] F. Tassone, C. Piermarocchi, V. Savona, A. Quattropani, P. Schwendimann, *Bottleneck effects in the relaxation and photoluminescence of microcavity polaritons*, Phys. Rev. B **56**, 7554 (1997)

[141] F. Tassone, Y. Yamamoto, *Exciton-exciton scattering dynamics in a semiconductor microcavity and stimulated scattering into polaritons*, Phys. Rev. B **59**, 10830 (1999)

[142] A. V. Kavokin, J. J. Baumberg, G. Malpuech, F. P. Laussy, *Microcavities, Appendix B* (Oxford University Press, Oxford, 2007)

[143] P. Kozodoy, H. L. Xing, S. P. DenBaars, U. K. Mishra, A. Saxler, R. Perrin, S. Elhamri, W. C. Mitchel, *Heavy doping effects in Mg-doped GaN*, J. Appl. Phys. **87**, 1832 (2000)

[144] J. M. Phillips, M. E. Coltrin, M. H. Crawford, A. J. Fischer, M. R. Krames, R. Mueller-Mach, G. O. Mueller, Y. Ohno, L. E. S. Rohwer, J. A. Simmons, J. Y. Tsao, *Research challenges to ultra-efficient inorganic solid-state lighting*, Laser & Photonics Reviews **1**, 307 (2007)

[145] Y. Narukawa, Y. Kawakami, S. Fujita, S. Nakamura, *Dimensionality of excitons in laser-diode structures composed of $In_xGa_{1-x}N$ multiple quantum wells*, Phys. Rev. B **59**, 10283 (1999)

[146] W. G. Scheibenzuber, U. T. Schwarz, L. Sulmoni, J. Dorsaz, J.-F. Carlin, N. Grandjean, *Recombination coefficients of GaN-based laser diodes*, J. Appl. Phys. **109**, 093106 (2011)

[147] Y. C. Shen, G. O. Mueller, S. Watanabe, N. F. Gardner, A. Munkholm, M. R. Krames, *Auger recombination in InGaN measured by photoluminescence*, Appl. Phys. Lett. **91**, 141101 (2007)

[148] T. Langer, A. Chernikov, D. Kalincev, M. Gerhard, H. Bremers, U. Rossow, M. Koch, A. Hangleiter, *Room temperature excitonic recombination in GaInN/GaN quantum wells*, Appl. Phys. Lett. **103**, 202106 (2013)

[149] X. B. Zhang, B. Gil edited by B. Gil, *Low-Dimensional Nitride Semiconductors* (Oxford University Press, Oxford, 2002)

[150] R. Truell, C. Elbaum, B. B. Chick, *Ultrasonic Methods in Solid State Physics* (Academic, New York, 1969)

[151] J. Levrat, R. Butté, E. Feltin, J.-F. Carlin, N. Grandjean, D. Solnyshkov, G. Malpuech, *Condensation phase diagram of cavity polaritons in GaN-based microcavities: Experiment and theory (vol 81, 125305, 2010)*, Phys. Rev. B **84**, 199908 (2011)

[152] J. Levrat, G. Rossbach, R. Butté, N. Grandjean edited by A. Bramati, M. Modugno, *Physics of Quantum Fluids: New Trends and Hot Topics in Atomic and Polariton Condensates* (Springer US, New York, 2013)

[153] G. Malpuech, A. Kavokin, A. Di Carlo, J. J. Baumberg, *Polariton lasing by exciton-electron scattering in semiconductor microcavities*, Phys. Rev. B **65**, 153310 (2002)

[154] R. Michalzik, *VCSELs: Fundamentals, Technology and Applications of Vertical-Cavity Surface-Emitting Lasers* (Springer US, New York, 2013)

[155] S. Pau, H. Cao, J. Jacobson, G. Björk, Y. Yamamoto, A. Imamoglu, *Observation of a laserlike transition in a microcavity exciton polariton system*, Phys. Rev. A **54**, R1789 (1996)

[156] L. A. Coldren, S. W. Corzine, *Diode Lasers and Photonics Integrated Circuits* (Wiley, New York, 1995)

[157] K. L. Lear, V. M. Hietala, H. Q. Hou, J. Banas, B. E. Hammons, J. Zolper, S. P. Kilcoyne, *Small and large signal modulation of 850 nm oxide-confined vertical-cavity surface-emitting lasers*, in *Conference on Lasers and Electro-Optics, CLEO 97, Baltimore, MD* (1997)

[158] G. Cosendey, J.-F. Carlin, N. A. K. Kaufmann, R. Butté, N. Grandjean, *Strain compensation in AlInN/GaN multilayers on GaN substrates: Application to the realization of defect-free Bragg reflectors*, Appl. Phys. Lett. **98**, 181111 (2011)

[159] M. Glauser, R. Butté, *Relative intensity noise and emission linewidth of polariton laser diodes*, Phys. Rev. B **88**, 115305 (2013)

[160] R. Olshansky, P. Hill, V. Lanzisera, W. Powazinik, *Frequency-response of 1.3-μm InGaAsP high-speed semiconductor-lasers*, IEEE J. Quantum Elect. **23**, 1410 (1987)

[161] F. Tassone, Y. Yamamoto, *Lasing and squeezing of composite bosons in a semiconductor microcavity*, Phys. Rev. A **62**, 063809 (2000)

[162] M. Nakazawa, K. Kikuchi, T. T. Miyazaki, *High Spectral Density Optical Communication Technologies* (Springer-Verlag Berlin, 2010)

[163] M. Lax, *Classical noise .v. noise in self sustained oscillators*, Phys. Rev. **160**, 290 (1967)

[164] H. Haug, T. D. Doan, H. Thien Cao, D. B. Tran Thoai, *Temporal first- and second-order correlations in a polariton condensate*, Phys. Rev. B **85**, 205310 (2012)

[165] J. Kasprzak, M. Richard, A. Baas, B. Deveaud, R. André, J. Ph. Poizat, Le Si Dang, *Second-order time correlations within a polariton Bose-Einstein condensate in a CdTe microcavity*, Phys. Rev. Lett. **100**, 067402 (2008)

[166] D. Porras, C. Tejedor, *Linewidth of a polariton laser: Theoretical analysis of self-interaction effects*, Phys. Rev. B **67**, 161310 (2003)

[167] A. P. D. Love, D. N. Krizhanovskii, D. M. Whittaker, R. Bouchekioua, D. Sanvitto, S. Al Rizeiqi, R. Bradley, M. S. Skolnick, P. R. Eastham, R. André, Le Si Dang, *Intrinsic decoherence mechanisms in the microcavity polariton condensate*, Phys. Rev. Lett. **101**, 067404 (2008)

[168] D. M. Whittaker, P. R. Eastham, *Coherence properties of the microcavity polariton condensate*, Europhys. Lett. **87**, 27002 (2009)

[169] H. Haken, *Cooperative phenomena in systems far from thermal equilibrium and in nonphysical systems*, Rev. Mod. Phys. **47**, 67 (1975)

[170] H. T. Grahn, *Introduction to Semiconductor Physics* (World Scientific Publishing Co. Pte. Ltd., Singapore, 1999)

[171] J. Levrat, R. Butté, G. Christmann, E. Feltin, J.-F. Carlin, N. Grandjean, *Tailoring the strong coupling regime in III-nitride based microcavities for room temperature polariton laser applications*, Phys. Stat. Sol. C **6**, 2820 (2009)

[172] G. Rossbach, J. Levrat, E. Feltin, J.-F. Carlin, R. Butté, N. Grandjean, *Impact of saturation on the polariton renormalization in III-nitride based planar microcavities*, Phys. Rev. B **88**, 165312 (2013)

[173] H. Fujiwara, *Spectroscopic ellipsometry: Principles and applications* (Wiley, Tokyo, 2007)

[174] www.filmetrics.com, J. R. Devore, *Refractive indices of rutile and sphalerite*, J. Opt. Soc. Am. **41**, 416 (1951)

[175] T. Ive, O. Brandt, H. Kostial, T. Hesjedal, M. Ramsteiner, K. H. Ploog, *Crack-free and conductive Si-doped AlN/GaN distributed Bragg reflectors grown on 6H-SiC(0001)*, Appl. Phys. Lett. **85**, 1970 (2004)

[176] G. S. Huang, T. C. Lu, H. H. Yao, H. C. Kuo, S. C. Wang, C. W. Lin, L. Chang, *Crack-free GaN/AlN distributed Bragg reflectors incorporated with GaN/AlN superlattices grown by metalorganic chemical vapor deposition*, Appl. Phys. Lett. **88**, 061904 (2006)

[177] C. Kruse, H. Dartsch, T. Aschenbrenner, S. Figge, D. Hommel, *Growth and characterization of nitride-based distributed Bragg reflectors*, Phys. Stat. Sol. B **248**, 1748 (2011)

[178] T. Wang, R. J. Lynch, P. J. Parbrook, R. Butté, A. Alyamani, D. Sanvitto, D. M. Whittaker, M. S. Skolnick, *High-reflectivity $Al_xGa_{1-x}N/Al_yGa_{1-y}N$ distributed Bragg reflectors with peak wavelength around 350 nm*, Appl. Phys. Lett. **85**, 43 (2004)

[179] O. Mitrofanov, S. Schmult, M. J. Manfra, T. Siegrist, N. G. Weimann, A. M. Sergent, R. J. Molnar, *High-reflectivity ultraviolet AlGaN/AlGaN distributed Bragg reflectors*, Appl. Phys. Lett. **88**, 171101 (2006)

[180] E. Feltin, J.-F. Carlin, J. Dorsaz, G. Christmann, R. Butté, M. Laügt, M. Ilegems, N. Grandjean, *Crack-free highly reflective AlInN/AlGaN bragg mirrors for UV applications*, Appl. Phys. Lett. **88**, 051108 (2006)

[181] S. Figge, H. Dartsch, T. Aschenbrenner, C. Kruse, D. Hommel, *Distributed Bragg reflectors in comparison to RUGATE and nested super lattices - growth, reflectivity, and conductivity*, Phys. Stat. Sol. C **5**, 1839 (2008)

[182] D. Brunner, H. Angerer, E. Bustarret, F. Freudenberg, R. Höpler, R. Dimitrov, O. Ambacher, M. Stutzmann, *Optical constants of epitaxial AlGaN films and their temperature dependence*, J. Appl. Phys. **82**, 5090 (1997)

[183] T. Kawashima, H. Yoshikawa, S. Adachi, S. Fuke, K. Ohtsuka, *Optical properties of hexagonal GaN*, J. Appl. Phys. **82**, 3528 (1997)

[184] S. Shokhovets, R. Goldhahn, G. Gobsch, S. Piekh, R. Lantier, A. Rizzi, V. Lebedev, W. Richter, *Determination of the anisotropic dielectric function for wurtzite AlN and GaN by spectroscopic ellipsometry*, J. Appl. Phys. **94**, 307 (2003)

[185] J.-F. Carlin, C. Zellweger, J. Dorsaz, S. Nicolay, G. Christmann, E. Feltin, R. Butté, N. Grandjean, *Progresses in III-nitride distributed Bragg reflectors and microcavities using AlInN/GaN materials*, Phys. Stat. Sol. B **242**, 2326 (2005)

[186] T. Aschenbrenner, H. Dartsch, C. Kruse, M. Anastasescu, M. Stoica, M. Gartner, A. Pretorius, A. Rosenauer, T. Wagner, D. Hommel, *Optical and structural characterization of AlInN layers for optoelectronic applications*, J. Appl. Phys. **108**, 063533 (2010)

[187] E. Sakalauskas, H. Behmenburg, C. Hums, P. Schley, G. Rossbach, C. Giesen, M. Heuken, H. Kalisch, R. H. Jansen, J. Blaesing, A. Dadgar, A. Krost, R. Goldhahn, *Dielectric function and optical properties of Al-rich AlInN alloys pseudomorphically grown on GaN*, J. Phys. D: Appl. Phys. **43**, 365102 (2010)

[188] K. Lorenz, N. Franco, E. Alves, I. M. Watson, R. W. Martin, K. P. O'Donnell, *Anomalous ion channeling in AlInN/GaN bilayers: Determination of the strain state*, Phys. Rev. Lett. **97**, 085501 (2006)

[189] V. Darakchieva, M. Beckers, M.-Y. Xie, L. Hultman, B. Monemar, J.-F. Carlin, E. Feltin, M. Gonschorek, N. Grandjean, *Effects of strain and composition on the lattice parameters and applicability of Vegard's rule in Al-rich Al(1-x)In(x)N films grown on sapphire*, J. Appl. Phys. **103**, 103513 (2008)

[190] J. Dorsaz, J.-F. Carlin, C. M. Zellweger, S. Gradecak, M. Ilegems, *InGaN/GaN resonant-cavity LED including an AlInN/GaN Bragg mirror*, Phys. Stat. Sol. A **201**, 2675 (2004)

[191] R. Butté, G. Cosendey, L. Lugani, M. Glauser, A. Castiglia, G. Perillat-Merceroz, J.-F. Carlin, N. Grandjean edited by B. Gil, *III-Nitride Semiconductors and Their Modern Devices* (Oxford University Press, Oxford, UK, 2013)

[192] G. Björk, H. Heitmann, Y. Yamamoto, *Spontaneous-emission coupling factor and mode characteristics of planar dielectric microcavity lasers*, Phys. Rev. A **47**, 4451 (1993)

[193] T. Tojyo, T. Asano, M. Takeya, T. Hino, S. Kijima, S. Goto, S. Uchida, M. Ikeda, *GaN-based high power blue-violet laser diodes*, Jpn. J. Appl. Phys. **40**, 3206 (2001)

[194] S. E. Bennett, D. Holec, M. J. Kappers, C. J. Humphreys, R. A. Oliver, *Imaging dislocations in gallium nitride across broad areas using atomic force microscopy*, Rev. Sci. Instrum. **81**, 063701 (2010)

[195] A. Gadanecz, J. Blaesing, A. Dadgar, C. Hums, A. Krost, *Thermal stability of metal organic vapor phase epitaxy grown AlInN*, Appl. Phys. Lett. **90**, 221906 (2007)

[196] T. C. Sadler, M. J. Kappers, R. A. Oliver, *Optimisation of GaN overgrowth of InAlN for DBRs*, Phys. Stat. Sol. C **6**, S666 (2009)

[197] J. Dorsaz, J.-F. Carlin, S. Gradecak, M. Ilegems, *Progress in AlInN-GaN Bragg reflectors: Application to a microcavity light emitting diode*, J. Appl. Phys. **97**, 084505 (2005)

[198] M. J. Bergman, H. C. Casey, *Optical-field calculations for lossy multiple-layer* $Al_xGa_{1-x}N/In_xGa_{1-x}N$ *laser diodes*, J. Appl. Phys. **84**, 1196 (1998)

[199] F. Yang, M. Wilkinson, E. J. Austin, K. P. O'Donnell, *Origin of the Stokes shift - a geometrical model of exciton spectra in 2D semiconductors*, Phys. Rev. Lett. **70**, 323 (1993)

[200] M. Glauser, C. Mounir, G. Rossbach, E. Feltin, J.-F. Carlin, R. Butté, N. Grandjean, *InGaN/GaN quantum wells for polariton laser diodes: Role of inhomogeneous broadening*, J. Appl. Phys. **115**, 233511 (2014)

[201] D. S. Chemla, D. A. B. Miller, P. W. Smith, A. C. Gossard, W. Wiegmann, *Room-temperature excitonic nonlinear absorption and refraction in GaAs/AlGaAs multiple quantum well structures*, IEEE J. Quantum Elect. **20**, 265 (1984)

[202] R. W. Martin, P. G. Middleton, K. P. O'Donnell, W. Van der Stricht, *Exciton localization and the Stokes' shift in InGaN epilayers*, Appl. Phys. Lett. **74**, 263 (1999)

[203] C. Weisbuch, B. Vinter, *Quantum semiconductor structures: Fundamentals and applications* (Academic Press Inc, San Diego, 1991)

[204] R. P. Stanley, R. Houdré, C. Weisbuch, U. Oesterle, M. Ilegems, *Cavity-polariton photoluminescence in semiconductor microcavities: Experimental evidence*, Phys. Rev. B **53**, 10995 (1996)

[205] F. Scholz, A. Sohmer, J. Off, V. Syganow, A. Dornen, J. S. Im, A. Hangleiter, H. Lakner, *In incorporation efficiency and composition fluctuations in MOVPE grown GaInN/GaN hetero structures and quantum wells*, Mat. Sci. Eng. B **50**, 238 (1997)

[206] T. Matsuoka, N. Yoshimoto, T. Sasaki, A. Katsui, *Wide-gap semiconductor InGaN and InGaAlN grown by MOVPE*, J. Electron. Mater. **21**, 157 (1992)

[207] M. Senthil Kumar, J. Y. Park, Y. S. Lee, S. J. Chung, C. . H. Hong, E. . K. Suh, *Effect of barrier growth temperature on morphological evolution of green InGaN/GaN multi-quantum well heterostructures*, J. Phys. D: Appl. Phys. **40**, 5050 (2007)

[208] L. W. Wu, S. J. Chang, Y. K. Su, R. W. Chuang, T. C. Wen, C. H. Kuo, W. C. Lai, C. S. Chang, J. M. Tsai, J. K. Sheu, *Nitride-based green light-emitting diodes with high temperature GaN barrier layers*, IEEE Trans. Electron Dev. **50**, 1766 (2003)

[209] G. Ju, Y. Honda, M. Tabuchi, Y. Takeda, H. Amano, *In situ X-ray investigation of changing barrier growth temperatures on InGaN single quantum wells in metal-organic vapor phase epitaxy*, J. Appl. Phys. **115**, 94906 (2014)

[210] M. Tanaka, H. Sakaki, *Atomistic models of interface structures of GaAs-$Al_xGa_{1-x}As$ (x=0.2-1) quantum-wells grown by interrupted and uninterrupted MBE*, J. Cryst. Growth **81**, 153 (1987)

[211] R. A. Oliver, F. C.-P. Massabuau, M. J. Kappers, W. A. Phillips, E. J. Thrush, C. C. Tartan, W. E. Blenkhorn, T. J. Badcock, P. Dawson, M. A. Hopkins, D. W. E. Allsopp, C. J. Humphreys, *The impact of gross well width fluctuations on the efficiency of GaN-based light emitting diodes*, Appl. Phys. Lett. **103**, 141114 (2013)

[212] H. Q. Lu, M. Thothathiri, Z. M. Wu, I. Bhat, *Study of indium droplets formation on the $In_xGa_{1-x}N$ films by single crystal x-ray diffraction*, J. Electron. Mater. **26**, 281 (1997)

[213] M. Pristovsek, A. Kadir, M. Kneissl, *Surface transitions during InGaN growth on GaN(0001) in metal-organic vapor phase epitaxy*, Jpn. J. Appl. Phys. **52**, UNSP 08JB23 (2013)

[214] H. K. Cho, J. Y. Lee, N. Sharma, C. J. Humphreys, G. M. Yang, C. S. Kim, J. H. Song, P. W. Yu, *Effect of growth interruptions on the light emission and indium clustering of InGaN/GaN multiple quantum wells*, Appl. Phys. Lett. **79**, 2594 (2001)

[215] T. M. Smeeton, M. J. Kappers, J. S. Barnard, M. E. Vickers, C. J. Humphreys, *Electron-beam-induced strain within InGaN quantum wells: False indium "cluster" detection in the transmission electron microscope*, Appl. Phys. Lett. **83**, 5419 (2003)

[216] A. A. Yamaguchi, M. Kuramoto, M. Nido, M. Mizuta, *An alloy semiconductor system with a tailorable band-tail and its application to high-performance laser operation: I. A band-states model for an alloy-fluctuated InGaN-material system designed for quantum well laser operation*, Semicond. Sci. Technol. **16**, 763 (2001)

[217] M. Leszczynski, R. Czernecki, S. Krukowski, M. Krysko, G. Targowski, P. Prystawko, J. Plesiewicz, P. Perlin, T. Suski, *Indium incorporation into InGaN and InAlN layers grown by metalorganic vapor phase epitaxy*, J. Cryst. Growth **318**, 496 (2011)

[218] M. Sarzynski, M. Leszczynski, M. Krysko, J. Z. Domagala, R. Czernecki, T. Suski, *Influence of GaN substrate off-cut on properties of InGaN and AlGaN layers*, Cryst. Res. Technol. **47**, 321 (2012)

[219] J. W. Matthews, A. E. Blakeslee, *Defects in epitaxial multilayers .1. Misfit dislocations*, J. Cryst. Growth **27**, 118 (1974)

[220] D. Holec, P. M. F. J. Costa, M. J. Kappers, C. J. Humphreys, *Critical thickness calculations for InGaN/GaN*, J. Cryst. Growth **303**, 314 (2007)

[221] A. V. Lobanova, A. L. Kolesnikova, A. E. Romanov, S. Yu. Karpov, M. E. Rudinsky, E. V. Yakovlev, *Mechanism of stress relaxation in (0001) InGaN/GaN via formation of V-shaped dislocation half-loops*, Appl. Phys. Lett. **103**, 152106 (2013)

[222] M. Pristovsek, A. Kadir, C. Meissner, T. Schwaner, M. Leyer, J. Stellmach, M. Kneissl, F. Ivaldi, S. Kret, *Growth mode transition and relaxation of thin InGaN layers on GaN (0001)*, J. Cryst. Growth **372**, 65 (2013)

[223] M. Pristovsek, *Wavelength limits for InGaN quantum wells on GaN*, Appl. Phys. Lett. **102**, 242105 (2013)

[224] M. Shimizu, Y. Kawaguchi, K. Hiramatsu, N. Sawaki, *Metalorganic vapor phase epitaxy of thick InGaN on sapphire substrate*, Jpn. J. Appl. Phys. **36**, 3381 (1997)

[225] C. A. Parker, J. C. Roberts, S. M. Bedair, M. J. Reed, S. X. Liu, N. A. El-Masry, *Determination of the critical layer thickness in the InGaN/GaN heterostructures*, Appl. Phys. Lett. **75**, 2776 (1999)

[226] M. J. Reed, N. A. El-Masry, C. A. Parker, J. C. Roberts, S. M. Bedair, *Critical layer thickness determination of GaN/InGaN/GaN double heterostructures*, Appl. Phys. Lett. **77**, 4121 (2000)

[227] M.-I. Richard, M. J. Highland, T. T. Fister, A. Munkholm, J. Mei, S. K. Streiffer, Carol Thompson, P. H. Fuoss, G. B. Stephenson, *In situ synchrotron x-ray studies of strain and composition evolution during metal-organic chemical vapor deposition of InGaN*, Appl. Phys. Lett. **96**, 051911 (2010)

[228] A. Yoshikawa, N. Hashimoto, N. Kikukawa, S. B. Che, Y. Ishitani, *Growth of InN quantum dots on N-polarity GaN by molecular-beam epitaxy*, Appl. Phys. Lett. **86**, 153115 (2005)

[229] S. M. de Sousa Pereira, K. P. O'Donnell, E. J. da Costa Alves, *Role of nanoscale strain inhomogeneity on the light emission from InGaN epilayers*, Adv. Funct. Mater. **17**, 37 (2007)

[230] R. People, J. C. Bean, *Calculation of critical layer thickness versus lattice mismatch for* Ge_xSi_{1-x}*/Si strained-layer heterostructures*, Appl. Phys. Lett. **47**, 322 (1985)

[231] A. Fischer, H. Kühne, H. Richter, *New approach in equilibrium-theory for strained-layer relaxation*, Phys. Rev. Lett. **73**, 2712 (1994)

[232] D. Holec, Y. Zhang, D. V. Sridhara Rao, M. J. Kappers, C. McAleese, C. J. Humphreys, *Equilibrium critical thickness for misfit dislocations in III-nitrides*, J. Appl. Phys. **104**, 123514 (2008)

[233] A. D. Bykhovski, B. L. Gelmont, M. S. Shur, *Elastic strain relaxation and piezoeffect in GaN-AlN, GaN-AlGaN and GaN-InGaN superlattices*, J. Appl. Phys. **81**, 6332 (1997)

[234] G. Schmidt, M. Müller, P. Veit, F. Bertram, J. Christen, M. Glauser, J.-F. Carlin, G. Cosendey, R. Butté, N. Grandjean, *Nano-scale luminescence characterization of individual InGaN/-GaN quantum wells stacked in a microcavity using scanning transmission electron microscope cathodoluminescence*, Appl. Phys. Lett. **105**, 032101 (2014)

[235] M. Glauser, G. Rossbach, G. Cosendey, J. Levrat, M. Cobet, J.-F. Carlin, J. Besbas, M. Gallart, P. Gilliot, R. Butté, N. Grandjean, *Investigation of InGaN/GaN quantum wells for polariton laser diodes*, Phys. Stat. Sol. C **9**, 5 (2012)

[236] N. A. K. Kaufmann, *Investigation of indium-rich InGaN alloys and kinetic growth regime of GaN*, PhD Thesis, EPFL (2013)

[237] S. Chichibu, K. Wada, S. Nakamura, *Spatially resolved cathodoluminescence spectra of InGaN quantum wells*, Appl. Phys. Lett. **71**, 2346 (1997)

[238] A. Hangleiter, F. Hitzel, C. Netzel, D. Fuhrmann, U. Rossow, G. Ade, P. Hinze, *Suppression of nonradiative recombination by V-shaped pits in GaInN/GaN quantum wells produces a large increase in the light emission efficiency*, Phys. Rev. Lett. **95**, 127402 (2005)

[239] S. Sonderegger, E. Feltin, M. Merano, A. Crottini, J.-F. Carlin, R. Sachot, B. Deveaud, N. Grandjean, J. D. Ganière, *High spatial resolution picosecond cathodoluminescence of InGaN quantum wells*, Appl. Phys. Lett. **89**, 232109 (2006)

[240] N. Grandjean, E. Feltin, R. Butté, J. . F. Carlin, S. Sonderegger, B. Deveaud, J.-D. Ganière, *Growth mode induced carrier localization in InGaN/GaN quantum wells*, Phil. Mag. **87**, 2067 (2007)

[241] N. K. van der Laak, R. A. Oliver, M. J. Kappers, C. J. Humphreys, *Characterization of InGaN quantum wells with gross fluctuations in width*, J. Appl. Phys. **102**, 013513 (2007)

[242] L. W. Wang, *Calculations of carrier localization in* $In_xGa_{1-x}N$, Phys. Rev. B **63**, 245107 (2001)

[243] S. F. Chichibu, A. Uedono, T. Onuma, B. A. Haskell, A. Chakraborty, T. Koyama, P. T. Fini, S. Keller, S. P. Denbaars, J. S. Speck, U. K. Mishra, S. Nakamura, S. Yamaguchi, S. Kamiyama, H. Amano, I. Akasaki, J. Han, T. Sota, *Origin of defect-insensitive emission probability in In-containing (Al, In, Ga) N alloy semiconductors*, Nature Mater. **5**, 810 (2006)

[244] D. M. Graham, A. Soltani-Vala, P. Dawson, M. J. Godfrey, T. M. Smeeton, J. S. Barnard, M. J. Kappers, C. J. Humphreys, E. J. Thrush, *Optical and microstructural studies of InGaN/GaN single-quantum-well structures*, J. Appl. Phys. **97**, 103508 (2005)

[245] M. J. Galtrey, R. A. Oliver, M. J. Kappers, C. J. Humphreys, P. H. Clifton, D. Larson, D. W. Saxey, A. Cerezo, *Three-dimensional atom probe analysis of green- and blue-emitting* $In_xGa_{1-x}N$*/GaN multiple quantum well structures*, J. Appl. Phys. **104**, 013524 (2008)

[246] S. Chichibu, T. Azuhata, T. Sota, S. Nakamura, *Spontaneous emission of localized excitons in InGaN single and multiquantum well structures*, Appl. Phys. Lett. **69**, 4188 (1996)

[247] D. Watson-Parris, M. J. Godfrey, P. Dawson, R. A. Oliver, M. J. Galtrey, M. J. Kappers, C. J. Humphreys, *Carrier localization mechanisms in* $In_xGa_{1-x}N$*/GaN quantum wells*, Phys. Rev. B **83**, 115321 (2011)

[248] H. Schömig, S. Halm, A. Forchel, G. Bacher, J. Off, F. Scholz, *Probing individual localization centers in an InGaN/GaN quantum well*, Phys. Rev. Lett. **92**, 106802 (2004)

[249] J. Laehnemann, O. Brandt, C. Pfueller, T. Flissikowski, U. Jahn, E. Luna, M. Hanke, M. Knelangen, A. Trampert, H. T. Grahn, *Coexistence of quantum-confined Stark effect and localized states in an (In,Ga)N/GaN nanowire heterostructure*, Phys. Rev. B **84**, 155303 (2011)

[250] S. De, A. Layek, S. Bhattacharya, D. K. Das, A. Kadir, A. Bhattacharya, S. Dhar, A. Chowdhury, *Quantum-confined Stark effect in localized luminescent centers within InGaN/GaN quantum-well based light emitting diodes*, Appl. Phys. Lett. **101**, 121919 (2012)

[251] G. Rossbach, J. Levrat, G. Jacopin, M. Shahmohammadi, J.-F. Carlin, J.-D. Ganière, R. Butté, B. Deveaud, N. Grandjean, *High-temperatureMott-transition in wide band-gap semiconductor quantum wells*, submitted to Phys. Rev. Lett. (2014)

[252] M. Funato, Y. Kawakami, *Excitonic properties of polar, semipolar, and nonpolar InGaN/-GaN strained quantum wells with potential fluctuations*, J. Appl. Phys. **103**, 093501 (2008)

[253] J. J. Olivero, R. L. Longbothum, *Empirical fits to Voigt line-width - brief review*, J. Quant. Spectrosc. Radiat. Transfer **17**, 233 (1977)

[254] J. G. Gay, *Screening of excitons in semiconductors*, Phys. Rev. B **4**, 2567 (1971)

[255] D. E. Aspnes, *Band nonparabolicities, broadening, and internal field distributions - spectroscopy of Franz-Keldysh oscillations*, Phys. Rev. B **10**, 4228 (1974)

[256] D. E. Aspnes, *Third-derivative modulation spectroscopy with low-field electroreflectance*, Surf. Sci. **37**, 418 (1973)

[257] B. V. Shanabrook, O. J. Glembocki, W. T. Beard, *Photoreflectance modulation mechanisms in GaAs-Al_xGa_{1-x}As multiple quantum-wells*, Phys. Rev. B **35**, 2540 (1987)

[258] F. H. Pollak, H. Shen, *Modulation spectroscopy of semiconductors - bulk thin-film, microstructures, surfaces interfaces and devices*, Mat. Sci. Eng. R. **10**, 275 (1993)

[259] O. J. Glembocki, *Modulation spectroscopy of semiconductor-materials, interfaces, and microstructures - an overview*, Proc. SPIE **1286**, 2 (1990)

[260] J. Misiewicz, P. Sitarek, G. Sek, *Photoreflectance spectroscopy of low-dimensional semiconductor structures*, Opto-electronics Review **8**, 1 (2000)

[261] S. Ghosh, H. T. Grahn, *Photoreflectance line shape of excitonic transitions analyzed with a redefined set of fitting parameters*, J. Appl. Phys. **90**, 500 (2001)

[262] C. Wetzel, T. Takeuchi, H. Amano, I. Akasaki, *Electric-field strength, polarization dipole, and multi-interface band offset in piezoelectric $Ga_{1-x}In_xN$/GaN quantum-well structures*, Phys. Rev. B **61**, 2159 (2000)

[263] P. Lefebvre, A. Morel, M. Gallart, T. Taliercio, J. Allegre, B. Gil, H. Mathieu, B. Damilano, N. Grandjean, J. Massies, *High internal electric field in a graded-width InGaN/GaN quantum well: Accurate determination by time-resolved photoluminescence spectroscopy*, Appl. Phys. Lett. **78**, 1252 (2001)

[264] E. Feltin, D. Simeonov, J.-F. Carlin, R. Butté, N. Grandjean, *Narrow UV emission from homogeneous GaN/AlGaN quantum wells*, Appl. Phys. Lett. **90**, 021905 (2007)

[265] F. Stokker-Cheregi, A. Vinattieri, E. Feltin, D. Simeonov, J.-F. Carlin, R. Butté, N. Grandjean, M. Gurioli, *Biexciton kinetics in GaN quantum wells: Time-resolved and time-integrated photoluminescence measurements*, Phys. Rev. B **77**, 125342 (2008)

[266] C. F. Klingshirn, *Semiconductor Optics* (Springer, Berlin, 1997)

[267] F. Stokker-Cheregi, A. Vinattieri, E. Feltin, D. Simeonov, J.-F. Carlin, R. Butté, N. Grandjean, F. Sacconi, M. Povolotskyi, A. Di Carlo, M. Gurioli, *Quantum confinement dependence of the energy splitting and recombination dynamics of A and B excitons in a GaN/AlGaN quantum well*, Phys. Rev. B **79**, 245316 (2009)

[268] J. Besbas, A. Gadalla, M. Gallart, O. Cregut, B. Honerlage, P. Gilliot, E. Feltin, J.-F. Carlin, R. Butté, N. Grandjean, *Spin relaxation of free excitons in narrow GaN/$Al_xGa_{1-x}N$ quantum wells*, Phys. Rev. B **82**, 195302 (2010)

[269] Y. H. Cho, G. H. Gainer, A. J. Fischer, J. J. Song, S. Keller, U. K. Mishra, S. P. DenBaars, *S-shaped temperature-dependent emission shift and carrier dynamics in InGaN/GaN multiple quantum wells*, Appl. Phys. Lett. **73**, 1370 (1998)

[270] K. Kazlauskas, G. Tamulaitis, P. Pobedinskas, A. Zukauskas, M. Springis, C. F. Huang, Y. C. Cheng, C. C. Yang, *Exciton hopping in $In_xGa_{1-x}N$ multiple quantum wells*, Phys. Rev. B **71**, 085306 (2005)

[271] M. S. Skolnick, P. R. Tapster, S. J. Bass, A. D. Pitt, N. Apsley, S. P. Aldred, *Investigation of InGaAs-InP quantum wells by optical spectroscopy*, Semicond. Sci. Technol. **1**, 29 (1986)

[272] L. E. Golub, S. V. Ivanov, E. L. Ivchenko, T. V. Shubina, A. A. Toropov, J. P. Bergman, G. R. Pozina, B. Monemar, M. Willander, *Low-temperature kinetics of localized excitons in quantum-well structures*, Phys. Stat. Sol. B **205**, 203 (1998)

[273] K. Wang, R. R. Reeber, *Thermal expansion and elastic properties of InN*, Appl. Phys. Lett. **79**, 1602 (2001)

[274] R. R. Reeber, K. Wang, *Lattice parameters and thermal expansion of GaN*, J. Mater. Res. **15**, 40 (2000)

[275] A. Morel, *Dynamique de recombinaison electron-trou dans les puits et les boîtes quantiques InGaN/(Al)GaN*, PhD Thesis, Université Montpellier II Science et Techniques du Longuedoc (2002)

[276] T. D. Veal, P. H. Jefferson, L. F. J. Piper, C. F. McConville, T. B. Joyce, P. R. Chalker, L. Considine, Hai Lu, W. J. Schaff, *Transition from electron accumulation to depletion at InGaN surfaces*, Appl. Phys. Lett. **89**, 202110 (2006)

[277] R. Kudrawiec, L. Janicki, M. Gladysiewicz, J. Misiewicz, G. Cywinski, M. Bockowski, G. Muziol, C. Cheze, M. Sawicka, C. Skierbiszewski, *Contactless electroreflectance studies of surface potential barrier for N- and Ga-face epilayers grown by molecular beam epitaxy*, Appl. Phys. Lett. **103**, 052107 (2013)

[278] G. Y. Zhang, Y. Z. Tong, Z. J. Yang, S. X. Jin, J. Li, Z. Z. Gan, *Relationship of background carrier concentration and defects in GaN grown by metalorganic vapor phase epitaxy*, Appl. Phys. Lett. **71**, 3376 (1997)

[279] M. J. Galtrey, R. A. Oliver, M. J. Kappers, C. J. Humphreys, P. H. Clifton, A. Cerezo, G. D. W. Smith, *Response to "Comment on 'Three-dimensional atom probe studies of an $In_xGa_{1-x}N$/GaN multiple quantum well structure: assessment of possible indium clustering'" [Appl. Phys. Lett. 91, 176101, (2007)]*, Appl. Phys. Lett. **91**, 176102 (2007)

[280] L. C de Carvalho, A. Schleife, J. Furthmueller, F. Bechstedt, *Distribution of cations in wurtzitic $In_xGa_{1-x}N$ and $In_xAl_{1-x}N$ alloys: Consequences for energetics and quasiparticle electronic structures*, Phys. Rev. B **85**, 115121 (2012)

[281] H. P. D. Schenk, M. Leroux, P. de Mierry, *Luminescence and absorption in InGaN epitaxial layers and the van Roosbroeck-Shockley relation*, J. Appl. Phys. **88**, PII [S0021 (2000)

[282] I. Gorczyca, S. P. Lepkowski, T. Suski, N. E. Christensen, A. Svane, *Influence of indium clustering on the band structure of semiconducting ternary and quaternary nitride alloys*, Phys. Rev. B **80**, 075202 (2009)

[283] L. Bellaiche, T. Mattila, L. W. Wang, S. H. Wei, A. Zunger, *Resonant hole localization and anomalous optical bowing in InGaN alloys*, Appl. Phys. Lett. **74**, 1842 (1999)

[284] P. R. C. Kent, A. Zunger, *Carrier localization and the origin of luminescence in cubic InGaN alloys*, Appl. Phys. Lett. **79**, 1977 (2001)

[285] S. Hammersley, D. Watson-Parris, P. Dawson, M. J. Godfrey, T. J. Badcock, M. J. Kappers, C. McAleese, R. A. Oliver, C. J. Humphreys, *The consequences of high injected carrier densities on carrier localization and efficiency droop in InGaN/GaN quantum well structures*, J. Appl. Phys. **111**, 083512 (2012)

[286] H.-M. Solowan, J. Danhof, U. T. Schwarz, *Direct observation of charge carrier diffusion and localization in an InGaN multi quantum well*, Japn. J. Appl. Phys. **52**, UNSP 08JK07 (2013)

[287] O. Aoudé, P. Disseix, J. Leymarie, A. Vasson, E. Aujol, B. Beaumont, *Femtosecond time-resolved interferences of resonantly excited excitons in bulk GaN*, Superlattice Microst. **36**, 607 (2004)

[288] J. Kasprzak, *Condensation of exciton polaritons*, PhD Thesis, Université Joseph Fourier - Grenoble 1 (2006)

[289] E. Peter, P. Senellart, D. Martrou, A. Lemaître, J. Hours, J. M. Gérard, J. Bloch, *Exciton-photon strong-coupling regime for a single quantum dot embedded in a microcavity*, Phys. Rev. Lett. **95**, 067401 (2005)

[290] D. Simeonov, E. Feltin, H.-. J. Buehlmann, T. Zhu, A. Castiglia, M. Mosca, J.-. F. Carlin, R. Butté, N. Grandjean, *Blue lasing at room temperature in high quality factor GaN/AlInN microdisks with InGaN quantum wells*, Appl. Phys. Lett. **90**, 061106 (2007)

[291] Z. Gacevic, G. Rossbach, R. Butté, F. Réveret, M. Glauser, J. Levrat, G. Cosendey, J. F. Carlin, N. Grandjean, E. Calleja, *Q-factor of (In,Ga)N containing III-nitride microcavity grown by multiple deposition techniques*, J. Appl. Phys. **114**, 233102 (2013)

[292] Y. Yamamoto, S. Machida, G. Björk, *Microcavity semiconductor-laser with enhanced spontaneous emission*, Phys. Rev. A **44**, 657 (1991)

[293] J. V. Moloney, J. Hader, S. W. Koch, *Quantum design of semiconductor active materials: laser and amplifier applications*, Laser and Phot. Rev. **1**, 24 (2007)

[294] W. W. Chow, A. F. Wright, A. Girndt, F. Jahnke, S. W. Koch, *Microscopic theory of gain for an InGaN/AlGaN quantum well laser*, Appl. Phys. Lett. **71**, 2608 (1997)

[295] U. T. Schwarz, E. Sturm, W. Wegscheider, V. Kümmler, A. Lell, V. Härle, *Excitonic signature in gain and carrier induced change of refractive index spectra of (In,Al)GaN quantum well lasers*, Appl. Phys. Lett. **85**, 1475 (2004)

[296] K. Kojima, U. T. Schwarz, M. Funato, Y. Kawakami, S. Nagahama, T. Mukai, *Optical gain spectra for near UV to aquamarine (Al,In) GaN laser diodes*, Opt. Express **15**, 7730 (2007)

[297] Y. K. Song, M. Kuball, A. V. Nurmikko, G. E. Bulman, K. Doverspike, S. T. Shepperd, T. W. Weeks, M. Leonard, H. S. Kong, H. Dieringer, J. Edmond, *Gain characteristics of InGaN/GaN quantum well diode lasers*, Appl. Phys. Lett. **72**, 1418 (1998)

[298] A. Satake, Y. Masumoto, T. Miyajima, T. Asatsuma, M. Ikeda, *Two-dimensional exciton dynamics and gain formation processes in $In_xGa_{1-x}N$ multiple quantum wells*, Phys. Rev. B **60**, 16660 (1999)

[299] J. Ding, T. Ishihara, M. Hagerott, A. V. Nurmikko, H. Luo, N. Samarth, J. Furdyna, *Excitonic gain and laser emission in ZnSe-based quantum wells*, Phys. Rev. Lett. **69**, 1707 (1992)

[300] J. D. Jackson, *Classical electrodynamics* (Wiley, New York, 1962)

[301] J. S. C. Prentice, *Coherent, partially coherent and incoherent ligth absorption in thin-film multilayer structures*, J. Phys. D: Appl. Phys. **33**, 3139 (2000)

[302] D. E. McCumber, *Intensity fluctuations in output of cw laser oscillators .1.*, Phys. Rev. **141**, 306 (1966)

[303] R. Kudrawiec, J. Misiewicz, *Photoreflectance and contactless electroreflectance measurements of semiconductor structures by using bright and dark configurations*, Rev. Sci. Instrum. **80**, 096103 (2009)

[304] H. Shen, M. Dutta, *Sweeping photoreflectance spectroscopy of semiconductors*, Appl. Phys. Lett. **57**, 587 (1990)

[305] D. Yan, H. Qiang, F. H. Pollak, *A new offset technique for suppression of spurious signals in photoreflectance spectra*, Rev. Sci. Instrum. **65**, 1988 (1994)

[306] Q. Li, H. H. Tan, C. Jagadish, *A new optical front-end compensation technique for suppression of spurious signal in photoreflectance spectroscopy using an antiphase signal*, Rev. Sci. Instrum. **81**, 043102 (2010)

[307] M. Sydor, A. Badakhshan, *Differential photoreflectance from a high-mobility and highly luminescent 2-dimensional electron-gas*, J. Appl. Phys. **70**, 2322 (1991)

[308] J. Shao, W. Lu, F. Yue, X. Lu, W. Huang, Z. Li, S. Guo, J. Chu, *Photoreflectance spectroscopy with a step-scan Fourier-transform infrared spectrometer: Technique and applications*, Rev. Sci. Instrum. **78**, 013111 (2007)

[309] T. Kita, M. Yamada, O. Wada, *Dual chopped photoreflectance spectroscopy for nondestructive characterization of semiconductors and semiconductor nanostructures*, Rev. Sci. Instrum. **79**, 046110 (2008)

Nomenclature

Acronyms

ac	alternative current
AFM	Atomic force microscope
AlN	Aluminum nitride
BEC	Bose-Einstein condensation
BS	Beamsplitter
CCD	Charged-coupled device
CL	Cathodoluminescence
CMi	Center of MicroNanoTechnology
cw	Continuous wave
DBR	Distributed Bragg reflector
dc	direct current
dDBRs	Dielectric DBRs
DHS	Double heterostructure
DMM	Digital multimeter
EBL	Electron blocking layer
EELD	Edge emitting LD
EPFL	École polytechnique fédérale de Lausanne
ER	Electroreflectance
FKO	Franz-Keldysh oscillations
FS	Free-standing
FWHM	Full width at half-maximum
GaN	Gallium nitride
HAADF	High angle annular dark field
InN	Indium nitride
IQE	Internal quantum efficiency
IR	Infrared
ITO	Indium tin oxide
Laser	Light amplification by stimulated emission of radiation
LASPE	Laboratory of Advanced Semiconductors for Photonics and Electronics
LD	Laser diode

LED	Light-emitting diode
LO	Longitudinal optical
LPB	Lower polariton branch
LT	Low temperature
MBE	Molecular beam epitaxy
MC	Microcavity
MD	Misfit dislocations
MOVPE	Metalorganic vapor phase epitaxy
MQW	Multiple quantum well
N.A.	Numerical aperture
NUV	Near UV
PL	Photoluminescence
PR	Photoreflectance
QCSE	Quantum confined Stark effect
QD	Quantum dot
QW	Quantum well
RCLED	Resonant-cavity LED
RIE	Reactive-ion etching
RIN	Relative intensity noise
RT	Room temperature
SCER	Semi-contactless electroreflectance
SCR	Strong coupling regime
SEM	Scanning electron microscope
SPS	Short-period superlattice
SQW	Single quantum well
SS	Stokes shift
STEM	Scanning transmission electron microscope
TCO	Transparent conducting oxide
TDD	Threading dislocation density
TEGa	Triethyl-gallium
TEM	Transmission electron microscope
TMAl	Trimethyl-aluminum
TMGa	Trimethyl-gallium
TMIn	Trimethyl-indium
TMS	Transfer matrix simulation
UPB	Upper polariton branch
UV	Ultra violet
VCSEL	Vertical-cavity surface-emitting laser
VRS	Vacuum Rabi splitting
XRD	X-ray diffraction

Symbols

a	Acoustic and optical phonon relaxation rate
A	Absorption
a_B	Exciton Bohr radius
a_{BE}	Bose-Einstein parameter
a_{sub}	Substrate in-plane lattice parameter
$a(x)$	Alloy in-plane lattice parameter
b	Exciton-exciton scattering rate
b_{BG}	Bandgap bowing
c	Exciton-free carrier scattering rate
C	Cavity mode
d	Dimension
E_B	Exciton binding energy
E_g	Energy bandgap
f_{osc}	Oscillator strength
F_{SQW}	Built-in electric field in SQW
g	Light-matter coupling constant
$g^{(1)}(\tau)$	First-order coherence function
h_{crit}	Critical thickness for relaxation
$H(\omega)$	Modulation transfer function
I_p	Excitation Intensity
J	Electric pumping rate
J_{thr}	Threshold current density
k_{op}	Imaginary part of the complex refractive index or extinction coefficient
l_B	Barrier thickness
L_c	Cavity length
L_{DBR}	DBR penetration depth
L_{eff}	Effective cavity length
l_W	Well thickness
m_e^*	Electron effective mass
m_h^*	Hole effective mass
m_{ph}^*	Photon effective mass
n_c	Cavity refractive index
n_d	Free-carrier density due to doping per unit surface
n_{e-h}	Electron-hole pair density
n_h (n_l)	Higher (lower) refractive index of DBR pair
n_{op}	Real part of the complex refractive index
n_p	Polariton concentration
n_x	Exciton concentration
n_e'	Free carrier concentration
N_{QW}	Number of QWs

$N_{QW/AN}$	Number of QWs per antinode
$N_{QW,eff}$	Number of QWs coupled to the cavity light field
P_0	Output power
P^{pz}	Piezoelectric polarization
P^{sp}	Spontaneous polarization
P_{thr}	Threshold pumping density
P_x	Pumping strength
Q	Quality factor
R	Reflectivity
S	Device size
T	Transmission
T_{latt}	Lattice temperature
u	Relative anion-cation bond length
u_c	Anion-cation bond length
v_g	Group velocity
w	Depletion width
W	Exciton formation rate
X	Free exciton mode
X_A	Free A exciton
X_B	Free B exciton
α_V	Varshni parameter
$\alpha(\omega)$	absorption coefficient
α^2	Linewidth enhancement factor
β	$1/k_B T$
β_V	Varshni parameter
γ_{LD}	Emission linewidth above threshold of conventional LDs
γ_{polLD}	Emission linewidth above threshold of polariton LDs
γ_{PR}	PR linewidth
γ_{ST}	Modified Schawlow-Townes linewidth
Γ_{abs}	Absorption linewidth
Γ_{cf}	Confinement factor
Γ_h	FWHM of the homogeneous absorption line
Γ_{inh}	FWHM of the inhomogeneous absorption line
Γ_{PL}	FWHM of the PL line
ϵ_r	Relative permittivity
$\epsilon(\omega)(\epsilon(\lambda))$	Dielectric function
δ	Detuning
Δ_{esc}	Energy splitting between LPB(0) and the LPB inflection point
δ_{opt}	Optimal detuning
η_{int}	IQE
Θ_{BE}	Bose-Einstein parameter

μ	Chemical potential
μ^*	Reduced mass
μ-PL	Micro-PL
μ-Transmission	Microtransmission
τ_c	Coherence time
τ_{cav}	Cavity lifetime
τ'_{cav}	Effective cavity lifetime
τ_{e-h}	Electron-hole pair lifetime
τ_p	Polariton lifetime
τ'_p	Effective polariton lifetime
τ_x	Exciton lifetime
Φ_B	Barrier height
Ω_{VRS}	Vacuum Rabi splitting
ω_{osc}	Relaxation resonance frequency
ω_{3dB}	Cut-off frequency
$\hbar\Theta$	Electro-optic energy
$\tilde{n}$	Complex refractive index

Constants

c	Speed of light	299792458	(m/s)
e	Elementary electric charge	$1.60217656535 \cdot 10^{-19}$	(C)
h	Planck constant	$4.13566751691 \cdot 10^{-15}$	(eV·s)
$\hbar$	Reduced Planck constant	$h/2\pi$	(eV·s)
k_B	Boltzmann constant	$8.617332478 \cdot 10^{-5}$	(eV/K)
m_0	Electron mass	$9.1093829140 \cdot 10^{-31}$	(kg)
$R_{y,H}$	Rydberg energy	13.605 692 53	(eV)
ϵ_0	Vacuum permittivity	$8.854187817 \cdot 10^{-12}$	(C/V·m)

Remerciements

La réalisation d'un travail de thèse représente un défi particulier qui ne demande pas seulement un grand investissement personnel, de la persévérance et beaucoup de détermination mais aussi le support des autres. C'est à cet endroit que je souhaite exprimer ma gratitude envers les chercheurs passionnés dont j'étais entourée pendant ces dernières 4 années.

En premier lieu, je remercie mon professeur, Nicolas Grandjean, pour m'avoir donné la possibilité de pouvoir travailler sur un sujet de recherche aussi passionnant. Il a toujours été disponible pour fournir des conseils précieux et des nouvelles idées stimulantes en me donnant la possibilité d'aborder ma recherche de manière très autonome.

J'ai eu la chance d'avoir Raphaël Butté comme co-directeur de thèse. Il a été la personne clé pour la réussite de ce travail. Je suis très reconnaissante de son incroyable disponibilité et de son soutient ininterrompu surtout pour tout son retour et input pour mes présentations et pour l'écriture d'articles et de la thèse.

Je voudrais ensuite remercier le Prof. Christophe Moser pour avoir présidé mon jury de thèse ainsi que tous les membres qui ont accepté de lire et de juger le présent travail: Prof. Tadek Suski, Dr. Bernard Gil et Dr. Marcia Portella-Oberli.

Je souhaiterais remercier mes collègues internationaux qui ont contribué à ce travail de thèse: Prof. Alexey V. Kavokin, Dr. Ivan Iorsh, et l'équipe de l'université d'Otto-von-Guericke de Magdeburg.

Ensuite, un grand merci à toutes les personnes qui ont fait un tour au LASPE. Ils ont volontairement partagé leur savoir-faire et en plus ils ont contribué à une atmosphère très amicale: Merci à Marco et Lorenzo pour être des collègues de bureau formidable, toujours intéressés par mon travail et fournisseurs de super conseils et idées. Merci à Lise pour le travail sur les couches épaisses à base d'InGaN. Merci à Noelia pour la fabrication des nano-colonnes. Merci à Gatien pour m'avoir introduit à la fabrication de microcavités et pour la collaboration

avec Xi sur les VECSEL. Merci à Jacques et Georg pour tout ce qui concerne la spectroscopie et les simulations de Matlab. Merci à Nils et Munise pour comprendre d'avantage l'InGaN soit pour la croissance soit pour le couplage fort. Merci à Etienne pour les simulations en Nextnano. Merci à Luca pour la collaboration pendant l'assistanat de physique générale et les mesures d'électroréflectance avec Christian. Merci à Jean-François pour m'avoir introduit à la croissance MOVPE. Merci à Julien pour m'avoir introduit à des techniques de salle blanches toujours avec un calme extraordinaire. Merci au sputtering-dream-team: Nicolas Leiser, François Morier-Genoud, Denis Martin, Jean-Michel Lamy (merci aussi pour toutes les astuces salles blanches & vélo). Merci à Mehran et Gwénolé pour les mesures de PL résolues en temps. Merci à Damien, Yoan, et Roger pour tout le support technique. Merci à Aline et Nadja pour le support administratif. Merci à mes deux étudiants de Master, Afsoon et Christian pour leur travail et surtout leur intérêt et enthousiasme. Et merci à tous les autres: Gabriel, Guillaume, Amélie, Alexei, Eric, Marco&Nino, Nicola, Yoshi, Jérôme, et Marcus.

Un grand merci aussi à mes amis, mes colocataires, ma famille et Jonas.

Lausanne, le 15 octobre 2014 Marlene Glauser

Marlene Glauser

Education

2010-2014	**PhD in Photonics**, EPFL, Lausanne.
2004-2010	**Bachelor and Master of Physics**, EPFL, Lausanne.
2001-2004	**Highschool**, Mathematisch-Naturwissenschaftliches Gymnasium Bern-Neufeld, Bern

Languages

German	**native**	*C2*	French	**fluently**	*C1*
English	**fluently**	*C1*	Italian	**basic**	*A2*

Skills

Computing: Software knowledge (Microsoft Office, Origin, LaTeX), Programming (C++, Python, Matlab, Mathematica).

Teaching: Maths (at Didac Schulen AG, Lausanne), General Physics I & II for the faculties of Maths and Microtechnics, and supervision of Physics master-students (at EPFL, Lausanne).

Semiconductor growth and processing: Metal organic chemical vapor deposition (MOCVD) of III-nitrides, photolithography, dry etching, sputtering.

Material characterization: Spectroscopy (photoluminescence, photoreflectance, ellipsometry, Fourier spectroscopy), X-ray diffraction, Atomic Force Microscopy (AFM), and Scanning Electron Microscopy (SEM).

Projects

9.2009-2.2010 — **Masterproject**, EPFL, Lausanne: **Fourier spectroscopy in the UV-visible range**: A powerful method for investigating the optical properties of III-nitride based microcavities and planar photonic crystals.
Main achievements: Built-up from scratch of a Fourier spectroscopy setup in the UV-visible range.

7.-8.2007 — **Undergraduate Trainee in Solid State Physics**, Paul Scherrer Institut, Villigen: Elaboration of thin high temperature superconducting layers by Pulsed Laser Deposition (PLD).

Internships

7.-9.2009 — **IAESTE Trainee in Greece**, Prime Laser Technology, Keratea (Athens): Participation in production of solar collector parts.

3.-6.2008 — **Undergraduate Trainee in Metrology**, Federal Office of Metrology METAS, Wabern (Bern): Testing, upgrading and characterizing differents generators of nanoparticles. For the characterization of the generateurs a SMPS (Scanning Mobility Particle Sizer) and a CPC (Condensation Particle Counter) has been used.

Chemin Aime-Steinlen 10 – 1004 Lausanne
mobile 079 265 20 74 • email marlene.glauser@hotmail.com
Date of Birth: 01.09.1985 - Nationality: Swiss - Marital Status: Single

Publications

- G. Schmidt, M. Müller, P. Veit, F. Bertram, J. Christen, **M. Glauser**, J.-F. Carlin, G. Cosendey, R. Butté, and N. Grandjean, *Nano-scale luminescence characterization of individual InGaN/GaN quantum wells stacked in a microcavity using scanning transmission electron microscope cathodoluminescence*, Appl. Phys. Lett. **105**, 032101 (2014).
- **M. Glauser**, C. Mounir, G. Rossbach, E. Feltin, R. Butté, J.-F. Carlin, N. Grandjean, *InGaN/GaN quantum wells for polariton laser diodes: Role of inhomogeneous broadening*, J. Appl. Phys. **115**, 233511 (2014).
- E. Hashemi, J. Bengtsson, J. Gustavsson, M. Stattin, **M. Glauser**, G. Cosendey, N. Grandjean, M. Calciati, M. Goano, and A. Haglund, *Triggering of guiding and antiguiding effects in GaN-based VCSELs*, Proc. SPIE **9001**, 90010A (2014).
- Ž. Gaevi, G. Rossbach, R. Butté, F. Réveret, **M. Glauser**, J. Levrat, G. Cosendey, J.-F. Carlin, N. Grandjean, and E. Calleja, *Q-factor of (In,Ga)N containing III-nitride microcavity grown by multiple deposition techniques*, J. Appl. Phys. **114**, 233102 (2013).
- **M. Glauser** and R. Butté, *Relative intensity noise and emission linewidth of polariton laser diodes*, Phys. Rev. B **88**, 115305 (2013).
- X. Zeng, D. L. Boïko, G. Cosendey, **M. Glauser**, J.-F. Carlin, and N. Grandjean, *In-depth analysis of injection-seeded long external cavity InGaN/GaN surface-emitting laser*, J. Appl. Phys. **113**, 043108 (2013).
- R. Butté, G. Cosendey, L. Lugani, **M. Glauser**, A. Castiglia, G. Perillat-Merceroz, J.-F. Carlin, and N. Grandjean in *'III-Nitride Semiconductors and Their Modern Devices'*, edited by B. Gil (Oxford University Press, Oxford, UK, 2013).
- J. Levrat, G. Rossbach, A. Dussaigne, G. Cosendey, **M. Glauser**, M. Cobet, R. Butté, and N. Grandjean, *Nonlinear emission properties of an optically anisotropic GaN-based microcavity*, Phys. Rev. B **86**, 165321 (2012).
- X. Zeng, D. L. Boïko, G. Cosendey, **M. Glauser**, J.-F. Carlin, and N. Grandjean, *Optically pumped long external cavity InGaN/GaN surface-emitting laser with injection seeding from a planar microcavity*, Appl. Phys. Lett. **101**, 141120 (2012).
- I. Iorsh, **M. Glauser**, G. Rossbach, J. Levrat, M. Cobet, R. Butté, N. Grandjean, M. A. Kaliteevski, R. A. Abram, A. V. Kavokin, *Generic picture of the emission properties of III-nitride polariton laser diodes: Steady state and current modulation response*, Phys. Rev. B **86**, 125308 (2012).
- **M. Glauser**, G. Rossbach, G. Cosendey, J. Levrat, M. Cobet, J.-F. Carlin, J. Besbas, M. Gallart, P. Gilliot, R. Butté, and N. Grandjean, *Investigation of InGaN/GaN quantum wells for polariton laser diodes*, Phys. Status Solidi C **9**, 1325 (2012).
- G. Rossbach, J. Levrat, A. Dussaigne, G. Cosendey, **M. Glauser**, M. Cobet, R. Butté, and N. Grandjean, H. Teisseyre, M. Bockowski, I. Grzegory, and T. Suski, *Tailoring the light-matter coupling in anisotropic microcavities: Redistribution of oscillator strength in strained m-plane GaN/AlGaN quantum wells*, Phys. Rev. B **84**, 115315 (2011).
- I. Gorczyca, A. Kamińska, G. Staszczak, R. Czernecki, S. P. Łepkowski, T. Suski, H. P. D. Schenk, **M. Glauser**, R. Butté, J.-F. Carlin, E. Feltin, N. Grandjean, N. E. Christensen, and A. Svane, *Anomalous composition dependence of the band gap pressure coefficients in In-containing nitride semiconductors*, Phys. Rev. B 81, 235206 (2010).
- J. Levrat, R. Butté, T. Christian, **M. Glauser**, E. Feltin, J.-F. Carlin, and N. Grandjean, *Pinning and Depinning of the Polarization of Exciton-Polariton Condensates at Room Temperature*, Phys. Rev. Lett. **104**, 166402 (2010).

Chemin Aime-Steinlen 10 – 1004 Lausanne
mobile 079 265 20 74 • email marlene.glauser@hotmail.com
Date of Birth: 01.09.1985 - Nationality: Swiss - Marital Status: Single

Presentations

- M. Glauser, C. Mounir, G. Rossbach, E. Feltin, J.-F. Carlin, **R. Butté**, and N. Grandjean, *InGaN/GaN quantum wells for polariton laser diode applications: what are the challenges?*, (invited Talk), International Workshop on Nitride Semiconductors (Wrocław, August 2014).
- M. Glauser, I. Iorsh, G. Rossbach, J. Levrat, M. Cobet, **R. Butté**, N. Grandjean, M. A. Kaliteevski, R. A. Abram and A. V. Kavokin, *Emission properties of III-nitride polariton laser diodes: steady state and current modulation response*, (contributed Talk), International Workshop on Nitride Semiconductors (Wrocław, August 2014).
- M. Glauser, C. Mounir, G. Rossbach, E. Feltin, J.-F. Carlin, **R. Butté**, and N. Grandjean, *InGaN/GaN quantum wells for polariton laser diode applications: what are the challenges?*, (contributed Talk), International Conference on Physics of Light-Matter Coupling in Nanostructures (Montpellier, June 2014).
- **M. Glauser** and R. Butté, *Emission properties of III-nitride polariton laser diodes: steady state, current modulation response and relative intensity noise*, (contributed Talk), International Conference on Physics of Light-Matter Coupling in Nanostructures (Crete, May 2013).
- **M. Glauser**, C. Mounir, G. Rossbach, J. Levrat, G. Cosendey, J.-F. Carlin, R. Butté, and N. Grandjean, *III-nitride based microcavities: Towards a Polariton Laser Diode*, (invited Talk) Optical Society of America EPFL Student Chapter, SPIE *Pizza-Optics* & *Beer* (POB) event (Lausanne, October 2013).
- **M. Glauser**, G. Cosendey, J. Levrat, G. Rossbach, M. Cobet, A. Althoukov, N. A. K. Kaufmann, J.-F. Carlin, R. Butté, and N. Grandjean, *In Depth Investigation of InGaN/GaN Multiple Quantum Wells Grown on III-Nitride Distributed Bragg Reflectors for Polariton Laser Applications*, (contributed Talk), International Conference on Nitride Semiconductors (Glasgow, July 2011).
- Poster presentations at International Conference on the Physics of Semiconductors (Zurich, August 2012), International Conference on Physics of Light-Matter Coupling in Nanostructures (Berlin, April 2011), and International Conference on spontaneous coherence in excitonic systems (Lausanne, February 2011).

Workshops and Schools

- **M. Glauser**, G. Cosendey, J. Levrat, G. Rossbach, M. Cobet, J.-F. Carlin, R. Butté, and N. Grandjean, *Toward InGaN/GaN quantum well based polariton laser diodes: experimental and theoretical status*, (contributed Talk), ESF PESC Exploratory Workshop: Polaritonics - From Basic Research to Device Applications, (Rom, March 2012).
- Singapore School of Physics: Strong Light-Matter Coupling: from atoms to solid-state systems, (Singapore, June 2012).

Chemin Aime-Steinlen 10 – 1004 Lausanne
mobile 079 265 20 74 • email marlene.glauser@hotmail.com
Date of Birth: 01.09.1985 - Nationality: Swiss - Marital Status: Single